Contributions to the design of

Energy Harvesting Systems for Autonomous Sensors

in low power marine applications

PhD Thesis

Matias Carandell Widmer

CONTRIBUTIONS TO THE DESIGN OF ENERGY HARVESTING SYSTEMS FOR AUTONOMOUS SENSORS IN LOW POWER MARINE APPLICATIONS

Article-based PhD Thesis

Thesis submitted in partial fulfillment of the requirement for the PhD Degree issued by the Universitat Politècnica de Catalunya, in its Electronic Engineering Program

Matias Carandell Widmer

Supervisors:

Dr. Joaquín del Río Fernández

Dr. Manel Gasulla Forner

April 2022

Matias Carandell Widmer, 2022

Contributions to the Design of Energy Harvesting Systems for Autonomous Sensors in Low Power Marine Applications

Matias Carandell Widmer

SARTI-MAR Research Group

Electronic Engineering Department

Universitat Politècnica de Catalunya

Rambla de l'Exposició 24, Edifici C, 08800

Vilanova i La Geltrú, Spain

<matias.carandell@upc.edu>

ABSTRACT

Oceanographic sensor platforms provide biological and meteorological data to help understand changes in marine environment and help to preserve it. Lagrangian drifters are autonomous passive floating platforms used in climate research to obtain surface marine data. They are low-cost, versatile, easy-to-deploy and can cover large extensions of the ocean when deployed in group. These deployments can last for years, so one of the main design challenges is the autonomy of the drifter. Several energy harvesting (EH) sources are being explored to reduce costs in battery replacement maintenance efforts such as solar panels. Drifters must avoid the impact of the wind because this may compromise proper surface current tracking and therefore, should ideally be mostly submerged. This interferes with the feasibility of solar harvesting, so other EH sources are being explored such as the oscillatory movement of the drifter caused by ocean waves. Wave energy converters (WEC) are the devices that turn this movement into energy.

The motion of the drifter can principally be described by 3 oscillatory degrees of freedom (DoF); surge, heave and pitch. The heave motion includes the buoyancy's response of the drifter, which can be explained by a mass-spring-damping model. By including the wave's hydrodynamic load in this model, it is converted into a nonlinear system whose frequency response includes the wave's frequency and the natural frequencies from the linear system. A smart option to maximize the captured energy is to design the inner WEC with a natural frequency similar to that of the drifter's movement. In this thesis, a 4 DoF model is obtained. This model includes the heave, the surge and the pitch motion of the drifter in addition to the inner pendulum motion relative to the buoy. Simultaneously, different pendulum-type WECs for small-size oceanic drifters are proposed. One of these converters consists of an articulated double-pendulum arm with a proof mass that generates energy through its relative motion with the buoy. Different experimental tests are carried out, with a prototype below 10 cm in diameter and 300 g of total mass, proving the capability of harvesting hundreds of microwatts in standard sea conditions

EH sources require an additional power management unit (PMU) to convert their variable output into a constant and clean source to be able to feed the sensor electronics. PMUs should also ensure that the maximum available energy is harvested with a maximum power point tracking (MPPT) algorithm. Some sources, such as WECs, require fast MPPT as its output can show relatively rapid variations. However, increasing the sampling rate may reduce the harvested energy. In this thesis, this trade-off is analyzed using the resistor-based fractional open circuit voltage-MPPT technique, which is appropriate for low-power EH sources. Several experiments carried out in marine environments demonstrate the need for increasing the sampling rate. For this purpose, the use of a commercial PMU IC with additional low-power circuitry is proposed. Three novel circuits with a sampling period of 60 ms are manufactured and experimentally evaluated with a small-scale and low-power WEC. Results show that these configurations improve the harvested energy by 26% in comparison to slow sampling rate configurations.

Finally, an EH-powered oceanographic monitoring system with a custom wave measuring algorithm is designed. By using the energy collected by a small-size WEC, this system is capable of transmitting up to 22 messages per day containing data on its location and measured wave parameters.

Keywords: Lagrangian Drifter, Energy Harvesting, Wave Energy Converter, Power Management Unit, Maximum Power Point Tracking, Fractional Open Circuit Voltage.

RESUM

Les plataformes d'observació oceanogràfiques integren sensors que proporcionen dades físiques i biogeoquímiques de l'oceà que ajuden a entendre canvis en l'entorn marí. Un exemple d'aquestes plataformes són les boies de deriva (*drifters*), que són dispositius autònoms i passius utilitzats en l'àmbit de la recerca climàtica per obtenir dades in-situ de la superfície marina. Aquests instruments són de baix cost, versàtils, fàcils de desplegar i poden cobrir grans superfícies quan s'utilitzen en grup. L'autonomia és un dels principals desafiaments en el disseny de *drifters*. Per tal d'evitar els costos en la substitució de bateries, s'estudien diferents fonts de captació d'energia com per exemple la solar. Els *drifters* utilitzats per l'estudi dels corrents marins superficials han d'evitar l'impacte directe del vent ja que afecta al correcte seguiment de les corrents i, per tant, cal que estiguin majoritàriament submergides. Això compromet la viabilitat de l'energia solar, fet que requereix l'estudi d'altres fonts de captació com el propi moviment de la boia causat per les onades. Els convertidors d'energia de les onades (*WEC, wave energy converters*) compleixen aquesta funció.

El moviment dels *drifters* pot explicar-se bàsicament a través de 3 graus de llibertat oscil·latoris: la translació vertical i la horitzontal i el balanceig. La translació vertical inclou la flotabilitat del dispositiu, que es pot descriure mitjançant el model massa-molla-amortidor. Incloure la càrrega hidrodinàmica de l'onada en aquest model el converteix en un sistema no lineal amb una resposta freqüencial que inclou la de l'onada i les naturals del sistema lineal. Una opció per maximitzar l'energia captada és dissenyar el *WEC* amb una freqüència natural similar a la del moviment de la boia. En aquesta tesis es proposa un model de 4 graus de llibertat per a l'estudi del moviment del *drifter*. Aquest inclou els 3 graus de llibertat de la boia i el moviment del pèndul relatiu a ella. En paral·lel, es proposen diferents *WEC* del tipus pendular per *drifters* de reduïdes dimensions. Un d'aquests *WEC* consisteix en un doble braç articulat amb massa flotant que genera energia a través del seu moviment relatiu al *drifter*. S'han dut a terme diferents proves experimentals amb un prototip inferior a 10 cm de diàmetre i 300 g de massa, les quals demostren la seva capacitat de captar centenars de microwatts en condicions marines estàndard.

Utilitzar fonts de captació d'energia requereix incloure una unitat gestora de potència (*PMU, power management unit)* per tal de convertir la seva sortida variable en una font constant i neta que alimenti l'electrònica dels sensors. Les *PMU* també tenen la funció d'assegurar que es recull la màxima energia mitjançant un algoritme de seguiment del punt de màxima potència. Els *WEC* requereixen un seguiment d'aquest punt ràpid perquè la seva sortida consta de variacions relativament ràpides. Tanmateix, augmentar la freqüència de mostreig pot reduir l'energia captada. En aquesta tesi, s'analitza a fons aquesta relació utilitzant la tècnica de seguiment de la tensió en circuit obert fraccionada basada en resistències, que és molt adequada per a fonts de baixa potència. Diversos experiments realitzats en el medi marí mostren la necessitat d'augmentar la freqüència de mostreig, així que es proposa l'ús de *PMU* comercials amb una electrònica addicional de baix consum. S'han fabricat tres circuits diferents amb un període de mostreig de 60 ms i s'han avaluat experimentalment en un *WEC* de reduïdes dimensions. Els resultats mostren que aquestes configuracions milloren l'energia recollida en un 26% en comparació a *PMU* amb mostreig més lent.

Finalment, s'ha dissenyat un sistema autònom de monitorització marina que inclou un algoritme de mesura d'ones propi. Aquest sistema és capaç de transmetre fins a 22 missatges al dia que contenen la seva ubicació i els paràmetres d'ona mesurats i que s'alimenta de l'energia recollida per un *WEC* de reduïdes dimensions.

UNIVERSITAT POLITÈCNICA
DE CATALUNYA
BARCELONATECH

ACKNOWLEDGEMENTS

After assiduous work, infinite experiments and endless hours of writing, this thesis would not have reached its final stage without the valuable insight and support of many people who have accompanied me throughout this inspiring and intellectually stimulating journey.

I would like to start by expressing my sincere gratitude to Dr. Joaquin del Rio for believing in me from the beginning and for his continued faith in me throughout the years. I am extremely grateful for all his guidance and for his willingness to always listen and come up with solutions during the tough times.

I am also very grateful to Dr. Manel Gasulla. This thesis could not have been possible without his invaluable supervision, support and tutoring. His immense knowledge and meticulous critiquing have been essential in shaping my work. Our numerous meetings and conversations encouraged me to think outside the box and to acquire a more critical perspective of my study.

I would also like to thank Dr. Daniel Mihai Toma for always being there; as a counselor, mentor, critic, revisor but most importantly, as a friend. I have benefited immeasurably from his wealth of knowledge and help in the experimental part of this thesis. I cherish the infinite phone calls, the stimulating discussions and all the laughs we shared during the process. No amount of coffee capsules would ever be enough to pay for his contribution to this thesis.

I am grateful to Enoc Martínez and Marc Nogueras for making SARTI a great working environment and for being the best dive buddies one could ask for; I know spotting Sunfishes during our dives is something they look forward to as much as I do. My appreciation also goes out to Ivan Masmitjà, Ahmad Falahzadeh, David Sarrià, Javier Cadena and all the other SARTI members for their kind help and support during all these years.

My sincere thanks also go out to Dr. Ana Barjau for her guidance throughout the mechanical modelling process. Her level of patience, knowledge and thoughtfulness is something that I hold in high esteem. I would also like to thank Dr. Andrew S. Holmes for allowing me to work alongside him during my stay in London and for his help with the design of the power management circuits. I extend my thanks to Dr. Panagiotis Alevras for the opportunity given to collaborate with him in Birmingham and for his assistance with the double-pendulum WEC model.

A very special gratitude goes out to the MELOA project for the uncountable opportunities, infrastructure and field experiment results they provided me with. The special trips to Oporto, Lisbon, Toulouse and La Palma were a great opportunity for me to broaden my vision and to step outside the lab.

My family deserves endless gratitude and recognition. My father, Juli, for his immeasurable encouragement and enthusiasm, my mother, Ana, for always being there and cooking for me when I was too tired to do so, and my sister, Lola, for making me laugh and for reminding me of what is truly important. I am very grateful that I had her by my side during the uncertain and challenging times of the Covid-19 confinement.

And last but not least, I would like to thank Christie, for listening to me for hours upon hours and for giving me the strength to complete my PhD thesis with endless enthusiasm. I am grateful for her unconditional love and support throughout this arduous process and most importantly, for being by my side every day.

UNIVERSITAT POLITÈCNICA DE CATALUNYA BARCELONATECH

CONTENT

LIST OF ACRONYMS

ABS	Acrylonitrile Butadiene Styrene
AC	Alternating current
ADC	Analog to Digital Converter
ADCP	Acoustic Doppler Current Profiler
AI	Analog Devices
AS	Autonomous Sensor
AUW	Autonomous Underwater Vehicle
CLS	Collecte Localisation Satellites
CNES	Centre National d'Études Spatiales
CODE	Coastal Ocean Dynamics Experiment
CV	Constant Voltage
DC	Direct current
DoF	Degree of Freedom
DW	Discrimination Window
DWS	Directional Wave Spectra
EB	Evaluation Board
EG	Electrical Generator
EH	Energy Harvesting
EMODnet	European Marine Observation and Data Network
EMSO	European Multidisciplinary Seafloor and water column Observatory
ES	Energy Supervision
ESE	Energy Storage Element
FC	Fuel Cell
FFT	Fast Fourier Transform
FOCV	Fractional Open Circuit Voltage
FW	Flywheel
GPS	Global Positioning System
GR	Gimbal Rings
GS	Gear System
GSM	Global System for Mobile communications
HPF	High Pass Filter
IC	Integrated Circuit
IMU	Inertial Measurement Unit
INESCTEC	Institute for Systems and Computer Engineering, Technology and Science

ISR	Institure for Systems and Robotics
LDO	Low Dropout regulator
LPWAN	Low-Power Wide Area Network
LT	Linear Technology
MELOA	Multi-purpose/Multi-sensor Extra Light Oceanography Apparatus
MPP	Maximum Power Point
MPPT	MPP Tracking
MR	Main Ring
NOAA	National Organization and Atmospheric Administration
OA	Operational Amplifier
OBSEA	Expandable Seafloor Observatory
OC	Open Circuit
O-H	Ochi-Hubble
OW	One-way Bearing
P&O	Perturb and Observe
PA	Pendulum Arm
PE	Power Extraction
PFM	Pulse Frequency Modulation
PM	Proof Mass
PMU	Power Management Unit
PSD	Power Spectral Density
PV	Photovoltaic
PVDF	Polyvinylidene Difluoride
PWM	Pulse Width Modulation
PZT	Piezoelectric device
RF	Radio Frequency
RO	Relaxation Oscillator
RTC	Real-time clock
S&H	Sample and Hold
SARTI	Sistemes d'Adquisició Remòta i Tractament de la Informació
SBCM	Statically Balanced Compliant Mechanism
SD	Secure Digital
SI	Storage Interaction
SPDT	Single Pole Double Throw
SR	Slew Rate
SVP	Surface Velocity Program
SWL	Still Water Line
TEG	Thermoelectric Generator
TI	Texas Instruments
µC	Microcontroller
UPC	Universitat Politècnica de Catalunya
VS	Voltage Supply
WEC	Wave Energy Converter
WEH	Wind Energy Harvester
WL	WAVY Littoral
WO	WAVY Ocean

Chapter 1
INTRODUCTION

1.1. Ocean Monitoring

Scientific community requirements related to oceanographic data availability are growing fast. Oceans and seas must be monitored to preserve their biodiversity and to predict their evolution. This means that large amounts of data from a very broad range of sensors must be acquired and delivered quickly. Nevertheless, seas are vast and hostile territories where instrumentation needs to be placed. Engineers have to deal with corrosion concerns, high tightness requirements and strong currents which can cause unquantifiable damage to the equipment. For this reason, technology is evolving. The times of research vessels collecting data from the ocean during extended periods are becoming unusual due to the vessel´s high-costs, low availability and ability to only cover small areas. According to [1], recent advances in oceanographic theory, instrumentation techniques and sensors have led to a new age of marine data collection.

As an example, ocean equipment is increasing its precision and achieving higher acquisition sampling rates. Communication channels now allow for higher bandwidth data transfer, sometimes real-time supported, so enormous amounts of raw data are generated and need to be processed. This means that storage units are required to be moved into cloud server-based services with high processing resources. Also, the analysis of this data has had to evolve and marine instrumentation is now equipped with embedded processing software in order to transmit just the crucial parameters.

Additionally, politicians are taking note of these advances and society is aware of the importance of monitoring the oceans. The European Commission invests in international projects that collect and distribute marine data such as EMODnet (refer to [2]), an online network that freely offers marine data products. Other initiatives, such as EMSO (refer to [3]), group a multidisciplinary network of European seafloor observatories in order to offer a long-term real-time marine monitoring infrastructure. All this amount of data, which comes from different sources and belongs to different scientific fields, need to be merged so efforts in the standardization are also becoming a must. [4] is a great example of this.

One key point of this growth in oceanographic data acquisition and availability is the evolution of sensor platforms. The scientific community now counts on an intelligent network of collecting devices distributed around the world. A wide range of sensor platforms are available, from autonomous to cabled, or from fixed to mobile and they can store the data or send it in real time. Some of these platforms are briefly presented below

Underwater cabled observatories are unmanned platforms placed on a fixed site, normally allocated on the seafloor, which contain an array of sensors and a command module. Thanks to the shore cable, these platforms offer very high power and bandwidth availability and the possibility for long-term, real-time deployments at a high sample rate. However, being fixed platforms, they can only effectively monitor a small portion of the ocean. One example is the OBSEA Observatory, described in P.[5] and placed at 4 km from the coast of Vilanova i la Geltrú, at 20 meters depth (Figure 1.a). Other cabled seafloor observatories can be found around the European waters, some of them reported in [6]–[9].

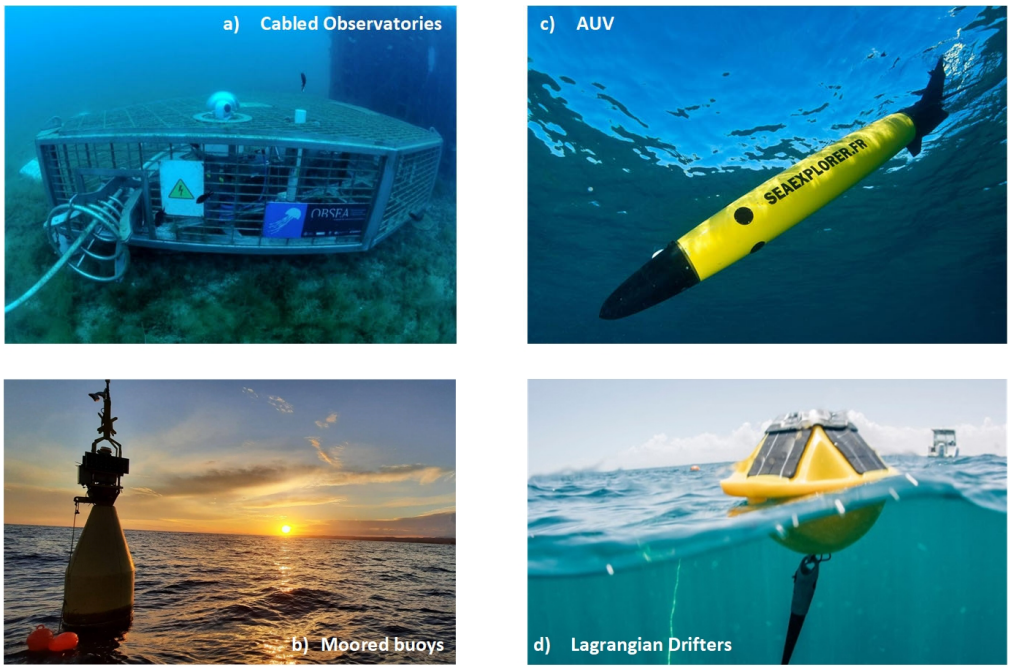

Figure 1. Oceanographic sensor platforms: (a) Cabled observatory - P.[5], (b) Moored buoy - [10] (c) Autonomous underwater vehicle (AUV) - [13] and (d) Lagrangian Drifter - [17].

Moored buoys (Figure 1.b from [10]) are instrumented to measure both upper ocean and surface data. Colum water analysis can also be performed. The cost of these units is relatively high but its power availability is not a major constraint thanks to a set of photovoltaic (PV) panels (normally included). The communication is commonly wireless, GSM-based or Satellite depending on the buoy's location. For example, in [11], GSM-based communication is used for near-coastal seismic data transfer. Others, like the one presented in [12], use satellite based communication.

Autonomous underwater vehicles (AUVs - Figure 1.c) are unmanned moving platforms that measure oceanographic parameters from the sea surface to the seafloor; e.g. article [13]. They sink for periods, collect data and then come up to send the data using a satellite connection. They can cover large portions of the ocean but they lack long-life autonomy. One specific application for these AUVs is the tracking of underwater species using acoustic modems as done in [14]. The vertical position into the water column is controlled in [15] by the buoyancy of the unit, inflating or deflating a ballast to sink or refloat. The horizontal movement can be controlled by propellers or just with the wings, turning the vertical motion into forward motion and thus expanding its autonomy. [16] reports an AUV moving forward with wings.

Lagrangian drifters (Figure 1.d - [17]) are small, low-cost, versatile and easy-to-deploy units that monitor the ocean while passively following the surface current. Drifters do not offer high volume of data compared to other platforms and its power availability is very low. Nevertheless, arrays of drifters can cover large oceanic areas, sending regular data for long periods that can reach up to 2 years of deployment. Consequently, the autonomy of these devices is crucial and this research work will contribute to this topic.

Platform	Measuring point	Depl. & maint. cost	Power availability	Comm.	Data volume
Cabled Obs.	Seafloor – fixed	Very high	Very high	Cabled – Real time	Very high
Moored Buoys	Water column – fixed	High	High	Wireless – Near real time	High
AUV	Sea-surface and underwater – mobie	Medium	Low	Wirerless – Limited	Low
Lagrangian Drifters	Sea-surface – mobile	Low	Very low	Wirerless – Very limited	Very low

Table 1. Qualitative comparison between some oceanographic sensor platforms.

To sum up, different oceanic sensor platforms are used to monitor the sea. They are complementary and each one fits into a different application. Table 1 qualitatively summarizes the differences between them.

1.2. **Lagrangian Drifters**

Lagrangian drifters are oceanographic measuring platforms mainly used to monitor surface circulation patterns. These are passive devices that follow the water flow without any propeller. Drifters help scientists to better understand the complex dynamics of the ocean as well as biological phenomena such as microorganism's movements. Applications where these platforms can be used are diverse; climate research, oil spill tracking, weather forecasting and search and rescue operations. Lately, drifters have found another field of work; the calibration of HF radar and satellite measuring systems for sea surface parameters.

Drifters consist of a buoy and a drogue at a certain depth (see Figure 2); the buoy provides floatability and the drogue is placed at the depth where the currents are to be studied, pushing the system forward. The sizes of the buoy ranges from 10 to 50 centimeters in diameter and drogues can reach 15 m depth such as in [18], [19]. Nevertheless, not all drifters are drogued. Some of them are designed to follow the upper surface level of current flow. In this case, the design of the unit is very important. If the drifter aims to follow the currents, the smallest buoy volume should be exposed to the wind. Yet, not all the buoy can be submerged, the antenna should be above the water line to ensure the communication link. This buoyancy trade-off must be considered in the design of the unit. In [20], [21], it was demonstrated that the downwind "slip" (percentage of drifter motion caused by the wind force) is around 0.1% of the motion in drogued drifters and 1% in undrogued drifters, which is quite significant.

In terms of communication, drifters are usually equipped with satellite based transmitting modules to ensure oceanic coverage. For this purpose , Iridium-[22] is the most common system, although Argos-[23] or Inmarsat-[24] are also used. In general, Iridium provides higher coverage and bandwidth while Argos is cheaper and less power consuming. Argos can also estimate the position from the transmission (100 m precision), so it can avoid the necessity for the GPS if no high precision is required. GSM communication is another option when the deployment is near the coast line; e.g. in [25]. In terms of energy, drifters are powered with batteries placed at the lower hemisphere of the buoy to stabilize its pendulum movement and to ensure that the antenna is always facing upwards. These batteries are normally rechargeable lithium-based cell packs that allow an autonomy ranging from a few hours to a couple of years. The autonomy of the drifter will be further analyzed in the next section.

The National Organization and Atmospheric Administration, NOAA, is an American institution that created the Global Drifter Array, online available at [26]. This program includes more than 1200 active units deployed world-wide and it normalizes the drifters' standards. The Surface Velocity Program (SVP - [27]) drifter is the most common one. It is a spherical buoy of 35 cm of diameter with a drogue placed at 15 meters (distance from the water line to the middle of the drogue). The SVP units uses Iridium

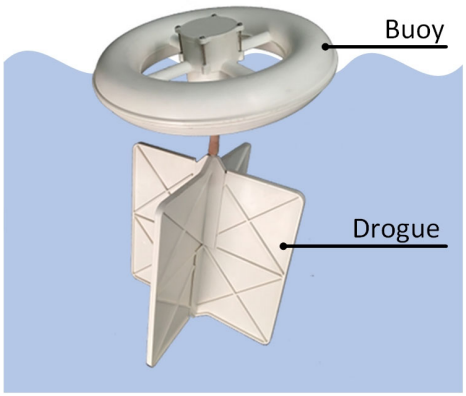

Figure 2. CARTHE drifter (by Pacific Gyre) reported in [29], including the buoy and a small-size drogue.

communications and are equipped with a near-surface temperature sensor. Several other devices evolved from the SVP; e SVP-S, with a salinity sensor, the SVP-B, for near surface air pressure studies and the Mini-Med, with a speed and direction wind sensor. In order to carry out current measurements at coastal zones the Coastal Ocean Dynamics Experiment (CODE - [28]) drifter was developed. It is a shorter unit, with a 1,5-meter drogue, that can reach shallow waters. The characteristics are quite similar to the SVP drifter and it may incorporate an inertial measurement unit (IMU) to determine the wave spectra. This platform evolved into the CARTHE drifter [29] (Figure 2), much smaller than CODE and biodegradable shaped. Finally, a family of undrogued drifters were set for directional wave spectra (DWS) analysis. These DWS units do not have drogue and are spherically shaped with a diameter of 35 cm. Apart from GPS, the sensors incorporated on them are near-surface temperature sensor and an IMU for wave spectra calculation.

The Multi-purpose/Multi-sensor Extra Light Oceanography Apparatus (MELOA) is an H2020 EC-funded project that is developing a new family of drifters called WAVY drifters. These units are low-cost, easy-to-handle, wave resilient, multi-purpose, multi-sensor and extra light and they are designed to work in all water environments; from deep-sea to inland waters, including coastal areas, river plumes and surf zones. The main objective can be read in [30]: "*Innovate the current market of in-situ measurement systems for marine environments, by providing a low-cost and easy-to-handle solution for in-situ water related data acquisition, in the form of the WAVY drifters family of products*". The MELOA consortium is composed of technology-driven organizations and institutions from Portugal (*Deimos Group, Instituto Hidrografico, ISR, OceanScan, Composite Solutions and*

Company	Name	Sensors	Communicatio n	Shape	Autonomy	EH
Pacific Gyre (USA [31])	Carthe [29]	GPS	Globalstar	Ø = 40 cm, h = 60 cm, P = 4 kg	3 months @ Ti = 5 min	-
	Microstar [32]	GPS, T	Iridium	Ø = 40 cm, h = 122 cm, P = 4,5 kg	1 – 12 months	-
	SVP [27]	GPS, T, B, W	Iridium	Stdm SVP	1 – 2 years @ Ti = 1 hour	-
SofarOcean (USA [17])	Spoondrift [38]	GPS, IMU, T, W	Iridium	h = 36 cm , a = b = 42 cm, P = 5,4 kg	Unlimited @ Ti = 1-2 hour	5x 2 W PV
Zunibal (ES [33])	Anteia	GPS, IMU	GSM or Iridium	Ø = 60 cm, P = 26 kg,	n/a	n/a PV
	ZGT	GPS	Iridium	Ø = 25 cm, h = 18 cm, P = 1.3 kg	n/a	1.7 W PV
Fastwave (AUS [34])	Voyager V3	GPS, T	Iridium	Ø = 25 cm, h = 66 cm, P = 6 kg	300 days @ Ti = 3 hours	-
	Voyager Solar	GPS, T	Iridium	Ø = 31 cm, h = 68 cm, P = 6,7 kg	Unlimited @ Ti = 3 hours	2,8 W PV
MetOcean (USA [35])	CODE/DAVIS	GPS, T	Iridium or Argos	Stdm CODE	3-12 months	-
	iSVP	GPS, T, B	Iridium	Ø = 40 cm, P = 18 kg	18 months	-
	iSPHERE	GPS, T	Iridium	Ø = 34 cm, P = 13,15 kg	6-12 months	-
QuinetiQ (USA [36])	Riverine [37]	GPS, T, D	Iridium	Ø = 15 cm, P = 1.8 kg	24 hours	-
MELOA (EU [30])	WAVY Ocean	GPS, T, IMU	Argos	Ø = 20 cm, P = 3.5 kg	3-4 months @ Ti = 20 min	0.6 W PV
	WAVY Littoral	GPS, IMU	GSM	Ø = 12 cm, P = 0.75 kg	n/a	-
	WAVY Basics	GPS, T	GSM	Ø = 10 cm, P = 0.4 kg	n/a	-

Table 2. Drifter compilation. T = Near Surface Sea Temperature, B = Near Surface Atmospheric Pressure, W = Wind Speed and Velocity, GPS = Position, IMU = Inertial Measurement Unit, Stdm = Standard Measure, D = Single Beam Depth Sensor, P = Weight, Ø = Diameter, h = Height, Ti = Transmission Interval, EH = Energy Harvesting.

INESCTEC), Ireland (*BlueWise Marine*), France (*CLS*) and Spain (*Universitat Politéctinca de Catalunya*), and is one of the economic umbrellas and use case scenario of this thesis.

Table 2 summarizes some of the commercial drifter products that can be found in the market. It shows the possible sensors that a drifter can carry, the different shapes used for the drifter shell and the potential communication systems. The MELOA consortium has designed a family of drifters that have turned out to be among the smallest in the market. The WAVY Ocean (WO) is suitable for open sea long-term studies, the WAVY Littoral (WL) for coastal short-term studies and the WAVY Basics for very specific few-hour deployments. These units will be used throughout this thesis for different purposes.

SofarOcean ([38] reported in Table 2) is a successful American company that sells oceanographic sensors and data services. This company has an array of over one thousand drifters deployed worldwide transmitting marine data hourly. One of these units was deployed back on 2018, it has travelled over 6500 kilometers and is still transmitting. This drifter demonstrates the unlimited life span capability of SofarOcean products.

1.3. **Drifter Autonomy**

According to [18], power autonomy is one of the main challenges in the evolution of drifters. Turning them into autonomous sensor (AS) nodes can only be achieved by drastically reducing their consumption and adding some type of energy harvesting (EH) system to exploit the environment energy sources. Both concepts are analyzed further in this section.

On the one hand, AS nodes mainly include the microcontroller (μC), the transmission module (T_X), the GPS system and the sensors (Figure 3). A significant part of their consumption comes from the transmission. To reduce it, keeping a low duty-cycle is crucial. The node should remain asleep at very low consumption levels and sporadically wake up, acquire data and transmit it. The power levels of several recently published AS nodes are summarized in [39], where common duty-cycles below 1%, sleep consumptions between 0.5 and 50 μW and average powers between 0.1 and 0.2 mW are reported. In the case of drifters, as reported in Table 2, manufacturers use transmission intervals of over one hour to successfully achieve unlimited autonomy ([34] and [38]). Applications that require a higher data rate (such as [30]) do not reach this level even though incorporating EH methods.

On the other hand, a reliable and long-lasting power source is needed to achieve long deployments and to avoid the cost and inconvenience associated with recharging batteries in the middle of the oceans. EH systems have proven to be a reasonably good option to feed AS nodes. Drifter manufacturers tend to use the sun's irradiation. By including PV panels around the drifters' shell, unlimited lifespan can be achieved at some low transmitting interval and favorable solar conditions. As an example, Spoondrift ([38] reported in Table 2) incorporates 2 solar panels of 5 watts each, which is enough to measure, unlimitedly, the directional wave spectra at a sampling rate of 2.5 Hz and a transmission interval of 1 hour. Fastwave designed the Voyager Solar Drifter ([34] reported in Table 2) with 2.8 Watt of PV, enough to transmit unlimitedly the position and the sea surface temperature every three hours. The WO from MELOA ([30]

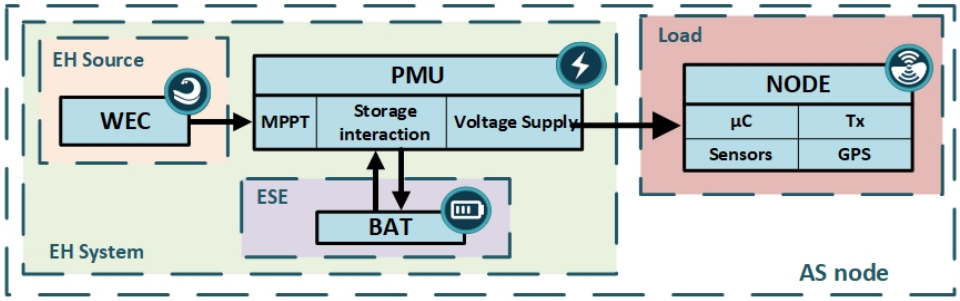

Figure 3. General structure of an Autonomous Sensor (AS) node powered by a wave energy converter (WEC).

reported in Table 2) is also designed to capture the energy from the sun including a PV array of 4 flexible of 150 mW each. Using a transmission interval of 20 minutes, it reaches up to 4 months of autonomy.

If the drifter is solely dedicated to current monitoring, its body should be mostly submerged to avoid the wind affecting its drifting path. The irradiation at the panels would then be greatly attenuated by the water column. Furthermore, solar irradiation could be very low in some oceanic regions during some periods of the year. Biofouling may also grow around drifter's body, reducing further the effectiveness of the PV. For all of these reasons, other energy sources may be explored such as the oscillatory movement of waves. A hybrid EH system could harvest energy from calm sunny days but also from rough and cloudy days. There are no commercial drifters that incorporate other EH sources other than PV, so this thesis addresses this need.

Whether having one or multiple EH systems to expand the drifter's autonomy, an additional power management unit (PMU) is required in order to adapt the low-voltage and random nature of the EH source to a constant and clean output to feed the node. Also, PMUs should manage the possible mismatch of energy between the source and the load by including an energy storage element (ESE) where energy could be stored or dispatched as required. A third function of the PMU is the maximum power point tracking (MPPT) to ensure that the maximum available energy is harvested continuously. As the environmental conditions may change, the PMU should ensure that the maximum power point (MPP) is achieved by continuously tracking the EH operation point. Some sources require a fast tracking of this MPP as its operation point may vary on the order of above 1 Hz. Wind energy harvester (WEH) or wave energy converters (WEC) are some examples of this necessity. [40] and P.[41] present a WEH and a WEC respectively, each with an output voltage oscillating at around 1.8 Hz; this is fast-varying compared to other types of EH sources such as PV devices. Further, in P.[42], we demonstrated that, by reducing the MPPT period in a WEC oscillating at 2 Hz, the harvested energy can improve by up to 25%. Figure 3 presents the general structure of an EH system powering an AS node such as a drifter.

Several companies offer PMU ICs with MPPT functionalities that are compact solutions for very low-power EH applications. These modules can work with multiple EH sources at a relatively low input voltage. The BQ25504/5 (*Texas Instruments*) and the ADP5091/2 (*Analog Devices*) are two of the most widely used devices. However, these PMU are designed for slow-varying EH sources like PV and its MPP update rate is fixed and too slow for some other applications. There is a lack of PMU circuits with MPPT capabilities suitable for fast-varying EH sources such as WEC. This thesis makes a contribution to this need.

1.4. **Objectives**

The need for ocean monitoring increases the importance of developing new low-cost and low-power instrumentation capable of covering large oceanic regions for long periods of time. Drifters are sensor platforms that can effectively provide superficial marine data continuously with low maintenance. Therefore, autonomy is crucial in order to guarantee long deployments reaching up to several years of operation. Many companies incorporate solar panels although they are not the definitive solution for the drifter's autonomy problems. Scavenging the energy of the drifter's motion may be a potential alternative that has not been deeply studied. For this purpose, the dynamics of the drifter under the wave excitation must be studied as well as the potential mechanisms for the mechanical-to-electric energy conversion.

Using an EH source to expand the drifter's autonomy requires including a PMU to fulfill the functionalities of the DC-DC conversion and control of power flow between the EH source, the ESE and the LOAD, depending on the available harvested power, the load requirements, and the charge state of the ESE. The PMU should also perform the MPPT to ensure a maximum energy extraction from the source. Fast-varying sources like the kinetic energy of the drifter call for the adaptation of the MPPT algorithms such as speeding up the update-rate of the MPP reference. Commercial PMUs do not contemplate these requirements.

The objective of this thesis is to contribute to the design of wave energy converter systems in order to increase the autonomy of drifters, or to work as an unlimited back-up battery for recovering the unit. In order to achieve this goal, four specific objectives are defined.

- **Objective 1. Optimize the WEC systems to increase the harvested power while reducing its volume to fit in small-size oceanographic drifters.**
- **Objective 2. Increase the energy extraction efficiency of PMUs by adapting the MPPT algorithms to fast-varying EH source such as the kinetic drifters' motion.**
- **Objective 3. Contribute to the design of low-cost, low-power and EH-powered marine instrumentation to monitor ocean surface parameters on long-term deployments.**
- **Objective 4. Demonstrate the contributions made to EH systems for drifters by performing field tests in different marine environments.**

1.5. Thesis Contributions

Throughout this thesis, different contributions are presented that meet the stated objectives. These contributions were also reported in our different articles, some of them included in appendix A.1 – A.6. To easily differentiate our articles from the rest of the references, they are cited using a prefix P; e.g. P.[60] refers to the article "*Electromagnetic Rolling Mass Wave Energy Harvester for Oceanic Drifter Applications*".

Although this thesis is carried out within the Electronic Engineering doctoral program, it contributes to the WEC systems and thus, to expand the drifters' autonomy from both a mechanical and electronical perspective. Having said this, major contributions have been made in regards to Objective 2, having a clear electronical fit.

- Regarding Objective 1, this thesis studies the wave-drifter interaction and provides a model that describes the motion of the drifter under common swell conditions. This model also includes the motion of an inner single pendulum with the perspective of its parametric excitation as a WEC, which is a novel approach. Simulated and experimental observations are also provided. Several small-scale low-power WEC designs are proposed with different testing status reaching up to experimental sea tests. Up to a few useful milliwatts are reached on average in the experimental tests, which would be enough to feed an ultra-low power ocean monitoring sensor.

Articles contributing to this objective: A.1 – P.[60], A.2 – P.[59], A.5 – P.[58] and A.6 – P.[57].

- This thesis demonstrates the necessity of improving the current PMU in terms of speeding up the sampling rate of its MPPT algorithms for fast-varying EH sources. Several techniques and circuits are proposed, one of them being a novel MPPT method which, to the best of the authors' knowledge, has not previously been reported. Experimental results show a 26 % improvement in the harvested power using the optimized PMU with respect to the commercial references, fulfilling Objective 2.

Articles contributing to this objective: A.2 – P.[59] and A.3 – P.[42].

- In terms of Objective 3, an algorithm to estimate several wave parameters from a buoy's vertical acceleration using very low power and computational resources is designed. An ultra-low power module, including a microcontroller, a 3-axis accelerometer, a GPS and an antenna, deployed in a mooring buoy and fed by a small-scale WEC demonstrates its long-term capability to properly monitor waves.

Articles contributing to this objective: A.4 – P.[130].

- Experimental tests carried out within this thesis include using a long-stroke lineal shaker emulating the drifter's surge motion, using a KUKA robotic arm to emulate the 6 DoF of a drifter under real conditions, deploying units on a wave flume with regular and irregular wave conditions and testing the different designs in open sea. All these tests fulfill Objective 4.

Articles contributing to this objective: A.1 – P.[60], A.2 – P.[59], A.3 – P.[42], A.4 – P.[130], A.5 – P.[58] and A.6 – P.[57].

1.6. Resources and Funding

This thesis was funded by the Secretary of Universities and Research of the Department of Companies and Knowledge of the Generalitat de Catalunya in the FI program (ref. BDNS 362582). The research was also supported by the project MELOA from the European Commission's Horizon 2020 Research and Innovation Program under Grant Agreement no. 776280 and by the Spanish Ministry of Economy and Competitiveness and the European Regional Development Fund under Project TEC2016-76991-P.

The project was done at the Universitat Politècnica de Catalunya (UPC), specifically in the SARTI and e-CAT facilities. The facilities of LIM-UPC wave flume were also used for some of the experimental validations. During the course of this thesis, two international stays were carried out; the first one at the University of Birmingham with Professor Panagiotis Alevras and the second one at the Imperial College of London with Professor Andrew Holmes.

This research work also received funding to cover the transnational access collaboration between the University Collage of Cork, the Tyndall National Institute and the Universitat Politècnica de Catalunya by the European Commission's Horizon 2020 - EnABLES Project under the Grant Agreement No.730957.

Orcina kindly provided the academic license of OrcaFlex under the number N2703 (2022) for the simulations of the drifter's motion under different wave environments, useful for the design of the WECs.

1.7. Content Structure

This thesis is structured as follows:

- Chapter 2 contains the study of the drifter motion under wave excitation, including the description of the wave kinematics and the drifter-water interaction. A general overview of small-scale, low-power WEC for oceanic sensor platforms is given with special attention to the pendulum converters and its parametric excitation. A summary of the proposed small-size WEC is finally given, including the design, manufacturing and experimental results.
- Chapter 3 describes the PMU main functionalities and presents several commercial boards and reported works for low-power EH applications. Second, the focus is on analyzing the MPPT methods for fast-varying EH sources with special attention to the fractional open circuit voltage (FOCV) technique. The proposed circuits for increasing the sampling rate on FOCV-MPPT are finally presented.
- Chapter 4 analyzes the consumption of different low-power oceanographic monitoring systems and the feasibility of powering them with small-scale WEC. A wave monitoring system based on a low-power wide area network (LPWAN) system is proposed for coastal moored buoys.
- Chapter 5 includes the conclusions and future lines of research.

Additionally, in appendix A a copy of the publications included in this article-based thesis can be found. It is worth noting that not all the publications resulting from the work of this thesis have been included. A complete list of the publications is listed in the Publications Section after section 5.

Chapter 2
HARVESTING ENERGY FROM THE DRIFTER'S MOTION

2.1. Drifter Motion under Wave Excitation

2.1.1. Wave Kinematics

Sea surface heights change over time under the influence of waves. These may range from long-period to short-period waves. The first are caused by gravitational forces, such as tidal waves. The second are known as wind waves and are caused by the wind's drag on the sea surface. Wind waves start with small height and short wavelength and grow as a function of wind strength and duration.

There are several approaches to describe the motion of the sea surface under the influence of wind waves. The simplest one, known as the linear wave theory (Airy in [43]), assumes the water surface as a regular sinusoidal periodic wave propagating in one single direction. Flatter valleys and peaked crests (typically seen in shallow coastal waters with relatively high waves) are not considered.

Airy's model is used in many engineering problems as it provides a satisfactory result for wave characterization. This model is based on several assumptions, the most important being the homogeneity and incompressibility of the fluid, the neglection of the surface tensions and Coriolis effect, the non-viscosity and just one single direction of propagation (2D). In Airy's theory, progressive waves are represented as a sinusoidal function with its phase being a combination of the horizontal position (y) and time (t). Waves are characterized by their amplitude ($H/2$), the wavelength (L) and the wave period (T), all described in Figure 4 (regular and irregular sea shown). As a result, the sea surface elevation (z_P) is

$$z_P(y,t) = \frac{H}{2} cos(\frac{2\pi}{L} y - \frac{2\pi}{T} t) \qquad (1)$$

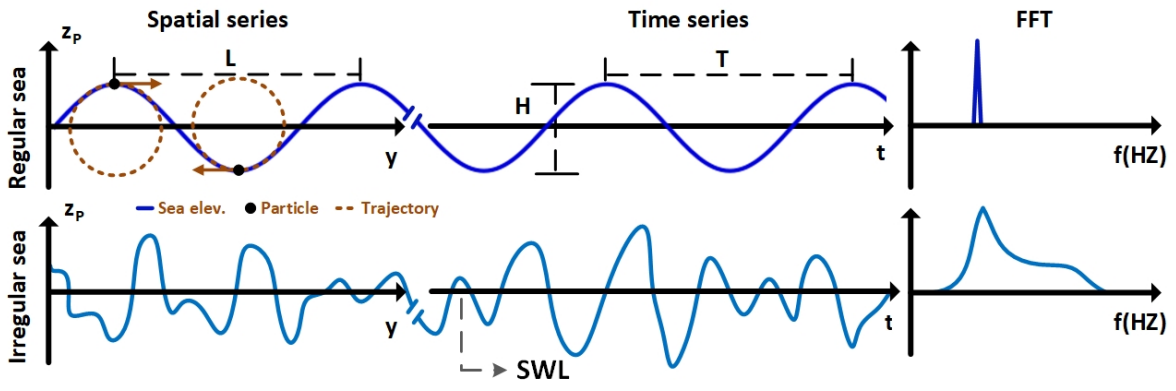

Figure 4. Spatial and time series of both regular and irregular sea surface elevations (z_P), where the Still Water Level (SWL) is shown together with the single wave length (L), wave height (H) and wave period (T).

Airy's model defines three regions depending on the seas' depth; shallow water (nearshore), transitional water and deep water. In all three regions, the water particle describes closed orbits for each period. However, in shallow and transitional waters, these orbits are elliptical while in deep water they are circular (marked in brown in Figure 4). Particle velocities, accelerations and other wave's kinematics can be obtained using Airy's model and all are fully described in [44].

However, the sea surface elevation is hardly regular and is composed of waves of different heights and periods such as the second profile shown in Figure 4. Because of this, the term of irregular waves is used to denote natural sea states in which the wave characteristics are expected to have statistical variability in contrast to the linear wave theory.

Wave parameters can be estimated for irregular seas by evaluating the time series of the sea surface elevation for a single point. The zero-upcrossing technique [44] uses the Still Water Level (SWL) reference from the time series data to obtain the height (H) and period (T) of each single wave, as represented in Figure 4. The SWL is the sea surface level in the absence of wind and waves. Then, multiple common parameters can be obtained such as H_3, which is the mean height of the third highest waves in the record, and T_3, which is the corresponding mean period. The maximum wave height (H_{max}) is the largest measured wave in the record.

Time series analysis may be a little daunting and not all the measuring devices have the technology to directly measure the surface's displacement. By measuring other wave related properties such as pressure and applying the spectral analysis described in [45], the wave parameters can also be obtained. This analysis provides the frequency domain wave parameters by using the Fast Fourier Transform (FFT) of the sea elevation. The resulting FFT energy moments ($m_K, k = 0,1,2, \ldots$ defined in [44]) are used to obtain the wave parameters, the widest known being the significant wave height (H_{m0}) and the significant wave period (T_{m2}) defined as (2) and (3) respectively. To provide a complete analysis of a real sea state both approaches (zero-crossing and spectral) must be considered.

$$H_{m0} = 4 * m_0 \tag{2}$$

$$T_{m2} = \sqrt{m_0/m_2} \tag{3}$$

There are several models that describe irregular sea using the spectra. The Ochi-Hubble (O-H), first presented in [46], is one of the most widely used. It allows to describe the sea surface elevation including the remotely generated swells and the local wind seas. O-H uses up two six combined waves with different frequency and height weighted with a specific coefficient each (λ_i, i =1-6). This model and others to describe the wave's particle motion are fully described in [44].

2.1.2. **Drifter-Water Interaction**

Understanding the interaction between the drifter and the water load is essential in order to properly design an EH converter collecting energy from sea waves. For the sake of simplicity, a spherical buoy is assumed with its center of mass (O) displaced H from the geometric center (Q), providing vertical stability. An accurate model for a spherical unmoored buoy should then include 6 degrees of freedom (DoF) (relative to the Earth); three of them correspond to translations (heave, surge and sway) and three of them corresponding to the rotations (pitch, yaw and roll). However, the model can be simplified to a planar motion by aligning the wave's propagation to Y axis. This simplification is justified by considering the buoy's motion aligned to the wave's propagation direction after a short transitory. Further, the buoy's symmetry along Z axis neglects the sway motion. Therefore, the model can be simplified to 2D with 3 DoF; surge, heave and pitch ($\dot{y}, \dot{z}, \dot{\psi}$ defined in Figure 5).

If the floating object is much smaller than the wavelength (L), it follows the circular path of the surface particle described with a dashed brown line in Figure 4. Then, both surge and heave can be described with

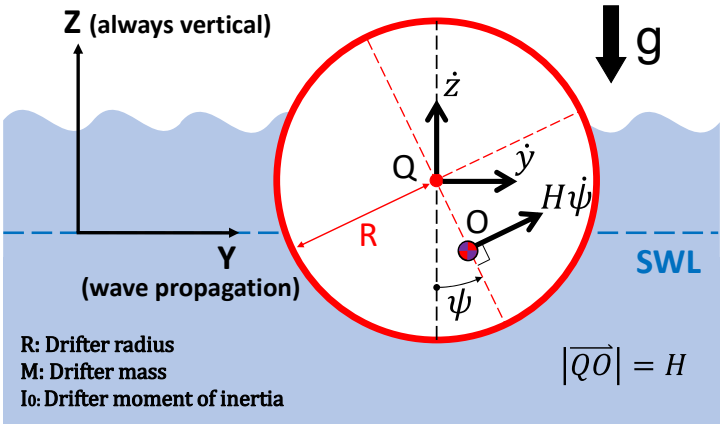

Figure 5. Free-floating buoy kinematics, physical parameters and local and general coordinates. $\dot{y}$ stands for the surge, $\dot{z}$ for the heave and $\dot{\psi}$ for the pitch.

an oscillatory path. The surge has also a superimposed drift generated by the horizontal particle displacement [47]. The heave includes the buoyancy response of the floating body that can be described with a mass-spring-damping model. This model has been thoroughly studied for moored [48], [49] and unmoored [47], [50] buoys under the influence of wave's loads. The pitch is also oscillatory due to the asymmetry of the displacement of O from Q that generates the rotation torque.

Apart from the weight and the buoyancy, the floating buoy is subject to external forces and torques induced by the waves action. These hydrodynamic loads can be described with Morison's equations, fully analyzed in [51]. Morison formulates the total wave force applied to the buoy as a sum of the added mass effect, caused by the acceleration of the surrounding water, and the drag effect of the relative velocity between the buoy and the surrounding fluid. As discussed in [50], including these loads in the mass-spring-damping model adds variable terms to the acceleration and velocity coefficients and turns it to a strongly nonlinear system. Therefore, the oscillatory response of the buoy will not only include the wave's frequency and the natural frequencies from the linear system, but many other frequencies according to its nonlinearity [52].

Analytical Model

Within the development of this thesis, we developed and validated in P.[53] the motion model of a floating, spherical, unmoored, small-size buoy using Lagrange formulation. Following Figure 5 nomenclature and reference system, the equations of motion are:

$$\begin{bmatrix} M & 0 & MH\cos\psi \\ 0 & M & MH\sin\psi \\ -M(R-H\cos\psi) & MH\sin\psi & I_0+MH(H-R\cos\psi) \end{bmatrix} \begin{Bmatrix} \ddot{y} \\ \ddot{z} \\ \ddot{\psi} \end{Bmatrix} = \begin{Bmatrix} F_y + MH\dot{\psi}^2\sin\psi \\ F_z - Mg - MH\dot{\psi}^2\cos\psi \\ -MH(R\dot{\psi}^2+g)\sin\psi \end{Bmatrix} \quad (4)$$

where M, I_0 and R are the buoy's mass, moment of inertia and radius respectively and H is the distance between O and Q. F_y and F_z are the horizontal and vertical hydrodynamic forces respectively that can be obtained using Morison as

$$F_y = \frac{1}{2}\rho C_D A_y (v_{fy} - \dot{y})|v_{fy} - \dot{y}| + \rho V_{SUB} C_M \dot{v}_{fy} \quad (5)$$

$$F_z = \frac{1}{2}\rho C_D A_z (v_{fz} - \dot{z})|v_{fz} - \dot{z}| + \rho V_{SUB}(g + C_M \dot{v}_{fz}) \quad (6)$$

ρ stands for the fluid density, C_D and C_M are the drag and inertia coefficients respectively (C_D=0.47 and C_M=1.5 for spheres [50]) and $A_{Z,Y}$ are the vertical and horizontal areas projected to the corresponding axis for the instantaneous submerged volume, that is V_{SUB}. Note that those areas and that volume are not constant. Finally, the vertical and horizontal velocity of the surrounding fluid are v_{fz} and v_{fz} respectively and can both be obtained with Airy (both expressions are defined in Figure II-1-9 from reference [44]). For this model, the torque resulting from the hydrodynamic forces is neglected due to the small size of the buoy and the small distance *H*. We have validated this model for both regular and irregular sea states in deep ocean areas; results are presented in P.[54].

By linearizing the system composed by (4), (5) and (6), the vertical coordinate is decoupled from the rest and its natural frequency is calculated as (7). This equation is in concordance with that obtained in [50] from a different approach of a free-floating spherical drifter's model. The two remaining DoF ($\dot{y},\ \dot{\psi}$) turn out to be coupled. As a result of uncoupling them, one natural coordinate oscillates proportionally to $\dot{\psi}$ and the other is a linear combination of $\dot{y}$ and $\dot{\psi}$ and has a frequency of 0. Therefore, the natural frequency of $\dot{\psi}$ and also $\dot{y}$ can be obtained as (8).

$$f_Z = \frac{1}{2\pi}\sqrt{\frac{\pi\rho g(R^2 - {z_0}^2)}{M + \frac{\pi\rho}{6}(2R^3 + 3R^2 z_0 - {z_0}^3)}} \tag{7}$$

$$f_\psi = \frac{1}{2\pi}\sqrt{\frac{MHg}{I_0}} \tag{8}$$

where z_0 is the distance from the SWL to the geometric center in still conditions and the term added to M in the denominator of f_Z corresponds to the buoy's hydrodynamic mass. We deduced this hydrodynamic mass equation and how it participates with f_Z in P.[55]. If these natural frequencies are close to the excitation frequency, a resonant response that amplifies the oscillatory amplitude may be found. That may be beneficial for EH purposes and many studies try to tune this physical parameters to maximize the energy extraction, as investigated in [56]. Nevertheless, that may also worsen the performance of the transmission, some sensor functionality or the GPS accuracy due to the non-vertical alignment of the drifter.

Numerical Simulation

Commercial software also allows the possibility of simulating a free-floating body under the effect of wave loads. OrcaFlex (*Orcina*) is the world's leading package for dynamic analysis of offshore marine systems. During this thesis and with the objective of better understanding the drifter's motion under different wave excitation, different free-floating buoys were modeled and simulated. Results helped to better design small-size WEC to harvest energy from different ocean waves conditions at drifters, and they can be found in P.[55], [57]–[61].

Specifically, we modelled an oceanic drifter in P.[60] using 25 stacked, flat cylinders of different diameter resulting in the following physical parameters; R = 0.1 m, M = 3.7 kg, H = 0.02 m, I_0 = $9{\cdot}10^{-3}$ kg/m² and z_0 = 0.053 m. The drifter emulates the WO from MELOA ([30] reported in Table 2). Sea elevation (z_P) was modelled using O-H wave spectra with just one predominant frequency; H_{m0} = 0.5 m, f_{m2} = 0.2 Hz and λ = 1. 40-seconds simulation results are shown in Figure 6, where the z_P is in blue, $\dot{y}$ in orange, $\dot{z}$ in purple and $\dot{\psi}$ in green. Results are taken at O of the drifter. The sea elevation is presented in the first pair of plots of Figure 6, with the common frequency distribution of O-H wave spectra around the main modal frequency (f_{m2}) of 0.2 Hz. The non-linear response of the drifter is consistent with the non-linarites expected on a body under wave influence [44], founding many other frequencies at each DOF response. $\dot{z}$ has a dominant frequency of 0.92 Hz, nearly matching f_Z = 1.01 Hz calculated from (7), with a maximum peak-to-peak amplitude of 0.5 g (time signal) and a mean value of 1 g due to the drifter's gravitational load. $\dot{\psi}$

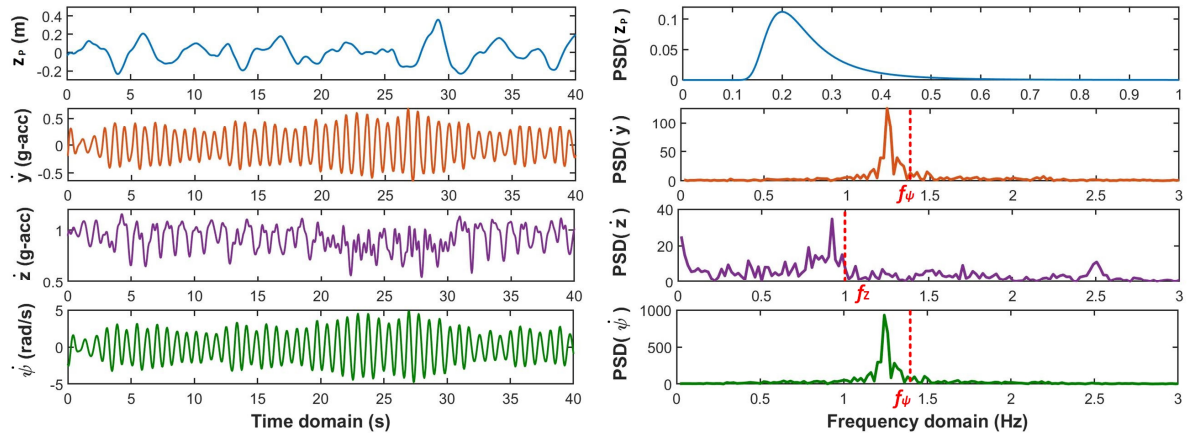

Figure 6. Simulated WO's heave and surge accelerations ($\dot{z}$, $\dot{y}$), pitch rotation ($\dot{\psi}$) and their respective PSD when placed in waters (z_p – elevation) with a significant wave height (H_{m0}) of 0.5 m and 0.2 Hz of O-H modal frequency (f_{m2}). The natural frequencies f_Z and f_ψ obtained from the analytical model are marked in red.

has a predominant frequency of 1.25 Hz, similar to f_ψ = 1.42 Hz calculated from (8), and a maximum peak-to-peak amplitude of 10 rad/s (time signal). A harmonic of f_ψ appears clearly in the power spectral density (PSD) of $\dot{z}$, presenting a peak at 2.5 Hz. $\dot{y}$ has a dominant frequency of 1.25 Hz with a maximum peak-to-peak amplitude of the time signal of 1.1 g. This frequency matches the simulated f_ψ due to the coupling of both DoF.

Experimental Observations

The drifter motion has also been studied within this thesis with the performance of several experimental tests. In the following lines, a brief summary of these tests is detailed. First, a horizontal long-stroke shaker with a WO drifter firmly mounted to the moving platform (Figure 7.a) was used to emulate the surge of a free-floating buoy. The objective was to assist the design of a WEC and characterize its energy output. We reported the results in P.[59]. Second, a robotic arm from KUKA [62] (Figure 7.b) was used emulating the

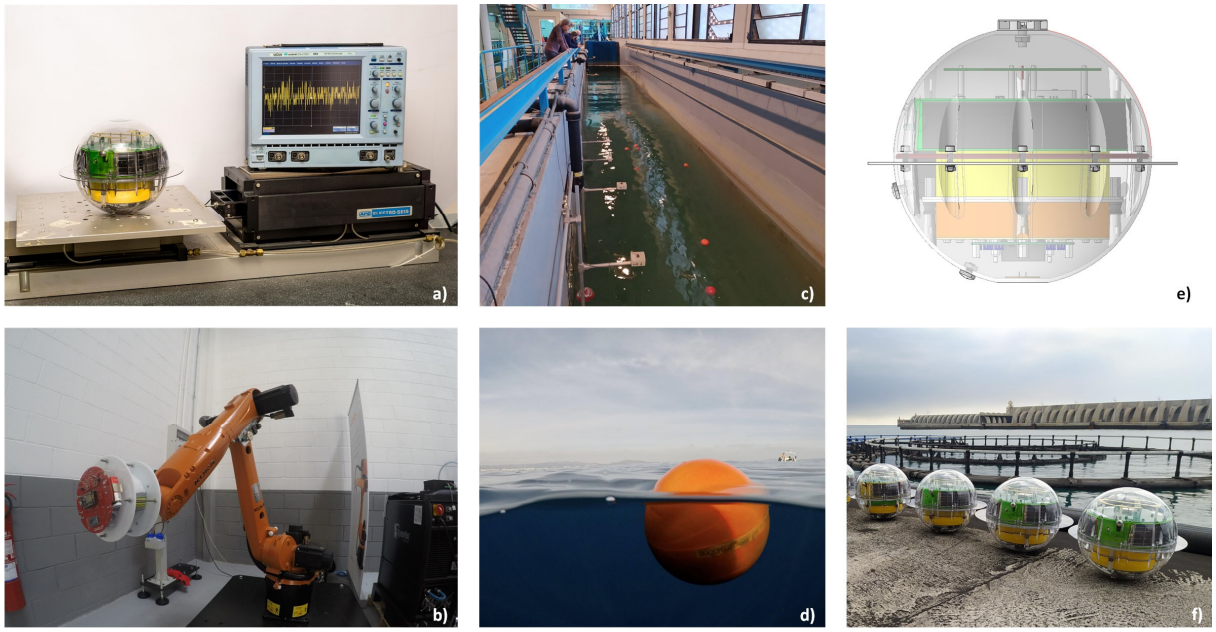

Figure 7. Experimental tests of the drifter motion under the waves excitation; a) Long-stroke shaker, b) KUKA robotic arm, c) LIM wave flume, d) Controlled sea area e) 3D model of a WO with ring, f) WO manufactured with rings.

3 DoF of an oceanic drifter under common swell conditions. The robot was controlled with the resulting vectors from an OrcaFlex simulation. The objective there was to define the potential energy that a WEC can harvest from a drifter, and we reported the results in P.[63]. Third, a wave flume emulating a real ocean scenario was used to determine the possible effect of a moving pendulum-type WEC on the wave parameter estimation at a WO. We summarized the results in P.[55]. The channel (Figure 7.c) is 100 m long, 3 m wide, and up to 7 m deep and capable of reproducing wave heights up to 1.6. Finally, several WL and WO (Table 2) drifters were deployed in monitored sea waters with embedded inertial measurement units (IMU) to experimentally analyze their motion (Figure 7.d) and how they can be harvested with a WEC under design. We reported these results in publications P.[58], [59], [64].

Some of the experimental results we obtained in P.[58] are reported in Figure 8 with the aim of comparing them with those previously presented in Figure 6 (simulated). In this occasion, a WO was deployed in a monitored sea area with incident waves composed of a H_{m0} of 0.49 m and a T_{m2} of 2.67 s, both measured with an acoustic doppler current profiler (ADCP). Figure 8 presents the heave and surge accelerations ($\dot{z}$, $\dot{y}$), the pitch rotation ($\dot{\psi}$) and their respective PSD measured with an IMU embedded in the WO's point O. From the time domain results, one may incur similar oscillatory behaviour with good agreement on the vectors peak-to-peak amplitudes, to that obtained from the numerical simulation. From the frequency domain results, predominant frequencies close to f_Z and f_ψ are observed.

In both Figure 6 and Figure 8, the natural frequencies f_Z and f_ψ obtained with equations (7) and (8) from our analytical model are represented in red. The aim is to compare the results obtained using the analytical model, the numerical simulation and the experimental test. Small differences may come from a non-accurate modelling of the sea state or from differences on the drifter model and the deployed WO. Notice the exact parameters of the drifter as the center of mass position are difficult to incur.

The mobility of the buoy may be a potential field of study to maximize the energy extraction, as previously mentioned. Even with this, communication problems may arise due to a high pitch oscillation generating a non-vertically aligned antenna affected by the surrounding water. DWS drifters equipped with IMU and dedicated to the wave parameters estimation may also find significant problems with high pitch oscillations. Mixing the drifter's local axis worsens the reconstruction of the sea surface elevation and thus the estimation of the wave parameters. To solve this issue, this work with the collaboration of the MELOA consortium changed the spherical design of the WO drifters adding an outer ring that minimized the rotation oscillation (Figure 7.e and Figure 7.f). This ring increases the hydrodynamic friction applied to the drifter and reduces the high frequency components of his pitch spectrum. Data from a deployment using WO drifters with different outer ring sizes can be found open in the MELOA catalogue in [65] and the detailed analysis of the results will be included in the project final report in [66], not yet published.

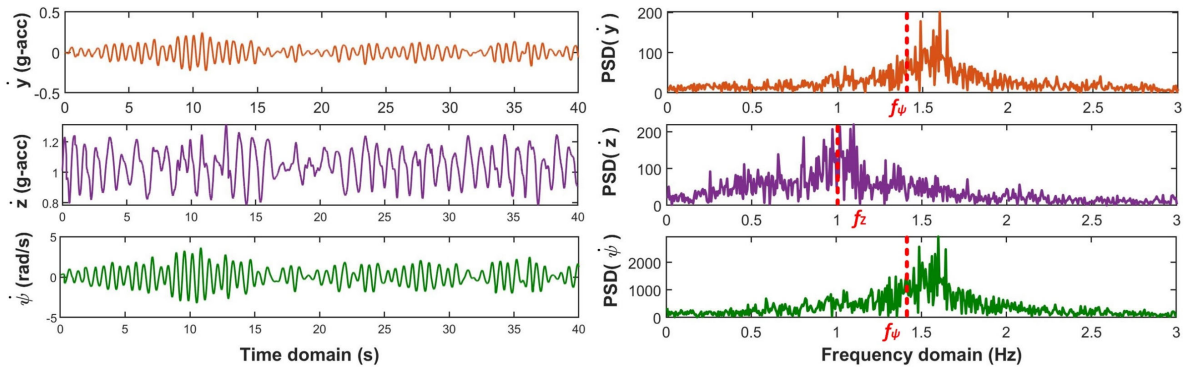

Figure 8. Experimental WO's heave and surge accelerations ($\dot{z}$, $\dot{y}$), pitch rotation ($\dot{\psi}$) and their respective PSD when placed in monitored sea waters with a H_{m0} of 0.5 m and a T_{m2} of 2.67s. The natural frequencies f_Z and f_ψ obtained from the analytical model are marked in red.

2.2. Harvesting Energy from Ocean Waves

2.2.1. Related Works

Thorner et al. defined in [67] different EH techniques specific to marine environment. Mainly, marine sources can be classified as Non-kinetic Energy (Solar, Salinity gradient and Thermal) and Kinetic Energy (Wind, Current, Tidal and Waves). This work focuses the attention on EH techniques capturing energy from surface waves, potentially useful in harvesting the drifter's oscillation.

An exhaustive report of WEC systems is presented in [68], where many large structures, either coastal or off-shore based, are presented. E.g., the oscillating water column converter (The Limped [69]) or the overtopping WEC (Wave Dragon [70]), both relying on a robust anchor system to generate power, or the surface buoyancy generator (The Heaving Buoy [71]), which harvest energy from the relative motion of two or more floating bodies. Small-size floating drifters could not apply this kind of techniques so inertial-based EH systems, classified into pendulum and gyroscope (Table 1 in [67]), are the remaining solution. Both systems, shown in Figure 9, derive electrical power by the relative movement of an inner proof mass mounted in a frame which is excited by the external load (waves). Furthermore, according to [71], the most suitable mechanical-to-electrical transducer for inertial EH are electromagnetic and piezoelectric devices.

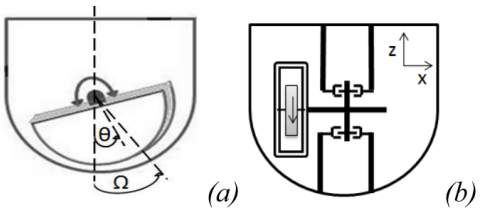

Figure 9. Inertial EH converters from sea motion; (a) pendulum and (b) gyroscope. Source: [67]

Pendulum WEC

A pendulum-type WEC was studied in [72] by researchers from *Politecnico di Torino*. It consists of a simple pendulum attached to the frame of a mooring buoy and driving an electrical generator. The pendulum's motion equation was obtained using Lagrange's approach, and the average power when exciting the buoy with regular waves estimated. This power mainly depends on the pendulum's mass and length, the distance from the buoy's geometric center and the pendulum's axis, the waves frequency and the buoy pitch amplitude. A relatively large size prototype was fabricated (0.9 m - 410 kg) and tested on a reduced wave tank (2.2 s waves) reporting an average power of around 20 W.

Ding et al. from *Xi'an Jaotong University* have reported several works attempting to design pendulum-type WEC for marine platforms such as underwater gliders [73] or submerged mooring buoys [74]. In the first test, an eccentric pendulum was attached to the rotor of an AC generator. In the second work, they took advantage of a horizontal pendulum to achieve complete turns on a DC generator (Figure 10.a). Both medium size and weight systems (1500 cm3 - 5 kg) were tested on a Stewart platform at the laboratory emulating fast waves (1.3 s) and reporting an average power production of hundreds of milliwatts.

The same idea of a horizontal pendulum-type WEC was used in [75] for mooring buoys (Figure 10.b). The proof mass oscillates around a vertical axis articulated to a gearbox that drives the electrical generator. Simulation results of a medium size pendulum (0.2 m – 20 kg) are presented with an estimated average power of around 10 W.

Li et al. designed a small size and weight pendulum WEC (630 cm3 - 0.3 kg) for non-anchored floating platforms such as ocean buoys [76], which is more aligned with the drifters used in this thesis. The system includes a small swing body, a gear train to speed up the axis rotation and a micro electrical generator (Figure 10.c). Laboratory tests are reported using a swing platform to excite the WEC charging a 50 mAh

rechargeable lithium battery. A sea test is also reported, in which only the AC open circuit voltage at the output of the harvester was measured by an embedded system. They reported a maximum peak-to-peak voltage of 15.9 V and from it, they inferred a maximum peak output power of 130 mW.

The concept of a multiple pendulum was used in [77] to develop a small size WEC to harvest energy from small buoys. In this article, they took advantage of a tri-pendulum with three magnetic masses (resulting in one pendulum) articulated to a previous single pendulum with another magnetic mass at its end. The repulsive force between the magnets, excited by the wave's load, causes the chaotic motion of the tri-pendulum. The motion of the magnets around a coil winding induces the desired energy. The so-called chaotic pendulum was manufactured with very small dimensions (10 × 16.7 cm) and tested, reporting output powers of some milliwatts.

Gyroscope WEC

Gyroscopic devices take advantage of the pitch oscillation of a floating body to accelerate an inertial disk and capture the wave's energy. People from Aalborg University designed the GyroPTO [78], a mechanical system made up of a spinning flywheel with its spin axis attached to a spherical buoy (Figure 10.d). In certain conditions, they were able to get the flywheel to continuously rotate at the wave's excitation frequency. A medium size prototype (0.5 m – 20 kg) was manufactured and tested in a wave tank [79]. They reported a mean output power of approximately 1 W with waves around 100 cm high and 1 - 3 s period. Nevertheless, they concluded that this kind of WECs strongly depend on the regularity of the waves, so changes in the behavior of the sea quickly affect the harvester's performance.

Townsend et al. proposed a gyroscopic-type WEC for vessels in [80], and then extended the model for AUV in [81]. The system utilizes the gyroscopic response of a gimballed flywheel mounted in oceanographic platforms to generate energy from wave induced rotational motions (Figure 10.e). They concluded that the performance of the device increases if its resonance frequency, determined by its physical parameters, matches the frequency of the excitation motion. The AUV model was manufactured (30 dm^3) and experimentally tested under regular waves (10 cm height and 1 Hz period) in a tank and it reached 0.8 W of mean output power.

The ISWEC (Figure 10.f) is another gyroscopic-based converter developed by researchers from *Politecnico di Torino*. This system, though, is for large-scale platforms but in [82] a scaled version (200 kg) was tested in a wave flume under the excitation of small waves (0.3 m – 2.37 s). A mean output power of 184.3 W is inferred from the measured device's torque.

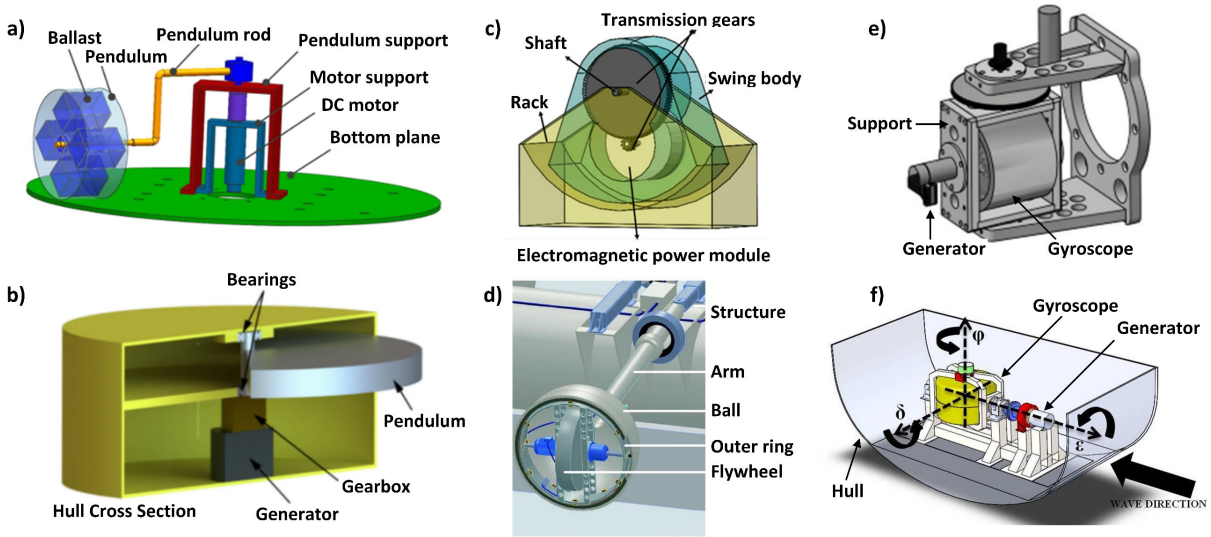

Figure 10. Pendulum and Gyroscopic -based WEC review; a) Horizontal pendulum-based WEC for submerged, moored buoys [74]**, b) Horizontal big-scale pendulum-based WEC for surface buoys** [75]**, c) Small-size pendulum WEC for drifting buoys** [76]**, d) GyroPTO for threaded spherical buoys** [79]**, e) Medium-size gyroscopic-based WEC for AUV** [81] **and f) ISWEC for surface vehicles** [82]**.**

2.2.2. The Parametric Pendulum in WEC

Pendulum WEC provides highly energetic rotational motion with very simple mechanisms, which is why this thesis focuses on this technique. The analysis of the dynamic response of a pendulum WEC is not that simple and has attracted significant interest in the last years. Exciting a pendulum with a periodic force whose frequency is close to the pendulum's natural frequency, can greatly increase the pendulum's motion amplitude. This concept is known as resonance. Another kind of resonance is parametric oscillation. In this case, the excitation is associated with the time-variation of one of the system's dynamical parameters (inertia, stiffness or damping). For the particular case of a pendulum whose articulation point has a vertical periodic motion, the time-variable parameter is the stiffness and can lead to the parametric oscillation. This has four possible responses; rest, oscillations, rotations and chaos depending on the pendulum's and excitation parameters.

Buoys under wave loads receive a stochastic excitation. However, a vertical sinusoidal excitation provides a fairly good description of this excitation because, in the long term, there are predominant values of frequency and amplitude. Therefore, a pendulum WEC excited by the heave motion of a buoy also becomes a parametric pendulum [83]. In this case, the most desirable response is the complete rotation of the pendulum. The more stable the pendulum´s rotation, the more energy an electrical generator can harvest attached to its axis. By tuning the pendulum's physical parameters, the power output of these WECs can be maximized.

Complete rotations are not possible for all the combinations of excitation parameters. To obtain parametric oscillation in a pendulum WEC resulting in complete rotations, at least a natural frequency of twice the excitation frequency is required. This leads to pendulum lengths of hundreds of meters for common swell conditions, which is not realistic for medium and small buoy sizes. Two solutions have then been suggested to mitigate this issue and both are shown in Figure 11. In one, a N-pendulum is proposed in [84] which can achieve low natural frequencies by adding multiple masses (m_i) distributed around an array of pendulum arms (l_i). This keeps the size of the device small. In the other, the concept of reduced gravity is proposed in [85]. By tilting the vertical axis of the pendulum, the effect of the gravity is reduced according to the inclination of the pendulum's axis. Both concepts allow the parametric oscillation of relatively small-size pendulum WEC [86].

Some authors suggest studying the parametric pendulum concept in WEC by imposing a sinusoidal motion on the pendulum's articulation. This results in a one DoF system (pendulum's rotation) with a known excitation. Alevras, Yurchenko et al. have gone further in these studies. In [87] they analyzed a parametric pendulum under the influence of irregular waves, which has commonly been studied under regular waves. In [88] they built a tri-pendulum (li = 0.3-0.5 – mi ≈5 kg) that achieved complete rotations in a laboratory test. The device was excited with a vertical oscillation (heave) generated by an electrical motor resulting on regular waves (T = 2-5 s – H ≈0.5 m).

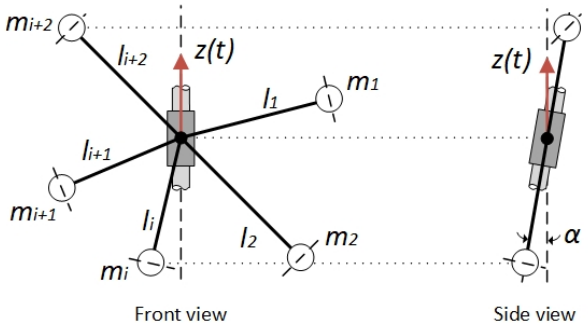

Figure 11. N-pendulum and reduced gravity concepts for reducing the natural frequency of a small-size pendulum.

Another approach that has not been studied is using the natural response of the spherical buoy, instead of forcing its heave, to obtain the parametric equations of the inner pendulum. That results in a much more complex problem because it adds the DoF of the buoy to that of the pendulum. For this purpose, the 3 DoF drifter's motion equation (4) developed within this thesis (section 2.1.2) was expanded to 4 DoF by including a simple pendulum attached to the buoy geometric center (Q). We presented the corresponding equations of motion, obtained through Lagrange's approach, in P.[53]. Figure 12 shows the 4 DoF system where $\dot{\theta}$ stands for the pendulum's motion relative to the buoy, m and L for the pendulum's mass and length respectively, I_G for the pendulum's moment of inertia and G for the pendulum's geometric center. The equations are:

$$\begin{bmatrix} M+m & 0 & mL\cos(\psi+\theta)+MH\cos\psi & mL\cos(\psi+\theta) \\ 0 & M+m & mL\sin(\psi+\theta)+MH\sin\psi & mL\sin(\psi+\theta) \\ mL\cos(\psi+\theta)-MH\cos\psi & mL\sin(\psi+\theta)+MH\sin\psi & I_0+MH^2+I_G+mL^2 & I_G+mL^2 \\ mL\cos(\psi+\theta) & mL\sin(\psi+\theta) & I_G+mL^2 & I_G+mL^2 \end{bmatrix} \begin{Bmatrix} \ddot{y} \\ \ddot{z} \\ \ddot{\psi} \\ \ddot{\theta} \end{Bmatrix} \tag{9}$$

$$= \begin{Bmatrix} F_y+MH\dot{\psi}^2\sin\psi+mL(\dot{\psi}+\dot{\theta})^2\sin(\psi+\theta) \\ F_z-MH\dot{\psi}^2\cos\psi-mL(\dot{\psi}+\dot{\theta})^2\sin(\psi+\theta)-(M+m+m_f)g \\ H(F_y\cos\psi+F_z\sin\psi)-MHg\sin\psi-mgL\sin(\psi+\theta) \\ -mgL\sin(\psi+\theta) \end{Bmatrix}$$

From the study of the equation of motion of $\dot{\theta}$ resulting from (9), an oscillatory response with a time-variable stiffness is found. Thus, the parametric study of this pendulum would be possible using the proposed system. However, this degree of analysis has not been reached during the course of this thesis and this study remains for future analysis.

The equations of motion shown in (9) were numerically integrated with the fixed-step 4th-order Runge-Kutta algorithm in MATLAB. Results were later compared with those obtained with the OrcaFlex numerical model of a free-floating buoy with an inner single mass articulated at its geometric center (acting as a pendulum). This validation comparison was presented in P.[53] and some results are illustrated in Figure 13. In both models, the sea state was described as the superposition of two regular waves (Airy) with amplitudes of 1.5 m and 0.3 m and periods of 8 s and 3.5 s respectively.

The vertical motion of the buoy's center (O) obtained through the analytical model matches with that given by OrcaFlex with an error lower than 1.5%. As for the horizontal displacement and the orientation angles (ψ, θ), both OrcaFlex and analytical results show the same qualitative tendency with quantitative discrepancies. The lower amplitude values of ψ and θ from OrcaFlex, compared to those obtained using

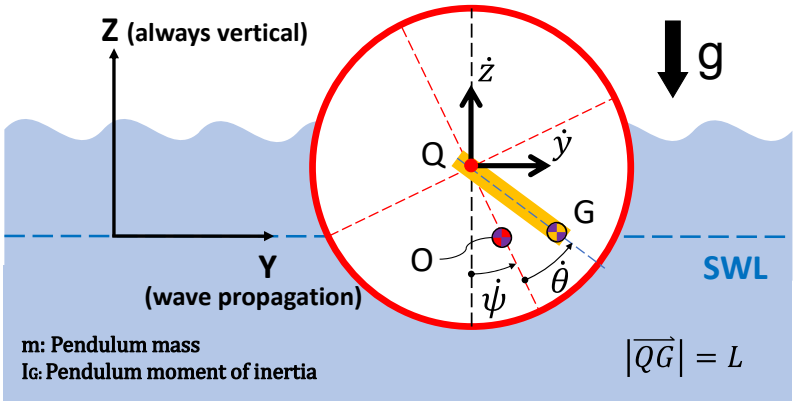

Figure 12. Free-floating buoy with an inner pendulum articulated at its geometric center. $\dot{y}$ stands for the surge, $\dot{z}$ for the heave, $\dot{\psi}$ for the pitch and $\dot{\theta}$ for the pendulum rotation relative to the buoy.

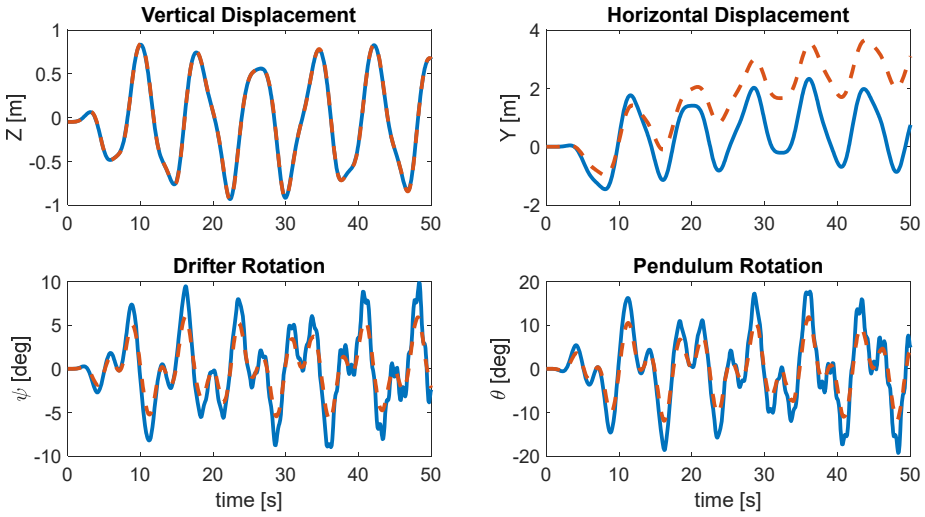

Figure 13. Time evolution of the drifter's 4 DoF obtained with OrcaFlex numerical model (dashed orange line) and with the analytical model shown in (9) (continuous blue line). From top to bottom and from left to right: drifter vertical displacement (z), drifter rotation (ψ), drifter horizontal displacement (y) and pendulum rotation ($\dot{\theta}$).

our model, are directly related to neglecting the dissipative moment associated with the sea-buoy interaction. The higher drift of the buoy obtained with OrcaFlex is related to a different modelling of the interaction between the waves and the sea bottom. In Orcaflex, the model considers a non-symmetric velocity profile, whereas the Morrison model implemented in (9) does not consider this phenomenon.

2.3. Proposed Small-Size WEC

The WO drifter from MELOA Consortium was designed to include two EH sources in order to expand its autonomy or work as an unlimited back-up battery for recovering the unit. This back-up battery works whenever the main battery is exhausted, allowing the drifter to send messages about its location in order to recover it. This hybrid EH system includes first a PV array of 0.6 W below the transparent shell and just above the equatorial line of the WO (Figure 7.e and Figure 7.f). Second, a small-size WEC to be embedded in the WO with the following restrictions; total diameter below 12 cm and maximum weight below 10% of the drifter's mass (360g). The WEC is placed in the center of mass of the WO, below the equatorial line, taking up part of the battery pack space. Therefore, the smaller the diameter of the WEC, the greater the number of battery cells that can be installed. The WEC should also not affect the WO measurements such as the estimation of the wave parameters, very sensitive to the drifter's motion as mentioned in Section 2.1.2 (inclusion of an external ring). In this section, the small-size WEC proposed within this thesis to be embedded in the WO are presented.

2.3.1. Double-Pendulum WEC

A first WEC prototype was designed in P.[57] and is shown in Figure 14.a. It is a combination of the pendulum and the gyroscopic methods. Three gimbal rings articulated to the WO are used, the inner and the outer with a proof mass mounted at its lower part. The waves excite both masses whose relative motion drives a gear system that amplifies the angular velocity. Thanks to a one-way bearing, unidirectional rotation is accumulated in a flywheel which finally drives the electrical generator shaft. The advantage of this device is that it can capture motion from all directions and turn it into rotation. A prototype of this WEC was manufactured with a mass of 360 g and a diameter of 12 cm. The electrical generator had 3 V of nominal voltage and the total gear ratio was 35. Gimbal arms were made of methacrylate and the green supports were manufactured in a 3D printer with ABS. We presented experimental results of this device in P.[57]. It

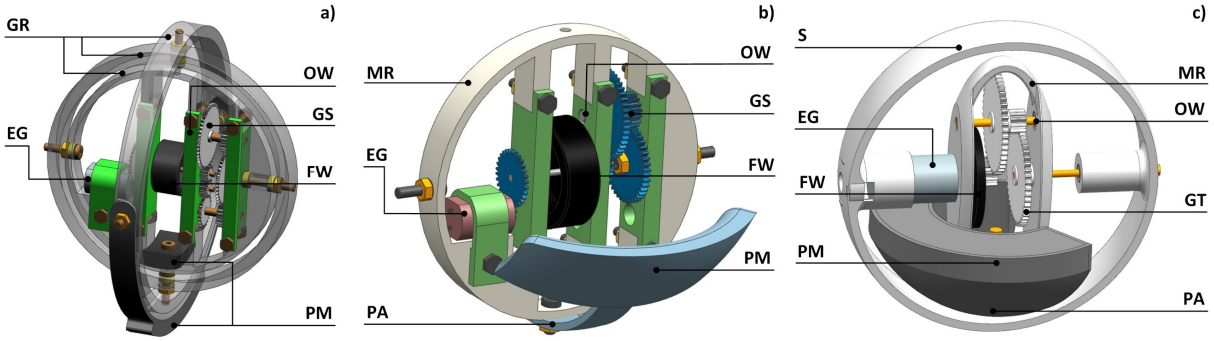

Figure 14. WEC model evolution. Nomenclature; Gimbal rings (GR), Electrical generator (EG), Proof mass (PM), Flywheel (FW), Gear System (GS), One-way bearing (OW), Main ring (MR), Pendulum arm (PA) and Support (S).

was tested in a water tank with waves of 10 cm high with 3 second periods generating 0.22 mW of mean output power across a 50 Ω resistor. A zoom-in of these results is reported in Figure 15, giving an idea of the power levels and the behaviour of this WEC. Although the frequency of the incident waves is 0.33 Hz, the response of the device corresponds to the natural frequency of the buoy where it is embedded. In the case of P.[57], a smaller buoy than the WO was used, so the frequency in which the device was moving was higher than the previous frequencies reported in section 2.1.2.

An evolution of this first design was presented in P.[58], [59] and it is shown in Figure 14.b. The design evolved into a pendulum-type WEC as the three gimbal rings were replaced by a double-pendulum system. A main ring articulated to the WO acts as the first pendulum. A proof mass placed on a pendulum arm and articulated to the main ring acts as the second pendulum. A gear train is coupled to the ring. Through that train, energy is accumulated in a flywheel which drives the electrical generator. The gear system amplifies the angular velocity and again, thanks to a one-way bearing, unidirectional rotation of the generator is ensured. The advantage of this system is that the second arm helps the pendulum align with the wave propagation direction and thus maximizes the pendulum's amplitude motion. A prototype of this WEC was manufactured with a total mass of 300 g and a diameter of 10 cm. The main body was 3D printed with polyamide and the proof mass was made with lead. The total gear ratio was 35 and the electrical generator employed was the 118391 model from Maxon Motors. This second model was placed in a WO prototype and deployed in the sea with H_{m0} of 0.49 m and T_{m2} of 2.67 s. The rotation of one of the gears was measured resulting in nearly continuous rotations at a frequency between 1 and 2 Hz, close to f_Z and f_ψ obtained from the WO's analytical model. We reported these results in P.[58]. The power generation of this second WEC was also measured in an ocean test and reported in P.[59] but, as the system included a PMU, results are presented later in section 3.3.

A third model evolved from previous designs (Figure 14.c). This model will be published in the MELOA's final report in [66], not yet published. This WEC is very similar to the second model but it reduces the total size and includes a support to fixate the WEC to the WO. The gear train is also reduced to four gears and the flywheel becomes thinner. A prototype of this third WEC was manufactured with a total mass of 245

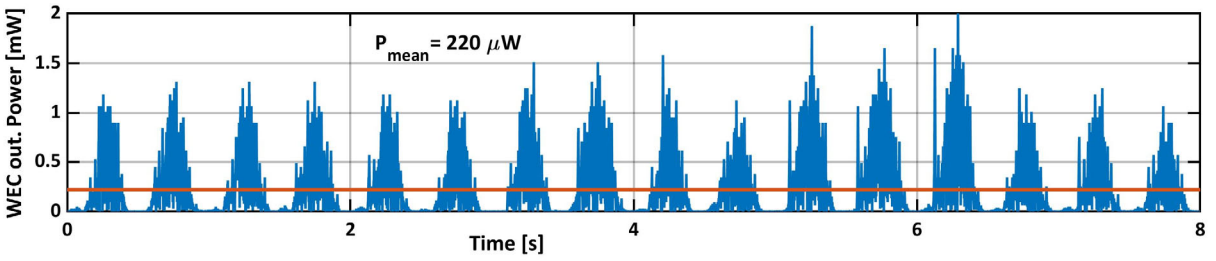

Figure 15. WEC output power across a 50 Ω resistor when placed on a water tank with incident regular waves of 10 cm height and 3 s period. The blue and orange lines represent the instantaneous and the average powers respectively.

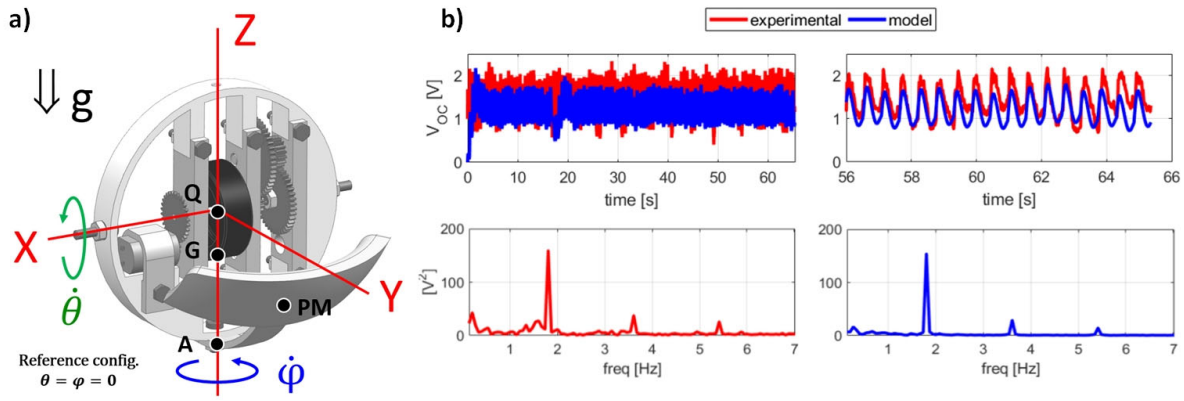

Figure 16. Double pendulum WEC model; a) 3D CAD model with the position of the main axis, the DoF and the reference points, b) Experimental and simulated model results for the open circuit voltage (V_{OC}) of the WEC's generator when fixing it on a horizontal long-stroke shaker oscillating at 1.8 Hz and 0.3 g.

g and a diameter of 8 cm. The main body was 3D printed with polyamide and the proof mass was made with lead. The total gear ratio was 14 and the electrical generator was the 106163 model from Maxon Motors.

To optimize the parameters of the WEC with a perspective similar to a parametric pendulum, its motion model must be obtained. The equations of motion of the double-pendulum shown in Figure 14.b (second model) when embedded into a floating buoy were obtained and validated in P.[41]. For that purpose, the 4 DoF system ($\dot{y}, \dot{z}, \dot{\psi}, \dot{\theta}$) presented in Figure 12 and reported in (9) should be expanded with the fifth DoF of the proof mass (PM) rotation relative to the main ring ($\dot{\varphi}$). The problem was simplified by considering just one of the buoy's DoF generated experimentally with a long-stroke linear shaker. The horizontal oscillation ($\dot{y}$ – surge) was chosen and considered roughly sinusoidal with a fixed frequency and amplitude. The shaker imposed that motion to point Q, which is the geometrical center of a ring, with the ring's rotation aligned to $\dot{y}$ (Figure 16.a). The ring's rotation about X, that is the first pendulum rotation ($\dot{\theta}$), is transmitted to a gear system and finally to the electrical generator. The proof mass is articulated to the ring about an axis orthogonal to X through point A ($\dot{\varphi}$). Figure 16.a presents the double pendulum we used in P.[41] with the main DoF of the system and the position of the reference points. Note that the system (not presented here) also accounts for the one-way bearing that engages, periodically, the gears to the ring oscillation. The measured generator's open circuit (OC) voltage (V_{OC}) was measured during the shaker test (1.8 Hz and 0.3 g) and compared to that obtained with the model. The good matching of the results is shown in Figure 16.b , where the time and frequency comparison is shown (DC component removed).

From an electrical point of view, the electrical generator is a miniature DC motor which can be modelled as a Thévenin circuit [89] like that shown in Figure 17, where R_G is the internal equivalent resistance, V_{OC} is the generated electromotive force in volts and V_{GEN} is the voltage at the output terminals. V_{OC} can be obtained as

$$V_{OC} = K_G \beta \omega \qquad (10)$$

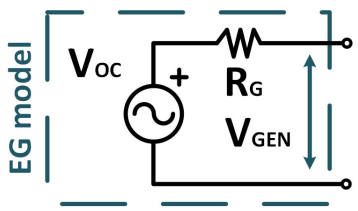

Figure 17. Thévenin equivalent circuit of the electrical generator (EG) placed on the double-pendulum WEC.

where K_G is the generator's constructive constant, β the magnet field generated by the permanent magnet, and ω the generator rotor speed [89]. Since K_G and β are constants, V_{OC} is proportional to ω. Within one single pendulum cycle, while the pendulum applies torque through the engaged one-way gear, the flywheel accelerates, increasing ω and thus V_{OC}, whereas, when the pendulum moves in the other direction the one-way gear is disengaged, so the flywheel slows down, thus reducing ω and V_{OC}. Therefore, ω and Voc will both have DC and AC components, even for a constant excitation source, as can easily be appreciated in Figure 16.b. The AC component will be periodic with the same frequency of the mechanical movement of the pendulum. Nevertheless, the flywheel increases the system inertia thus reducing the variability (i.e. the amplitude of the AC component) on ω and thus on Voc.

The effect of this pendulum-type WEC, shown in Figure 14.b (second model), on the wave parameters estimation at an ocean drifter, was studied in one of our publications P.[55]. This analysis aims to validate that the motion of the proof mass does not have a significant influence on the WO motion itself and thus its wave measuring capability. A zero-upcrossing algorithm was developed in MATLAB to obtain the wave parameters from the vertical acceleration provided by an IMU embedded in the drifter. Two oceanic drifters, one with the WEC embedded and one without, were deployed in the wave flume shown in Figure 7.c under different sea conditions. Results show there is no significant difference in the estimated wave parameters between both units.

2.3.2. **Other WEC Approaches**

Z. Hadas from *Brno University (Check Republic)* designed and developed in [90] a novel EH device capable of capturing energy from very low excitation frequencies (<10 Hz). It is, in fact, a pendulum-type converter with a custom electromagnetic transducer designed for applications with low frequency and magnitude that are typically associated with human motion. The device is based on a proof mass rolling in a circular cavity in a Tusi couple configuration. The rolling mass includes an array of permanent magnets that induce current in a coil winding fixed to the circular frame (Figure 18.a). A small size prototype was manufactured (50 cm^3 – 56.3 g) and tested in an oscillator shaker (2-6 Hz and 0.1-1 g) reporting average output powers across a 2 kΩ resistor in the order of some milliwatt.

During the development of this thesis, this rolling mass EH device was redesigned in P.[60] to become a WEC and harvest energy from the drifter's motion. The objective was to tune the natural frequency of the rolling mass to resonate with that of the drifter's motion, maximizing the amplitude of its circular path and thus the harvested energy. The constructive parameters of the device were tuned to achieve this purpose resulting in a rolling mass of 165 g and a frame cavity diameter of 46 mm. The targeted frequencies were those presented in Figure 6 resulting from an OrcaFlex simulation (oceanic drifter under O-H waves of H_{m0} = 0.5 m, f_{m2} = 0.2 Hz and λ = 1). A multi-body model was developed with ADAMS software and excited with the OrcaFlex vectors (drifter motion) resulting in an average output power across a 2 kΩ resistor of 0.4 μW with peaks up to 7 mW (Figure 18.b). The manufacturing and testing of this device is still ongoing.

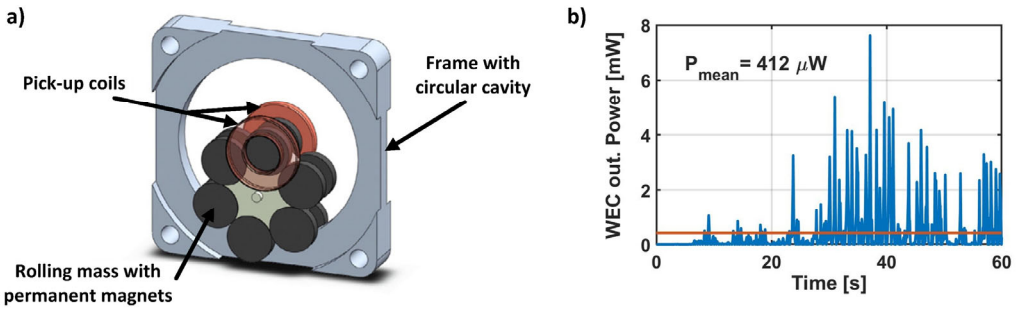

Figure 18. Other WEC approaches; a) Rolling mass EH device to capture energy from human motion presented, analyzed and tested in [90], b) Simulated WEC output power under the excitation of O-H waves with H_{m0} = 0.5 m and f_{m2} = 0.2 presented in P. [60]

Liang et al. presented in [91] an ultra-low wide-bandwidth vibrational EH device which captures vertical oscillation from multiple sources. It is a statically balanced compliant mechanism (SBCM) based on the concept of stiffness compensation between a linear component with positive-stiffness and a nonlinear component with negative-stiffness (Figure 19.a). The mechanical-to-electrical conversion is done using piezoelectric capacitors made of PVDF films. The dynamic model is obtained and defined in COMPSOL software to analyze the device's response. A small-size prototype (600 cm^3 – 850 g) was manufactured and tested in a permanent magnet shaker (6-20 Hz and 0.1 – 0.25 g) resulting in an average output power across a 1.12 MΩ resistor of up to 0.5 μW.

Under the coverage of a transnational action funded by EnABLES project (refer to [92]) the SBCM mechanism embedded into a drifter was simulated. The excitation vectors were those presented in Figure 6 resulting from an OrcaFlex simulation (oceanic drifter under O-H waves of H_{m0} = 0.5 m, f_{m2} = 0.2 Hz and λ = 1). Under these exciting conditions and with the same configuration as in [91], we demonstrated in P.[61] this device's ability to harvest energy from the sea. Figure 19.b shows the power production of this device, with an average of of 0.2 μW and peaks up to 2.4 μW. The lower power levels provided by this WEC is due to the small size of the PZT and demonstrates that it still requires further optimization. The testing of this device in a real oceanic scenario is a pending task.

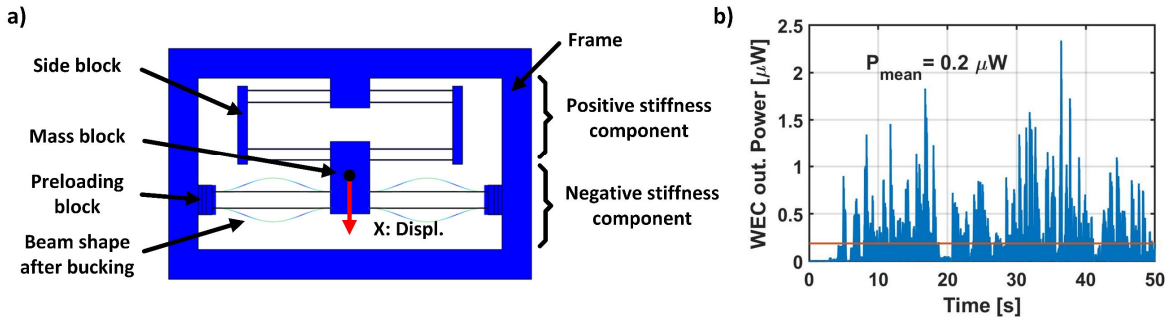

Figure 19. Other WEC approaches; a) Statically balanced compliant mechanism (SBCM) with PVDF piezoelectric films [91]**. b) Simulated WEC output power under the excitation of O-H waves with H_{m0} = 0.5 m and f_{m2} = 0.2.**

➢ In relation with chapter 2, main contributions to **objective 1** were published in "*European Physical Journal Special Topics - 2022*" in P.[60] included in **appendix A.1**, in "*IEEE Sensors Journal - 2020*" in P.[59] included in **appendix A.2**, in "*IEEE OES/MTS Oceans – 2019 Marseille*" in P.[58] included in **appendix A.5** and in "*IEEE International Instrumentation and Measurement Technology Conference – 2019 Auckland*" in P.[57] included in **appendix A.6**, that are part of this thesis compendium.

Chapter 3
POWER MANAGEMENT

3.1. General Overview

3.1.1. PMU Functionalities

EH systems use the energy of the environment to provide electrical energy dedicated to feeding low-power devices such as AS nodes. The available power is variable and limited, normally between 10 μW and 100 μW depending on the energy source [93], and it should be converted into a constant and clean supply to feed the AS node. By properly managing this energy, both the autonomy and the AS data rate can be expanded. A PMU is the electronic interface that plays this roll and accomplishes the following main functions:

- Maximizing the **power extraction (PE)** from the EH source.
- Providing a regulated **voltage supply (VS)** to the AS node.
- Controlling the **storage interaction (SI)** with the ESE
- Handling the **energy supervision (ES)** of the entire system.

The PMU should first ensure the maximum **PE** from the EH source. This energy depends on the environmental conditions (e.g. irradiation, wind speed) and the EH device voltage operating point (V_{GEN} in Figure 17). As the environmental conditions may change, the MPPT algorithm continuously tracks this operation point and places it at the MPP. An input DC/DC converter is usually responsible for this. There are several methods to perform the MPPT, further explored in section 3.2.2.

The second PMU function is to provide a regulated **VS** to feed the AS node, typically 3.3 V or 5 V for microcontrollers or embedded sensors. Commonly, a secondary DC/DC converter is used with a feedback configuration to regulate the output voltage.

The **SI** with the ESE is the third requirement of the PMU. Normally, secondary batteries (e.g. Li-ion, LiPo) are used. The control of its state of charge is needed as well as its protection with overcharge and discharge limits.

Finally, an **ES** module manages the possible mismatch of energy between the source and the load. This power flow depends on the available harvested power, the load requirements and the state of charge of the ESE. This module (typically a low-power μC) covers the high-order functions of the power management by sensing internal states of the system and providing control signals for the other PMU modules.

The complexity of PMU is growing, and the diagram previously presented in Figure 3 may become that presented in Figure 20. Multiple PMU inputs give the opportunity for scavenging different EH sources with different temporal availabilities. For example, a hybrid EH system placed on a drifter and collecting energy from calm-sunny days using a PV but also from rough cloudy days using a WEC (Figure 20). Furthermore, the AS nodes may require different voltage supplies to feed the internal modules (e.g. μC, T_X, Sensors and GPS). In these cases, a specific DC/DC input converter is needed for the MPPT of each EH source and one DC/DC output converter is needed for each desired voltage level.

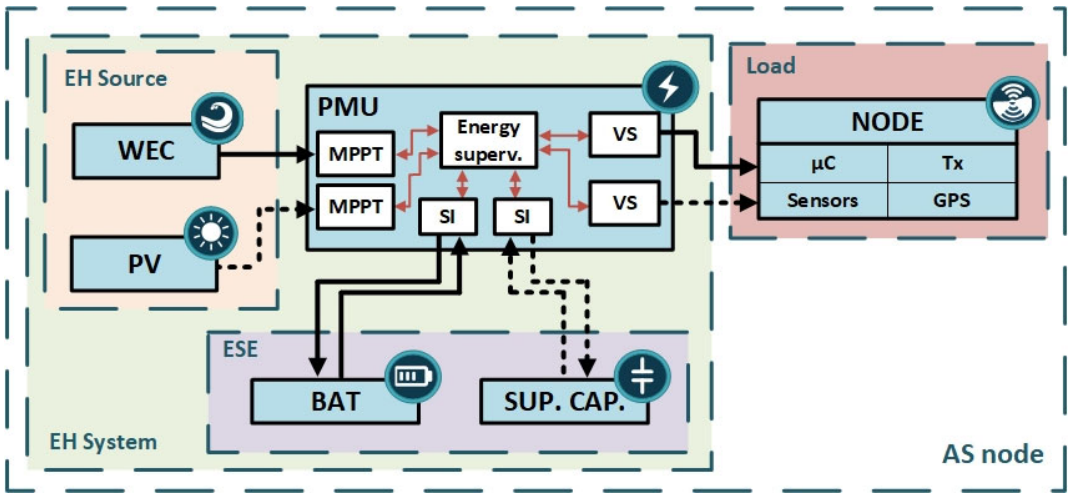

Figure 20. General structure of an AS node powered by a EH system. The hybrid EH source contains a WEC and an array of PV. A hybrid ESE is also considered with a secondary battery and a super capacitor. The PMU performs the Energy supervision of the system, each EH source MPPT, the storage interaction (SI) with the ESE and the two-level voltage supply (VS).

The load consumption of the AS node is rarely constant. When waking up or transmitting, it generates high current peaks that can exceed 100 mA. These can cause instantaneous voltage drops in the ESE that may get to switch the node off. The combination of supercapacitors with batteries shown in Figure 20 is a possible solution to resolve this. Work done in [94] proves an extension of the lifetime and an increase of robustness by using hybrid storage units. These storage topologies take advantage of the high energy density of the battery, guaranteeing a long deployment, and of the high-power density of the super capacitor to provide the high-current activation peaks.

3.1.2. Commercial Solutions

Several companies offer PMU ICs that are compact solutions covering all the functionalities stated above, including specific MPPT methods for different types of EH sources. They are ultra-low power modules for a wide range of EH sources at a relatively low input voltage, suitable for small-scale WEC. Some of them are examined below.

ADP5091/2 and BQ25504/5

The BQ25504/5 (*Texas Instruments*) and the ADP5091/2 (*Analog Devices*) are two of the most widely-used devices in low power applications (< 10 mW). They both offer efficient power extraction (70-90%) from microwatts to milliwatts at very low input voltages (>80 mV) with ultra-low quiescent currents (<500 nA). They also allow starting the energy management at relatively low input voltages (0.3-0.5 V) at what is known as the cold start-up. Both PMU's offer an input for EH sources with adjustable MPPT functionalities, a protected battery output and the main load's output. Among the differences, the ADP5091/2 incorporates a regulated output while the BQ25504/5 allows up to 5 volts at the input (3.3 V in ADP5091/2). In P.[63], we demonstrate their very similar efficiency by testing them on a WEC attached to the KUKA robotic arm of Figure 7.b emulating common swell condition. Given the similarities between both PMU's and because the ADP5091/2 has been used numerous times throughout this thesis (P.[42], [57], [59], [95]), just the ADP5091/2 PMU is further analyzed below.

The ADP5091/2 is based on a boost regulator working on PFM mode [96] with adjustable MPPT functionalities. It also includes an LDO for one adjustable regulated output. Figure 21.a shows the circuit schematic of this PMU (highlighted in blue) with a WEC (orange, defined in Figure 17) connected at its input terminal (V_{IN}). Three outputs are available; the battery charging terminal (BAT), in which the ESE (purple) is connected to, the main output terminal (SYS) and a regulated output terminal (REG). The load

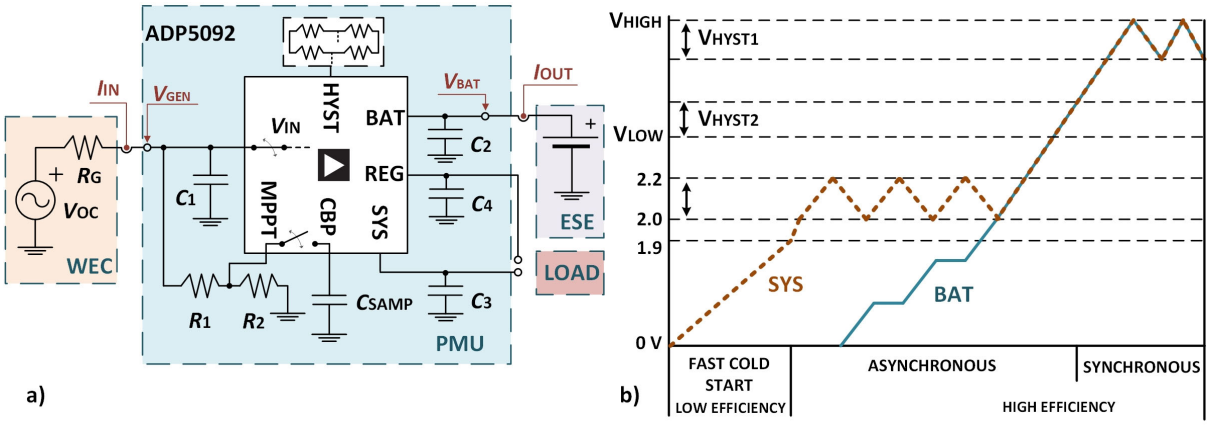

Figure 21. ADP5092 PMU. a) Circuit schematic of the ADP5092 configured to work as the PMU (center-blue), harvesting energy from a WEC (left-orange - Thévenin equivalent) and storing in a battery-based ESE (right-purple). The electrical load (right-red) is not connected. b) Fast Cold Start-Up Sequence at the PMU followed with the asynchronous and synchronous high-efficiency modes.

(highlighted in red) can either be connected to SYS or to REG. A capacitor C_1 is placed as a buffer between the EH source and the PMU and capacitors C_2, C_3 and C_4 are connected to BAT, SYS and REG respectively. Further, BAT pin is protected with overcharge (V_{HIGH}) and discharge (V_{LOW}) voltages to protect the ESE, e.g. a rechargeable battery. Each voltage counts on a hysteresis range (V_{HYST1} and V_{HYST2}) to prevent the PMU from switching on and off continuously when achieving these voltage thresholds (see Figure 21.b). Thresholds and hysteresis limits are programable by a resistor array connected to HYST and represented in the upper part of the PMU in Figure 21a.

The PMU can work in three modes, depending on the voltages at the SYS and BAT terminals: Fast-Cold Start-Up, Asynchronous and Synchronous. Figure 21.b illustrates the temporal evolution of these voltages from the Fast-Cold Start-Up mode, when there is an eruption of energy.

- **Fast Cold Start-Up** [$V_{SYS} < 1.9$ V, $V_{BAT} < 2.4$ V]: The PMU extracts the energy available at V_{IN} and charges SYS up to 1.9 V, while V_{BAT} is discharged. The main boost is off and the efficiency is low.
- **Asynchronous** [$1.9\text{ V} < V_{SYS} < 2.4$ V, $V_{BAT} < 2.4$ V]: The main boost is turned on and the efficiency increases. While V_{SYS} is between 2 and 2.2 V and above V_{BAT}, the PMU moves energy from V_{IN} to SYS and from SYS to BAT if there is exceedance. Second, when $V_{BAT} = V_{SYS}$, the PMU connects these terminals together and moves energy from V_{IN} to them.
- **Synchronous** [$2.4\text{ V} < V_{BAT} = V_{SYS} < 3.7$ V]: BAT and SYS are connected and the MPPT starts working. By moving energy from the input, the PMU raises them up to 4.2 V where they are finally disconnected from V_{IN} to prevent the battery from over-charging.

As for the MPPT functionality, this PMU performs the fractional open circuit voltage (FOCV) technique, deeply studied later in section 3.2.3. The selection of the resistor divider (R_1 and R_2) allows an adjustable percentage of the MPP, whose voltage is held in C_{SAMP} and updated every 16 seconds.

Other Commercial ICs

Even though the ADP5091/2 and the BQ25504/5 are the widest PMU used for low-power applications, there are several other options in the market. Table 3 summarizes some of them highlighting their main characteristics and some of their noteworthy details are commented below.

The LTC3105 (*Linear Technology)* is based on a boost converter with an input voltage of up to 5 V, designed for PV applications. The MPPT is set with a constant voltage (CV) by placing a resistor that programs the desired MPP voltage (V_{MPP}), which is a fixed value. A relatively high input voltage of 18 V is allowed in the SPV1050 (*ST Microelectronics*), based on a buck-boost converter. *ST* also sell a low-power PMU with true-MPPT functionalities (later defined in section 3.2.2), which is the SVP1040. This PMU IC implements the wide known method of Perturb and Observe (P&O) for solar applications with up to 3 watt of input power.

The MB39C831 (*Cypress*) allows the option to set a programable MPPT sampling period (T_{MPPT}) by modifying the value of four peripheric capacitors. The range of this programable T_{MPPT} is not specified.

The recently launched AEM30330 (*e-Peas*) is another PMU IC that offers a sampling period down to 18 ms, which is very interesting for fast-varying sources such as WEC. Nevertheless, the sampling time at this operation point is 3.8 ms which represents 20% of the operation time and drastically reduces its overall efficiency. Another interesting feature of the *e-Peas* ICs (AEM30330 and AEM30940) is the two output LDO providing different regulated voltages.

The NH2D0245 (*NOWI*) is another recently launched PMU IC that stands out for its simplicity. This chip targets ultra-low EH applications offering just the battery output (no load output is provided). It just needs one external component and it performs the high climbing MPPT.

Model	Manufact.	DC-DC	V_{IN} (V)	V_{CSU} (mV)	I_Q (µA)	P_{IN} (mW)	MPPT / T_{MPPT}	Source*
ADP5092	*AD*	Boost	0.08 – 3.3	> 380	0.51	0.006 – 600	FOCV / 4-16 s	PV, TEG
BQ25505	*TI*	Boost	0.1 – 5	> 600	0.32	< 510	FOCV / 16 s	PV, TEG
LTC3105	*LT*	Boost	0.22 – 5	> 250	24	< 300	CV / -	PV
SPV1050	*ST*	Buck-Boost	0.08 – 18	> 550	2.6	< 400	FOCV / 12-20 s	PV, TEG
SVP1040		Boost	0.3 – 5.5	> 800	60	< 3000	P&O / n/a	PV, FC
MB39C831	*Cypress*	Boost	0.3 – 4.8	> 350	41	< 300	FOCV / prog.	PV, TEG
AEM30330	*e-Peas*	Buck-Boost	0.1 – 4.5	> 275	0.87	< 500	FOCV / 20 – 70 ms	PV, PZT, TEG, RF
AEM30940		Buck-Boost	0.05 – 5	> 380	0.6	<500	FOCV / 0.33 s	
NH2D0245	*NOWI*	Boost	n/a – 5	V_{BAT} > 2.5 V	0.63	< 2	Hill climb. / 0.7 – 1 s	PV, PZT

Table 3. Commercial PMU ICs report; V_{IN}: input voltage, V_{CSU}: cold start-up voltage, I_Q: quiescent current, P_{IN}: input power, T_{MPPT}: MPPT sampling period. *Declared input sources: Photovoltaic (PV), Thermoelectric generator (TEG), Piezoelectric device (PZT), Radio-frequency (RF), Fuel Cells (FC).

3.1.3. Related Works

Many works design its own PMU to better meet the specifications of the application. The state-of-the art of AS nodes powered by EH sources whose energy is managed by a custom PMU is presented here. For each work, special attention is given to the energy supervision, the power extraction, the storage interaction and the voltage supply modules. Table 4, previously presented in [97], shows a summary of this review. Some works include a commercial PMU while others combine different DC-DC converters with wise control methods.

AmbiMax, presented in [98], is based on a hybrid EH system (solar + wind). Each MPPT is independently managed by two boost converters (LTC3401 – *Linear Technology Corporation*) controlled by a hysteresis comparator (LTC1440 – *Linear Technology Corporation*), which tracks the MPP using a pilot element (light or speed sensors). Energy is buffered using an 11 F super capacitor for the solar system and a 5 F for the wind system. The charge/discharge control of the secondary LiPo battery is managed by another comparator (LTC1441 – *Linear Technology Corporation*) and a current-limiting switch (ST890 – *STMicroelectronics*).

A solar EH system is presented in [99]. The BQ25504 deals with the MPPT under the control of a Complex Programmable Logic Device (CPLD), based on a pilot cell signal. Even though the BQ25504 integrates an FOCV-MPPT, it is not used here. A custom H-bridge bidirectional Buck-Boost converter is designed as a storage controller to balance energy between a 5 F supercapacitor and a 350 mAh battery. Finally, an off-the-shelf buck converter (TPS6220x – *Texas Instruments*) powers the load.

An AS node powered by a solar source is presented in [100]. The energy of the PV is extracted by a single-ended primary-inductor converter (SEPIC TPS43000 – *Texas Instruments*) controlled by a μC (PIC18F2620 – *Microchip Technology*). A main 3.3 V dc bus is proposed and the link between the 350 F supercapacitor and 680 mAh battery is done with two bidirectional dc-dc converters (TPS43000 – *Texas Instruments*).

A thermoelectric EH device is proposed in [101]. Energy is extracted using a DC-DC boost converter (TPS61020 – *Texas Instruments*) with a step-up charge pump (S-882Z – *Seiko Instruments*). A supercapacitor is placed as an intermediate storage device and a boost converter (TPS61220 – *Texas Instruments*) powers the load. A microcontroller (Atmga1281 – *Atmel*) acts as the energy supervisor of the system.

Li et. al. presented an hybrid system in [102] which is powered by solar and vibrating energy sources. On the one hand, a boost converter (LTC3401 – *Linear Technology Corporation*) controlled by a hysteresis comparator (LTC1440 – *Linear Technology Corporation*) and a pilot cell extracts the energy from the PV array. On the other hand, the extraction of the piezoelectric EH is done by a full bridge (FB) rectifier and a buck converter (LTC3632 – *Linear Technology Corporation*) controlled by another comparator (LTC1440 – *Linear Technology Corporation*). A novel passive storage control strategy is presented. Depending on the voltage at the different EH systems and thanks to the voltage drop at the corresponding Schottky diodes, the system balances which source feeds the load and the charging/discharging status of the battery. A super capacitor is also employed to reduce the fast fluctuations in the battery

InfiniTime, for human body EH, is presented in [103]. It is composed of a solar panel and a TEG. The extraction of power from the panel and its MPPT is done with a BQ25504, and from the thermoelectric generator with a Boost (LTC3108 – *Linear Technology Corporation*). Energy is merged into a LiPo battery by passive diodes and an internal extra Buck converter of the BQ25570 is used to feed the load.

Ref.	EH source(s)	Power Extraction	Energy Supervisor	Storage intraction	ESE(s)	Voltage Supply
[98]	Solar + Wind (0.3 + 0.5 W)	Boost [LTC3401] + Hyst. comp. [LTC1440] + pilot element	Hysteresis comp. [LTC1441]	Current limiti. Switch [ST890]	Supercaps 11 F and 5 F + LiPo battery	pMOSFET selects source
[99]	10 PV cells (18 mW)	Boost [BQ25504] + CPLD + pilot cell	CPLD	Custom H-bridge Buck-Boost	Supercap 5 F + 350 mAh LiIon battery	Buck conv. [TPS6220x]
[100]	Solar 5 W	SEPIC converter [TPS43000]	Microcontroller [PIC18F2620]	Bidir. Buck and Boost [TPS43000]	Supercaps 350 F 2.7 V + 680 mAh battety	3.3 V bus
[101]	TEG (250 mV at 4 K)	Charge pump [S-882Z] and Boost [TPS61020]	Microcontroller [Atmega1281]	Boost [TPS61020]	Supercap 2.5 F 5 V	Boost [TPS61220]
[102]	Solar + Vibration	Boost [LTC3401] + FB rectifier and Buck [LTC3632]	passive: or-ing diodes	resistor divider, pMOSFET and Schottky diodes	Supercap 25 mF 5 V + 130 mAh Li battery	Buck-Boost conv. (n/a)
[103]	TEG + solar	Boost [LTC3108] + Boost [BQ25504]	passive: or-ing diodes	Boost [LTC3108] + PMU [BQ25504]	40 mAh LiPo battery	Buck [BQ25570]

Table 4. State-of-the-art of power management systems with their EH and Storage technology [97].

3.2. Maximum Power Point Tracking

3.2.1. General Overview

The harvested energy from an EH source strongly depends on the environmental conditions (e.g. irradiation, wind speed) and the device's voltage operating point (V_{GEN} in Figure 17). As the environmental conditions continuously change, a MPPT algorithm should track this operation point and place it at the MPP.

This can be understood with the aid of Figure 22. It shows the corresponding I-V and P-V characteristic curves of the DC electrical generator placed in the WEC presented in P.[59] and modeled with the Thévenin circuit of Figure 17. Different rotation excitations were driven in the electric generator axis and the corresponding output currents were read at different voltages. There is an MPP found at each rotation with a corresponding voltage defined as V_{MPP}; placing the WEC's output voltage at V_{MPP} maximizes the power output (P_{MPP}). A change in the rotation leads to a different P-V curve. The V_{MPP} that previously maximized the output power (P_{MPP}) now is far from its optimum point, so V_{GEN} should be properly modified to reach the new MPP. This is known as the MPPT and it is one of the PMU responsibilities.

In the case of thermoelectric, piezoelectric or electromagnetic devices, the MPP is reached when the load resistor (R_{LOAD}) matches with the EH device's internal resistor (R_G in Figure 17). Then, according to (10), the maximum power point at a certain condition (e.g. ω rotation in the electro generator axis) is

$$P_{MPP} = \frac{{V_{OC}}^2}{4 \cdot R_G} = \frac{(K_G \beta \omega)^2}{4 \cdot R_G} \qquad (11)$$

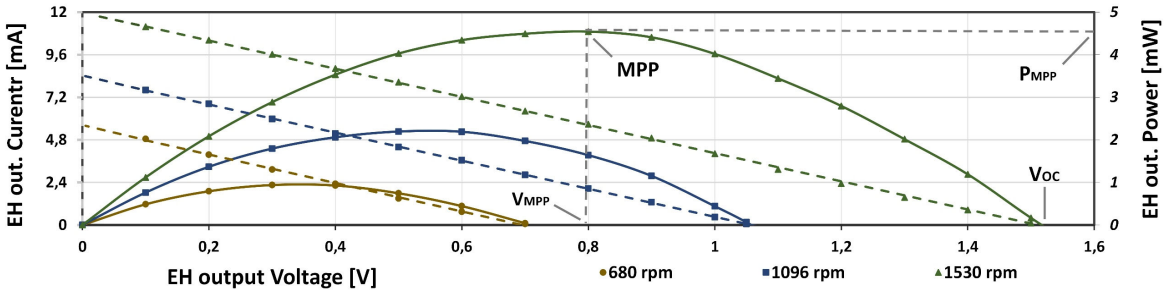

Figure 22. I-V and P-V characteristic curves from the DC electrical generator placed in the WEC presented in P.[59]. The maximum power point (MPP), its corresponding voltage (V_{MPP}) and power (P_{MPP}) and the open circuit voltage (V_{OC}) are shown. Solid lines correspond to P-V (left axis) and dashed lines to I-V (right axis).

3.2.2. Existing MPPT Techniques

Esram et al. summarized in [104] many of the large number of MPPT techniques that were proposed. This section only presents the ones appropriate for low-power EH sources (input power below 10 mW). Later, section 3.2.3 analyses deeply and reviews the FOCV method, which is the one used throughout this thesis.

A DC/DC converter is usually placed at the EH source output to control its operation point and execute the PMU energy extraction (Section 3.1.1). By controlling the converter input voltage (EH source output), the MPP can periodically be achieved. This control can either be done with a pulse width modulation (PWM), such as in [105], or with a pulse frequency modulation (PFM), such as in [106]. Both methods require the MPP voltage reference (V_{MPP}). There are two ways of generating this reference. The more precise the MPP needs to be, the more complex the circuit becomes. The indirect methods, also called open-loop or near-MPPT methods, estimate the V_{MPP} of the EH source. The direct methods, also called

closed-loop or true-MPPT methods, periodically measure the converter's input power (P_{IN}) to generate the next V_{MPP}. As several parameter measurements and the generation of a reference are required, the energy supervisor module (typically a μC as in Figure 20) is also involved.

Figure 23 shows the schematic of a PMU capturing energy from an EH source (WEC model) with a focus on the MPPT implementation. In this case, V_{GEN} and I_{IN} are measured to provide V_{MPP}, implementing a true-MPPT. In a near-MPPT method, this value would be estimated. From the difference between V_{GEN} and V_{MPP}, either a PWM or a PFM controls the switching of a DC/DC converter and thus its input voltage to reach the MPP of the EH source. An ensuring DC-DC converter adjusts the voltage supply level at the load.

Near-MPPT Methods

Near-MPPT methods, also called Indirect or Open-loop methods, estimate the V_{MPP} and avoid adding measurement circuitry or a μC that may increase the consumption and reduce the efficiency of the PMU. These methods are used for ultra-low EH applications where this rise in the consumption does not pay off for the increase of energy obtained in following the MPP.

One of the simplest methods is the **constant voltage (CV)** MPPT. It consists of selecting a CV for V_{GEN}, which should be selected near the average MPP expected during the operation. In the case of Figure 22, placing a V_{MPP} of around 0.5 volts will not reach the MPP in practically any of the rotation conditions but it may provide a near-MPPT for all of them. Particularly, this method lacks the ability to adapt the MPP to a change in the environmental conditions. Another disadvantage of this method is the requirement of having to previously characterize the EH source. The boost-based LTC3105 (*Linear Technology)* reported in Table 3 applies the CV by placing a resistor at one of its pins. The CV method can also be performed with the *ADP5092*, as we did in P.[95]. In this work, we compared the performance of two near-MPPT techniques, the CV and the FOCV, by deploying a WEC embedded in an oceanic drifter in a wave flume. Results from this comparison are later analyzed in section 3.3.

Another near-MPPT method is the **resistor emulator**. This method is based on changing the impedance seen by the EH source (R_A in Figure 23) to reach the MPP. By tuning the duty cycle of the input PMU converter, R_A, which is normally much higher than that of the EH source (R_G), is adjusted. In the case of electromagnetic sources, an $R_G \approx R_A$ places the desired MPP. A flyback converter PMU is designed in [107] to capture energy from microbial fuel cells using a resistor emulator method. From the internal resistor of each cell (previously characterized), the frequency and duty cycle of the flyback converter that matches the load and the EH source impedances were set. Another resistor emulator method is presented in [108], aiming to capture from 8 to 420 μW of an RF antenna. The matching of R_A and the EH source resistors is achieved by placing a boost converter between them.

The **FOCV** is another near-MPPT method, widely used in low-power EH applications and also implemented in several commercial low-power chips, some of them reported in Table 3. This method, thoroughly explained in [109], exploits the nearly linear relationship between V_{MPP} and V_{OC} of the EH

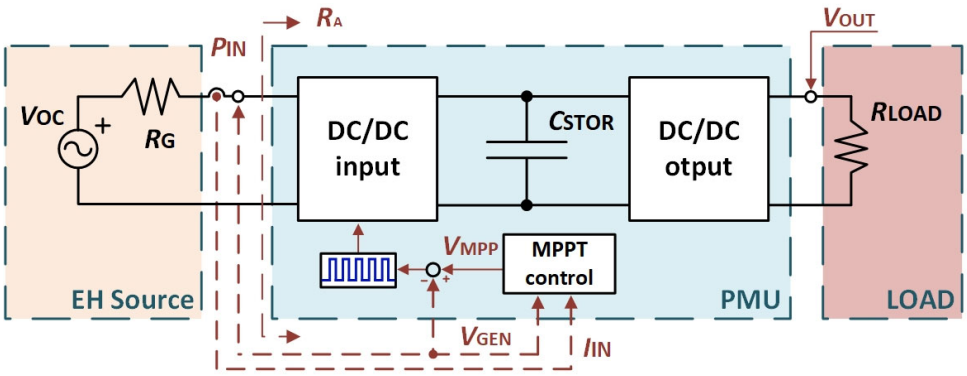

Figure 23. Main schematic of a PMU implementing the true-MPPT.

source (Figure 22). So, maximum energy is harvested by fixing the output voltage of the EH source to a percentage of V_{OC}. This percentage is typically 50% for thermoelectric, piezoelectric or radio frequency sources, and 60-80% for PV sources. Typically, V_{OC} is periodically measured with a sample and hold (S&H) circuit by momentarily disconnecting the EH source from the PMU. So, this method, unlike the previous ones, is capable of periodically updating the estimated MPP and adapting it to the new environmental conditions. As this method is one of the main topics of this thesis, section 3.2.3 deeply analyzes its implementation and reviews some related works for low-power EH sources.

One of the main drawbacks of the FOCV method is that the harvester output is periodically disconnected from the PMU reducing the global efficiency. There are some methods that can solve this problem such as the one reported in [110], where a parallel pilot PV cell is used to estimate the V_{OC} of the whole PV array. A similar idea is used in [111], where the MPP is estimated from the rotation velocity of a WEH turbine Even though this method does not provide a true MPP, it is a viable solution for continuously tracking the MPP without disconnecting the EH source.

True-MPPT Methods

True-MPPT methods, also called Direct or Closed-loop methods, continuously measure the output power of the EH source, e.g. the PMU input power, to properly update the V_{MPP} reference. These methods are more complex and may require more power consuming modules but they are also found in low-power EH applications. As some computational resources are needed to process the measured input parameters and provide the V_{MPP}, normally a low-power μC is included.

The widest used true-MPPT method is the **perturb and observe** (P&O) one. This method, first presented in [112], is based on periodically perturbing the output voltage of the EH source, measuring its new power point (P_{IN} in Figure 23), and finally acting consequently. Figure 24 shows the principle of operation of this method. The PMU slightly perturbs V_{GEN} and observes the change on P_{IN}, usually by measuring the output voltage and current (V_{GEN} and I_{IN}). Whenever the measured power increases ($\Delta P > 0$), the MPP is assumed to be at the right hand of the current operation point and, therefore, it must be further perturbed in the same direction ($\Delta V > 0$). Otherwise, if the power decreases ($\Delta P < 0$), the next perturbation must be made in the opposite direction ($\Delta V < 0$) because MPP is found at the left hand of the current operation point. A small-size shunt resistor and an analog-to-digital converter (ADC) are normally used to sense V_{GEN} and I_{IN}.

In general, P&O is more accurate than other methods, but in low-power harvesters, the extra generated power may not compensate for the power consumed by the required computation resources which typically amounts to hundreds of microwatts (110 μW in [113] or 350 μW in [106]). Two crucial design parameters of the P&O method are the voltage and time steps (ΔV and Δt). Small steps are desired so as to achieve precision while big steps allow for higher capability to approach the MPP at high environmental changes. For this reason, variable temporal and voltage steps are suggested in [114].

The **hill climbing** true-MPPT method is very similar to the P&O as, instead of perturbing the voltage, it perturbs the switch frequency of the input DC/DC converter. The NH2D0245 (*NOWI*) reported in Table 3 uses this technique.

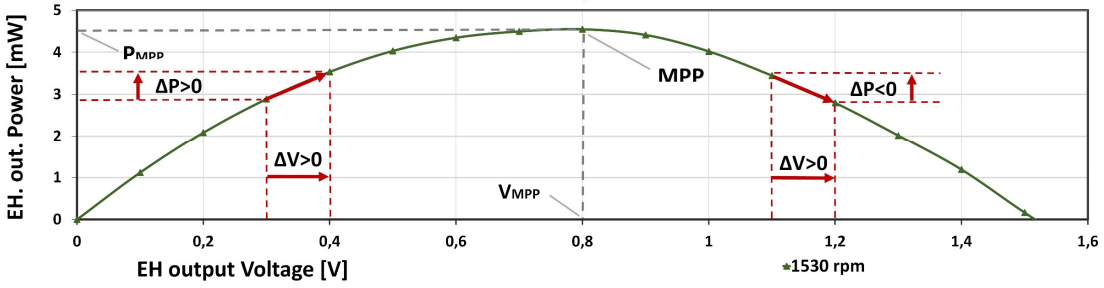

Figure 24. P-V characteristic curves from the DC electrical generator placed in the WEC presented in P.[59] **showing the principle of operation of the perturb and observe (P&O) MPPT method.**

The **impedance matching** is an evolution of the resistor emulation that includes a closed loop to dynamically update either the duty cycle or the frequency of the input DC/DC converter to reach the MPP. Toh et al. early designed in [115] an impedance matching system to follow the MPP of a rotating EH device. A control loop measures the input voltage at the boost converter and obtains an input current reference by knowing the desired system's impedance ($R_A \approx R_G$). The existing boost input current (I_{IN} in Figure 23) is measured using a sense resistor and later amplified and filtered. From the difference of the input and the desired currents a PI control provides the new duty cycle of a PWM that controls the main boost. For this work, a microcontroller (PIC18F452 – *Microchip*) was used as energy supervisor to implement the PI and generate the control signals. Other impedance matching methods can be found in [116] for a low-power fast-varying EH source such as a PZT vibrating at 40 Hz.

3.2.3. Implementation of the FOCV Technique and Related Works

There are two ways to implement the S&H function in a FOCV-MPPT circuit: resistor-based or capacitor-based. The implementation of both circuits is analyzed and reviewed below. The focus is on how different papers deal with the implementation of a fast sampling rate ($f_{MPPT} \geq 1$ Hz), applicable to fast-varying sources such as a WEC, and dedicated to low-power EH sources (input power below 10 mW). Table 5 later summarizes the main characteristics of the reported FOCV works, describing the EH source and frequency, input voltage range and sampling technique, timings, and control signal strategy.

Resistor-Based FOCV Technique

In resistor-based FOCV, a resistor divider is used to generate the desired fraction of V_{OC} and then stores it in a small sampling capacitor (C_{SAMP}). Figure 25.a shows the block diagram of a standard PMU with resistor-based FOCV-MPPT, such as the ADP5091/2. An EH source (WEC model) is connected at the input whereas an ESE and a load are connected at the output. The figure focuses on the S&H circuit of the MPPT controller, which is higlighted in grey. However, it is noted that the PMU includes other funcionalities such as the energy supervision (ES) of the system, the power extraction (PE) from the EH source, the storage interaction (SI) with the ESE and the voltage supply (VS) to the LOAD (e.g. a sensor node). Figure 25.b shows the evolution of the voltages V_{GEN} and V_{OC} (defined in Figure 25.a) during two sampling events. The sampling period (T_{MPPT}), which is the inverse of the sampling rate (f_{MPPT}), is composed of the sampling time (t_{SAMP}) and the harvesting time (t_{HARV}).

At the PMU input (V_{GEN}), a capacitor C_1 is placed as a buffer between the PMU and the EH source. Further, two more capacitors (C_2 and C_3) are placed at the ESE (V_{BAT}) and LOAD (V_{LOAD}), respectively. At each sampling event, the PMU IC opens the switch S_1 and closes switch S_2 during t_{SAMP}. Thus, V_{GEN} rises to V_{OC}, the desired V_{MPP} appears at the output of the resistive divider formed by R_1 and R_2 and is stored at C_{SAMP}. Then, during t_{HARV}, S_1 closes and S_2 opens, and the PMU forces V_{IN} to the last sampled value of V_{MPP} by periodically moving energy from C_1 to C_2 and C_3.

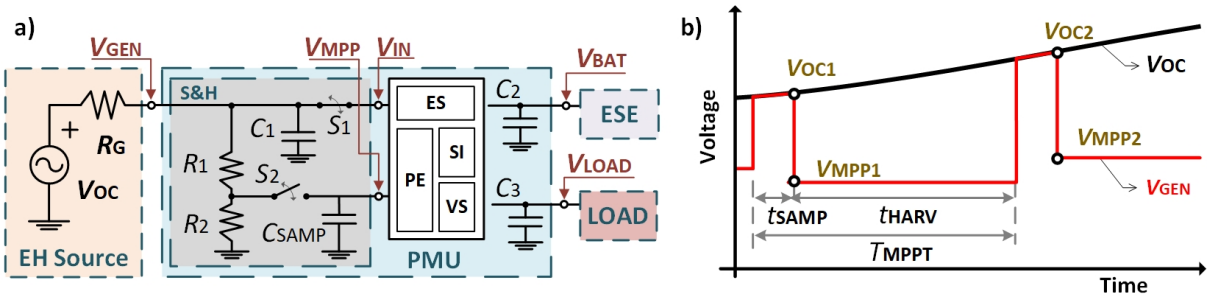

Figure 25. Resistor-based sample and hold (S&H) implementation of a FOCV-MPPT technique. a) S&H circuit. b) V_{OC} and V_{GEN} evolution during two sampling intervals.

The Everlast system was early presented in [117] consisting in a solar-powered wireless sensor node. A custom circuit is designed with the sampling events controlled by an IC timer (555) generating pulses at 10 Hz and 5% of duty cycle (t_{HARV} = 100 ms and t_{SAMP} = 5 ms). The input converter is controlled by PFM and the ESE is a 50 F/ 5 V super capacitor. A step-down converter and an LDO regulator feed the μC and the sensors respectively.

Shao et al. designed in [105] a PMU to harvest energy from PV panels and feed an AS node. The PWM is used to control a DC/DC input converter. A 60 mAH / 4 V Li-ion rechargeable battery acts as the ESE and a regulated output feeds the node. In this work, an IC timer generates the sampling pulses of 300 Hz and 1 % of duty cycle (3.33 ms and 33 μs).

A full-wave rectifier AC-DC converter is used in [118] to capture energy from a PZT device vibrating at 80 Hz and 7 m/s². A boost converter later acts as the power extraction module applying a FOCV-MPPT. A ring-type oscillator is used as the sampling controller refreshing the MPP every second with a sampling time of 15 ms. The ESE and the load are simply a 100 μF capacitor and a 1 kΩ resistor respectively.

An advanced technique is implemented in [119] for PV applications. The main boost converter captures energy from the panels and stores it in a small output capacitor of 1 mF. Changes in the solar irradiance are detected in the input voltage using a custom circuit that makes the MPPT sampling period variable around an average of 25 ms. The sample time is not specified.

Capacitor-Based FOCV Technique

In capacitor-based FOCV, V_{OC} is stored in a first sampling capacitor (C_{S1}) which is then connected to a second capacitor (C_{S2}) chosen such that the final voltage after charge-sharing is the targeted fraction of V_{OC}. Figure 26 shows the block diagram of a standard PMU with capacitor-based FOCV-MPPT. As in figure Figure 25.a, an EH source (WEC model) is connected at the input whereas an ESE and a load are connected at the output. The figure focuses on the S&H circuit of the MPPT controller, which is higlighted in grey. The rest of the PMU fuctionalities are represented in the white box (as in Figure 25.a). For the capacitor-based FOCV, the evolution of the voltages V_{GEN} and V_{OC} can be seen in Figure 25.b (same behavior as in resistor-based).

For this technique, shown in Figure 26, four switches are used. Switches S_1 and S_3 use the same control signal whereas switches S_2 and S_4 share a control signal opposite to that used in the first pair. At each sampling event, the PMU IC opens the switches S_1 - S_3 and closes the S_2 - S_4 during t_{SAMP}. Thus, V_{GEN} rises to V_{OC}, C_{S1} holds this voltage and C_{S2} gets totally discharged. Then, the state of all switches is changed and C_{S1} is connected to C_{S2}, chosen such that the final voltage (V_{MPP}) after charge-sharing is the targeted fraction of V_{OC}. Finally, during t_{HARV}, the PMU forces V_{IN} to the last sampled V_{MPP} by periodically moving energy from C_1 to C_2 and C_3.

In [120], a boost converter is used to harvest energy from a thermoelectric generator. The input voltage is relatively low (< 150 mV) and the application works just up to 2.7 mW of input power. A clock signal controls the sampling period and time of 20 ms and 4 ms respectively. In this work, a 10 μF capacitor is used as the ESE and two capacitors of 1 nF are used as C_{S1} and C_{S2}, achieving the typical ratio of 50% for TEGs.

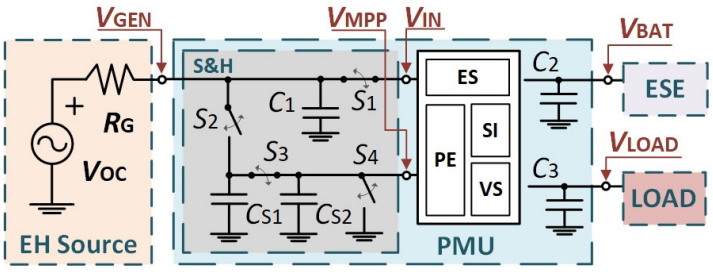

Figure 26. Capacitor-based sample and hold (S&H) implementation of a FOCV-MPPT technique.

Dini et al. designed, in [121], a custom circuit to harvest energy from different EH sources simultaneously. It is based on a boost input converter, an LDO that allows a regulated output and a 33 μF capacitor as the ESE. By selecting different values of C_{S2}, the MPP ratio can be selected for different input EH sources. A clock signal controls an extremely low sampling time of 2 μs and a sampling period of 150 ms. The size of the sampling capacitors is not given.

Another implementation was presented in [122] for PZT EH sources vibrating between 20 and 200 Hz. In this work, the pulses of the EH's rectified V_{OC} are used as the sampling control signal making the f_{MPPT} variable and adaptable to the source's frequency. Every 50 cycles (1 s in the test) the PMU opens the EH output and samples its V_{OC} during one cycle (20 ms). The sampling control signal is then implemented with a peak detector in the buck-boost input converter.

A simulated resistor-based circuit is presented in [123] with a sampling control signal whose frequency increases with the available energy at the harvester input. By using several comparators and a clock signal, this work achieves an average sampling period of 4 ms with a sampling time of 16 μs. The selected C_{S1} and C_{S2} are 1.6 pF each. The structure of the system uses an input boost converter as energy extraction module and a consecutive buck converter for the voltage supply. The ESE and the load are simply a 1 μF capacitor and a 100 kΩ resistor respectively.

A complex method was implemented in [124] for different selectable DC input sources, achieving a very short sampling time and period (1 μs/10 μs). The control signal is generated using a digitally controlled oscillator circuit.

Finally, in [125], this technique was implemented in a hybrid PMU with 4 selectable DC EH inputs. It is a custom system designed to feed low power AS nodes with an ESE of hundreds of microfarads. In this case, the capacitor-based FOCV-MPPT technique is applied at each EH source with a fix sampling time and period of 86 μs and 25 ms respectively. The control signal is implemented with an internal logic sequence and the size of the sampling capacitors is around 2.7 pF.

Ref.	EH source(s) and freq.	Input Voltage	Technique	t_{SAMP} / T_{MPPT}	Control signal strategy
[117]	Solar PV	2-5 V	Resistive	5 ms / 100 ms	IC timer (555)
[105]	Solar PV	2-4 V	Resistive	33 us / 3.33 ms	IC timer
[118]	Vibration-PZT @ 80 HZ	1-3 V	Resistive	15 ms / 1 s	Ring-type oscillator
[119]	Solar PV	0.1 – 3 V	Resistive	Variable ~ n/a / 25 ms	Irradiance change detector
[120]	TEG	20 – 150 mV	Capacitive	4 ms / 20 ms	IC timer
[121]	Selectable DC source	40 mV – 2.5 V	Capacitive	2 μs / 150 ms	IC timer
[122]	Vibration-PZT @ 20-200 Hz	1-7 V	Capacitive	Variab.~ 20 ms / 1 s	Peak detection
[123]	Simulated DC source	0-0.5 V	Capacitive	Variab. ~ 16 μs / 4-8 ms	Adaptative with input energy
[124]	Selectable DC source	0.25 – 1.1 V	Capacitive	1 μs / 10 μs	Digitally controlled oscillator
[125]	4 different DC sources	0.3 – 0.8 V	Capacitive	86 μs / 25 ms	Internal logic sequence

Table 5. Fast-sampling FOCV-MPPT works for low-power energy harvesting systems.

Table 5 summarizes the reported publications for both techniques. In general, resistor-based circuits offer greater precision in the MPP tracking and require a smaller number of switches. On the other hand, capacitor-based circuits allow a fast charging of the sampling capacitor, leading to a drastic reduction of t_{SAMP}. The main drawback is the potential for parasitic interference and charge injection at the small sensing capacitors.

3.2.4. Increasing the Sampling Rate in Resistor-Based FOCV-MPPT Techniques

Some sources, such as WEH or WEC, require fast tracking of the MPP because V_{OC} shows relatively rapid variations. For example, [40] and P.[41] present a WEH and a WEC respectively, each with V_{OC} oscillating at around 1.8 Hz; this is fast-varying compared to other types of EH sources such as thermoelectric or PV devices. In P.[42], we experimentally demonstrated that, by increasing the sampling rate in a WEC oscillating to 2 Hz, the harvested energy improves by up to 25%. A similar conclusion was reached in [126], where an increase of 22 % and 44 % of the extracted energy was achieved for weakly- and strongly-coupled piezoelectric vibration EH sources, respectively

This can be understood with the aid of Figure 27 (zoom-out of figure Figure 25.b). It shows a sinusoidal V_{OC} waveform with positive offset and period (T_{EH}) as well as the V_{MPP} (50 % of V_{OC} in this example). This V_{OC} is similar to that obtained in P.[41] and shown in Figure 16. The evolution of the output of the EH source (V_{GEN}) is also represented (except the detail of the sampling instants) for three different T_{MPPT} using a FOCV-MPPT technique. T_{MPPT} of 12, 3 and 0.1 samples per period of the sinusoid are represented with red (V_{GEN1}), blue (V_{GEN2}) and green (V_{GEN3}) lines respectively. V_{GEN} is held constant between the sampling instants. As can be seen, the faster the sampling rate, the more time V_{GEN} spends near V_{MPP} and, therefore, the more energy will be extracted.

However, as can be seen in more detail in Figure 25.b (inset zoom), some time is spent in the sampling event (t_{SAMP}), during which the EH source is open-circuit, and no energy is harvested. During t_{SAMP}, V_{GEN} reaches V_{OC}, follows it, and finally drops to the new V_{MPP}. This voltage is then held during a time t_{HARV} until the next sampling instant. Since t_{SAMP} is fixed to a minimum time, as required by the S&H circuit to settle to the new MPP, increasing f_{MPPT} reduces t_{HARV} and thus the time percentage of harvesting energy from the EH source. So, there is a trade-off in increasing the sampling rate.

Table 5 summarizes some resistor- and capacitor-based FOCV-MPPT works that deal with a relatively fast sampling rate. T_{MPPT} down to some milliseconds are reported, which would be enough to properly track the operation point of a WEC such as that presented in P.[41] (results shown in Figure 16). For example, a T_{MPPT} of 50 ms sampling a WECs output voltage oscillating at a T_{EH} of 0.56 s (1.8 Hz) would mean around 10 samples per period. Nevertheless, works presented in Table 5 are mainly on-chip complex solutions incorporating significant power losses which may not pay off for the increase of energy obtained in following the MPP closer. Furthermore, in many cases, details of the implementation of the S&H circuit are not provided.

Table 3 summarizes several companies offering PMU ICs with FOCV-MPPT capabilities for very low-power EH applications. The BQ25504/5 and the ADP5091/2 offer a fix T_{MPPT} of 4-16 seconds, which is extremely slow for tracking some EH sources. The AEM30330 offers a T_{MPPT} down to 18 ms with a t_{SAMP} of 3.8 ms, which represents 20% of the operation time and drastically reduces its overall efficiency. No specific details of their implementation are provided either, so it is not clear which S&H method is used. . To conclude, there is a lack of commercial products designed for EH sources in which a fast update of the MPP is required.

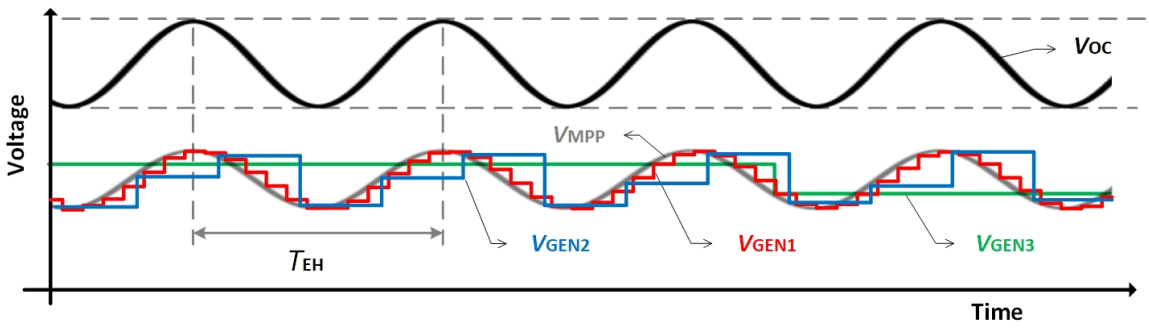

Figure 27. Sinusoidal *Voc* waveform with positive offset for a harvester (black line), the corresponding V_{MPP} (½V_{OC}) and the EH output (V_{GEN}) for three sampling periods (green, blue and red lines) using the FOCV-MPPT method.

Limitations for Speeding Up the Sampling Rate

Resistor-based FOCV-MPPT circuits generally offer greater precision in the MPP tracking and require a smaller number of switches. This makes them more appropriate for ultra-low power EH applications. In this section, limitations on speeding up the f_{MPPT} using these circuits are analyzed. Nomenclature shown in Figure 25.a is used for this purpose.

To increase the sampling rate, T_{MPPT} must be reduced, which is composed of both t_{SAMP} and t_{HARV}. To avoid decreasing the harvested energy, t_{SAMP} must be reduced proportionally. Therefore, the sampling ratio defined as

$$r_S = \frac{t_{SAMP}}{T_{MPPT}} \tag{12}$$

should be kept constant. This sampling ratio is commonly kept below 2% in commercial PMUs. During t_{SAMP}, C_{SAMP} must be updated to a new value of V_{MPP}. In order for the error in the sampled voltage to be e.g. < 1 %, we require the charging ratio defined as

$$r_C = \frac{t_{SAMP}}{\tau} \tag{13}$$

to be higher than 4.6, where τ is the capacitor's constant of charge given by

$$\tau = R_{TH} C_{SAMP} \tag{14}$$

R_{TH} is equivalent to R_1 in parallel with R_2, assuming the equivalent output resistance of the EH source (R_G) neglectable (Figure 17). Thus, for a fixed value of r_C, a reduction of t_{SAMP} implies decreasing τ and therefore either R_{TH} or C_{SAMP}.

On the one hand, R_{TH} can be decreased by reducing the values on the sampling resistor divider. This leads to an increase of the wasted power (reduction of the global efficiency in the PMU) because the resistor divider is always connected to V_{GEN}. Thus, a significantly high resistor divider ($R_1+R_2 >> R_G$) is required, to also attain an accurate V_{MPP}. On the other hand, reducing C_{SAMP} has two potential limitations. First, it should hold V_{MPP} during t_{HARV} in spite of any leakage current at the PMU pin connected to C_{SAMP}. Second, C_{SAMP} should also deal with the charge injection produced by at the nearby switch.

As an example, the resistor-based FOCV-MPPT circuit suggested for the ADP5092 does not deal with these issues and offers relatively large sampling times and periods of t_{SAMP} = 256 ms and T_{MPPT} = 16 s (r_S = 1.6 %), which are inadequate for applications requiring a fast-sampling. This is probably due to the suggested values for R_1+R_2 (20 MΩ) and C_{SAMP} (10 nF), leading to τ = 50 ms), so that r_C = 5.12.

Reported Solutions for Speeding Up the Sampling Rate

Several ideas can be found documented to address these limitations (some of them previously reported in Table 5), but they are complex and give few details on the implementation of the S&H circuit. A solution to deal with the problem of leakage on C_{SAMP} was presented in [119] and [125] and is shown in Figure 28. Both works share the same idea even though [119] is resistor-based and [125] is capacitor-based FOCV-

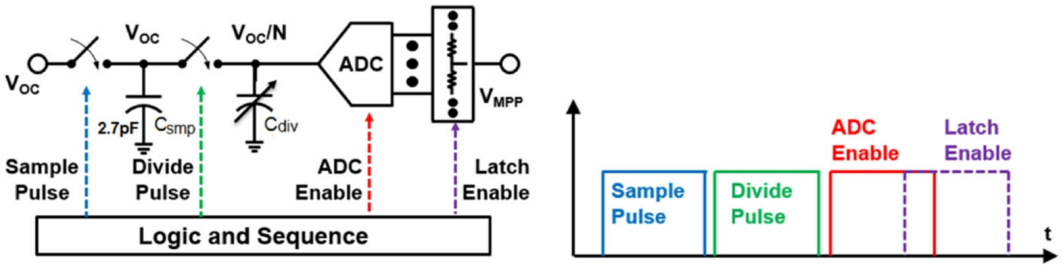

Figure 28. S&H circuit proposed in [125] for the capacitor-based FOCV-MPPT technique.

MPPT. It consists in comparing the sampled V_{MPP} (V_{OC}/N in Figure 28) with a number of fixed voltage references from a resistor string and choosing the closest one as the new V_{MPP}. This is a complex solution requiring a comparator in [119] or a digital ADC in [125], which also adds to the error of the resistor string accuracy.

A solution for the problem of the charge injection on C_{SAMP} was proposed in [121], where a pair of dummy switches driven in counter phase mitigate the increase of voltage on the sampling capacitor.

Finally, in [127], Shrivastava et al. suggested adding a third switch to the standard resistor-based S&H circuit as that shown in Figure 25.a. This switch, connected between the EH source and the resistor divider, disconnects R_1 during t_{HARV}, leading to a reduction of power loses. Then, the resistor divider can also be decreased to reduce the time of charge of C_{SAMP} and allow faster sampling rates.

3.3. Proposed Fast-Tracking Resistor-Based FOCV-MPPT Techniques and Circuits

A WEC such as one of those reported in section 2.3 embedded on a WO will ideally respond with a voltage output similar to that shown in Figure 16. This OC voltage consists of a waveform oscillating between 1 and 2 volts at around 1.8 Hz. To track the MPP of this kind on fast-varying EH sources with at least 10 samples per period (T_{EH} = 0.56 s) a fast sampling period of at least 50 ms is required. Other fast-varying sources vibrating at higher frequencies may require even lower T_{MPPT}. In this section, the contributions made within this thesis to prove the necessity of increasing the sampling rate in fast-varying EH sources are presented in subsection 3.3.1. The proposed techniques to meet this necessity and their implementation are in subsections 3.3.2 and 3.3.3 respectively. Finally, subsection 3.3.4 reports some experimental results.

3.3.1. MPP Fast-Tracking Necessity

To demonstrate the necessity of increasing the sampling rate of PMU working with fast-varying EH sources, we have conducted three experimental tests, each reported in different publications.

First Test in a Controlled Sea Area

The double-pendulum WEC reported in section 2.3 (model Figure 14.b) was embedded in a WO and deployed in a monitored sea area (Figure 31.a) with incident waves composed of an H_{m0} of 1.43 m and an T_{m2} of 3.45 s (measured with an ADCP). The commercial ADP5092 was used as the PMU with a 50% resistor-based FOCV-MPPT technique. The sampling parameters were those found by default (t_{SAMP} = 256 ms and T_{MPPT} = 16 s). The configuration of Figure 21.a was used with a 2.2 Ah and 3.6 V Li-ion rechargeable battery connected to BAT and no load. A real-time monitoring system was designed to measure the PMU input and output voltages and currents (V_{GEN}, I_{IN}, V_{BAT} and I_{OUT} defined in Figure 21.a) and to estimate the rotation in the EG shaft. From these measurements, the PMU input (P_{IN} – output of the WEC) and output powers (P_{OUT} – input of the ESE) were obtained. The measurement system also includes an IMU to study the motion of the drifter and a Wi-Fi module for real-time data communication at short distances. The whole measurement system and setup is described in P.[59], which is included in appendix A2.

Figure 29 shows the results we reported in P.[59], where 140 seconds of acquired data are included. The first plot show V_{GEN} together with the EG rotation, which is averaged over time intervals of 6 s to reduce their high variability. The global average rotation speed was 437 rpm. The different MPP levels forced by the PMU can be appreciated in V_{GEN}. The PMU efficiency (averaged for 20 s intervals) is shown in the second plot, ranging from 70 to 90 %. Finally, the third and the fourth plots show P_{IN} and P_{OUT} with average values of 225 and 179 μW respectively.

Although the WEC worked properly under the wave excitation and the PMU charged the ESE with a mean power of 179 μW, the proper track of the WEC's MPP resulted questionable. A stochastic and

pulsating P_{IN}, with an average frequency almost equal to that found on the drifter's angular velocity (pitch), resulted from the WEC's output. Therefore, a T_{MPPT} of 16 s is not suitable to track the MPP. We also observed that when the electrical generator rotated at low motion or even stopped instantaneously, V_{GEN} felt to 0 V. At this moment, P_{IN} drops to zero during the next 16 seconds and no energy is harvested until the MPP is updated again. The reason for this is the sampling of a null V_{OC}, which drastically drops the overall PMU efficiency.

Second Test in a Wave Flume

Using the same configuration and set-up as in P.[59], we deployed the WO in the wave flume (shown in Figure 7.c.) under the excitation of regular waves of 30 cm height and 1.25 s period. The commercial ADP5092 was set this time with two MPPT configurations; the FOCV with the default sampling values (t_{SAMP} = 256 ms and T_{MPPT} = 16 s) and the CV at 0.4 volts (most suitable MPP according to previous

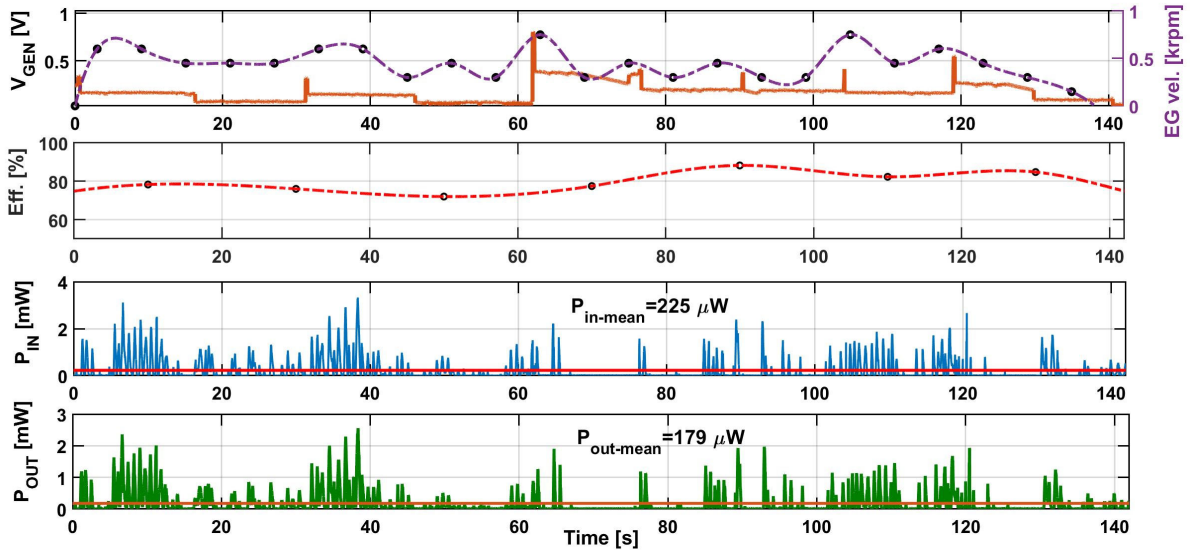

Figure 29. First test in a controlled sea area. From top to bottom; 1) PMU input voltage (V_{GEN} – orange – left axis) and generator shaft rotation (purple – right axis). 2) PMU averaged efficiency (red). 3) PMU input power (P_{IN} - Blue). 4) PMU output power (P_{OUT} - Green). For the powers, the mean value is shown with a solid line.

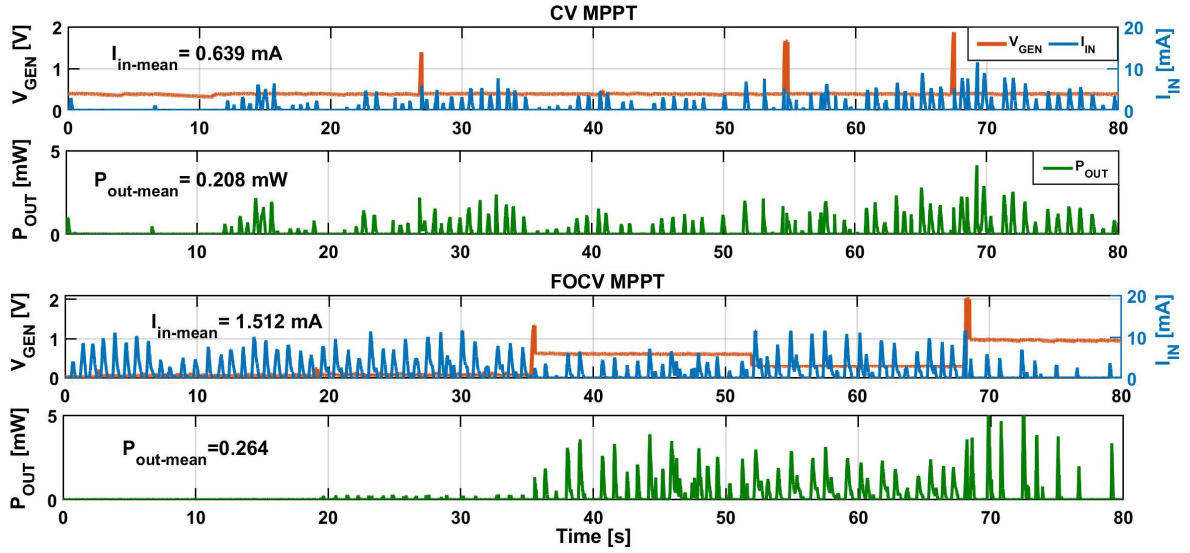

Figure 30. Second test in wave flume. Plots 1) and 3): PMU input voltage (V_{GEN} – orange – left axis) and current (I_{IN} – dark blue – right axis). Plots 2) and 4): PMU output power (P_{OUT} – green). Plots 1-2 are for the FOCV technique and 3-4 for the CV technique.

characterizations). Results are reported in P.[95] and shown in Figure 30 where the PMU input voltage (V_{GEN}) and current (I_{IN} - WEC output) and the PMU output power (P_{OUT} - ESE input) are shown. In the CV configuration, the PMU held V_{MPP} at 0.4 V and charged the battery with a mean power of 0.208 mW. In the FOCV configuration, different V_{MPP} were set according to each measured V_{OC}. In this second case, the PMU charged the battery with a mean power of 0.264 mW. Even though the power harvested in the FOCV was higher, the PMU did not follow the fast dynamics of the WEC, appreciable in the current input. Further, during the first 35 seconds (almost two sampling periods), the input voltage was nearly null for the FOCV. The reason for this is that the PMU sampled two consecutive null voltages for V_{OC} (generator not spinning). So, although the generator of the WEC device started to rotate and thus provide current to the PMU, the generator output voltage (V_{GEN}) and thus power (input for the PMU) were null.

Third Test in a Linear Shaker

A wise method to state the necessity of increasing f_{MPPT} was presented in P.[42]. The double-pendulum WEC reported in section 2.3 (model Figure 14.b) was now attached to the linear shaker shown in Figure 31.a with its pendulum aligned to the movement axis. The shaker was forced to oscillate with a peak-to-peak acceleration of 0.3 g and a frequency of 2 Hz. The commercial ADP5092 was again set with two MPPT configurations; the FOCV with the default sampling values (t_{SAMP} = 256 ms and T_{MPPT} = 16 s) and an emulated fast FOCV. In this second configuration, a signal synchronized with the shaker motion and previously tuned to the desired levels was given to the PMU as V_{MPP} reference. Therefore, the PMU emulated a fast FOCV method without the necessity of sampling V_{OC}. Results showed that harvested energy improves by up to 25% by providing an V_{MPP} signal that nearly matches half the open circuit voltage. Therefore, we stated the necessity of implementing a circuit with a fast refresh of the MPP for fast-varying sources such as WEC.

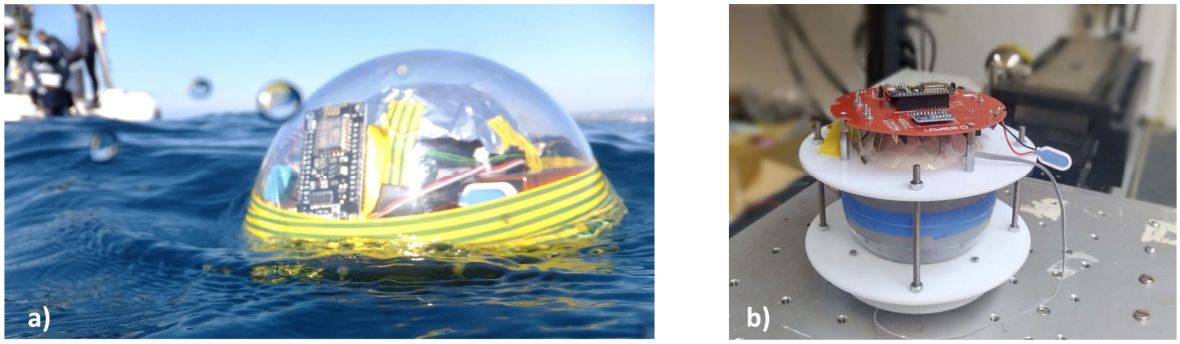

Figure 31. Proving the need for fast-tracking MPPT: a) Deployment of a WO in a controlled sea area, b) Test of the WEC on a linear shaker.

3.3.2. Proposed Resistor-Based FOCV-MPPT Techniques

Within this thesis, we proposed three new circuits to increase the sampling rate of resistor-based FOCV-MPPT techniques and thus improving the efficiency of low-power PMU dedicated to fast-varying EH sources. Specifically, in P.[128] we used a commercial PMU IC with additional low-power circuitry to adapt its sampling parameters. The main objective was to take advantage of the robustness and ultra-low power consumption of a widely-used PMU IC while drastically increasing the sampling rate. Also, a novel FOCV-MPPT method was introduced and validated which, to the best of the authors' knowledge, had not previously been reported.

A typical configuration of the ADP5092, such as the one found in its evaluation board (EB-ADP5092), was used as the reference configuration to be compared to three new proposed and fast-sampling PMU configurations where T_{MPPT} was greatly reduced. Figure 32 shows schematics of the 3 new PMU circuit together with the reference configurations. The WEC model reported in P.[59] was used as EH input and a 165 mAh - 3.7 V Li-Ion polymer battery charged at 3.8 V was used as ESE. No load was connected to

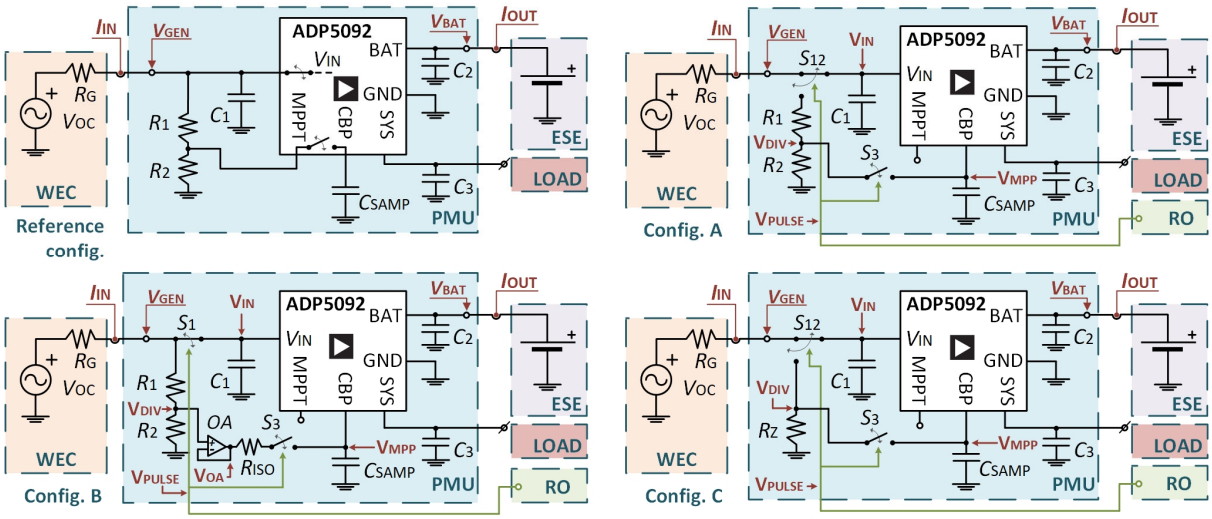

Figure 32. Proposed PMU configurations: Reference (top left), A (top right), B (bottom left), and C (bottom right). All configurations include the WEC electrical model as the input source and an ESE as the sole output load.

SYS. In the proposed configurations the MPPT pin was left floating since V_{MPP} is provided to C_{SAMP} at the CBP pin through the external switch S_3, which works as described in Section 3.2.3. Next, the particularities of the proposed configurations are described.

1) Config. A. A Single Pole Double Throw (SPDT) switch S_{12} connects V_{GEN} with either V_{IN} or the resistor divider. During t_{SAMP}, V_{GEN} connects to the resistor divider, leaving V_{IN} floating. Then, during t_{HARV}, S_{12} connects again V_{GEN} with V_{IN}, disconnecting the resistor divider to avoid losses. So, R_1 and R_2 can be small to reduce t_{SAMP} and to achieve a fast MPPT while resistive power losses are kept low.

2) Config. B. An operational amplifier (OA) working as a voltage follower was included with a series resistor (R_{ISO}) to faster stabilize its output (V_{OA}). C_{SAMP} is directly charged from the OA output, so that its charging time mainly depends on the slew rate (SR) and bandwidth of the OA. Thus, R_1 and R_2 can be increased again to minimize losses without affecting t_{SAMP}, as long as the effect of the OA small input parasitic capacitance (C_{OA}) is small enough.

3) Config. C. During t_{SAMP}, S_{12} connects V_{GEN} to an impedance reference R_Z (=R_G), so that V_{DIV} and V_{MPP} remain as $V_{OC}/2$. Thus, the WEC must be previously characterized to know R_G and this value should not change significantly over time. During t_{HARV}, S_{12} connects V_{GEN} to V_{IN}, disconnecting R_Z. Given R_Z is small, t_{SAMP} can be drastically reduced. This configuration is in fact a novel MPPT method not reported in earlier works and inspired in a working mode of the *e-Peas* chips. It combines the MPPT techniques of resistor emulation [116] and FOCV.

The same sampling control signal is used for all three proposed configurations. Figure 33 shows the implemented circuit based on a relaxation oscillator (RO) using two comparators (CMP). With the appropriate resistive and capacitive components (R_{21}, R_{22}, R_{23}, C_{21} and C_{22}), the first stage generates a squared wave (V_A) while the second stage generates the desired sampling control signal (V_{PULSE}).

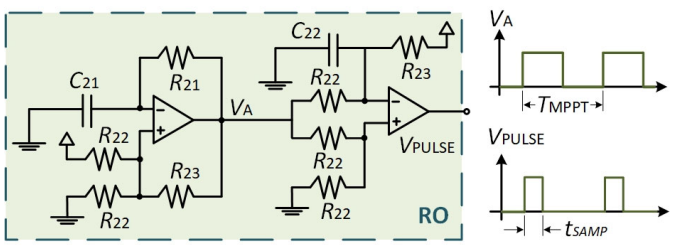

Figure 33. Relaxation oscillator (RO) for the generation of the sampling control signal.

3.3.3. Implemented Resistor-Based FOCV-MPPT Circuits

In P.[128] we also reported the implementation of the proposed circuits. A generic modular circuit board was produced to hold the three proposed PMU configurations, which included the ADP5092 IC, the additional sampling circuitry and the RO circuit (respective boxes highlighted in Figure 32).

Table 7 lists the important components used for each of the four PMU configurations while Table 6 details the components for the RO circuit. Figure 34 shows the implemented board. The active components of the proposed configurations were carefully chosen to be low-power. For the OA, a MAX40007 (*Maxim*, 0.7 µA of typical supply current, rail-to-rail output) was selected. A MCP6542 (*Microchip*, 0.6 µA) includes both comparators of the RO circuit. In addition, a low switching time and on-state resistance (R_{ON}) are sought for the switches. In particular, $R_{ON} << R_G$ for S_{12} and S_1 to reduce losses during t_{HARV} and for S_{12} in config. C to set an accurate V_{MPP} during t_{SAMP}. A low charge injection is sought for S_3 to minimize its effects at C_{SAMP} after the sampling time. For S_{12}, a MAX4714 (*Maxim*, 0.04 µA, 13 ns, 0.6 Ω) was selected, for S_1 a MAX4716 (*Maxim*, 0.04 µA, 12 ns, 0.3 Ω), and for S_3 a MAX4594 (~0.02 µA, 25 ns, 6.5 Ω, 2pC).

According to the values in Table 6, a T_{MPPT} of 24 ms was selected to have a relative high sampling rate and a t_{SAMP} of 0.5 ms to have r_S = 2.1 %, similar to that of the reference config. (1.6 %). According to the values chosen for the S&H circuit, the resulting τ and r_C are reported for each config. at the end of Table 7. Specifically, in config. A, R_1 and R_2 were lowered to 100 kΩ (10 MΩ in the reference and B config.) to lower τ and still have negligible losses and an accurate V_{MPP}. With C_{SAMP} also lowered to 1.2 nF, τ = 60 µs and thus r_C = 8.3, large enough to let V_{MPP} to settle within t_{SAMP}. In config. B, the OA buffers C_{SAMP} and τ was thus calculated as $R_{TH}C_{OA}$ (C_{OA} = 1.5 pF), which allows keeping high values for R_1 and R_2 and still achieve a low value of τ, in particular τ = 7.5 µs (r_C = 67). Here, the OA SR (12 V/ms) needs also to be considered for the charging time of C_{SAMP}. Config. C uses $R_Z = R_G$ (127 Ω, 0.1%) and thus τ = 0.7 µs (accounting R_{ON} of S_3 too) and $r_C \approx 700$, much higher than needed.

	Ref. config.	Config. A	Config. B	Config. C
PMU IC	ADP5092	ADP5092	ADP5092	ADP5092
S_{12} / S_1	-	MAX4714	MAX4716	MAX4714
S_3	-	MAX4594	MAX4594	MAX4594
R_1 / R_2	10 MΩ	100 kΩ	10 MΩ	-
OA	-	-	MAX40007	-
R_{ISO}	-	-	3.3 kΩ	-
R_Z	-	-	-	127 Ω
C_1	10 || 0.1 µF	10 || 0.1 µF	10 || 0.1 µF	10 || 0.1 µF
C_{SAMP}	10 nF	1.2 nF	10 nF	10 nF
C_2	220 µF	220 µF	220 µF	220 µF
C_3	4.7 µF	4.7 µF	4.7 µF	4.7 µF
T_{MPPT}	16 s	24 ms	24 ms	24 ms
t_{SAMP}	256 ms	0.5 ms	0.5 ms	0.5 ms
r_S	1.6%	2.1%	2.1%	2.1%
τ	**50 ms**	**60 µs**	**7.5 µs***	**0.7 µs**
r_C	5.1	8.3	67	≈700

Table 7. Component list for each PMU configuration. *Calculated with the OA input capacitance instead C_{SAMP}.

	RO
CMP	MCP6542
R_{21}	2 MΩ
R_{22}	1 MΩ
R_{23}	5 MΩ
C_{21}	33 nF
C_{22}	1.2 nF

Table 6. Component list for the relaxation oscillator.

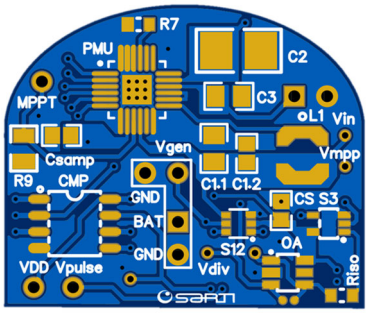

Figure 34. Implemented circuit board to hold the three proposed PMU configurations.

3.3.4. **Performance of the Circuits**

Some of the results we reported in P.[128] are briefly summarized in this section. Further details on the set-up of the test or on the analysis of the results are found in the paper.

To assess the differences in the performance between the three configurations, a function generator was set to provide a sinusoid with a voltage in the range 1-3 V and a frequency of 1.8 Hz, emulating a small-scale WEC under sea-wave excitation (highlighted in an orange box in Figure 32). An external series resistor is added to that of the function generator to obtain the desired value to emulate the WEC's R_G (127 Ω characterized in P.[59]). For the ESE (highlighted in a purple box in Figure 32), a 165 mAh - 3.7 V Li-Ion polymer battery charged at 3.8 V was selected and no load was connected to SYS. A four-channel oscilloscope was used to measure the voltage test points defined in red in Figure 32. In this test, the input power is higher to that given by the WEC seen in previous results.

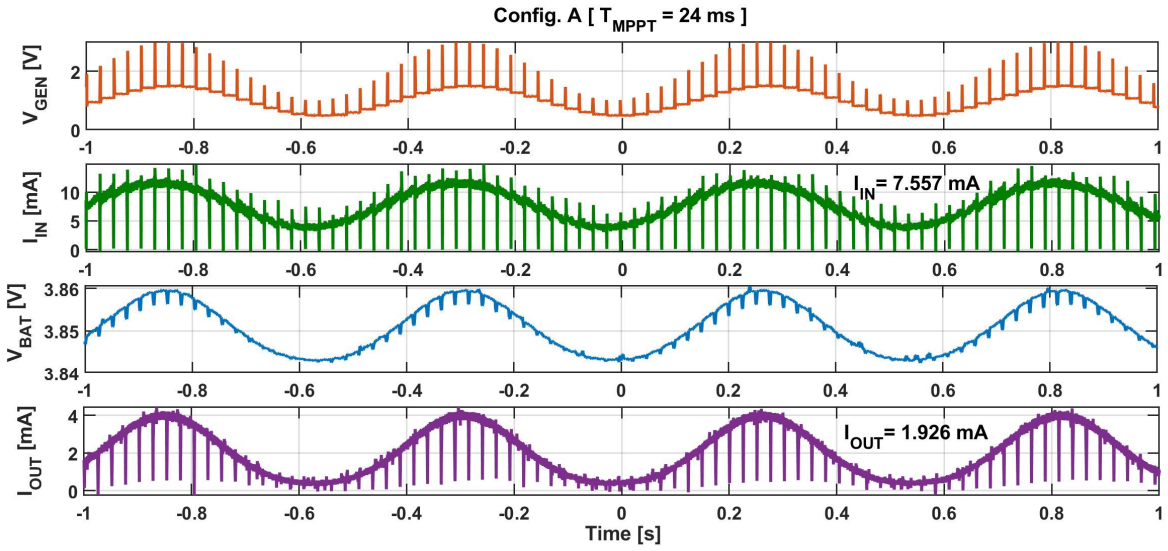

Figure 35. Performance of the config. A PMU using the fast FOCV-MPPT with T_{MPPT} = 24 ms. From top to bottom; 1) PMU input voltage (V_{GEN} – orange), 2) PMU input current (I_{IN} – green), 3) PMU output voltage (V_{BAT} - Blue) and 4) PMU output current (I_{OUT} - purple).

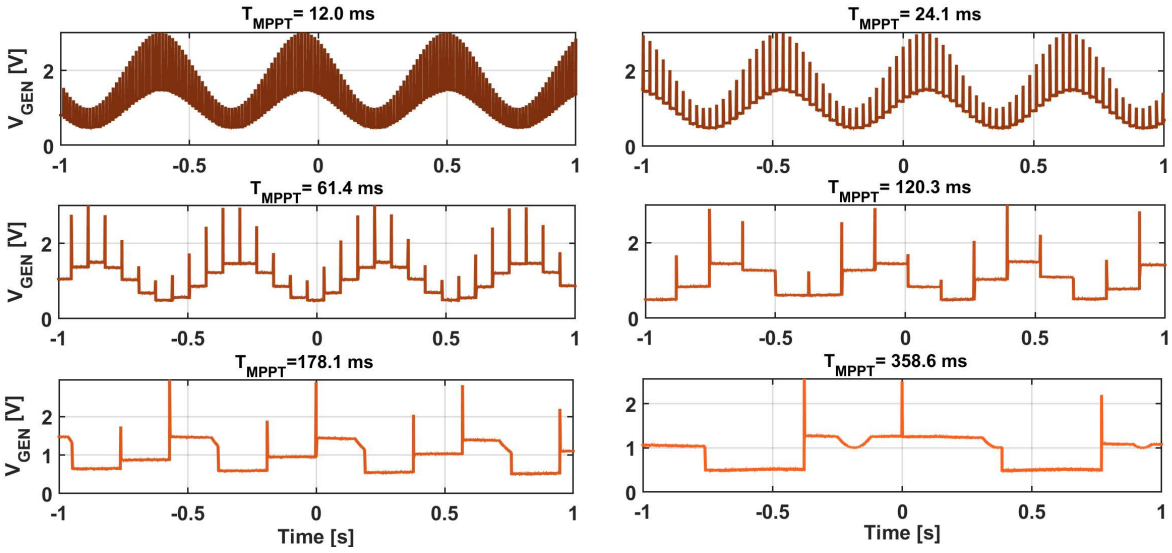

Figure 36. Performance of the config. A over different T_{MPPT}. For all figures, the PMU input voltage (V_{GEN} – orange) is shown.

Figure 35 shows two seconds of measured data from config. A (V_{GEN}, I_{IN}, V_{BAT} and I_{OUT}), selected as example. As can be seen, when the PMU opens the source's output every 24 ms, V_{GEN} rises to V_{OC} (1-3 V) during t_{SAMP} and then settles to $V_{OC}/2$ (0.5-1.5 V) during t_{HARV}, following the behavior shown in Figure 25. During t_{SAMP}, both I_{IN} and I_{OUT} drop to zero because the PMU is disconnected from the WEC. During t_{HARV}, I_{IN} is around $V_{OC}/(2R_G)$, thus between 3.9 and 11.8 mA. V_{BAT} shows a small sinusoidal ripple (< 20 mV) due to the variation of I_{OUT} and the shunt resistor (3.3 Ω) used to measure it.

Second, the performance of config. A over different sampling periods was evaluated. Config. A was selected for this test as the configuration with the best overall performance given the parameters of Table 7. Six values of T_{MPPT} were selected (12, 24.1, 61.4, 120.3, 178.1 and 368.6 ms) while t_{SAMP} was kept constant at 0.5 ms. To modify T_{MPPT} we just changed the value of R_{21}. Figure 36 shows the evolution of V_{GEN} over the different values of T_{MPPT}. Results show that as T_{MPPT} decreases (f_{MPPT} increases), V_{GEN} follows better the sinusoidal shape of V_{OC}. Nevertheless, there is an optimal sampling frequency in which the harvested power reaches its maximum, which in this case happened at T_{MPPT} = 61.4 ms. From this point on, reducing T_{MPPT}, is not worthwhile due to the associated losses of increasing r_S (t_{SAMP} was kept constant). This could be slightly improved by reducing t_{SAMP} and thus r_S. Specifically, in config. C, which is the one with more room for improvement, by reducing C_{SAMP} to 1.2 nF (as in config. A), τ would be reduced to 76 ns. With a r_C of 5, a **t_{SAMP} of 380 ns** could be successfully used without affecting the charge of C_{SAMP}. Then, using a r_S of 1.6 % (as in the commercial ADP5092), a **T_{MPPT} of 24 µs** could be used. This is a great increase of the sampling rate and a great reduction of the time of sample comparing to the previous resistor-based FOCV-MPPT works reported in Table 5, which can significantly increase the energy extraction even further in other faster-varying EH sources.

Finally, we compared the performance of the reference config. (t_{SAMP} = 256 ms and T_{MPPT} = 16 s) and config. A with the optimum sampling rate (t_{SAMP} = 5 ms and T_{MPPT} = 61.4 ms). The WEC such as that of Figure 14.b was placed in the linear shaker shown in Figure 7.a to emulate the surge motion of the drifter under the excitation of waves (1.8 Hz). The WEC was attached to the shaker's moving platform with the device's pendulum aligned to the movement axis.

Figure 37 presents the experimental results of V_{GEN} and P_{OUT} using config. A (left) and the reference config. (right), with a window of two and nine seconds, respectively. The averaged P_{OUT} is also plotted with a dashed pink line. Config. A opens the input circuit every 64 ms (for 0.5 ms) during which no energy is harvested (P_{OUT} = 0 mW). V_{GEN} has sinusoidal-shape in concordance with the shaker's acceleration, as happened in P.[42]. P_{OUT} presents a square sinusoidal-shape following the pendulum's back-and-forward

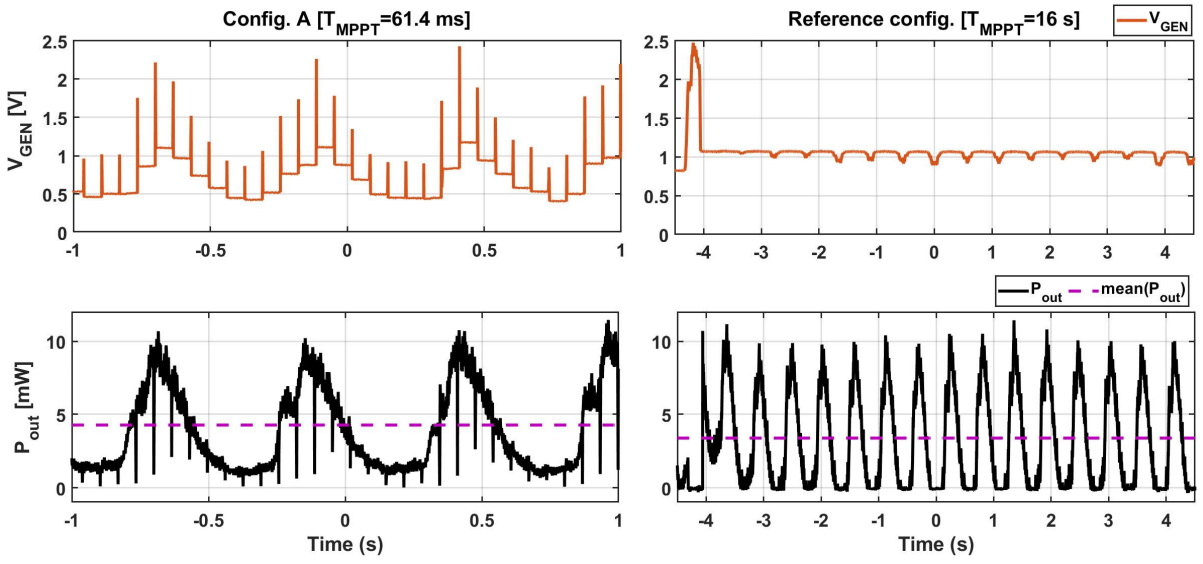

Figure 37. Comparison of the performance between the config. A and the Reference config. Top: PMU input voltage (V_{GEN} – orange). Bottom: PMU output power (P_{OUT} - Black). The mean output power is shown with a dashed pink line.

motion. Thanks to the flywheel that keeps the generator rotating, P_{OUT} only drops to zero during the sampling time. The reference config. only samples V_{OC} every 16 seconds so in the window of 9 seconds shown in Figure 37 (right), just one sampling event can be seen. In this case, P_{OUT} drops to zero during part of every shaker cycle. This happens when the WEC's V_{OC} falls below the current V_{MPP} in which moments the PMU's main converter shuts down.

As for the quantitative results, P_{OUT} is 4.26 mW and 3.38 mW for config. A and the reference, respectively. So, config. A improves P_{OUT} by 26%. This means harvesting 0.88 mW more power. This percentage match with P.[42], where the WEC was placed at the shaker with similar excitation and the fast tracking was emulated by providing an external sinusoidal V_{MPP}.

- In relation with chapter 3, main contributions to **objective 2** were published in "*IEEE Sensors Journal - 2020*" in P.[59] included in **appendix A.2** and in "*IEEE Sensors Conference - 2020 Rotterdam*" in P.[42] included in **appendix A.3**, that are part of this thesis compendium.

Chapter 4
LOW-POWER OCEANOGRAPHIC MONITORING SYSTEMS

Increasing the harvested energy and raising the efficiency of PMUs are crucial factors towards the autonomy of EH-powered AS nodes. Yet, the optimization of the node's consumption should be considered in order to effectively maximize the lifespan of the unit. The most important contributions to the consumption of an AS node is the current during transmission and that during acquisition. Sleep current is another important factor because, although not high, it makes up for a significant percentage of time. Reducing these currents can greatly increase the autonomy of the AS node.

It is mandatory to find the balance between the input energy and that spend on the load. Some recent works try to dynamically balance the harvested energy with that consumed by the AS node. This equilibrium is called the energy neutral operation (ENO) point. The objective of these works is to maximize the number of transmitted packages by measuring the power spent at each transmission and tuning the duty cycle of the device accordingly. This is achieved by using a predictive transmission power control such as that presented in [129].

A low-power oceanographic monitoring system mainly includes the μC, GPS and transmission (Tx) modules and the sensors; e.g. accelerometer or temperature. Depending on its consumption and its duty cycle, its power supply can be composed either of a battery, an EH source or both. In this chapter, an analysis is made of how a low-power oceanographic monitoring system becomes an EH-powered AS sensor such as that of Figure 38. Section 4.1 analyzes the consumption profiles of different low-power oceanographic monitoring systems. Section 4.2 introduces the ultra-low system we presented in P.[130] for the ocean waves monitoring, including the method and some preliminary results. Finally, the feasibility of powering this system with the small-scale WEC is also presented.

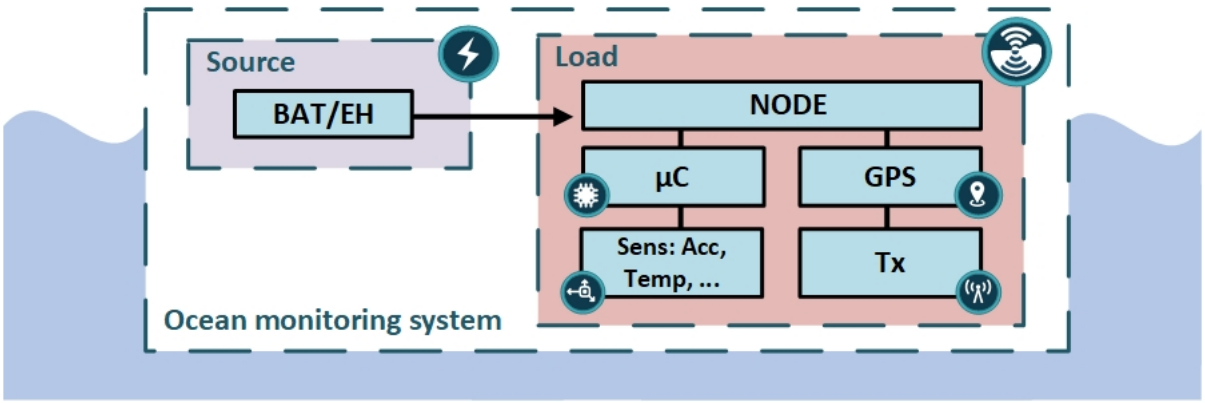

Figure 38. Oceanographic monitoring system powered with a battery pack, an EH source or both.

4.1. Consumption Analysis

4.1.1. WAVY-OCEAN

The consumption profile of the WO from the MELOA consortium is analyzed. This drifter was designed with the contribution of the work done within this thesis, so its consumption levels associated to its internal operation stages are presented. The objective is to define the power requirements of a drifter at full operation.

The WO is an undrogued drifter designed for long-term, offshore deployments consisting in a spherical shape of 20 cm diameter and 3.7 kg of weight (shown in Figure 7.e and f). This results in an overhang of 5 cm from the SWL in rest conditions, reducing the impact of the wind in the WO's shell and making it suitable for wave spectra analysis. The WO includes the Argos Antenna, the Li-Ion battery pack, the PV cells and the main electronics. It is equipped with two thermistor (temperature sensor) measuring air and subsurface temperature, an IMU for the wave parameter measurement and a GPS for the current tracking. By placing the battery pack below the WO's geometric center, its center of mass is shifted 2 cm downwards, making it stable and thus ensuring that the antenna is always above the waterline.

In more detail, Argos is a global satellite-based data collection and positioning system dedicated to the study of the earth's environment and the behavior of species. For example, Argos communication system is used in [23] to transmit data from a oceanographic profiling float or in the WO to transmit the drifter measurements. Argos was developed by CLS, one of the partners of the MELOA consortium and a subsidiary of CNES (French spatial agency). According to Table 2, most of the drifters use Iridium rather than Argos for satellite communication. Differences between both communication systems are presented in [23]. Basically, Iridium provides higher uplink throughput (1000 bits/s) than Argos-3 (latest Argos system – 400 bits/s) and it has 24 hours coverage while Argos needs the satellite pass prediction. Yet, Argos is considered for low-power remote devices and includes the functionality of estimating the position from the transmission using Doppler (250 m accuracy). This makes it very interesting for ultra-low power trackers placed on small animals or AS nodes because it reduces the need for spending energy on the GPS fixing.

Figure 39 shows part of the current profile of a WO (acquired every 20 ms), where a logarithmic scale is used for the current to account for its large dynamic range. These data will be published in the MELOA final report in [66]. The WO is mainly kept asleep at low consumption (marked with an S in the figure). Once per hour, the main electronics wakes up and starts the IMU acquisition (A). To obtain the acceleration power spectrum and calculate the wave parameters, 18 minutes of data at 4 Sa/s are acquired. The algorithm to acquire these wave parameters is described in P.[130] (using a different ocean monitoring system). Then, the GPS module is activated to fix the position while the two thermistors measure the corresponding temperature (stage G). The GPS fixing time is variable and depends on the instantaneous satellite constellation. For comparison purposes with other low power oceanographic monitoring systems described

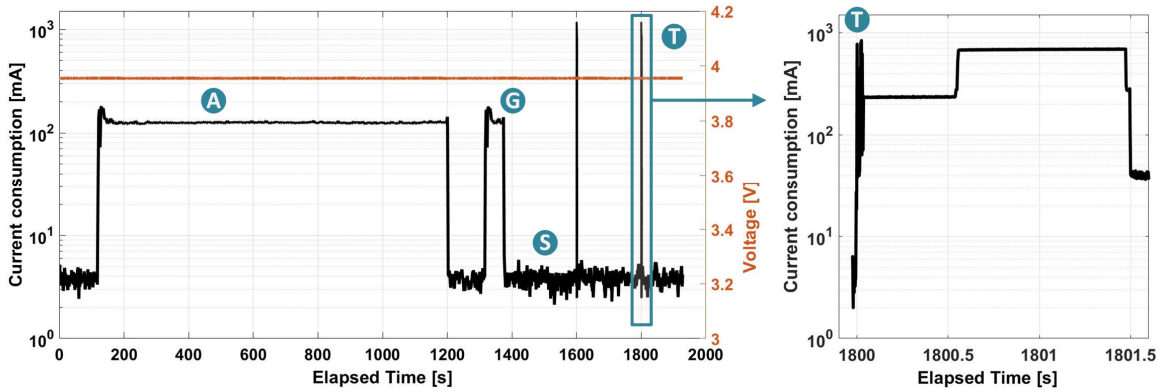

Figure 39. WAVY OCEAN consumption profile (black – left axis) and supply voltage (orange – right axis). A zoom-in of one of the transmissions is shown at the right side of the figure.

in section 4.1, this time will always be computed as 30 s (80 s in Figure 39 for the first fix). Finally, the WO uses the Argos satellite network described in [23] to send two messages; the first containing the wave data and the second containing the temperature and position. To ensure the messages gets to the Argos satellites, both are sent twice. As the Argos coverage is intermittent, the WO buffers all the messages and transmits them during the satellite pass. This way, the average number of hourly messages transmitted is four (the wave and the GPS messages plus one repetition each). Figure 39 shows the transmission of two messages (T) and a zoom-in of one of them to see its profile consumption in detail (acquisition every 10 µs), reaching up to 650 mA. The transmission reaches two consumption levels, in the first level the message is packaged and in the second it is sent. Between the different stages (A, G and T) and during the rest of the hour, the WO is kept asleep.

Table 8 reports the current levels and times spent on the different stages. Other low-power monitoring systems are included for comparative purposes, which are commented in the next subsections. The column Avg. current reports the average hourly current consumption of each stage and the column Tot. avg. curr. reports the aggregation of the average currents of all stages. As for the WO acquiring hourly the wave spectra, stage A is the most significant in terms of consumption. The total average hourly current is 43.5 mA, which results in an average power of 174 mW assuming a voltage supply of 4 V. The WO is currently equipped with a rechargeable battery pack of 36 Li-ion cells arranged in parallel with a total capacity of 126 Ah at a nominal voltage of 3.6 V (consumption test reported in Table 8 fully charged to 4V). With this acquisition and transmitting interval and assuming their full capacity, a lifetime of almost 4 months is estimated (PV harvesting not included). With this fully operation mode, the WO does not reach long-term offshore deployments and it can just be used for middle-term experiments. To fulfill deployments of over one year, the wave acquisition interval can be reduced to 3 measurements per day (instead of 24 – average power around 45 mW).

Other commercial drifters, such as those reported in Table 2, are briefly analyzed with the little information given on the technical specifications. The full capacity of the battery pack is again assumed for all the calculations. The MicroStar (*Pacific Gyre* - [32]) is fed with an Alkaline battery pack of 15 Ah at 12 V and includes a GPS module and a near-surface thermistor. Accounting for the maximum deployment of one year, a minimum average consumption of at least 20 mW is estimated. The SVP drifter (*Pacific Gyre* -

Syst.	Stage	Current (A)	Time (s)	Avg. current (A)	Tot. avg. curr. (mA)	Voltage (V)	Avg. pow. (mW)
WO (MELOA) Full Op.	A	126.3 m	1082	38.0 m	43.5	4	≈174
	G	158.5 m	30	1.32 m			
	T	519.7 m	1.5*(4)	0.9 m			
	S	4.8 m	rest.	3.3 m			
WO (MELOA) Survival	A	0	0	0	1.45	4	≈5.8
	G	0	0	0			
	T	380.6 m	0.8*(2)	0.17 m			
	S	1.3 m	rest.	1.28 m			
LINKIT (*CLS*)	A	n/i	n/i	n/i	0.298	4.2	≈1.25
	G	23.9 m	30	199.2 µ			
	T	38.4 m	6.7	71.5			
	S	28 µ	rest.	27.7 µ			
TD1205P (*TD next*)	A	14 µ	300	1.2 µ	0.295	3.3	≈1.0
	C	3.7	0.5	0.5 µ			
	G	26.4 m	30	220 µ			
	T	46.5 m	5.5	71.0 µ			
	S	3 µ	rest.	2.7 µ			

Table 8. Current consumption report for different low-power ocean monitoring system. n/i: not included. 30 seconds are computed for the GPS fix time for all platforms even figures show other times.

[27]) is fed with an Alkaline battery of 56 Ah at 12 V and includes the GPS module, one thermistor and one weather station for air pressure and wind. Accounting for the maximum deployment of two years, a minimum average consumption of 38 mW is estimated. Finally, the Voyager (*Fastwave* - [34]) uses a pack of 12 D-alkaline-cells of 30 Ah at 9 V to feed the drifter electronics including the GPS and a thermistor. Accounting for the maximum deployment of 300 days, a minimum average consumption of 38 mW is estimated.

According to Table 8, the WO working at full operation mode has a duty cycle of around 31% (assuming 30 s as a mean GPS fix time), an average power of 174 mW and a sleep power of up to 19.2 mW. This is far from the typical consumptions of drifters aiming for long deployments and even more so for low-power AS nodes, demonstrating that the MELOA consortium should further optimize it to reach longer autonomy. For example, the power levels of several recently published AS nodes are summarized in [39], where common duty-cycles below 1%, sleep consumptions between 0.5 and 50 μW and average powers between 0.1 and 0.2 mW are reported.

MELOA consortium has designed the survival mode. This mode is activated when the main battery is exhausted and the electronics is fed from an EH source (either PV or WEC). This is also reported in Table 8. In survival mode, the main electronics are turned off, as well as the acquisition of the sensors and the GPS fix. This makes the sleeping current lower. In this mode, a message is sent every hour containing only the device ID and repeated once. By receiving this message (with no GPS), Argos can estimate its position with an accuracy of 250 m. The time of transmission is lower because the payload is just the ID of the WO (no measurements) and the mean current is also lower due to less time in the high current level (650 mA in Figure 39). With this mode, power consumption is greatly reduced down to 5.8 mW. Although with this, survival mode does not allow for any measurements so other low-power oceanographic monitoring systems are analyzed in the following sections.

4.1.2. **Satellite Trackers**

CLS is now developing the Linkit series, a new family of low-power satellite trackers capable of sending small-size messages of 32 bytes, containing the location, using the Argos network. The transmission ratio can be sped up to 10 minutes (144 messages per day). The Linkit modules include the main μC, a GPS module and the Argos communication transceiver. These trackers also include the possibility of integrating an ultra-low power 3D accelerometer whose measurements are embedded in its transmitted packages, making them a very interesting proposal for low-power oceanographic monitoring systems.

CLS kindly provided information on one of these tracker's consumption, set with the following hourly routine; (G) wake-up and acquire the GPS position with a timeout of 100 seconds and (T) package the data and transmit it using Argos network. The acquisition of the accelerometer and thus the calculation of the wave parameters was not included here. Figure 40 shows the supply current and voltage profiles of a Linkit

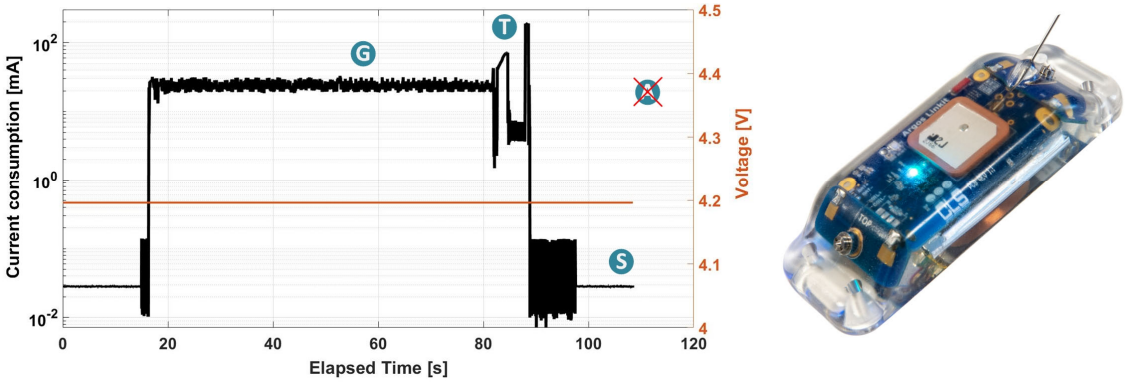

Figure 40. Linkit (*CLS*) module consumption profile (black – left axis) and supply voltage (orange – right axis) using Argos as communication system.

module. The voltage supply is 4.2 V and, as in Figure 39, a logarithmic scale is used for current. Table 8 includes the data of the consumption levels. Even though Figure 39 shows a fixing time of around 70 seconds, that time was set again to 30 s, which according to CLS, is enough for a GPS fix with less than 2-meter accuracy. The transmission has an average current of 38.4 mA with a peak of 180 mA. This is much lower than that of the WO because it requires less power in the antenna for transmission. The total average current is lower than 0.3 mA and the average power 1.25 mW, so much lower than the systems presented above in section 4.1.1, even compared with the WO in survival mode.

The Linkit device is encapsulated in resin within a box of 12×4.2×2.2 cm weighing around 140 g. It is designed to reach depths of down to -1500 m to be attached to ocean mammals or oceanic platforms such as an AUV. With the consumption presented in Table 8 (IMU acceleration not included), acquiring the GPS and transmitting the position hourly, and with the recommended Li-Po battery of 2.2 Ah, the expected autonomy of the Linkit is around 300 days (full capacity assumed). Even though the acquisition of the accelerometer data is not included here, the Linkit series tracking modules are a suitable platform for low-power oceanographic monitoring systems with a high potential to be fed by EH sources. Nevertheless, these devices are still in a preliminary phase and CLS is still working on them to improve their performance.

4.1.3. **Low-Power Wide Area Networks**

Low-Power Wide Area Networks (LPWAN) have recently begun to be used in coastal marine monitoring because they transmit small-size packages with relatively low power and costs. Among these, LoRa and Sigfox excel [131]. Some implementations of these technologies are presented below. A LoRa communication system was used in [132] to transmit temperature and humidity from an Indonesian island. In [133], authors reached data transmission over the sea at distances up to 28 km by placing expensive antennas between 50 and 100 meters above the sea level. An interesting LoRa system was proposed in [134] for coastal drifting buoys equipped with an embedded system to acquire some wave parameters, although it has not been fully implemented.

Specifically, Sigfox provides longer communication ranges than LoRa [131], making it more suitable for marine offshore applications. The payload of Sigfox messages is smaller than LoRa's, just small amounts of data can be transmitted, but it is enough for remote marine coastal monitoring. Yet, very few works can be found using Sigfox; e.g. that presented in [135] aiming to track endangered salmons in Sweden river zones.

In more detail, Sigfox is a communication technology using Ultra Narrow Band to transmit packages of 12 bytes at a very low byte rate (<100 bits/s) and up to 140 messages/day per device. It is a paid service that includes both the Base Stations and the Backend Services and works at 868 MHz. For example, the TD1205P tracker (*TDnext*) is a small-size (30×38×10.5 mm) module that includes an EFM32G (32-bit ARM

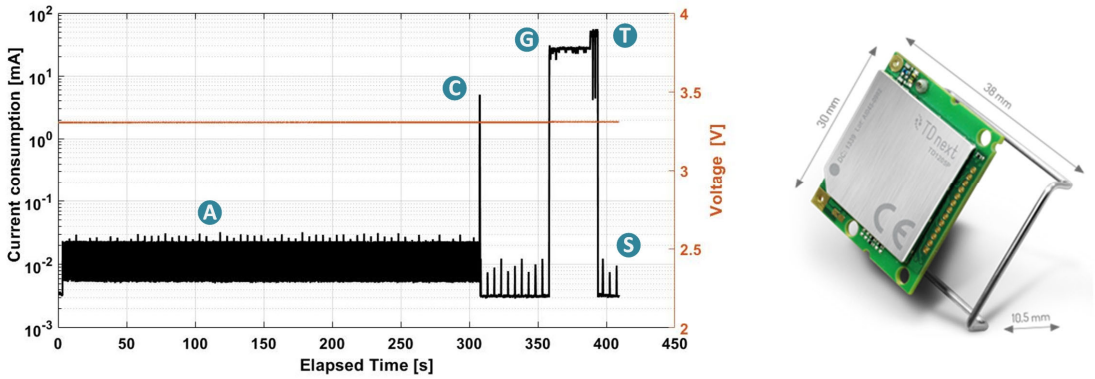

Figure 41. TD1205P (*TDnext*) module consumption profile (black – left axis) and supply voltage (orange – right axis) using Sigfox as communication system.

Cortex-M3-based) μC, an ultra-low power 3D Accelerometer, a GPS module and a Sigfox communication transceiver.

For consumption analysis, a TD1205P module was programed with the following hourly routine; (A) acquire 300 s of the vertical acceleration (a_z) at 5 Sa/s, resulting in 1500 data samples; (C) calculate some wave parameters using the algorithm described in P.[130] (later described in 4.2), (G) fix the GPS position with a time limited to 60 s to avoid excessive power consumption; (T) send the data through the Sigfox network in a 12 bytes message that includes the wave parameters, an internal temperature, the battery voltage and the GPS latitude and longitude; and (S) returns to sleep mode.

Figure 41 shows the supply current and voltage profiles of the TD1205P module (acquired every 10 ms). Voltage is 3.3 V and, as in Figure 39, a logarithmic scale is used for current to account for the large dynamic range. All stages occur sequentially, with stage S also taking place between stages C and G. Table 8 summarizes the average value of the measured current for each stage as well as the associated time durations and hourly average currents. For stage G an average time of 30 s is again used. The two main contributors are stages G and T, whereas the current wasted in the rest of the stages is negligible. The average power is even lower than that of the satellite tracker presented in section 4.1.2 and much lower than those of section 4.1.1.

With a battery pack of two CR123A-3V connected in parallel providing an overall capacity of around 3 Ah, the estimated life is about 420 days (assuming their full capacity). A significant increase could be achieved by decreasing the duration of stage G, e.g. by shifting the estimation of the GPS position from the device to a database. This is a paid service offered by some companies [136] but it cannot be implemented in the Sigfox modules of *TDnext*, such as the TD1205P yet. Another option would be to save the current ephemeris during the sleep mode. As we reported in P.[137], stage G can be reduced down to about 4 seconds at the cost of increasing the current consumption of stage S up to 16 μA. However, ephemeris is valid for only 4 hours, hence it must be updated regularly. Overall, the battery lifetime could be almost nearly doubled.

To sum up, Table 8 exposes the power consumption of the WO, the Linkit module (Argos) and the TD1205P (Sigfox). The WO, at full operation mode, is a relatively high consuming oceanographic monitoring platform, hardly feedable with EH sources. By reducing the acquisition interval of the accelerometer to 3 samples per day, the WO consumption can be greatly reduced to levels similar to other oceanic drifters. The WO survival mode reduces this consumption further but the WO become just a tracker with 250 m accuracy. The Linkit and the TD1205P modules are low-power solutions for oceanographic monitoring systems. Even though the acquisition of the accelerometer data of the Linkit is not included in Table 8, the consumption of both modules is comparable: ≈30 mA for the GPS fix and ≈40 mA for the transmission, with a communication time of ≈6 seconds. The main difference is found in the sleep consumption; 3 μA for the TD1205P and 28 μA for the Linkit. However, differences between the WO and these low-power devices are very large. Both alternatives only transmit very small packages of data and, in the case of the TD1205P, just from near-shore ubications (up to 50 km offshore according to [131]). Further, the μC computing limitations are substantial; notice the TD1205P could not work with more than 1500 samples (just acquires 300 s).

4.2. **Proposed Low-Power Oceanographic Monitoring Systems**

In P.[130] we suggested measuring coastal waves with a low-power, Sigfox-based oceanographic monitoring system. Specifically, the objective was to obtain the position of a coastal buoy hourly and some wave parameters using the zero-upcrossing technique (described in 2.1.1) as well as wirelessly transmit them using the Sigfox network. Given its very-low consumption shown in Table 8, the TD1205P module was selected for this purpose. Later, in P.[64], we proposed using this same low power device but switching the power to a WEC source. Some preliminary results demonstrate the potential of the application.

4.2.1. Estimation of the Wave Parameters

The wave estimation procedure is briefly presented here. For additional information, consult the full algorithm in P.[130] (included in appendix A.4). As an IMU is not available in the TD1205P but just a 3-axis accelerometer, the gyroscope data cannot be used to correct the potential tilt of the buoy. Therefore, the vertical acceleration (a_z) is used to reconstruct the sea surface elevation (z_P defined in 2.1.1). This simplification was also used in [138] and proved to be accurate enough. Then, the zero-upcrossing technique is used to obtain some wave parameters. Given the memory and processing constrains of the µC (EFM32G), just H_{MAX} and T_Z are estimated. Figure 42 shows the steps followed for that.

First, the TD1205P module is programed to acquire 300 s of a_z at 5 Sa/s, resulting in a record of 1500 data samples. The gravity effect is then removed from a_z by subtracting its mean value, incrementally calculated as

$$M[i] = \frac{(i-1)M[i-1] + a_z[i]}{i} \tag{15}$$

where i is the number of the current sample. Second, a discrimination window (DW), consisting in assigning a zero value to values of $a_z \leq 5$ mg, smooths out accelerometer's errors due to mechanical noise during flat sea states. Third, a digital first-order, high-pass filter (HPF) removes the slow motion of the infra-gravity waves (periods larger than 30 s), resulting in the wave orbital acceleration. The implementation of the HPF in discrete-time is given by

$$y[i] = \alpha \cdot (y[i-1] + x[i] - x[i-1]) \tag{16}$$

where $x[i]$ and $y[i]$ are the data set of samples before and after the HPF, respectively, and α is given by

$$\alpha = \frac{1}{1 + 2\pi f_c T_s} \tag{17}$$

where T_s is the sampling period of the accelerometer data and f_c is the cut-off frequency of the HPF. Fourth, the vertical velocity v_z is obtained performing a numerical time integration given by [139]

$$v_z[i] = v_z[i-1] + \frac{a[i-1] + a[i]}{2} T_s \tag{18}$$

with the first value forced to zero. Again, (16) is used to filter v_z and z_P is obtained by integrating the velocity using

$$z_P[i] = z_P[i-1] + \frac{v_z[i-1] + v_z[i]}{2} T_s \tag{19}$$

with the first value forced to zero. Then, (16) is subsequently applied. Overall, applying three concatenated HPFs removes the slow motion of infra-gravity waves better. Finally, T_Z is obtained by dividing the time length of the record by the number of zero-upcrossings in that record. H_{MAX} is determined by the difference of the maximum and the minimum values of the z_P record.

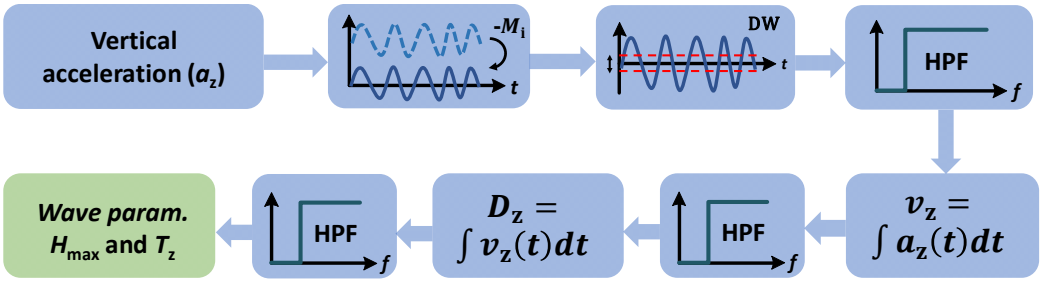

Figure 42. Steps for the estimation of the wave parameters H_{MAX} and T_Z.

The TD1205P module was encapsulated for validation test within an IP64 case (83×35×57 mm) that also included two CR123A-3V connected in parallel. The system was set with the hourly working procedure previously described in 4.1.3. The data was sent in a 12 bytes message that included H_{MAX}, T_Z, an internal temperature, the battery voltage and the GPS position.

The algorithm was validated on a real sea test by comparing the TD1205P wave results (H_{MAX} and T_Z) with that provided by a seafloor ADCP (1 MHz – Nortek), used as a reference. To do so, the encapsulated system was attached to the upper part of a moored buoy placed at 4 km off the coast. This buoy is above a 20 meters depth underwater cabled observatory (OBSEA, defined in P.[5]) to which the ADCP is connected. Mainly, it acquires 10 minutes of wave data each hour, calculates the wave parameters and transmits the data through the OBSEA network. Both, the encapsulated TD1205P module and the ADCP, were deployed during the summer of 2020. A correlation analysis between the ADCP and the TD1205P measurements is presented in P.[130] (appendix A.4) validating the herein designed algorithm. To sum up, the TD1205P successfully measured some wave parameters using an ultralow power oceanographic monitoring system which also includes a GPS tracker.

4.2.2. Main Structure and Acquired Data

Given the good performance of the wave measurement system and its low consumption, throughout this thesis we proposed to go even further and to modify the battery power supply proposed in P.[130] by a small-scale WEC source. Therefore, we suggest a system such as that shown in Figure 43.

The double-pendulum WEC reported in section 2.3 (model Figure 14.b) is selected here as the EH source. It is manufactured with a total mass of 300 g and a diameter of 10 cm. The main body is 3D printed with polyamide and the proof mass is made with lead. The total gear ratio is 35 and the electrical generator is the 118391 model from Maxon Motors

The improved circuit based on the ADP5092 IC and presented in P.[128] is selected as the PMU. This circuit implements the 50% resistor-based FOCV-MPPT on the EH source and controls the energy flow between the WEC, the ESE and the LOAD. Config. A (shown Figure 32) with a T_{MPPT} of 60 ms and a t_{SAMP} of 0.5 ms is selected as the configuration with the best overall performance.

The Sigfox-based TD1205P module described in section 4.1.3 is selected as the ocean monitoring system (LOAD in Figure 32). The functionalities of this device are measuring the wave's H_{MAX} and T_Z, fixing the GPS position and transmitting wirelessly the data using Sigfox.

An ESE needs to be placed at the BAT output of the PMU to store or dispatch energy as required. The ESE also accounts for the instantaneous power peaks of the load generated during the transmission. The ESE is designed to meet with the following requirements; a minimum capacity to feed the load for a week of no energy production (later analysed in section 4.2.3), a maximum discharge current capable of fulfilling the load's consumption profile (46.5 mA during 5.5 s) and an internal consumption below 1% of the load average consumption (I_C < 3 μA). The 3/V80H Ni-MH rechargeable battery with a capacity of 80 mAh and a nominal voltage of 3.6 V meets these requirements.

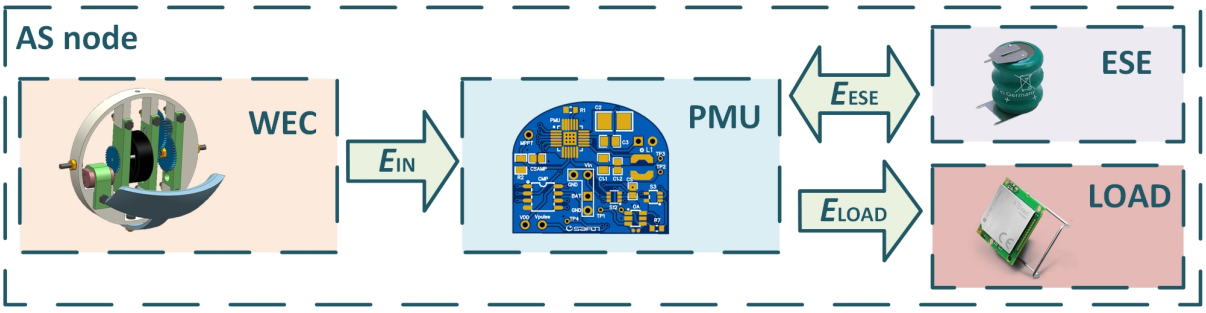

Figure 43. AS node as an oceanographic monitoring system based on the TD1205P (*TDnext*) device (implemented in P.[130]) and powered by the WEC designed in P.[59]. The PMU is based on the improved ADP5092 presented in P.[128] and the ESE is a 80 mAh Ni-MH rechargeable battery

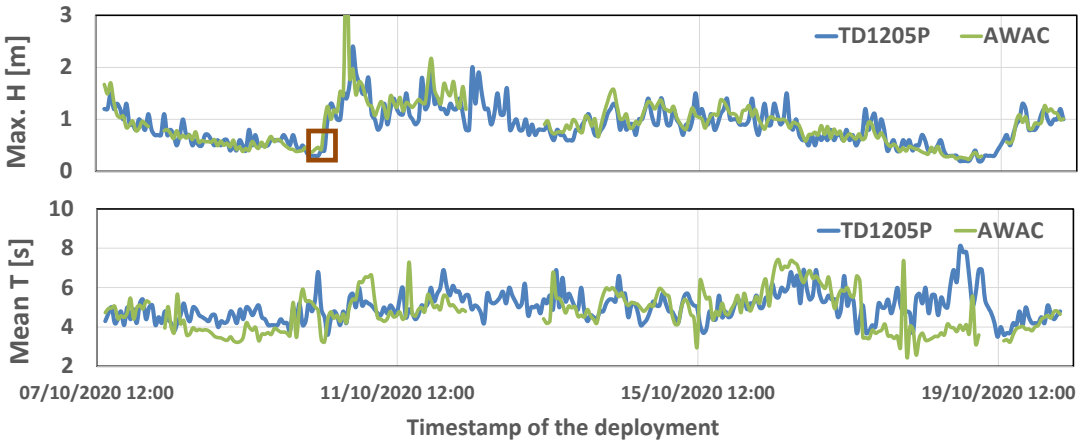

Figure 44. H_{MAX} and T_Z measurements using the low-power ocean monitoring system based on the TD1205P (blue) and using the seafloor ADCP (green).

A similar system to that presented in Figure 43 has already been tested and reported in P.[64]. The only difference is in the PMU. In this test, a PMU with a CV-MPPT technique based on the ADP5092 IC such as that we reported in P.[95] was used. The reason for not using the fast-sampling FOCV-MPPT technique is that, at that time, it had not been fully implemented yet. The whole AS node working as an oceanographic monitoring system was placed on a moored buoy of 37.5 cm of diameter and 14.5 kg, which means that the buoy's waterline was at its equator. The buoy was moored above the OBSEA observatory to again take advantage of the ADCP in terms of comparing wave results.

Figure 44 shows the hourly measured H_{MAX} and T_Z using the ocean monitoring system (blue) between the 7th and the 20th of October of 2020. The same hourly measured parameters using the ADCP are also shown (green). The figure shows the concordance of the results transmitted by the Sigfox network and those measured by the ADCP. As we analyzed in P.[130], this concordance is greater for the measurement of H_{MAX} than for T_Z. Note that a strong storm was measured during the 10th of October where the ADCP measured waves of up to 5 meters (peak not included for better resolution), which is very high for shallow waters.

During this deployment, an independent power measuring system was also included to monitor the PMU input and output voltages and currents (V_{GEN}, I_{IN}, V_{BAT} and I_{OUT} defined in Figure 21.a). From these measurements, the PMU input (P_{IN} – output of the WEC) and output powers (P_{OUT} – input of the ESE) were obtained. The measurement system also includes an IMU to study the motion of the drifter. A real time clock (RTC) and an SD module were used to log the data with a sampling period of 100 ms. This is not enough to measure the fast dynamics of the pendulum but it gives a good idea of the power production. The measurement system was independently fed by a battery to avoid interfering with the AS node's autonomy. The entire measurement system and set-up is described in depth in P.[59], which is included in appendix A2.

Figure 45 shows part of the logged results obtained from the SD card after recovering the buoy. It shows about one hour of the 10th of October (marked with an orange box in Figure 44), just when the big storm started. In the figure, P_{IN} (blue) and V_{BAT} (orange) are shown, both plotted with a moving average of 100 samples (10 s) to facilitate understanding. During the first 800 second, P_{IN} is zero probably due to calm sea conditions. During this time interval, V_{BAT} drops around 3 mV due to the consumption of the TD1205P or the internal consumption of the battery. Then, the storm started to increase the mobility of the buoy, P_{IN} rises above the milliwatt level and V_{BAT} started to increase. During that hour, the mean P_{IN} was 3.935 mW and, during the last 2500 s, the battery voltage increased by 18 mV. During this storm, the measuring system collapsed and this was the last record of data found in the SD card. Hopefully, the AS node kept working and the TD1205P kept transmitting the data shown in Figure 44.

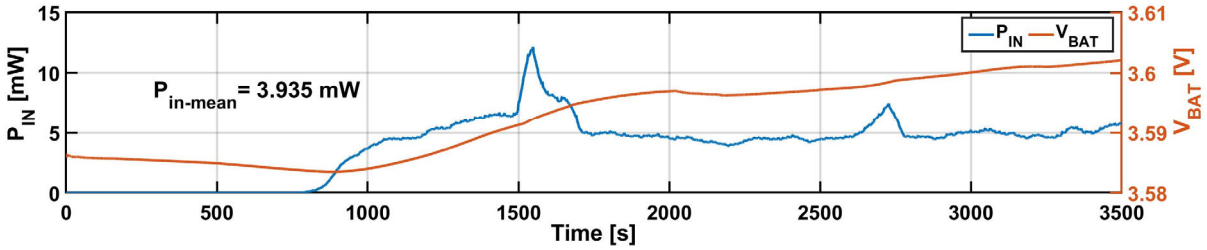

Figure 45. Energy production of the double-pendulum WEC during the storm on the 10th of October of 2020. In this figure V_{BAT} (orange – right axis) and P_{IN} (blue – left axis) are shown.

4.2.3. WEC-Powered Oceanographic Monitoring Systems Possibilities

This subsection briefly analyzes the long-term feasibility of the system presented in Figure 43 with the aim of establishing the number of measurements that can be transmitted under standard wave conditions.

Throughout this thesis, the double-pendulum WEC reported in section 2.3 (Figure 14.b) was tested in different scenarios with different harvesting results. In order to determine the average power that can potentially generate, these tests are summarized in Table 9 in order of execution. Notice the reported P_{OUT} is the power output of the PMU to the ESE. In the case no PMU is placed it is directly the power given by the WEC.

Ref.	Test	Excitation	PMU/MPPT	ESE	LOAD	P_{OUT} (mW)
P.[57]*	**Wave Tank**	Reg.waves: 10 cm, 3 s	-	-	50 Ω	0.22
P.[95]	**Wave flume**	Reg.waves: 30 cm, 1.25 s	FOCV, T_{MPPT}=16s	Li-ion, 2.2Ah @ 4.1 V	-	0.264
P.[59]	**Sea (free)**	H_{m0}= 1.43m, T_{m2}= 3.4s	FOCV, T_{MPPT}=16s	Li-ion, 2.2Ah @ 3.6 V	-	0.18
P.[64]	**Sea (moored)**	H_{m0}> 2m, T_{m2}= 4-6s	CV	Po-Li, 0.3 Ah @ 3.7 V	TD1205P	3.93
P.[42]	**Linear shaker**	0.3 g (ptp), 2 Hz	Emul. fast-FOCV	Po-Li, 0.3 Ah @ 3.7 V	-	5.07
P.[128]	**Linear shaker**	0.3 g (ptp), 1.8 Hz	FOCV, T_{MPPT}=60ms	Li-ion, 0.16 Ah @ 3.8 V	-	4.26

Table 9. Summary of the reported experimental results using the double-pendulum WEC shown in Figure 14.b. *In this article the previous model of the WEC was used. ptp stands for peak-to-peak acceleration.

According to Table 9, P_{OUT} strongly depends on the excitation. These results from the linear shaker show much higher power since the movement is always aligned with the pendulum arm and the WEC works to its maximum possibility. On the other hand, the first test in the sea reported in P.[59] produced low power (0.18 mW) because the drifter was not moored. This entails following the free buoy with a boat and thus requires a relatively calm sea to ensure human safety, which of course does not benefit the collection of energy. Powers reported in the wave tank and flume are also relatively low compared to those from the linear shaker because not high waves were forced. However, in the last sea test reported in P.[64], the buoy was moored and no human interaction was required. During that test, the buoy suffered very adverse sea conditions and the WEC proved its capability of reaching high P_{OUT} also in the sea. Thus, for the feasibility study of permanently powering the AS node, both the worst and the best-case conditions are considered. It is assumed a day of strong wave conditions, like those measured in P. [64], and six days of calm sea, like that measured in P.[59], for a weekly average. The resulting average P_{OUT} is 0.72 mW with a production of 61.8 J/day (E_{LOAD} + E_{ESE} in Figure 43).

As we proved in P.[128], using config. A (shown Figure 32) with a T_{MPPT} of 60 ms and a t_{SAMP} of 0.5 ms on EH sources oscillating at around 1.8 Hz, the energy production improves by 26 % comparing to slow

MPPT techniques. The experiments carried out in the articles found in P.[59] and P.[64] use low (T_{MPPT} of 16 s) or null (CV) sampling ratios respectively. For this reason, an increase of 26% in the energy production is assumed, resulting in 77.3 J/day.

According to Table 8, the Sigfox-based TD1205P module requires 3.5 J/event, which includes A, C, G and T and lasts 336 s. The sleep current consumption is 3 μA and the time of sleep is the rest of those used during all the events. Accounting for 22 events per day, the total spent energy is 77.2 J/day (E_{LOAD}). Therefore, almost one transmission per hour could be achieved with the proposed system. One of the requirements of the ESE stated in 4.2.2 was a minimum capacity to feed the load for a week of no energy production (E_{ESE} > 509.5 J). With the 80mAh Ni-MH rechargeable battery at 3.6 V this stipulation is successfully met.

To sum up, feeding an ultra-low power oceanographic monitoring system with a small-scale WEC is feasible. The herein proposed system accounts for an unlimited autonomy with a data rate of up to 22 transmissions per day and is capable of assuming non-harvesting periods of more than one week.

- In relation with chapter 4, main contributions to **objective 3** were published in "*IEEE International Instrumentation and Measurement Technology Conference – 2021 Glasgow*" in P.[130] included in **appendix A.4,** that are part of this thesis compendium.

Chapter 5
CONCLUSIONS AND FUTURE WORK

5.1. Harvesting Energy from the Drifter's Motion

The motion of the drifter can be mainly described with 3 DoF: surge, heave and pitch. All of which are oscillatory, according to the circular path of the sea surface particle under the influence of waves. The surge includes a superimposed drift generated by the horizontal particle displacement. The heave includes the buoyancy response of the drifter, which can be described with a mass-spring-damping model. Apart from the weight and the buoyancy, the drifter is subject to the external forces and torques induced by the wave's action. Including these hydrodynamic loads in the mass-spring-damping model turns it into a nonlinear system. Therefore, the oscillatory response of the drifter in all three DoF will not just include the wave's frequency and the natural frequencies from the linear system, but also a wide range of frequencies according to its nonlinearity.

Through an analytical model developed within this thesis, the natural frequencies of an undrogued spherical drifter were analysed. The natural frequency of the heave greatly depends on its mass, its size and the distance between the SWL and its geometric center. The natural frequencies of the surge and the pitch are coupled, and basically depend on the mass, the distance from the geometric center to the center of mass and the inertia of the drifter. These results were validated with numerical simulations as well as with experimental results. If these frequencies are close to the excitation frequency, a resonant response that amplifies the oscillatory amplitude may result. That is beneficial for EH purposes because, even if a WEC embedded in the drifter is extremely efficient, the energy it can potentially collect is directly proportional to the drifter's accelerations. Therefore, if the drifter can be designed to have the natural frequencies close to the most common frequencies present in a particular part of the ocean, the WEC has a much higher probability of harvesting more energy. Nevertheless, this optimization also worsens the performance of the data transmission, the wave measurement or the GPS accuracy due to the non-vertical alignment of the drifter. Therefore, it is not a proper approach for this specific application.

Additionally, the captured energy can be maximized without compromising the performance of the drifter by properly designing the inner WEC with a natural frequency close to that of the drifter's movement. Specifically, this can be achieved using parametric excitation in pendulum-type WECs. These WECs provide highly energetic rotational motion with very simple mechanisms. This is a relatively new approach with high EH potential. The main idea is based on approximating the heave of the buoy with a sinusoidal movement which forces the parametric movement of the pendulum. By tuning the pendulum's physical parameters, complete rotations can be achieved and thus the WEC's output power maximized. Nevertheless, this is not possible for all combinations of pendulum and excitation parameters. Often, the resulting optimized device is not feasible; e.g. pendulum arms longer than the diameter of the drifter. Several ideas are reported dealing with this issue; the N-pendulum or the reduced gravity concepts are both promising ideas for the design of pendulum-type WECs.

Within this thesis we suggested using the natural response of the spherical buoy, instead of forcing its heave, so as to obtain the parametric equations of an inner pendulum. This results in a much more complex

problem, not yet studied, because it adds the DoF of the pendulum to those of the buoy. We provided a 4 DoF model which includes the heave, the surge and the pitch of the buoy plus the inner pendulum motion relative to the buoy. The model was validated through a numerical simulator resulting in an oscillatory pitch with a time-variable stiffness. With this, the parametric study of this pendulum would be possible using the proposed system.

Throughout this thesis we have proposed different WECs which comply with the restrictions of the WO drifter model of the MELOA consortium; the most important being a total diameter below 12 cm and a maximum weight below 10% of the drifter's mass (350g). One of these is a double-pendulum WEC. It consists of an articulated pendulum arm with a proof mass. This mass moves relatively with respect to the main body, attached to the drifter, with pendulum motion. Then, through a gear system, rotation is accumulated in a flying wheel which drives a DC electrical generator. The gear system increases the rotation velocity with a ratio of 35 and, due to a one-way gear mechanism, the flying wheel only rotates in one direction, at which energy is accumulated. This WEC was manufactured with a pendulum length of 5 cm, a total diameter of 10 cm and a proof mass of 300 g. After testing several times in various sea conditions, emulated in platforms, wave channels or real waves, we can conclude it harvests anywhere from hundreds of microwatts on average with peaks of up to a few milliwatts. One of the benefits of this device is that its articulated arm allows the WEC to align itself with the direction of wave propagation, thus capturing more energy. In addition, through the one-way gear system plus the flywheel, it is possible to distribute the kinetic energy over time, making the rotations in the EG more stable.

Another WEC was designed complying with the requirements of the WO, which is still in a design phase. It consists of a custom electromagnetic device based on a proof mass rolling in a Tusi circular cavity. The rolling mass includes an array of permanent magnets that induce currents in a coil winding fixed to the circular frame. The WEC's natural frequency was tuned to match with that of the drifter's movement resulting in a rolling mass of 165 g, a cavity radius of 2,3 cm and a total frame size of around 8 cm. From the simulation of this WEC under common wave conditions, an average output power of around hundreds of microwatts was inferred, very similar to that obtained with the double-pendulum.

Thus, pendulum devices with electromagnetic conversions are appropriate for capturing energy in drifting buoys. Expected power levels in standard sea conditions are in the hundreds of microwatts for devices below 10 cm in diameter and 300 g of prof mass. The optimization of this power can be done by modifying the frequency of the WEC to have the natural frequencies close to the most common frequencies of the drifter's movement. These frequencies are normally found around 1 Hz in heave and 1.5 Hz in pitch and surge for buoys such as the WO of the MELOA consortium.

5.2. **Power Management**

EH sources have proven to be capable of feeding low-power AS nodes. However, a PMU is required to convert the EH's variable output to a constant and clean supply to feed the sensor electronics. PMUs should also manage any power mismatch between the source and the load by including an ESE where energy can be stored or dispatched as required. An additional function of the PMU is the MPPT, which has the purpose of continuously ensuring that the maximum available energy is harvested from the EH source.

This thesis reports several works implementing custom PMUs. Normally, a specific DC/DC input converter is placed for implementing the MPPT of each EH source and one DC/DC output converter for providing each desired voltage level supply. The interaction with the ESE can either be implemented with another converter or more simply, with a current limiting switch, for example. To control the entire system, a low-power microcontroller is sometimes placed, although at times a passive system with or-ing diodes fulfils this function. At present, several companies offer PMU ICs with all these functionalities for very low-power EH applications. They are efficient modules which harvest power from microwatts to milliwatts at very low input voltages with ultra-low quiescent currents.

As for the MPPT, there are many reported techniques which can be divided into two types: true-MPPT or near-MPPT. The former measures the output power of the EH source continuously, in order to properly

update the MPP reference. The latter estimates the MPP and avoids adding measurement circuitry or a microcontroller that may increase the consumption and reduce the efficiency of the PMU. Due to the very low power provided by small-scale WEC, near-MPPT systems are more adequate for them. Specifically, the FOCV method gives relatively good accuracy in tracking the MPP while being simple and not incurring large losses. Furthermore, unlike other near-MPPT methods, the FOCV method does not require prior characterization of the WEC. For these reasons, we have leaned toward this method during most of the tests carried out throughout this thesis.

The FOCV-MPPT method exploits the nearly linear relationship between the MPP and the OC voltage. Maximum energy is then harvested by fixing the output voltage of the EH source to a percentage of this OC voltage. This voltage is typically sampled with a S&H circuit that can either be resistor- or capacitor-based. In resistor-based FOCV-MPPT, a resistor divider is used to generate the desired fraction of voltage and then stored in a small sampling capacitor. In capacitor-based FOCV-MPPT, the OC voltage is stored in a sampling capacitor which is then connected to a second capacitor chosen such that the final voltage after charge-sharing is the targeted fraction of voltage. In general, resistor-based circuits offer greater precision in the MPP tracking and require a smaller number of switches. In contrast, capacitor-based circuits allow a fast charging of the sampling capacitor, leading to a drastic reduction of the sampling time. The main drawback is the potential for parasitic interference and charge injection at the small sampling capacitors.

The output voltage of fast-varying EH sources such as a WEC normally oscillates at the frequency of motion of the drifter that supports it, which in the case of the WO, is around 1.5 Hz. Therefore, a fast update of the MPP is required in order to maximize the power extraction. The faster the sampling rate of the FOCV-MPP, the more time the EH source spends near the MPP and, therefore, the more energy is extracted. However, some time is spent in the sampling process during which the EH source is in open-circuit and no energy is harvested. In other words, there is a trade-off on increasing the sampling rate of the MPPT.

Commercial PMUs rarely contemplate the possibility of a fast MPP sampling and normally offer fixed sampling periods in the order of several seconds, which is extremely slow to be able to track some EH sources. Within this thesis, we have demonstrated the need for increasing the sampling rate in fast-varying EH sources through different experimental tests. The most significant of these consisted in emulating a fast FOCV-MPPT by providing an MPP reference synchronized with the motion of the WEC and previously tuned to the desired levels. Results showed that harvested energy can improve by up to 26 % by using the fast FOCV-MPPT technique.

To increase the sampling rate on resistor-based FOCV-MPPT, it is necessary to reduce the charge time of the sampling capacitor. This can either be achieved by reducing the values of the resistor divider or the sampling capacitor. However, there are two limitations. First, reducing the resistor divider values leads to an increase in wasted power. Secondly, reducing the sampling capacitor leads to an MPP voltage reference more vulnerable to the capacitor's leakage current and to the charge injection of the nearby switches. Different solutions have been reported to addressing these issues but they are quite complex solutions requiring additional circuitry which also contributes to power loses.

In this thesis, a commercial PMU IC was used with additional low-power circuitry to adapt its sampling parameters. The main objective was to take advantage of the robustness and ultra-low power consumption of a widely-used PMU IC while drastically increasing the sampling rate. We proposed three novel fast-sampling, resistor-based FOCV-MPPT circuits where the sampling rate was greatly increased. The first includes an additional switch to disconnect the resistor divider during the harvesting time allowing for a drastic reduction in its resistor values. The second adds an operational amplifier working as a voltage follower through which the sampling capacitor is rapidly charged. The third uses an impedance reference, equal to the WEC's internal one, to implement the resistor divider. Given the small size of these resistors, the sampling time can be greatly reduced. This third configuration is, in fact, a novel MPPT method which has not been reported in earlier works and is inspired by the working mode of the *e-Peas* chips. We have implemented these three circuits with a sampling time of 0.5 ms and a sampling period down to 12 ms. However, we justify how in the third circuit, which is the one with more area for improvement, the sampling

period can be decreased to 24 μs. This is a significant reduction in the sampling rate, being a much smaller rate than in all related works reported in this thesis. This reduction can significantly increase the energy extraction even further in faster varying EH sources.

The performance of the commercial PMU, with a sampling period of 16 s, was finally compared with one of the implemented circuits with a sampling period of 61.4 ms. The double-pendulum WEC designed and manufactured within this thesis and placed on a linear shaker emulating the surge motion of the drifter under the excitation of waves was used for this purpose. As we have previously stated, the harvested power output was increased by 26 % with the fast MPPT circuit. Thus, fast-varying sources would greatly be favored by the use of FOCV circuits such as the ones we propose.

5.3. **Low-Ppower Oceanographic Monitoring Systems**

The WO drifter, working at full operation mode, has a duty cycle of approximately 31%, an average power of 173 mW and a sleep power of up to 20 mW. This is a relatively high consuming oceanographic monitoring platform, far from the typical consumption of drifters aiming for long deployments and even more so, for low-power AS nodes. By reducing the acquisition interval of the accelerometer to 3 samples per day, the WO consumption can be greatly reduced to levels similar to those of other oceanic drifters, but still far from the production levels of the herein reported WEC. The WO's survival mode reduces this consumption further, but the WO just becomes a tracker with a 250 m accuracy.

The Linkit and the TD1205P modules are low-power alternatives for oceanographic monitoring systems. The consumption of both modules is comparable; ≈30 mA for the GPS fix and ≈40 mA for the transmission, with a communication time ≈6 seconds for a similar payload. The main difference is found in the sleep consumption; 3 μA for the TD1205P and 28 μA for the Linkit. However, differences between the WO and these low-power devices are enormous. Both alternatives just transmit very small packages of data and, in the case of the TD1205P, just up to 50 km offshore. Further, the μC computing limitations are substantial.

Within this thesis we suggested measuring coastal waves with a low-power, Sigfox-based oceanographic monitoring system. Specifically, we used the TD1205P to obtain the hourly position of a coastal buoy as well as some wave parameters using the zero-upcrossing technique. The data was then transmitted wirelessly using the Sigfox network. This device was fed by a small battery-pack and placed on a moored buoy for a 3-month deployment. The wave measurements were compared with those provided by a seafloor ADCP with a satisfactory result.

Given the good performance of the wave measurement system, but especially the ultra-low consumption of the TD1205P module, we proposed going further and modifying the battery power supply by a WEC source. Therefore, an AS node was designed including the following components proposed in this thesis: double-pendulum WEC, fast-tracking PMU and a low-power wave measurement system. From the different tests executed in different environments (linear shaker, wave flume or sea), we estimated a potential mean EH production of around 77 J/day. With a small rechargeable battery of 80 mAh and using a data rate of up to 22 transmissions/day, the proposed system accounts for an unlimited autonomy and is capable of assuming non-harvesting periods of more than one week.

5.4. **Future Work**

This thesis contributes in the mechanical field of small-scale EH power generation and in the electronic field of low-power energy management. The results achieved have fully met the objectives and tasks set from the onset. There are certain tasks and lines of research, however, which have been left open and that pose exciting technological challenges for future work.

Examining further the 4-DoF pendulum-drifter model with a focus on the parametric pendulum to optimize the WEC is a promising field of study. The objective would be to use the parametric excitation to

achieve full rotations in a small-scale pendulum device embedded in a drifter for standard wave conditions. Further, contemplating the electro-mechanical coupling in the electromagnetic generator model and its adequate optimization is a field that has not been studied in this thesis and could greatly increase the energy produced by the WEC. Moving forward with the manufacturing of the current WECs under design is another line of research. Specifically, we have already started to manufacture the rolling mass WEC that was developed in collaboration with researchers from BRNO University with the idea of testing it in real conditions.

The improvements made in the energy extraction using the herein proposed resistor-based FOCV-MPPT method has already been demonstrated in the laboratory. However, it would be recommended to continue with this line of research by proving similar advances in a real environment such as a wave flume. Testing other fast-sampling and low-power MPPT techniques is another future task, not contemplated in this thesis. The implementation of real-MPPT techniques such as the P&O with a low-power circuitry is a challenging task which can also lead to an increase of energy in fast-varying EH sources. One of the proposed fast-sampling FOCV circuits (config. C) has great potential for further increasing the sampling rate. Studying the possible contributions of this circuit in even more fast-varying EH sources is also recommended for future study.

Finally, a low-power oceanographic monitoring system including a double-pendulum WEC, a fast-tracking PMU and a low-power wave measurement system have been designed. Yet, the long-term test of this system remains pending. Implementing a low-power oceanographic monitoring system with global coverage is also a task not assessed within this thesis. Argos has a high potential for being able to accomplish this. Linkit has proven to be as low power consuming as the TD1205P module but with satellite coverage. Moving the implemented wave estimation algorithm to this platform is a challenging and promising task.

PUBLICATIONS

Publications Directly Associated to the Thesis

Those publications used to fulfil the thesis per compendium requirements are included in Appendix A and highlighted here with a bold reference.

Journals

[59] **M. Carandell,** D. M. Toma, M. Carbonell, J. del Río, and M. Gasulla, "Design and Testing of a Kinetic Energy Harvester Embedded into an Oceanic Drifter," *IEEE Sens. J.*, vol. 20, no. 23, 2020.

[60] **M. Carandell** *et al.*, "Electromagnetic Rolling Mass Wave Energy Harvester for Oceanic Drifter Applications," *Eur. Phys. J. Spec. Top.*, pp. 1–10, 2022.

[128] **M. Carandell,** A. S. Holmes, D. M. Toma, J. del Río, and M. Gasulla, "Techniques and Circuits for Increasing the Sampling Rate of Resistor-Based FOCV-MPPT Units," IEEE Trans. Power Electron., [Submitted], 2022.

Conferences

[41] **M. Carandell,** D. M. Toma, P. Alevras, M. Gasulla, J. del Río, and A. Barjau, "Nonlinear Dynamic Analysis of a Small-Scale Pendulum-Type Wave Energy Converter for Low-Power Marine Monitoring Applications," in *14th European Wave and Tidal Energy Conference - Plymouth*, 2021.

[42] **M. Carandell,** D. M. Toma, J. del Río, and M. Gasulla, "Optimum MPPT Strategy for Low-Power Pendulum-Type Wave Energy Converters," in *IEEE Sensors Conference - Rotterdam*, 2020.

[55] **M. Carandell,** D. M. Toma, J. P. Pinto, M. Gasulla, and J. del Río, "Impact on the Wave Parameters Estimation of a Kinetic Energy Harvester Embedded into a Drifter," in *IEEE OES/MTS OCEANS - Singapur and U.S. Gulf Coast*, 2020.

[57] **M. Carandell,** D. M. Toma, M. Carbonell, M. Gasulla, and J. del Río, "Design and development of a kinetic energy harvester device for oceanic drifter applications," in *IEEE International Instrumentation & Measurement Technology Conference - Auckland*, 2019, pp. 1718–1723.

[58] **M. Carandell,** D. Mihai Toma, M. Gasulla, and J. del Río, "Experimental Validation of a Kinetic Energy Harvester Device for Oceanic Drifter Applications," in *IEEE OES/MTS OCEANS-Marseille*, 2019, p. 17.

[61] H. Liang, **M. Carandell,** O. Z. Olszewski, and G. Hao, "A New Nonlinear Compliant Mechanism for Harvesting Energy from Ocean Waves," in *IEEE OES/MTS OCEANS - Chennai*, 2022.

[130] **M. Carandell,** D. M. Toma, C. Artero, M. Gasulla, and J. del Rio, "Real-time Wave Monitoring on Coastal Areas Using LPWAN-Based Embedded Systems," in *IEEE International Instrumentation & Measurement Technology Conference - Glasgow*, 2021.

[140] **M. Carandell,** D. M. Toma, M. Gasulla, and J. del Río, "Pendulum-Type Wave Energy Converter System for Low-Power Marine Monitoring Applications," *Int. Conf. Adv. Energy Harvest. Technol. - Lublin*, 2021.

[141] **M. Carandell,** D. M. Toma, M. Gasulla, and J. del Río, "Kinetic energy harvester device for oceanic drifter applications," in *1st Materials for Clean Energy Conference - Exeter*, 2019.

Presentations at Workshops

[54] J. Ortiz, **M. Carandell,** and A. Barjau, "Dynamic Analysis of a Pendulum-Type Wave Energy Converter for Oceanic Drifters by means of a 4 DoF Model," in *9th International Workshop on Marine Technologies - Vigo*, 2021.

[95] **M. Carandell,** D. M. Toma, M. Gasulla, and J. del Río, "Evaluation of two MPPT techniques in Low-Power Pendulum-Type Wave Energy Converters," in *9th International Workshop on Marine Technologies - Vigo*, 2021.

[137] **M. Carandell,** D. Mihai, J. del Río, K. Ganchev, and J. Peudennier, "Evaluation of Sigfox LPWAN technology for autonomous sensors in coastal applications," in *8th International Workshop on Marine Technologies - Oporto*, 2018.

[142] D. M. Toma, **M. Carandell,** L. Vals, and J. Del Rio, "A Nonlinear Kinetic Energy Harvester for Light Surface Ocean Drifters," *8th Int. Work. Mar. Technol. - Oporto*, 2018.

[143] **M. Carandell,** D. M. Toma, M. Gasulla, and J. del Río, "Contributions to the pendulum-type wave energy converter system for oceanic drifter applications," in *VI Expanding Ocean Frontiers Conference - Barcelona*, 2021.

[144] **M. Carandell,** D. M. Toma, M. Gasulla, and J. del Río, "Kinetic Energy Harvester embedded on a Drifter," in *10th Energy Harvesting Anual Meeting - Birmingham*, 2020.

Bachelor Thesis Supervision

[53] J. Ortiz, "Simulation of a Pendulum-Type Wave Energy Converter for Oceanic Drifters," *Bachelor Thesis. Univ. Politècnica Catalunya*, 2021.

[63] D. Lahire, "Caracterización experimental de una Power Management Unit para aplicaciones de Energy Harvesting," *Bachelor Thesis. Univ. Politècnica Catalunya*, 2020.

[64] S. Álvarez and M. Perera, "Sistema de monitorización y registro de datos para la asistencia al diseño de boyas de deriva," *Bachelor Thesis. Univ. Politècnica Catalunya*, 2020.

[145] D. Bonilla, "Estudio y caracterización de sistemas electrónicos para la captación de energía de baja potencia.," *Bachelor Thesis. Univ. Politècnica Catalunya*, 2018.

[146] L. Valls, "Estudi d'un captador d'energia electromagnètic a partir de les vibracions generades per l'onatge incident en una boia," *Bachelor Thesis. Univ. Politècnica Catalunya*, 2018.

[147] B. Zambrano and I. Cascos, "Simulación del movimiento de un captador de energía mareomotriz situado en el interior de una boya de deriva," *Bachelor Thesis. Univ. Politècnica Catalunya*, 2019.

[148] Á. C. Quispe, "Sistemas de medida de energía para dispositivos de bajo consumo," *Bachelor Thesis. Univ. Politècnica Catalunya*, 2019.

[149] L. Valls, "Sistema de monitorització y caracterització del sistema de captació d'energia d'una boia de deriva per mesura de corrents marins," *Bachelor Thesis. Univ. Politècnica Catalunya*, 2019.

[150] R. Flix, "Estudi i optimització de la dinàmica no lineal del pèndul paramètric com a sistema de captació de l'energia de les onades en un Drifter Lagrangià," *Bachelor Thesis. Univ. Politècnica Catalunya*, 2022.

Publications Indirectly Associated to the Thesis

Journals

[5] J. Del-Rio ***et al.,*** "Obsea : A Decadal Balance for a Cabled Observatory Deployment," *IEEE Access*, vol. 8, pp. 33163–33177, 2020.

Conferences

[151] I. Masmitja, **M. Carandell,** P. J. Bouvet, J. Aguzzi, S. Gomariz, and J. Del Rio, "Underwater acoustic slant range measurements related to weather and sea state," *XXII World Congr. Int. Meas. Confed. - IMEKO 2018*, vol. 1065, no. 5, 2018.

[152] J. del Río ***et al.,*** "Obsea, ten years of coastal ocean monitoring and test site observatory," in *American Geophysical Union Fall Meeting - New Orleans*, 2021.

Presentations at Workshops

[153] **M. Carandell,** M. Nogueras, R. Chumbinho, and C. Molina, "Data comparison between three acoustic doppler current profilers deployed in OBSEA platform in north-western Mediterranean," in *International Workshop on Marine Technology*, 2016, pp. 116–119.

[154] **M. Carandell,** A. Garcia-Benadí, and J. Del Rio, "OBSEA, a marine sensor testing site for metrology," in *IMEKO TC19 Workshop on Metrology for the sea - Naples*, 2017, pp. 78–82.

[155] **M. Carandell** *et al.*, "JERICO-Next cabled coastal observatories : Harmonization of technologies and methodologies for coastal cabled observatories - technical strategy," in *Copernicus Marine Week - Brussels*, 2017.

[156] **M. Carandell,** J. del Río, and D. Mihai Toma, "Energy harvesting system placed at WAVY drifters," in *2nd Marine Technologies Workshop - Oporto*, 2017.

[157] A. Falahzadeh ***et al.,*** "Remotely-operated Ecological Monitoring at the Seafloor Observatory (OBSEA)," in *VI Expanding Ocean Frontiers Conference - Barcelona*, 2021.

[158] A. Falahzadeh ***et al.,*** "Tele-operated ecological monitoring at the seafloor observatory (OBSEA)," in *9th International Workshop on Marine Technologies - Vigo*, 2021.

[159] D. M. Toma ***et al.,*** "An integrated biogeochemistry observation system at Besòs estuary," in *9th International Workshop on Marine Technologies - Vigo*, 2021.

BIBLIOGRAPHY

[1] R. E. Thomson and W. J. Emery, *Data Analysis Methods in Physical Oceanography*. 2014.

[2] B. M. Míguez *et al.*, "The European Marine Observation and Data Network (EMODnet): Visions and roles of the gateway to marine data in Europe," *Front. Mar. Sci.*, vol. 6, pp. 1–24, 2019.

[3] P. Favali and L. Beranzoli, "EMSO: European multidisciplinary seafloor observatory," *Nucl. Instruments Methods Phys. Res. Sect. A Accel. Spectrometers, Detect. Assoc. Equip.*, vol. 602, no. 1, pp. 21–27, 2009.

[4] E. Martínez, D. M. Toma, S. Jirka, and J. Del Río, "Middleware for plug and play integration of heterogeneous sensor resources into the sensor web," *Sensors*, vol. 17, no. 12, pp. 1–28, 2017.

[5] J. Del-Rio *et al.*, "Obsea : A Decadal Balance for a Cabled Observatory Deployment," *IEEE Access*, vol. 8, pp. 33163–33177, 2020.

[6] L. Laakso, S. Mikkonen, A. Drebs, A. Karjalainen, P. Pirinen, and P. Alenius, "100 Years of atmospheric and marine observations at the Finnish Utö Island in the Baltic Sea," *Ocean Sci.*, vol. 14, no. 4, pp. 617–632, 2018.

[7] M. Cannat *et al.*, "EMSO-Azores: Monitoring seafloor and water column processes at the Mid-Atlantic Ridge," *Fix03-Project Newsletter. Serv. Act. Spec.*, vol. 3, no. 1, pp. 16–17, 2016.

[8] O. Rune Godø, S. Johnsen, and T. Torkelsen, "The LoVe Ocean Observatory is in Operation," *Mar. Technol. Soc. J.*, vol. 48, no. 2, pp. 24–30, 2014.

[9] J. Ryan, C. N. Aonghusa, and E. Sweeney, "SmartBay, Ireland: Design and planning for a cabled ocean observatory off the west coast of Ireland," *Ocean. Conf. Rec.*, 2007.

[10] SARTI Research Group. Universitat Politecnica de Catalunya, "Obsea Observatory." [Online]. Available: http://www.obsea.es/. [Accessed: 01-Feb-2022].

[11] D. M. Toma, C. Artero-Delgado, J. Del Rio, E. Trullol, and X. Roset, "Near real-time determination of earthquake source parameters from the coastal ocean," in *IEEE OES/MTS OCEANS - Aberdeen*, 2017, pp. 1–5.

[12] M. Mcphaden, K. Ando, B. Bourlès, H. P. Freitag, R. Lumpkin, and Y. Masumoto, "The Global tropical moored buoy array," *Proc. Ocean.*, no. 1, pp. 668–682, 2010.

[13] "ALSEAMAR-ALCEN." [Online]. Available: https://www.alseamar-alcen.com/. [Accessed: 01-Feb-2022].

[14] K. L. Dodge, A. L. Kukulya, E. Burke, and M. F. Baumgartner, "TurtleCam: A 'Smart' Autonomous Underwater Vehicle for Investigating Behaviors and Habitats of Sea Turtles," *Front. Mar. Sci.*, vol. 5, no. March, pp. 1–10, 2018.

[15] S. Gomáriz, I. Masmitjà, J. González, G. Masmitjà, and J. Prat, "GUANAY-II: an autonomous underwater vehicle for vertical/horizontal sampling," *J. Mar. Sci. Technol.*, vol. 20, no. 1, pp. 81–93, 2015.

[16] H. Claustre and L. Beguery, "SeaExplorer Glider Breaks Two World Records," *Sea Technol.*, vol. 55, no. 3, pp. 19–21, 2014.

[17] "SofarOcean." [Online]. Available: https://www.sofarocean.com/. [Accessed: 01-Feb-2022].

[18] R. Lumpkin, T. Özgökmen, and L. Centurioni, "Advances in the Application of Surface Drifters," *Ann. Rev. Mar. Sci.*, vol. 9, no. 1, pp. 59–81, 2017.

[19] S. Subbaraya *et al.*, "Circling the seas: Design of lagrangian drifters for ocean monitoring," *IEEE Robot. Autom. Mag.*, vol. 23, no. 4, pp. 42–53, 2016.

[20] R. Lumpkin, S. A. Grodsky, L. Centurioni, M. H. Rio, J. A. Carton, and D. Lee, "Removing spurious low-frequency variability in drifter velocities," *J. Atmos. Ocean. Technol.*, vol. 30, no. 2, pp. 353–360, 2013.

[21] P. M. Poulain, R. Gerin, E. Mauri, and R. Pennel, "Wind effects on drogued and undrogued drifters in the eastern Mediterranean," *J. Atmos. Ocean. Technol.*, vol. 26, no. 6, pp. 1144–1156, 2009.

[22] S. R. Pratt, R. A. Raines, C. E. Fossa, and M. A. Temple, "An operational and performance overview of the IRIDIUM low earth orbit satellite system," *IEEE Commun. Surv. Tutorials*, vol. 2, no. 2, pp. 2–10, 1999.

[23] X. André, B. Moreau, and S. Le Reste, "Argos-3 satellite communication system: Implementation on the Arvor oceanographic profiling floats," *J. Atmos. Ocean. Technol.*, vol. 32, no. 10, pp. 1902–1914, 2015.

[24] J. L. Wang and C. S. Liu, "Development and application of INMARSAT satellite communication system," *Int. Conf. Instrumentation, Meas. Comput. Commun. Control*, pp. 619–621, 2011.

[25] D. Roig Broman and G. Donaire Pascual, "New designs of sea current tracking buoys," *Instrum. Viewp.*, vol. 15, p. 4755, 2012.

[26] "National Organization and Atmospheric Administration. NOAA." [Online]. Available: https://www.noaa.gov/. [Accessed: 03-Feb-2022].

[27] A. Sybrandy and N. Pearn, *The WOCE/TOGA SVP Lagrangian Drifter Construction Manual*. University of California, San Diego, Scripps Institution of Oceanography, 1991.

[28] R. E. Davis, "Drifter observations of coastal surface currents during CODE: The statistical and dynamical views," *J. Geophys. Res.*, 1985.

[29] G. Novelli *et al.*, "A biodegradable surface drifter for ocean sampling on a massive scale," *J. Atmos. Ocean. Technol.*, vol. 34, no. 11, pp. 2509–2532, 2017.

[30] "MELOA project." [Online]. Available: https://www.ec-meloa.eu/. [Accessed: 21-Oct-2021].

[31] "Pacific Gyre." [Online]. Available: https://www.pacificgyre.com/. [Accessed: 21-Nov-2021].

[32] C. Ohmann, "Drifter Observations of Small-Scale Flows in the Philippine Archipelago," *Oceanography*, 2011.

[33] "Zuníbal." [Online]. Available: https://zunibal.com/. [Accessed: 03-Feb-2022].

[34] "Fastwave." [Online]. Available: http://www.fastwave.com.au/. [Accessed: 05-Mar-2022].

[35] "MetOcean." [Online]. Available: https://www.metocean.com/. [Accessed: 20-Mar-2022].

[36] "Quinetiq." [Online]. Available: https://www.qinetiq-na.com/. [Accessed: 05-Mar-2022].

[37] L. Emery, R. Smith, R. McQuary, B. Hughes, and D. Taylor, "Autonomous River Drifting Buoys," *IEEE OES/MTS Ocean. - Santander*, pp. 1–5, 2011.

[38] K. Raghukumar, G. Chang, F. Spada, C. Jones, W. Gans, and T. Janssen, "Wave-Measuring Performance Characteristics of Spoondrift Spotter," *5th Annu. Mar. Energy Technol. Symp.*, 2017.

[39] D. Newell and M. Duffy, "Review of Power Conversion and Energy Management for Low-Power, Low-Voltage Energy Harvesting Powered Wireless Sensors," *IEEE Trans. Power Electron.*, vol. 34, no. 10, pp. 9794–9805, 2019.

[40] M. Shi, A. S. Holmes, and E. M. Yeatman, "Nonlinear Wind Energy Harvesting Based on Mechanical Synchronous Switch Harvesting on Inductor," in *21st International Conference on Solid-State Sensors, Actuators and Microsystems (Transducers) - Virtual*, 2021, vol. 1.

[41] M. Carandell, D. M. Toma, P. Alevras, M. Gasulla, J. del Río, and A. Barjau, "Nonlinear Dynamic Analysis of a Small-Scale Pendulum-Type Wave Energy Converter for Low-Power Marine Monitoring Applications," in *14th European Wave and Tidal Energy Conference - Plymouth*, 2021.

[42] M. Carandell, D. M. Toma, J. del Río, and M. Gasulla, "Optimum MPPT Strategy for Low-Power Pendulum-Type Wave Energy Converters," in *IEEE Sensors Conference - Rotterdam*, 2020.

[43] G. B. Airy, *Tides and Waves*. B. Fellowes, 1845.

[44] Z. Demerbilek, "Water Wave Mechanics," in *Coastal Engineering Manual*, vol. Part II, 2008.

[45] M. S. Liew, E. S. Lim, and T. N. T. Shahdan, "Spectral Analyses of Sea-State Wave Data for the Development of Offshore Metocean Applications : A Malaysian Case Study," *Univ. Teknlogi Petronas, Malaysia.*, pp. 246–253, 2015.

[46] M. K. Ochi and E. N. Hubble, "Six-parameter wave spectra," in *Coastal Engineering*, 1976, pp. 301–328.

[47] H. H. Shen and Y. Shong, "Theoretical study of drift of small rigid floating objects in wave fields," *J. Waterw. port, coastal, Ocean Eng.*, vol. 127, no. 6, pp. 343–351, 2001.

[48] E. B. Carpenter, J. W. Leonard, and S. C. S. Yim, "Experimental and numerical investigations of tethered spar and sphere buoys in irregular waves," *Ocean Eng.*, vol. 22, no. 8, pp. 765–784, 1995.

[49] H. Lin and S. C. Yim, "Coupled Surge-Heave Motions of a Moored System. I: Model Calibration and Parametric Study," *J. Eng. Mech.*, vol. 132, no. 6, pp. 671–680, 2006.

[50] Z. Ballard and B. P. Mann, "Two-Dimensional Nonlinear Analysis of an Untethered Spherical Buoy Due to Wave Loading," *J. Comput. Nonlinear Dyn.*, vol. 8, no. 4, p. 12, 2013.

[51] J. R. Morison, J. W. Johnson, and S. A. Schaaf, "The Force Exerted by Surface Waves on Piles," *J. Pet. Technol.*, 1950.

[52] H. Lin and S. C. S. Yim, "Experimental investigation of stability and bifurcation of nonlinear moored structural responses," in *Proceedings of the International Offshore and Polar Engineering Conference - Montreal*, 1998, vol. 8th, pp. 485–489.

[53] J. Ortiz, "Simulation of a Pendulum-Type Wave Energy Converter for Oceanic Drifters," *Bachelor Thesis. Univ. Politècnica Catalunya*, 2021.

[54] J. Ortiz, M. Carandell, and A. Barjau, "Dynamic Analysis of a Pendulum-Type Wave Energy Converter for Oceanic Drifters by means of a 4 DoF Model," in *9th International Workshop on Marine Technologies - Vigo*, 2021.

[55] M. Carandell, D. M. Toma, J. P. Pinto, M. Gasulla, and J. del Río, "Impact on the Wave Parameters Estimation of a Kinetic Energy Harvester Embedded into a Drifter," in *IEEE OES/MTS OCEANS - Singapur and U.S. Gulf Coast*, 2020.

[56] B. Teillant, J. C. Gilloteaux, and J. V. Ringwood, "Optimal damping profile for a heaving buoy wave energy converter," in *8th IFAC Conference on Control Applications in Marine Systems Rostock Warnemünde, Germany*, 2010, vol. 43, no. 20, pp. 360–365.

[57] M. Carandell, D. M. Toma, M. Carbonell, M. Gasulla, and J. del Río, "Design and development of a kinetic energy harvester device for oceanic drifter applications," in *IEEE International Instrumentation & Measurement Technology Conference - Auckland*, 2019, pp. 1718–1723.

[58] M. Carandell, D. Mihai Toma, M. Gasulla, and J. del Río, "Experimental Validation of a Kinetic Energy Harvester Device for Oceanic Drifter Applications," in *IEEE OES/MTS OCEANS-Marseille*, 2019, p. 17.

[59] M. Carandell, D. M. Toma, M. Carbonell, J. del Río, and M. Gasulla, "Design and Testing of a Kinetic Energy Harvester Embedded into an Oceanic Drifter," *IEEE Sens. J.*, vol. 20, no. 23, 2020.

[60] M. Carandell *et al.*, "Electromagnetic Rolling Mass Wave Energy Harvester for Oceanic Drifter Applications," *Eur. Phys. J. Spec. Top.*, pp. 1–10, 2022.

[61] H. Liang, M. Carandell, O. Z. Olszewski, and G. Hao, "A New Nonlinear Compliant Mechanism for Harvesting Energy from Ocean Waves," in *IEEE OES/MTS OCEANS - Chennai*, 2022.

[62] "KUKA Roboter GmbH." [Online]. Available: https://www.kuka.com/. [Accessed: 15-Feb-2022].

[63] D. Lahire, "Caracterización experimental de una Power Management Unit para aplicaciones de Energy Harvesting," *Bachelor Thesis. Univ. Politècnica Catalunya*, 2020.

[64] S. Álvarez and M. Perera, "Sistema de monitorización y registro de datos para la asistencia al diseño de boyas de deriva," *Bachelor Thesis. Univ. Politècnica Catalunya*, 2020.

[65] "MELOA geoportal. Spanish coast campaign." [Online]. Available: https://geoportal.ec-meloa.eu/#/geoportal/campaign/spanishwocampaign. [Accessed: 16-Feb-2022].

[66] U. Horizon2020, "MELOA Deliverables - CORDIS." [Online]. Available: https://cordis.europa.eu/project/id/776825/results/es. [Accessed: 29-Mar-2022].

[67] L. D. A. Thorner, P. D. Mitcheson, A. S. Holmes, and E. M. Yeatman, "Scaling laws for energy harvesters in a marine environment," in *PowerMEMS - Washington DC*, 2009, pp. 249–252.

[68] B. Drew, A. R. Plummer, and M. N. Sahinkaya, "A review of wave energy converter technology," *Proc. Inst. Mech. Eng. Part A J. Power Energy*, vol. 223, no. 8, pp. 887–902, 2009.

[69] M. Folley, T. Whittaker, and M. Osterried, "The Oscillating Wave Surge Converter," *Proc. Int. Offshore Polar Eng. Conf.*, 2004.

[70] J. P. Kofoed, P. Frigaard, E. Friis-Madsen, and H. C. Sørensen, "Prototype testing of the wave energy converter wave dragon," *Renew. Energy*, vol. 31, no. 2, pp. 181–189, 2006.

[71] P. D. Mitcheson, E. K. Reilly, T. Toh, P. K. Wright, and E. M. Yeatman, "Performance limits of the three MEMS inertial energy generator transduction types," *J. Micromechanics Microengineering*, vol. 17, no. 9, 2007.

[72] N. Pozzi, G. Bracco, B. Passione, A. S. Sergej, G. Vissio, and G. Mattiazzo, "Wave Tank Testing of a Pendulum Wave Energy Converter 1:12 Scale Model," *Int. J. Appl. Mech.*, vol. 9, no. 2, p. 30, 2017.

[73] W. Ding, B. Song, Z. Mao, and K. Wang, "Experimental investigation on an ocean kinetic energy harvester for underwater gliders," in *IEEE Energ. Conv. Congr. and Expos. - Montreal*, 2015, pp. 1035–1038.

[74] W. Ding, K. Wang, Z. Mao, and H. Cao, "Layout optimization of an inertial energy harvester for miniature underwater mooring platforms," *Mar. Struct.*, vol. 69, no. 102681, p. 17, 2020.

[75] C. Dizon, R. J. Cavagnaro, B. Robertson, and T. K. Brekken, "Modular horizontal pendulum wave energy converter: Exploring feasibility to power ocean observation applications in the U.S. pacific northwest," *IET Renew. Power Gener.*, no. March, pp. 1–14, 2021.

[76] Y. Li *et al.*, "Study of an Electromagnetic Ocean Wave Energy Harvester Driven by an Efficient Swing Body Toward the Self-Powered Ocean Buoy Application," *IEEE Access*, vol. 7, pp. 129758–129769, 2019.

[77] X. Chen *et al.*, "A chaotic pendulum triboelectric-electromagnetic hybridized nanogenerator for wave energy scavenging and self-powered wireless sensing system," *Nano Energy*, vol. 69, no. December 2019, 2020.

[78] M. Mejlhede, A. F. Pecher, I. Guraldi, M. T. Andersen, and J. P. Kofoed, "Hydraulic evaluation of Joltech's GyroPTO for wave energy applications," *DCE Tech. Rep. No. 178*, 2015.

[79] Z. Zhang, B. Chen, S. R. K. Nielsen, and J. Olsen, "Gyroscopic power take-off wave energy point absorber in irregular sea states," *Ocean Eng.*, vol. 143, pp. 113–124, 2017.

[80] N. Townsend and A. Shenoi, "A gyroscopic wave energy recovery system for marine vessels," *IEEE J. Ocean. Eng.*, vol. 37, no. 2, pp. 271–280, 2012.

[81] N. C. Townsend, "Self-powered autonomous underwater vehicles: results from a gyroscopic energy scavenging prototype," *IET Renew. Power Gener.*, vol. 10, no. 8, pp. 1078–1086, 2016.

[82] G. Bracco, A. Cagninei, E. Giorcelli, G. Mattiazzo, D. Poggi, and M. Raffero, "Experimental validation of the ISWEC wave to PTO model," *Ocean Eng.*, vol. 120, pp. 40–51, 2016.

[83] F. E. Dotti, F. Reguera, and S. P. Machado, "A review on the nonlinear dynamics of pendulum systems for energy harvesting from ocean waves," in *Pan-American Congress on Computational Mechanics - Buenos Aires*, 2015, pp. 1516–1529.

[84] D. Yurchenko and P. Alevras, "Dynamics of the N-pendulum and its application to a wave energy converter concept," *Int. J. Dyn. Control*, vol. 1, no. 4, pp. 290–299, 2013.

[85] D. Yurchenko and P. Alevras, "Parametric pendulum based wave energy converter," *Mech. Syst. Signal Process.*, vol. 99, pp. 504–515, 2018.

[86] F. E. Dotti and J. N. Virla, "Nonlinear dynamics of the parametric pendulum with a view on wave energy harvesting applications," *J. Comput. Nonlinear Dyn.*, vol. 16, no. 6, 2021.

[87] T. Andreeva, P. Alevras, A. Naess, and D. Yurchenko, "Dynamics of a parametric rotating pendulum under a realistic wave profile," *Int. J. Dyn. Control*, vol. 4, no. 2, pp. 233–238, 2016.

[88] P. Alevras, I. Brown, and D. Yurchenko, "Experimental investigation of a rotating parametric pendulum," *Nonlinear Dyn.*, vol. 81, no. 1–2, pp. 201–213, 2015.

[89] M. E. El-Hawary, "Principles of Electric Machines with Power Electronic Applications," in *IEEE*

Power Engineering Society, 2n ed., 2002, pp. 185-187.

[90] J. Smilek, Z. Hadas, J. Vetiska, and S. Beeby, "Rolling mass energy harvester for very low frequency of input vibrations," *Mech. Syst. Signal Process.*, vol. 125, pp. 215–228, 2019.

[91] H. Liang, G. Hao, O. Z. Olszewski, and V. Pakrashi, "Ultra-low wide bandwidth vibrational energy harvesting using a statically balanced compliant mechanism," *Int. J. Mech. Sci.*, p. 107130, 2022.

[92] U. Horizon2020, "EnABLES project." [Online]. Available: https://www.enables-project.eu/. [Accessed: 31-Mar-2022].

[93] H. Liu, H. Fu, L. Sun, C. Lee, and E. M. Yeatman, "Hybrid energy harvesting technology : From materials, structural design, system integration to applications," *Renew. Sustain. Energy Rev.*, vol. 137, p. 110473, 2020.

[94] M. T. Penella and M. Gasulla, "Runtime extension of low-power wireless sensor nodes using hybrid-storage units," *IEEE Trans. Instrum. Meas.*, vol. 59, no. 4, pp. 857–865, 2010.

[95] M. Carandell, D. M. Toma, M. Gasulla, and J. del Río, "Evaluation of two MPPT techniques in Low-Power Pendulum-Type Wave Energy Converters," in *9th International Workshop on Marine Technologies - Vigo*, 2021.

[96] F. Reverter and M. Gasulla, "Optimal Inductor Current in Boost DC/DC Converters Regulating the Input Voltage Applied to Low-Power Photovoltaic Modules," *IEEE Trans. Power Electron.*, vol. 32, no. 8, pp. 6188–6196, 2017.

[97] J. Kokert, T. Beckedahl, and L. M. Reindl, "Medlay: A reconfigurable micro-power management to investigate self-powered systems," *Sensors*, vol. 18, no. 1, p. 259, 2018.

[98] C. Park and P. H. Chou, "AmbiMax: Autonomous energy harvesting platform for multi-supply wireless sensor nodes," *2006 3rd Annu. IEEE Commun. Soc. Sens. Adhoc Commun. Networks, Secon 2006*, vol. 1, no. c, pp. 168–177, 2007.

[99] J. Varley, M. Martino, S. Poshtkouhi, and O. Trescases, "Battery and Ultra-Capacitor Hybrid Energy Storage System and Power Management Scheme for Solar-Powered Wireless Sensor Nodes," in *IECON - 38th Annual Conference on IEEE Industrial Electronics Society*, 2012, pp. 4806–4811.

[100] F. Ongaro, S. Saggini, and P. Mattavelli, "Li-Ion battery-supercapacitor hybrid storage system for a long lifetime, photovoltaic-based wireless sensor network," *IEEE Trans. Power Electron.*, vol. 27, no. 9, pp. 3944–3952, 2012.

[101] W. Wang, V. Cionca, N. Wang, M. Hayes, B. O'Flynn, and C. O'Mathuna, "Thermoelectric energy harvesting for building energy management wireless sensor networks," *Int. J. Distrib. Sens. Networks*, vol. 2013, 2013.

[102] H. Li, G. Zhang, R. Ma, and Z. You, "Design and experimental evaluation on an advanced multisource energy harvesting system for wireless sensor nodes," *Sci. World J.*, vol. 2014, 2014.

[103] M. Magno *et al.*, "InfiniTime: Multi-sensor wearable bracelet with human body harvesting," *Sustain. Comput. Informatics Syst.*, vol. 11, pp. 38–49, 2016.

[104] T. Esram and P. L. Chapman, "Comparison of photovoltaic array maximum power point tracking techniques," *IEEE Trans. Energy Convers.*, vol. 22, no. 2, pp. 439–449, 2007.

[105] H. Shao, X. Li, C. Y. Tsui, and W. H. Ki, "A novel single-inductor dual-input dual-output DC-DC converter with PWM control for solar energy harvesting system," *IEEE Trans. Very Large Scale Integr. Syst.*, vol. 22, no. 8, pp. 1693–1704, 2014.

[106] O. López-Lapeña, M. T. Penella, and M. Gasulla, "A new MPPT method for low-power solar energy harvesting," *IEEE Trans. Ind. Electron.*, vol. 57, no. 9, pp. 3129–3138, 2010.

[107] F. Khaled, O. Ondel, and B. Allard, "Optimal energy harvesting from serially connected microbial fuel cells," *IEEE Trans. Ind. Electron.*, vol. 62, no. 6, pp. 3508–3515, 2015.

[108] T. Paing, J. Shin, R. Zane, and Z. Popovic, "Resistor emulation approach to low-power RF energy harvesting," *IEEE Trans. Power Electron.*, vol. 23, no. 3, pp. 1494–1501, 2008.

[109] M. T. Penella and M. Gasulla, "A simple and efficient MPPT method for low-power PV cells," *Int. J. Photoenergy*, vol. 2014, no. 1, pp. 1–8, 2014.

[110] W. Wang, N. Wang, M. Hayes, B. O'Flynn, and C. O'Mathuna, "Power management for sub-mW energy harvester with adaptive hybrid energy storage," *J. Intell. Mater. Syst. Struct.*, vol. 24, no. 11, pp.

1365–1379, 2013.

[111] Z. Zeng, J. J. Estrada-López, B. Wang, and E. Sánchez-Sinencio, "A CMOS energy harvesting interface circuit with cycle-to-cycle frequency-to-amplitude conversion MPPT for centimeter-scale wind turbine," *IEEE Trans. Circuits Syst. I Regul. Pap.*, vol. 68, no. 9, pp. 3587–3597, 2021.

[112] O. Wasynczuk, "Dynamic Behavior of a Class of Photovoltaic Power Systems," *IEEE Trans. Power Appar. Syst.*, vol. PAS-102, no. 9, pp. 3031–3037, 1983.

[113] H. Kim, Y. J. Min, C. H. Jeong, K. Y. Kim, C. Kim, and S. W. Kim, "A 1-mW solar-energy-harvesting circuit using an adaptive MPPT with a SAR and a counter," *IEEE Trans. Circuits Syst. II Express Briefs*, vol. 60, no. 6, pp. 331–335, 2013.

[114] S. Jain and V. Agarwal, "A new algorithm for rapid tracking of approximate maximum power point in photovoltaic systems," *IEEE Power Electron. Lett.*, vol. 2, no. 1, pp. 16–19, 2004.

[115] T. T. Toh, P. D. Mitcheson, A. S. Holmes, and E. M. Yeatman, "A continuously rotating energy harvester with maximum power point tracking," *J. Micromechanics Microengineering*, vol. 18, no. 10, 2008.

[116] S. Fan, R. Wei, L. Zhao, X. Yang, L. Geng, and P. X. L. Feng, "An Ultralow Quiescent Current Power Management System with Maximum Power Point Tracking (MPPT) for Batteryless Wireless Sensor Applications," *IEEE Trans. Power Electron.*, vol. 33, no. 9, pp. 7326–7337, 2018.

[117] F. I. Simjee and P. H. Chou, "Efficient charging of supercapacitors for extended lifetime of wireless sensor nodes," *IEEE Trans. Power Electron.*, vol. 23, no. 3, pp. 1526–1536, 2008.

[118] C. G. Yu, "A vibrational energy harvesting interface circuit with maximum power point tracking control," *Int. J. Appl. Eng. Res.*, vol. 12, no. 22, pp. 12102–12107, 2017.

[119] M. K. Rajendran, V. Priya, S. Kansal, G. Chowdary, and A. Dutta, "A 100-mV-2.5-V burst mode constant on-time-controlled battery charger with 92% peak efficiency and integrated FOCV technique," *IEEE Trans. Very Large Scale Integr. Syst.*, vol. 27, no. 2, pp. 430–443, 2019.

[120] J. P. Im, S. W. Wang, S. T. Ryu, and G. H. Cho, "A 40 mV transformer-reuse self-startup boost converter with MPPT control for thermoelectric energy harvesting," *IEEE J. Solid-State Circuits*, vol. 47, no. 12, pp. 3055–3067, 2012.

[121] M. Dini, A. Romani, M. Filippi, and M. Tartagni, "A Nanocurrent Power Management IC for Low-Voltage Energy Harvesting Sources," *IEEE Trans. Power Electron.*, vol. 31, no. 6, pp. 4292–4304, 2016.

[122] M. Shim, J. Kim, J. Jeong, S. Park, and C. Kim, "Self-Powered 30 μW to 10 mW Piezoelectric Energy Harvesting System With 9.09 ms/V Maximum Power Point Tracking Time," *IEEE J. Solid-State Circuits*, vol. 50, no. 10, pp. 2367–2379, 2015.

[123] G. Saini and M. S. Baghini, "An Energy Harvesting System for Time-Varying Energy Transducers with FOCV based Dynamic and Adaptive MPPT for 30 nW to 4 mW of Input Power Range," *Microelectronics J.*, vol. 114, no. 105080, 2021.

[124] S. Carreon-Bautista, L. Huang, and E. Sanchez-Sinencio, "An Autonomous Energy Harvesting Power Management Unit with Digital Regulation for IoT Applications," *IEEE J. Solid-State Circuits*, vol. 51, no. 6, pp. 1457–1474, 2016.

[125] J. J. Estrada-Lopez, A. Abuellil, A. Costilla-Reyes, M. Abouzied, S. Yoon, and E. Sanchez-Sinencio, "A Fully Integrated Maximum Power Tracking Combiner for Energy Harvesting IoT Applications," *IEEE Trans. Ind. Electron.*, vol. 67, no. 4, pp. 2744–2754, 2020.

[126] L. Costanzo, A. Lo Schiavo, and M. Vitelli, "Performance of the Open-Circuit Voltage MPPT Technique for Piezoelectric Vibration Harvesters," in *Proceedings - IEEE International Symposium on Circuits and Systems*, 2020, no. 1, pp. 0–4.

[127] A. Shrivastava, N. E. Roberts, O. U. Khan, D. D. Wentzloff, and B. H. Calhoun, "A 10 mV-Input boost converter with inductor peak current control and zero detection for thermoelectric and solar energy harvesting with 220 mV Cold-Start and -14.5 dBm, 915 MHz RF Kick-Start," *IEEE J. Solid-State Circuits*, vol. 50, no. 8, pp. 1820–1832, 2015.

[128] M. Carandell, A. S. Holmes, D. M. Toma, J. del Río, and M. Gasulla, "Techniques and Circuits for Increasing the Sampling Rate of Resistor-Based FOCV-MPPT Units," *IEEE Trans. Power Electron.*, no. [Submitted], 2022.

[129] A. Castagnetti, A. Pegatoquet, T. N. Le, and M. Auguin, "A joint duty-cycle and transmission power management for energy harvesting WSN," *IEEE Trans. Ind. Informatics*, vol. 10, no. 2, pp. 928–936, 2014.

[130] M. Carandell, D. M. Toma, C. Artero, M. Gasulla, and J. del Rio, "Real-time Wave Monitoring on Coastal Areas Using LPWAN-Based Embedded Systems," in *IEEE International Instrumentation & Measurement Technology Conference - Glasgow*, 2021.

[131] K. Mekki, E. Bajic, F. Chaxel, and F. Meyer, "Overview of Cellular LPWAN Technologies for IoT Deployment: Sigfox, LoRaWAN, and NB-IoT," *PerIoT'18 - Second IEEE Int. Work. Mob. Pervasive Internet Things*, pp. 413–418, 2018.

[132] N. A. Azmi Ali and N. A. Abdul Latiff, "Environmental Monitoring System Based on LoRa Technology in Island," in *IEEE International Conference on Signals and Systems - Bandung*, 2019, pp. 160–166.

[133] N. Jovalekic, V. Drndarevic, E. Pietrosemoli, I. Darby, and M. Zennaro, "Experimental study of LoRa transmission over seawater," *Sensors*, vol. 18, no. 9, 2018.

[134] I. B. Shirokov, A. S. Mironov, and A. N. Grekov, "Ocean Surface State Monitoring with Drifters Array," in *Zooming Innovation in Consumer Technologies Conference - Novi Sad*, 2020, pp. 113–117.

[135] M. Blinge, "Construction of an IoT-device transmitting data of the endan- gered Atlantic salmon via Sigfox-LPWAN," *Master's Thesis. Chalmers University of Technology*. 2019.

[136] Ubiscale, "UbiGNSS: low-power geolocation." [Online]. Available: https://ubiscale.com/. [Accessed: 10-Jan-2022].

[137] M. Carandell, D. Mihai, J. del Río, K. Ganchev, and J. Peudennier, "Evaluation of Sigfox LPWAN technology for autonomous sensors in coastal applications," in *8th International Workshop on Marine Technologies - Oporto*, 2018.

[138] E. D. Skinner, M. M. Rooney, and M. K. Hinders, "Low-cost wave characterization modules for oil spill response," *J. Ocean Eng. Sci.*, vol. 3, pp. 96–108, 2018.

[139] K. Seifert and O. Camacho, "Implementing positioning algorithms using accelerometers," *App. Note, Free. Semicond. -NXP*, pp. 1–13, 2007.

[140] M. Carandell, D. M. Toma, M. Gasulla, and J. del Río, "Pendulum-Type Wave Energy Converter System for Low-Power Marine Monitoring Applications," *Int. Conf. Adv. Energy Harvest. Technol. - Lublin*, 2021.

[141] M. Carandell, D. M. Toma, M. Gasulla, and J. del Río, "Kinetic energy harvester device for oceanic drifter applications," in *1st Materials for Clean Energy Conference - Exeter*, 2019.

[142] D. M. Toma, M. Carandell, L. Vals, and J. Del Rio, "A Nonlinear Kinetic Energy Harvester for Light Surface Ocean Drifters," *8th Int. Work. Mar. Technol. - Oporto*, 2018.

[143] M. Carandell, D. M. Toma, M. Gasulla, and J. del Río, "Contributions to the pendulum-type wave energy converter system for oceanic drifter applications," in *VI Expanding Ocean Frontiers Conference - Barcelona*, 2021.

[144] M. Carandell, D. M. Toma, M. Gasulla, and J. del Río, "Kinetic Energy Harvester embedded on a Drifter," in *10th Energy Harvesting Anual Meeting - Birmingham*, 2020.

[145] D. Bonilla, "Estudio y caracterización de sistemas electrónicos para la captación de energía de baja potencia.," *Bachelor Thesis. Univ. Politècnica Catalunya*, 2018.

[146] L. Valls, "Estudi d'un captador d'energia electromagnètic a partir de les vibracions generades per l'onatge incident en una boia," *Bachelor Thesis. Univ. Politècnica Catalunya*, 2018.

[147] B. Zambrano and I. Cascos, "Simulación del movimiento de un captador de energía mareomotriz situado en el interior de una boya de deriva," *Bachelor Thesis. Univ. Politècnica Catalunya*, 2019.

[148] Á. C. Quispe, "Sistemas de medida de energía para dispositivos de bajo consumo," *Bachelor Thesis. Univ. Politècnica Catalunya*, 2019.

[149] L. Valls, "Sistema de monitorització y caracterització del sistema de captació d'energia d'una boia de deriva per mesura de corrents marins," *Bachelor Thesis. Univ. Politècnica Catalunya*, 2019.

[150] R. Flix, "Estudi i optimització de la dinàmica no lineal del pèndul paramètric com a sistema de captació de l'energia de les onades en un Drifter Lagrangià," *Bachelor Thesis. Univ. Politècnica Catalunya*,

2022.

[151] I. Masmitja, M. Carandell, P. J. Bouvet, J. Aguzzi, S. Gomariz, and J. Del Rio, "Underwater acoustic slant range measurements related to weather and sea state," *XXII World Congr. Int. Meas. Confed. - IMEKO 2018*, vol. 1065, no. 5, 2018.

[152] J. del Río *et al.*, "Obsea, ten years of coastal ocean monitoring and test site observatory," in *American Geophysical Union Fall Meeting - New Orleans*, 2021.

[153] M. Carandell, M. Nogueras, R. Chumbinho, and C. Molina, "Data comparison between three acoustic doppler current profilers deployed in OBSEA platform in north-western Mediterranean," in *International Workshop on Marine Technology*, 2016, pp. 116–119.

[154] M. Carandell, A. Garcia-Benadí, and J. Del Rio, "OBSEA, a marine sensor testing site for metrology," in *IMEKO TC19 Workshop on Metrology for the sea - Naples*, 2017, pp. 78–82.

[155] M. Carandell *et al.*, "JERICO-Next cabled coastal observatories : Harmonization of technologies and methodologies for coastal cabled observatories - technical strategy," in *Copernicus Marine Week - Brussels*, 2017.

[156] M. Carandell, J. del Río, and D. Mihai Toma, "Energy harvesting system placed at WAVY drifters," in *2nd Marine Technologies Workshop - Oporto*, 2017.

[157] A. Falahzadeh *et al.*, "Remotely-operated Ecological Monitoring at the Seafloor Observatory (OBSEA)," in *VI Expanding Ocean Frontiers Conference - Barcelona*, 2021.

[158] A. Falahzadeh *et al.*, "Tele-operated ecological monitoring at the seafloor observatory (OBSEA)," in *9th International Workshop on Marine Technologies - Vigo*, 2021.

[159] D. M. Toma *et al.*, "An integrated biogeochemistry observation system at Besòs estuary," in *9th International Workshop on Marine Technologies - Vigo*, 2021.

UNIVERSITAT POLITÈCNICA
DE CATALUNYA
BARCELONATECH

Appendix A
ARTICLE COMPENDIUM

A.1 Article 1

P.[60] - Electromagnetic Rolling Mass Wave Energy Harvester for Oceanic Drifter Applications

---

Journal: European Physical Journal Special Topics
Publisher: Springer
Date of Publication: 05 March 2022
Impact Factor: 2.707
JCR Rank: Q2 Multidisciplinary Physics
DOI: 10.1140/epjs/s11734-022-00499-5

Eur. Phys. J. Spec. Top.
https://doi.org/10.1140/epjs/s11734-022-00499-5

THE EUROPEAN PHYSICAL JOURNAL SPECIAL TOPICS

Regular Article

Electromagnetic rolling mass wave energy harvester for oceanic drifter applications

Matias Carandell[1,a], Jiri Tichy[2], Jan Smilek[2], Daniel Mihai Toma[1], Manel Gasulla[1], Joaquín del Río[1], and Zdenek Hadas[2]

[1] Electronic Engineering Department, Universitat Politècnica de Catalunya, Vilanova i la Geltrú, Spain
[2] Faculty of Mechanical Engineering, Brno University of Technology, Brno, Czech Republic

Received 23 July 2021 / Accepted 20 February 2022

Abstract Ocean monitoring requirements have fomented the evolution of sensor platforms such as Lagrangian drifters, whose autonomy is a critical factor in the design process. Energy Harvesting (EH) has proven to be a sound option as an autonomous power source for sensor platforms. This paper deals with the design and simulation of a kinetic energy harvester (KEH) that captures energy from a drifter's motion under wave excitation. This KEH is based on a rolling mass resonator with permanent magnets that oscillate with respect to a frame which includes a coil system. The induced current on the coil results from the relative motion of the rolling mass, whose natural frequency is tuned to match the drifter's to achieve resonance. Preliminary simulations using OrcaFlex provide the motion vectors of the drifter, used to excite the KEH's frame. A multi-body MSC.ADAMS model has been developed consisting of a simple DOF mass-spring-damper system that includes the frame motion and the electrical and electromagnetic models. Results provide an estimation of the power generated on a resistive load, showing 23 mJ harvested during a one-minute simulation.

1 Introduction

GLOBAL warming is an emergency that must be tackled at all levels as it threatens the stability of our planet. Marine biodiversity is highly affected by this phenomenon. Almost 90% of the heat produced during the last decade has been absorbed by oceans and the effects of this rise in temperature are unknown as 95% of them remain unexplored. For this reason, ocean monitoring is essential to preserve not only marine species, but also to maintain the earth's health. Oceanographic sensor platforms provide biological and meteorological data to help understand changes in the marine environment and thus help preserve it. For example, underwater cabled observatories as the one presented in [1] provide huge amounts of data from a specific seafloor point. They do not have power or bandwidth restrictions, but they are expensive, high-maintenance platforms that cannot cover large ocean regions. Underwater autonomous vehicles (UAV) [2] are able to cover higher areas but are also costly to run.

Lagrangian drifters (Fig. 1) are autonomous floating passive devices used in marine climate research or oil spill tracking that provide surface marine data [3]. They are low-cost, versatile and easy-to-deploy instrumentation, so many of them can be deployed in large oceanic regions forming a surface sensors network. Drifter deployments can last for years, so autonomy is one of the main design challenges [4]. Several Energy Harvesting (EH) sources are being explored to reduce costs in battery replacement maintenance tasks. Solar panels have been the most common commercial solution to expand a drifter's autonomy (Sofar: Spotter, Fastwave: Voyager Solar). Drifters must however avoid the impact of the wind because this may compromise proper superficial current tracking [5]. Consequently, they must be mostly submerged, thus interfering with the feasibility of solar harvesting. Also, depending on a single EH source will have little effect on making the unit more autonomous. For this reason, other EH sources are being explored, including the oscillatory movement of the drifter itself caused by the interaction with the ocean waves.

Thorner et al. classified in [6] the different EH methods related to marine environment sources, leading pen-

This work was supported by a grant from the Secretariat of Universities and Research of the Ministry of Business and Knowledge of the Government of Catalonia on the FI program (ref. BDNS 362582). The project MELOA from the European Commission's Horizon 2020 research and Innovation program under Grant Agreement No. 776280 support the development of the oceanic drifter. The design of the Energy Harvesting system was supported by the university program FSI-S-17-4334 at Brno University of Technology.

[a] e-mail: matias.carandell@upc.edu (corresponding author)

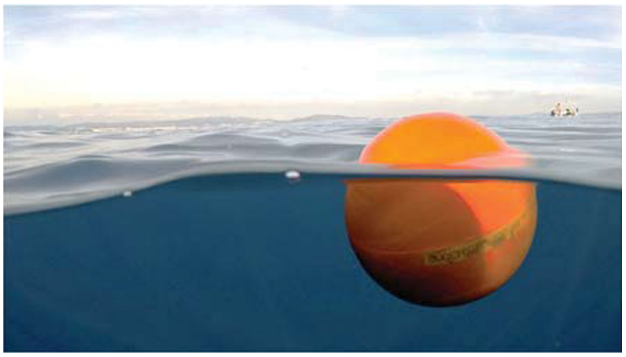

Fig. 1 Drifter deployed at the surroundings of OBSEA observatory [1], at the Mediterranean Sea, within the tests of the EC-founded MELOA project [3]

dulum and gyroscope devices as the most appropriate technologies to scavenge the drifter's motion. Recent advances have proven the value of electromagnetic techniques as suitable Power Take Off (PTO) elements for small-scale, low-power floating monitoring devices [7–10].

In [11] and [12], a novel small-scale pendulum-type Wave Energy Converter (WEC) which uses the wave motion and current flow to generate power from a drifter was presented. It consists of a double pendulum containing an arm with a proof mass guaranteeing the alignment of the main body with the wave direction. The arm is articulated to a ring which is in turn articulated to the buoy, so it participates in the ring oscillation relative to the buoy. A gear train is coupled to the ring. Through that train, energy is accumulated in a flywheel which drives a DC electrical generator acting as the PTO. The gear system amplifies the angular velocity with a positive ratio of 35 and, by means of a one-way bearing, unidirectional rotation of the generator is ensured.

A first prototype of this WEC was embedded into an oceanic drifter and tested in shallow waters [13]. The main purpose of this test was to measure the drifters' motion and analyse how it transduces into energy production. Results showed a useful mean power in the order of milliwatts, which can be used as a backup powering system. When the primary batteries are exhausted, it allows the drifter to send messages about its location so it can be recovered.

In this paper, a different approach of WEC has been proposed using a Kinetic Energy Harvesting (KEH) device. The design of this harvester is based on a rolling mass resonator, previously introduced in [14], developed for human wearable applications. General body movements provide the motion of a magnetic rolling mass that induces voltage on a coil conductor. In this field, very low operation frequencies are observed, normally within the $2-3$ Hz frequency bandwidth. Very similar conditions are expected in the ocean drifter's motion under sea excitation, with some lower dominant frequencies. This paper presents the redesign of the rolling mass resonator to work as a KEH for oceanic drifter applications and attempts to expand its autonomy. Design parameters and electromechanical responses of this EH system are analysed to adjust the KEH's natural frequency to the drifter's. Work also includes the estimation of the harvested power for a specific simulated sea state.

To fulfil this objective, several dynamic simulations have previously been performed in OrcaFlex to understand the drifter's behaviour in common swell conditions. This simulation provides important inputs for the appropriate design of the WEC based on the rolling mass resonator. Also, a multibody system with a coupled electro-mechanical model [15] has been used for the simulation of the output power responses [16] under the assumed sea conditions.

The paper is organized as follows: Section 2 presents the simulation of a drifter in the sea using commercial software (OrcaFlex). Section 3 presents the coupled model and preliminary design of the rolling mass energy harvester. Section 4 presents multi-body model and simulation results of the proposed rolling mass harvester under sea conditions. Finally, Section 5 presents the conclusions.

2 Drifter dynamics under the wave excitation

The EC-founded MELOA project [3] is developing a new family of low-cost, versatile and easy-to-deploy drifters for marine climate research. One of these units, WAVY-Ocean (WO), will be designed to collect and transmit offshore oceanic data using a satellite link. Fig. 1 shows one of these units deployed in a controlled sea area during a validation test. The WO includes the Argos Antenna, the Li-Ion battery pack, the PV cells and the main electronics. It is equipped with two thermistor measuring sensors (air and subsurface temperature), an Inertial Measurement Unit (IMU) for the wave parameter estimation and a GNSS for the current tracking. The KEH system designed in this paper should be embedded at the centre of the WO to work as a hybrid EH system together with the PV cells. The WO has a spherical shape of 20 cm diameter and weighs 3.7 kg. This results in an overhang of 5 cm from the Still Water Line (SWL) in rest conditions, reducing the impact of the wind in the WO shell. Also, placing the battery pack below the drifter's geometric centre (c_g) shifts its centre of mass (c_m) downwards by 2 cm, making the drifter stable and thus ensuring the antenna is always above the waterline.

The drifter motion has been simulated through OrcaFlex, a dynamic analysis software for offshore marine systems to understand the interaction between the sea waves and the drifter and to help design a successful KEH. This package has been used to emulate an ocean with common swell conditions and provide the vectors of motion of a free-floating buoy. These motion vectors were then used in the KEH design phase. Only

Table 1 Ocean drifter parameters

Symbol	Parameter	Value	Units
m_b	WO mass	3.7	kg
R	WO radius	0.1	m
c_m	Centre of mass[A]	0.08	m
d	SWL-c_g distance	0.053	m
I_X, I_Y	WO horizontal inertia	$9 \cdot 10^{-3}$	$Kg \cdot m^2$
I_f	WO hydrodyn. inertia	$2 \cdot 10^{-3}$	$Kg \cdot m^2$

[A]Center of mass taken from the bottom of the drifter body

Table 2 Environment parameters

Symbol	Parameter	Value	Units
h	Ocean depth	20	m
ρ	Ocean density	1024	Kg/m^3
g	Gravity acceleration	9.81	m/s^2
H_{S1}	Sig. Wave Height	0.5	m
f_{m1}	O-H modal frequency[B]	0.2	Hz
λ_1	O-H shape parameter 1	1.0	–

[B]Ochi-hubble model with just one predominant frequency

the kinematics results and not the forces have been considered in the design. The spherical drifter was modelled with the parameters shown in Table 1, using 24 stacked, flat cylinders of appropriate diameters. Fig. 2a shows the resulting modelled WO with the location of the WO's local coordinates origin at the bottom of the sphere. The sea state was modelled using the Ochi-Hubble wave spectrum [17], a sea model that statistically describes the behaviour of the water particles in shallow waters. In our case, we have used only one predominant frequency with the parameters reported in TABLE 2 and without any current or wind influence. That results in a bandwidth distribution of frequencies around the predominant frequency, as can be later seen in Fig. 3 from the results. OrcaFlex uses the Morrison equations [18] to obtain the contact forces of the interaction between the drifter and the sea. This model includes two components; an inertia force in phase with the water acceleration and a drag force proportional to the square of the instantaneous water velocity. The simulation has been performed with a time step of 50 milliseconds and a total time of 40 seconds.

Figure 2.b defines the drifter's local axis, where X is the horizontal axis and Z the vertical axis. It also defines the concepts of wave height (H) and period (T) among the SWL. For the sake of simplicity, the wave propagation direction has been aligned with the horizontal drifter's local axis X, leading to a simpler model of 2D with 3 Degrees Of Freedom (DOF). The interaction with the wave motion causes the oscillation acceleration in the vertical (heave - A_Z) and horizontal (surge - A_X) axis and a rotation (pitch - G_Y) among the perpendicular axis Y. These three DOF were the main components of the drifter's motion that would be later used on the design of the WEC.

Simulation results are shown in Fig. 3, where the sea elevation is in blue, A_X in orange, A_Z in purple and G_Y in green. For this figure, sea elevation is in meters, linear accelerations are in g-acc and angular rotations are in rad/s. Also, results are taken at the geometric centre (c_g) of the drifter. The sea elevation is presented in the first pair of plots of Fig. 3, with the common frequency distribution of Ochi-Hubble wave spectra around the main modal frequency (f_{m1}) of 0.2 Hz. The non-linear response of the drifter is in concordance with the non-linearities expected on a body under wave influence [19], as one natural frequency (f_n^X, f_n^Y *and* f_n^Z) is found for each DOF. The horizontal acceleration A_X has a dominant frequency of 1.25 Hz (as shown in the spectrum), with a maximum peak-to-peak amplitude of the time signal of 1.1 g. The dominant frequency of the vertical acceleration A_Z is 0.92 Hz with a maximum peak-to-peak amplitude of 0.5 g (time signal) and a mean value of 1 g due to the drifter's gravitational load. Finally, the frequency dominating the pitch angular velocity G_Y is around 1.25 Hz with a maximum peak-to-peak amplitude of 10 rad/s (time signal). A harmonic of the main G_Y frequency is induced at A_Z, presenting a peak at 2.5 Hz.

The natural frequency at A_Z (f_n^Z) can be analytically validated following the procedure reported in [20], where a drifter with similar characteristics was deployed in a wave flume. There, f_n^Z is obtained using

$$f_n^Z = \frac{1}{2\pi}\sqrt{\frac{\rho g \pi (R^2 - d^2)}{m_b + m_f}} \tag{1}$$

where m_b is the total drifter mass, ρ is the fluid density, g is the gravity acceleration, R is the radius of the buoy,

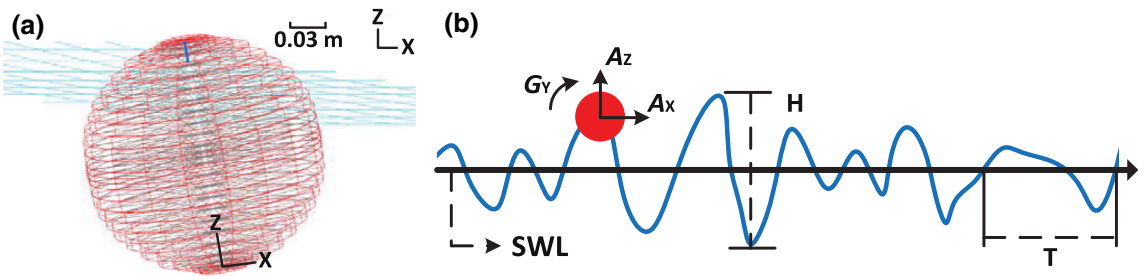

Fig. 2 **a** Spherical modelling of the drifter in OrcaFlex using 24 stacked flat cylinders. **b** 2D scheme of the drifter's motion with the description of its main 3 Degrees of Freedom (DOF)

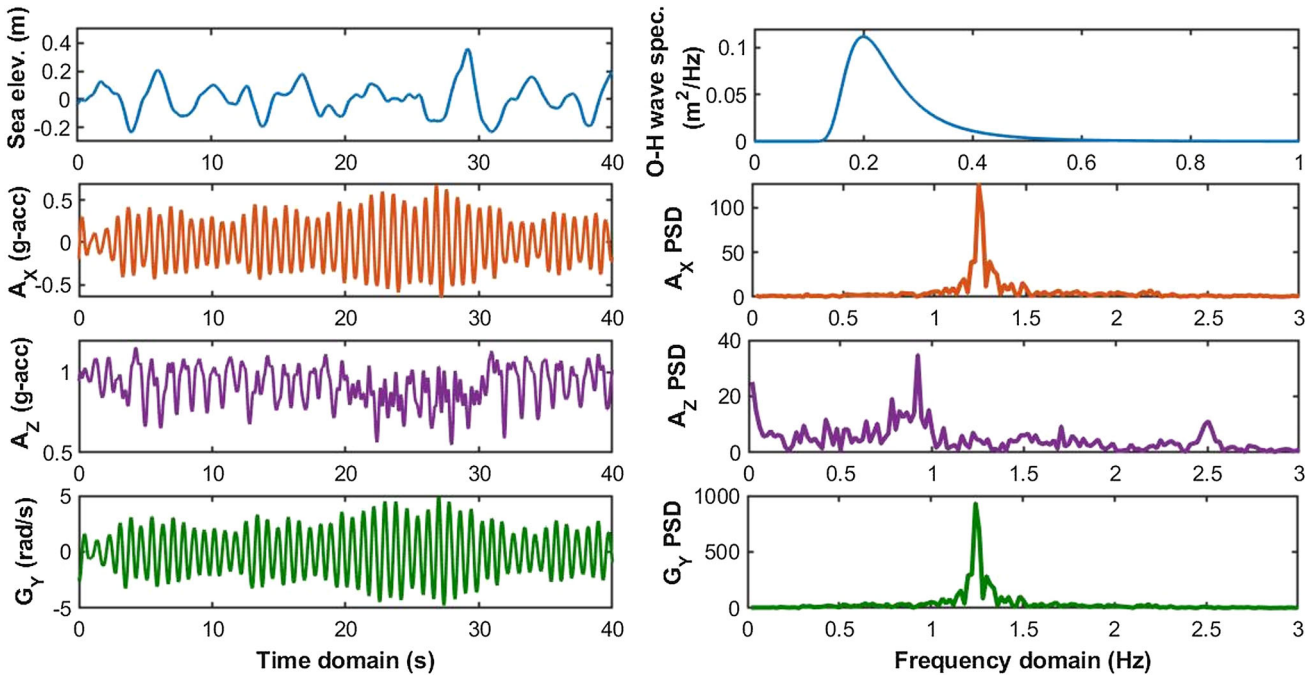

Fig. 3 Simulated drifter linear horizontal and vertical accelerations (A_X, A_Z) and angular velocity around Y (G_Y) and their respective PSD when placed in waters with a significant wave height (H_S) of 0.5 m and 0.2 Hz of O–H modal frequency (f_m). For this figure, blue has been used for sea elevation, orange for the A_X aligned with the wave's direction, purple for the vertical A_Z and green for the rotation G_Y

d is the distance between the SWL and c_g and m_f is the hydrodynamic mass. m_f can be estimated using

$$m_f = \frac{\rho\pi}{6}(2R^3 + 3R^2 d - d^3) \tag{2}$$

Using the parameters from Tables 1 and 2 on equation (1), the simulated natural frequency from the vertical acceleration A_Z of 0.92 is validated. Results also solidly tally with the experimental ones previously reported in [13], where a similar ocean drifter presented a vertical f_n^Z of around 1 Hz when deployed in the Mediterranean sea. The small differences found in the frequency come from the differences on the drifter's constructive parameters. Regarding the natural frequency on G_Y (f_n^Y), it can be analytically obtained using

$$f_n^Y = \frac{1}{2\pi}\sqrt{\frac{m_b g c_m}{I_Y + I_f}} \tag{3}$$

where I_Y is the drifter's inertia around Y-axis and I_f is the hydrodynamic inertia. Using the parameters from Tables 1 and 2 on equation (3), a f_n^Y of 1.25 is analytically validated. Finally, regarding the natural frequency on A_X (f_n^X), as data is taken at the geometric centre of the unit and rotation occurs around its centre of masses, it is obvious that this point will horizontally oscillate with a motion of the same frequency. Therefore, the natural frequency in these last two DOF is the same $(f_n^X = f_n^Y)$. Again, results are similar to the experimental ones reported in [13] with small discrepancies generated from the drifter's constructive parameters.

3 Model and design of rolling mass wave energy harvester

The previous section presents the analysis of the sea conditions that provide ambient kinetic energy with the potential to be converted into useful electricity. An analysis of input vibrations is fundamental for the appropriate design of the KEH [21]. A schematic diagram of the KEH with an electro-magnetic converter embedded in the oceanic drifter is shown in Fig. 4. This KEH is excited by the horizontal and vertical accelerations (A_X, A_Z) and the rotation angular velocity around Y (G_Y) presented in Fig. 3. The operation of this device is based on the excited movement of a rolling mass embedded into the drifter's frame. This rolling mass includes an electromagnetic circuit which rotates with relative velocity $\mathbf{v}$ against the fixed coil placed on the drifter's frame. The motion of this magnetic system changes the magnetic field $\mathbf{B}$ through the fixed coil. In accordance with Faraday's Law, an electromotive voltage is induced on the conductor of the fixed coil. Should an electrical load (e.g. resistive load) be connected, then a current flow through the coil will provide an additional electro-magnetic damping force which would be proportional to the consumed electrical power, including electrical losses.

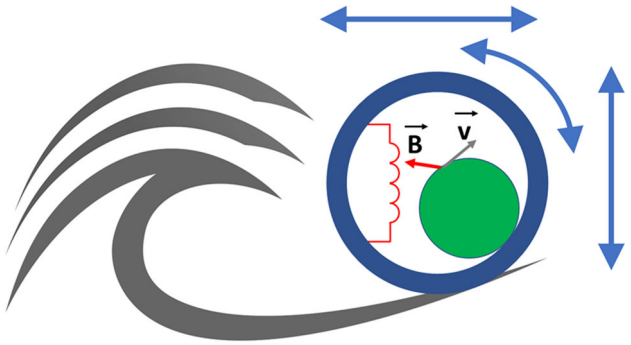

Fig. 4 Schematic diagram of the rolling mass energy harvester inside the oceanic drifter; horizontal and vertical accelerations (A_X, A_Z) and angular velocity around Y (G_Y) are used for excitation

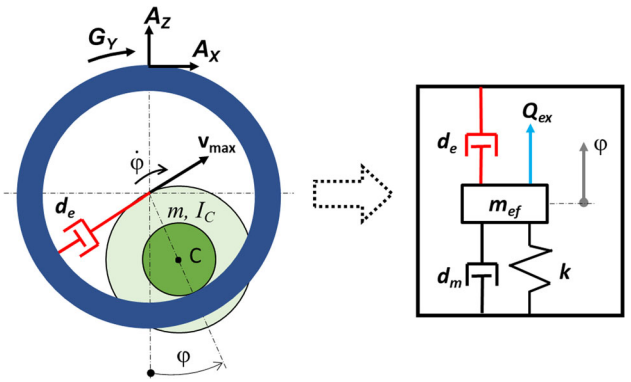

Fig. 5 Rolling mass resonator modelled as a mass-spring-damper system with 1 DOF; horizontal and vertical accelerations (A_X, A_Z) and angular velocity around Y (G_Y) are used to obtain the general excitation Q_{ex}

Based on the KEH description above, a concept of rolling mass resonator model is designed and shown in Fig. 5. This kinetic harvester provides a complex multidisciplinary system whose model includes; the input frame's motion (A_X, A_Z and G_Y), the rolling mass resonator dynamics and an electromagnetic model of the energy converter. This system integrates the author's experience with KEH and oceanic drifter dynamics. In this work, the mass ratio of the rolling mass and the drifter is low (0.04) as in [20] (0.06), where it has been experimentally proven that the rolling mass does not have a significant effect on the measured wave parameters. Therefore, the value of contact force between both bodies is also low and does not influence the drifter dynamics. The whole system can be modelled with a simple 1 DOF system of mass-spring-damper, which is suitable for a preliminary analysis of the KEH. However, several assumptions are required:

- The dynamics of the rolling mass do not affect the drifter motion itself.
- The mechanical energy of all excited bodies is modelled with a general excitation Q_{ex}.
- The weight and inertia moment of the rolling system is included in effective mass m_{ef}.
- The rolling system is expected to rotate, so the amplitude of angle φ is small.
- Due to the small movement of φ around the equilibrium position, the non-linear operation of this system in the gravity field is linearized by a constant value of stiffness k.
- The consumption of the harvested power is depicted by linear damping d_e.

The herein presented design respects all the stated assumptions. This approach is based on the fact that the rolling resonator shows linear operation with very low amplitudes around the equilibrium position. Therefore, the linearized approach and the equivalent linear model can be used to obtain the mechanical and electrical parameters. These parameters will be further used in the multibody model presented in Section II.A, where the nonlinear operation is included.

The transformation of the rolling mass resonator into a mass-spring-damper system with 1 DOF is based on the mechanical Lagrange formulation which is described in [14]. The resulting differential motion Eq. (4) with a generalized coordinate of angular position φ (see Fig. 5) could be used in the analysis of resonance frequency and the tuning up of its geometrical parameters. For this reason, a preliminary design of the KEH, shown in Fig. 6, was proposed.

$$m_{ef} \cdot \ddot{\varphi} + (d_m + de) \cdot \dot{\varphi} + k \cdot \varphi = Q_{ex} \tag{4}$$

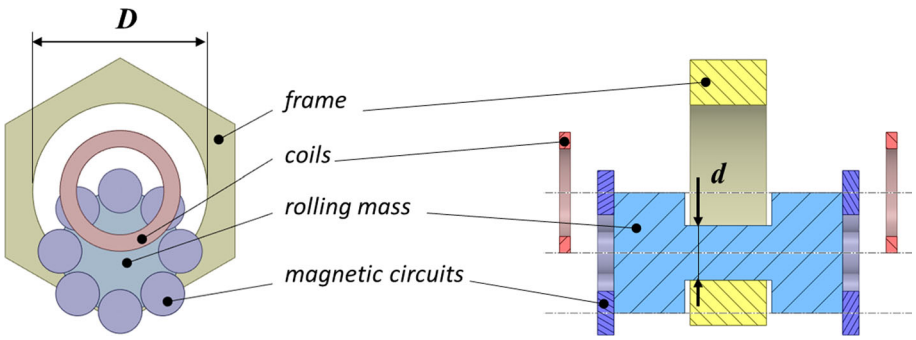

Fig. 6 Preliminary design of rolling mass energy harvester inside the drifter

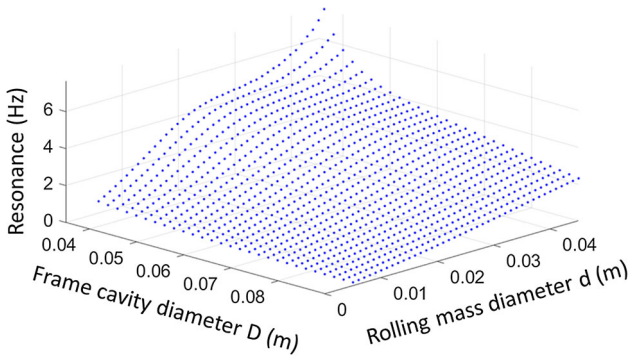

Fig. 7 Rolling mass energy harvester resonance frequency depending on the frame diameter D and the rolling diameter d

The effective mass m_{eff} can be obtained from the rolling diameter d, its weight m and the moment of inertia of the roller I. The stiffness k is calculated from the potential energy of the rolling mass and it has a non-linear proportionality with diameter D and position φ. The operation of this softening nonlinear system is linearized around equilibrium. Both m_{eff} and k formulation can be found in [14].

$$\Omega_0 = \sqrt{\frac{k}{m_{ef}}} \tag{5}$$

The natural frequency of the rolling mass motion can be calculated with Eq. (5) depending mainly on the ratio of both diameters d and D. A sensitivity study of the already presented design was done by tuning these parameters. Results of this sensitivity study based on formula (5) using the linearized model are shown in Fig. 7. We conclude that a combination of a smaller rolling diameter d and a bigger cavity diameter D is required with respect to the previous prototype published in [14]. Resulting D and d from this study are shown later in Table 3.

However, due to the softening nonlinear system, the operation frequency of this harvester is lower than natural frequency presented in Eq. (5). Then, the value of resonance frequency depends on the amplitude of the nonlinear oscillation. This concept of a softening nonlinear system is designed for a frequency bandwidth operation of around 0.4–0.5 Hz.

The aim of this paper is to achieve resonance between the rolling mass and the drifter motion to maximize the amplitude of the rolling mass motion and increase the energy harvested. Amplitudes of the rolling resonator in resonance operation are determined by the mechanical damping d_m and electro-mechanical damping d_e. The mechanical damping is assumed from the publication [14] and, together with k and m_{eff}, they determine the mechanical quality factor Q of this resonator as (6).

$$Q = d_m \cdot \sqrt{k \cdot m_{ef}} \tag{6}$$

Table 3 Physical parameters of rolling mass harvester

Symbol	Parameter	Value	Units
m	Rolling mass weight	165	g
I	Inertia moment of rolling mass	25,000	g mm^2
D	Frame cavity diameter	46	mm
d	Rolling mass diameter	13	mm
Ω_0	Natural frequency of linearized model	1.6	Hz
Q	Mechanical quality factor [14]	4.5	–
c	Coupling coefficient [14]	0.2	Wb/rad
–	Coil diameter	32	mm
–	Coil height	3	mm
N	Coil turns	2000	–
R_C	Coil resistance	2	kΩ
R_L	Resistive load	2	kΩ

The electro-mechanical damping coefficient d_e depends on the design of electro-magnetic converter and the connected electrical load. Regarding the electro-magnetic converter, the design of the coils and the magnetic circuits with rare earth permanent magnets is also adopted from the previous wearable harvester published in [14]. The frame cavity diameter D and the rolling mass diameter d have been analysed in this paper for the specific case of the drifter under sea excitation with the goal of maximizing the harvested power, which would happen in resonance operation.

As the design of the electro-magnetic converter was successfully tested for a wearable energy harvester in [14], where dimensions and electrical parameters of the coils and the permanent magnets were chosen, the model has been extended here with the addition of the electrical part. The electrical circuit of the current KEH is simple because the coil (with inductance L and resistance R_C) is connected in series with the resistive load R_L. This resistance represents the useful electrical load and the harvested power is analysed at its terminals. When the electromotive voltage u_i is induced, a current i flows through the electrical circuit as described by Eq. (7), where u_i is equal to the sum of the voltage drops around the coil and the load.

$$u_i = L \cdot \frac{di}{dt} + R_c \cdot i + R_L \cdot i \tag{7}$$

In accordance with Faraday's Law, the induced voltage can be obtained as (8).

$$u_i = c \cdot \dot{\varphi} \tag{8}$$

where $\dot{\varphi}$ is the rolling mass angular velocity and c is the coupling coefficient of the electromagnetic converter, calculated as (9).

$$c = \frac{\mathrm{d}\phi}{\mathrm{d}\varphi} = B \cdot N \cdot L_C \tag{9}$$

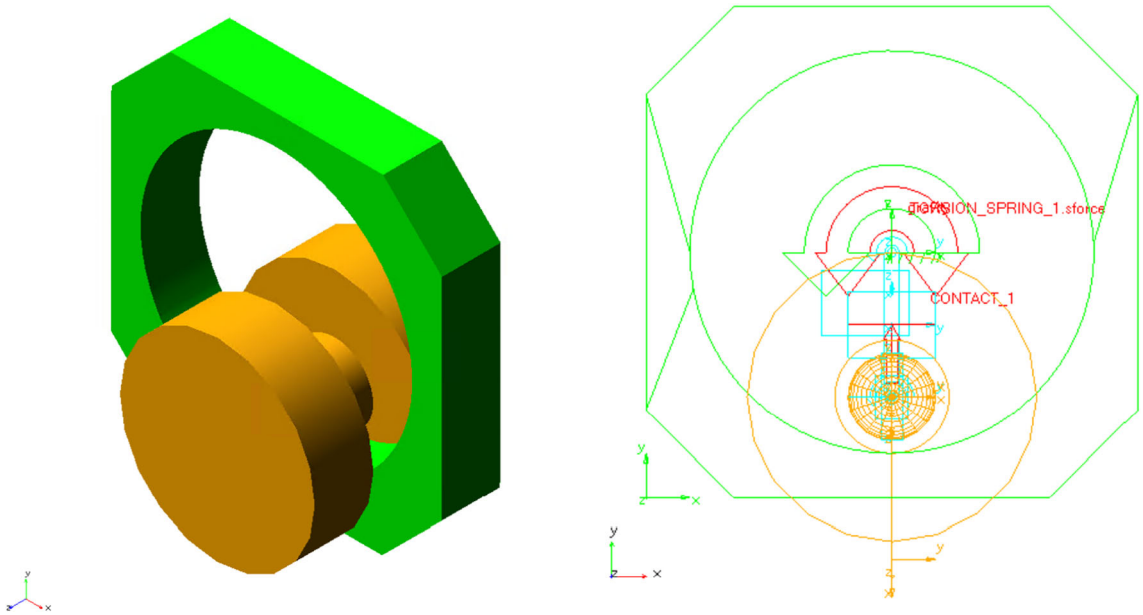

Fig. 8 Multi-body model of rolling mass energy harvester in MSC.ADAMS environment; CAD model and multi-body model with mechanical joints

In Eq. (9), φ is total magnetic flux through the coil, B is the magnetic flux density through the coil, N is the number of turns in the coil and L_C is the active length of the coil. The current flow through the coil provides back electromotive force which is represented both in Fig. 5 and Eq. (4) by a damping force d_e. This relation can be formulated as (10).

$$de \cdot \dot{\varphi} = c \cdot i \tag{10}$$

On the basis of the previous analysis of the linearized model, the final coupled electro-mechanical system results in the linearized differential motion Eq. (11) and the sum of voltages in the electrical circuit shown at (12). Inductance L has been neglected due to the low dynamics of the designed coils.

$$m_{e_f} \cdot \ddot{\varphi} + c \cdot i + d_m \cdot \dot{\varphi} + k \cdot \varphi = Q_{ex} \tag{11}$$

$$c \cdot \dot{\varphi} - R_c \cdot i - R_L \cdot i = 0 \tag{12}$$

On the base of the parametric study in Fig. 7 and the analysis of the coupled system, resulting physical parameters of the rolling mass KEH have been chosen and are presented in Table 3.

4 Multi-body simulation of the rolling resonator under sea excitation

4.1 Multi-body model of multidisciplinary energy harvester

The presented coupled electro-mechanical model resulting in Eqs. (11) and (12) is useful to analyse the system's movement close to the equilibrium. However, the behaviour of the rolling mass resonator under sea conditions could provide high excitation inertia forces which would create a wide range of motions of the rolling mass, some of them outside the operation range where the linearized coupled equations are valid. Therefore, MSC.ADAMS software has been chosen for the analysis of the rolling mass harvester under sea conditions. A multi-body model of the proposed KEH was created using the proposed parameters and geometry of Table 3. The multi-body model reproduced in MSC.ADAMS replaced both the linear differential equation (11) and the electrical model (12). A simplified geometry of both bodies (frame and roller) and its joints is shown in Fig. 8. The frame is actuated by the resulting OrcaFlex motion vectors which are used as input excitation for the MSC.ADAMS multi-body simulation. Such data represents the sea drifter's (parameters in Table 1) behaviour under Table 2 sea conditions. The operation of the KEH under sea excitation will be efficient when its nonlinear resonant frequency is similar to the typical excitation frequency. Due to the non-linear operation of the multi-body model with a real softening stiffness, the initial natural frequency is slightly bigger than dominant frequency in Fig. 3. This concept expects amplitudes which provide a frequency bandwidth at around 0.4 Hz for this softening nonlinear system. This means that this resonator could effectively operate in a frequency range of 1.2–1.6 Hz.

The contact between both bodies transfers an excitation to the roller, whose movement dynamics in the gravity field is simulated. This model could define both rolling and sliding movements which are observed for high excitation. The mechanical damping model is described by a damping plus a friction coefficient, placed at the point of contact between both bodies. This damping model provides a resonator's mechani-

cal quality factor Q of 4.5. The electromagnetic damping model is described by a spring torsion force which includes both electrical Eqs. (10) and (12). The induced voltage of Eq. (8) is obtained from the simulated angular velocity.

4.2 Simulation result for different sea conditions

The multi-body MSC.ADAMS model of the designed KEH has been excited with the drifter's motion obtained from OrcaFlex. Ochi-Hubble wave spectrum provides an irregular sea state which proved interesting in terms of energy generation for drifter applications using the herein presented KEH. This device has been designed using parameters from the already tested KEH presented in [14] with some modifications to tune-up its resonance frequency to the current application of oceanographic drifters. This design provides an advantage in nonlinear frequency response, where the operation bandwidth is extended, as described above. The simulation under these irregular sea conditions provides the relative movement of the rolling mass with the magnetic circuit with respect to the frame, the coil and the resistive load. The peaks on the output voltage have been found in the range of 1–5 V on a 1-min simulation. In this scenario, the total harvested energy has been 23 mJ. Fig. 9 shows the simulated output power, presenting promising peaks up to 7 mW that can be used to expand the drifter's autonomy. As the parameters of the coil and the magnetic circuit have not been optimized for this application, there is still room to increase the output power.

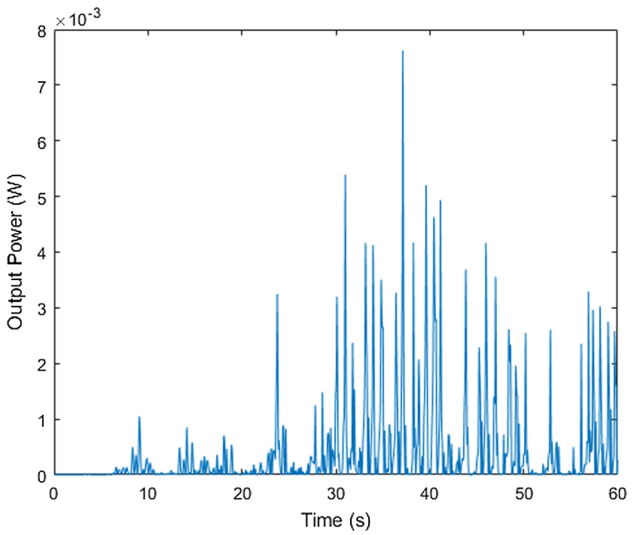

Fig. 9 Simulation results of the instantaneous harvested power; 23 mJ have been harvested energy on the resistive load for this one-minute simulation

The non-optimized parameter c provides a weak electromagnetic coupling between the movable magnets and the coil, resulting in a low output power. Several simulations have been performed to analyse how the electromagnetic coupling coefficient c affects the total harvested electrical energy. These simulations have been done for different c and resistive loads, and the resulting harvested energy is presented in Fig. 10. Coefficient c used in the previous simulation (Fig. 9) was 0.2 Wb/rad, showing a non-optimal design of the rolling mass under sea excitation. The output results of the weak coupling stage are presented in dark blue in Fig. 10.

On the basis of the simulated results of tuning c, it is obvious that an optimized coil and magnetic circuit could provide significantly higher power on drifters under sea excitation. However, the mechanical fabrication of the roller provides limitation on the maximal theoretical value of c. Based on our experience in designing electromagnetic converters and according to [22], the coupling coefficient could be increased up to 1.5 Wb/rad. Then, according to results shown in Fig. 10, the harvested energy using the designed KEH could increase up to 600 mJ, meaning that an average power

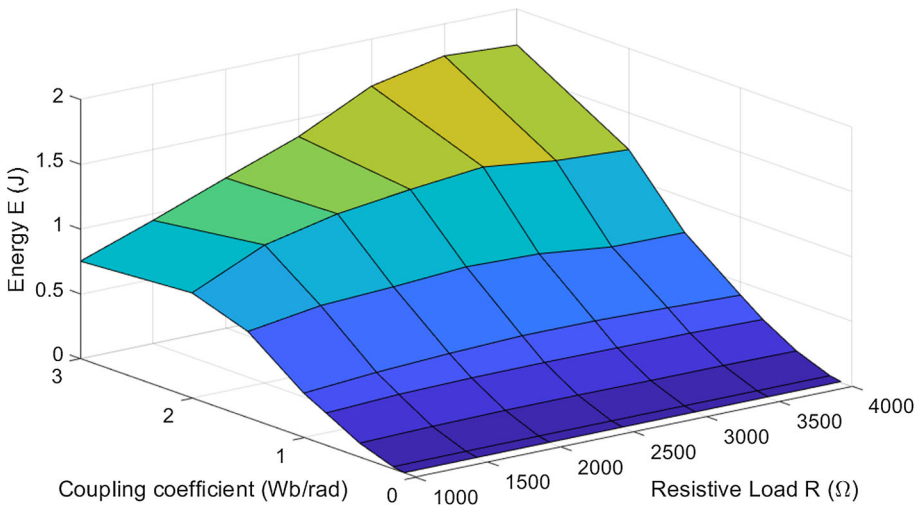

Fig. 10 Simulation results of the optimization on the coupling coefficient and the resistive load

of around 10 mW could be feasible for this application. The fabrication, optimization and the experimental test in real conditions of the herein presented KEH are future aims of our development.

5 Conclusions

The main aim of this paper is to present an innovative concept of Kinetic Energy Harvester (KEH) for oceanic drifter applications. The presented system could provide an unlimited source of energy for low-power, long-time monitoring systems. The proposed concept of KEH is based on a rolling mass resonator with an electromagnetic converter. This converter includes a magnetic system of permanent magnets that oscillates with respect to a coil fixed to the frame. The motion of the roller and the magnets caused by the waves induces a current on the coil that would potentially power the drifter electronics. The geometrical parameters of KEH have been designed for this purpose and some of them have been assumed from a wearable application previously presented in [14]. The herein scientific contribution is based on the model-based design of this KEH adapted for oceanic drifter applications.

On the one hand, simulation using OrcaFlex provides data of the motion of a specific drifter and its frequency under known sea conditions. Resulting natural frequencies at each DOF of the drifter have been analytically validated. Also, they have been compared with the experimental results reported in previous papers where similar oceanic drifters have been deployed in controlled sea areas. The KEH have been designed to capture the energy from the drifter's motion, composed of surge and heave oscillation and pitch rotation. These oscillation and rotation movements have been used as input vectors for the multibody model of the KEH.

On the other hand, the multibody system of rolling mass has been defined in MSC.ADAMS. It includes the excitation of the frame forced by the drifter and the mechanical and electro-mechanical damping models. Results show how the motion of the rolling mass is transformed into electrical power by the coil's induced current. Using the initial physical parameters and the obtained OrcaFlex motion vectors, around 23 mJ of electrical energy have been harvested during a 60-s simulation. Furthermore, simulations performed with different parameters of the electro-mechanical coupling model show that its optimization leads to an improvement of up to 600 mJ of electrical energy under the same sea conditions.

The presented design and simulations show that this energy harvesting application could be successfully employed to expand the autonomy of oceanic drifters. The fabrication, optimization and the experimental test in real conditions of the herein presented KEH are future aims of our development.

Acknowledgements The authors extend their thanks to Orcina for their kind support and offer of the academic license OrcaFlex N2703 (2018) to Universitat Politècnica de Catalunya.

Funding Information Open Access funding provided thanks to the CRUE-CSIC agreement with Springer Nature.

Data Availability Statement This manuscript has associated data in a data repository. [Authors' comment: Data from the deployment of three WO (TABLE I) drifting around the Catalan coast, between the 9/06/2021 and the 22/06/2021 is available in the MELOA catalogue in [23].]

References

1. J. Del-Rio et al., Obsea : A Decadal Balance for a Cabled Observatory Deployment.IEEE Access, pp. 33163–33177 (2020)
2. S. Gomáriz, I. Masmitjà, J. González, G. Masmitjà, J. Prat, GUANAY-II: an autonomous underwater vehicle for vertical/horizontal sampling. J. Mar. Sci. Technol. **20**(1), 81–93 (2015)
3. MELOA project. [Online]. Available: https://www.ec-meloa.eu/. Accessed: 21 Oct 2020
4. R. Lumpkin, T. Özgökmen, L. Centurioni, Advances in the application of surface drifters. Ann. Rev. Mar. Sci. **9**(1), 59–81 (2017)
5. P.M. Poulain, R. Gerin, E. Mauri, R. Pennel, Wind effects on drogued and undrogued drifters in the eastern Mediterranean. J. Atmos. Ocean. Technol. **26**(6), 1144–1156 (2009)
6. L.D.A. Thorner, P.D. Mitcheson, A.S. Holmes, E.M. Yeatman, Scaling laws for energy harvesters in a marine environment. in *PowerMEMS - Washington DC*, pp. 249–252 (2009)
7. W. Ding, B. Song, Z. Mao, K. Wang, Experimental investigation on an ocean kinetic energy harvester for underwater gliders. In *IEEE Energ. Conv. Congr. and Expos. - Montreal*, pp. 1035–1038 (2015)
8. G. Bracco, A. Cagninei, E. Giorcelli, G. Mattiazzo, D. Poggi, M. Raffero, Experimental validation of the ISWEC wave to PTO model. Ocean Eng. **120**, 40–51 (2016)

9. Y. Li et al., Study of an electromagnetic ocean wave energy harvester driven by an efficient swing body toward the self-powered ocean Buoy application. IEEE Access **7**, 129758–129769 (2019)
10. W. Ding, K. Wang, Z. Mao, H. Cao, Layout optimization of an inertial energy harvester for miniature underwater mooring platforms. Mar. Struct. **69**(102681), 17 (2020)
11. M. Carandell, D.M. Toma, M. Carbonell, M. Gasulla, J. del Río, Design and development of a kinetic energy harvester device for oceanic drifter applications. In *Instr. and Measur.Techn. Conf. - Auckland*, pp. 1718–1723 (2019)
12. M. Carandell, D. Mihai Toma, M. Gasulla, J. del Río, Experimental Validation of a Kinetic Energy Harvester Device for Oceanic Drifter Applications. in *OCEANS - Marseille*, p. 17 (2019)
13. M. Carandell, D.M. Toma, M. Carbonell, J. del Río, M. Gasulla, Design and testing of a kinetic energy harvester embedded into an oceanic drifter. IEEE Sens. J. (2020)
14. J. Smilek, Z. Hadas, J. Vetiska, S. Beeby, Rolling mass energy harvester for very low frequency of input vibrations. Mech. Syst. Signal Process. **125**, 215–228 (2019)
15. T. Brezina, Z. Hadas, J. Vetiska, Using of co-simulation ADAMS-SIMULINK for development of mechatronic systems. In: *Proceedings of 14th International Conference on Mechatronics, MECHATRONIKA 2011*, pp. 59–64 (2011)
16. Z. Hadas, L. Janak, J. Smilek, Virtual prototypes of energy harvesting systems for industrial applications. Mech. Syst. Signal Process. **110**, 152–164 (2018)
17. M.K. Ochi, E.N. Hubble, Six-parameter wave spectra. In: *Coastal Engineering*, pp. 301–328 (1976)
18. J.R. Morison, J.W. Johnson, S.A. Schaaf, The Force Exerted by Surface Waves on Piles. J. Pet. Technol. (1950)
19. Z. Demerbilek, Water wave mechanics. In: *Coastal Engineering Manual*, vol. Part II (2008)
20. M. Carandell, D.M. Toma, J.P. Pinto, M. Gasulla, J. del Río, Impact on the Wave Parameters Estimation of a Kinetic Energy Harvester Embedded into a Drifter. in *OCEANS - Singapur and U.S. Gulf Coast* (2020)
21. J. Smilek, Z. Hadas, Improving power output of inertial energy harvesters by employing principal component analysis of input acceleration. Mech. Syst. Signal Process. **85**, 801–808 (2017)
22. Z. Hadas, J. Kurfurst, C. Ondrusek, V. Singule, Artificial intelligence based optimization for vibration energy harvesting applications. Microsyst. Technol. **18**(7–8), 1003–1014 (2012)
23. MELOA geoportal. Spanish coast campaign. https://geoportal.ec-meloa.eu/#/geoportal/campaign/spanishwocampaign. Accessed 16 Feb 2022

A.2 Article 2

P.[59] - Design and Testing of a Kinetic Energy Harvester Embedded into an Oceanic Drifter

---

Journal: IEEE Sensors Journal
Publisher: IEEE
Date of Publication: 28 February 2020
Impact Factor: 3.301
JCR Rank: Q2 Electrical and Electronic Engineering, Q2 Instruments and Instrumentation, Q2 Applied Physics
DOI: 10.1109/JSEN.2020.2976517

Design and Testing of a Kinetic Energy Harvester Embedded Into an Oceanic Drifter

Matias Carandell, Daniel Mihai Toma, Montserrat Carbonell, Joaquín del Río, *Member, IEEE*, and Manel Gasulla, *Senior Member, IEEE*

***Abstract*—A novel Kinetic Energy Harvester (KEH) has been developed for powering oceanic undrogued drifters. It consists on a double pendulum system capable of transforming the wave oscillations into rotation on a flywheel. This rotation is converted into DC current by an electrical generator and further processed by a power management unit (PMU). The PMU includes a "maximum power point tracking" system to maximize energy production by the generator. An oceanic drifter has also been designed to embed the KEH and a custom-made measurement system to perform real sea tests. It counts on an Inertial Measurement Unit to study the motion of the drifter and an embedded measurement system to estimate the rotation speed of the generator and the power at both the input and output of the PMU. A Wi-Fi connection is also included for data transfer at short distances. The generator was firstly characterized at the laboratory; the drifter was then placed on a linear shaker to assess its performance. Finally, the drifter was deployed in a controlled sea area with average values of wave height and frequency of 1.43 m and 0.29 Hz, respectively. In these conditions, the drifter showed horizontal and vertical oscillations with peak-to-peak accelerations of 0.8 g and power spectra centered around 1.5 Hz and 1 Hz, respectively. As a result, the KEH generated a mean output power of 0.18 mW, with peaks of 2.5 mW.**

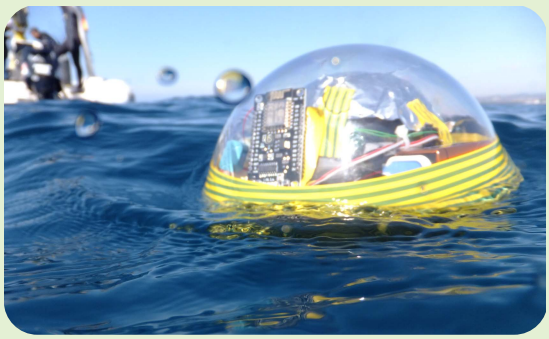

***Index Terms*—Lagrangian drifter, natural frequency, kinetic energy harvester (KEH), microgenerator, power management unit (PMU), maximum power point tracking (MPPT).**

I. Introduction

THE scientific community requirements related to oceanographic data availability are growing fast. Oceans and seas must be monitored to preserve their biodiversity and to predict their evolution. This means that huge amounts of data from a very wide range of sensors should be acquired and delivered as fast as possible. Research vessels collecting data from the ocean during long periods are not suited for this task due to their high-cost [1]. As a consequence, cabled observatories, gliders, profiling floats and long-term moorings are taking their place and are delivering enormous amounts of real or near-real time data to the scientific community [2], [3]. Other ocean platforms that collect data are Lagrangian drifters, which are autonomous floating passive devices that provide oceanographic surface data. They are low-cost, versatile and easy-deployable marine instrumentation used in climate research, oil spill tracking, or search and rescue operations.

A wide range of commercial drifters can be found in the market. Basic drifters offer ocean current tracking and near surface temperature, but growing science requirements are pushing their evolution. Consequently, some of them can now be found with Acoustic Doppler Current Profilers (ADCP), salinity sensors, or weather stations [4], [5]. Drifters use wireless GSM-based communications, in near-shore deployments, or satellite-based (mostly Iridium-based [6]) for off-shore communications.

Manuscript received November 30, 2019; revised February 2, 2020; accepted February 23, 2020. Date of publication February 28, 2020; date of current version November 5, 2020. This work was supported in part by the project MELOA from the European Commission's Horizon 2020 research and Innovation program under Grant Agreement No. 776280 and in part by the Spanish Ministry of Economy and Competitiveness and the European Regional Development Fund under project TEC2016-76991-P. The work of Matias Carandell was supported by the Secretariat of Universities and Research of the Ministry of Business and Knowledge of the Government of Catalonia on the FI Program under Grant BDNS 362582. This article was presented in part at the I2MTC 2019, Auckland, New Zealand, and in part at the OCEANS 2019, Marseille, France. The associate editor coordinating the review of this article and approving it for publication was Prof. Boby George. *(Corresponding author: Matias Carandell.)*

Matias Carandell, Daniel Mihai Toma, Montserrat Carbonell, and Joaquín del Río are with the SARTI Research Group, Electronics Engineering Department, Universitat Politècnica de Catalunya, 08034 Barcelona, Spain (e-mail: matias.carandell@upc.edu).

Manel Gasulla is with the e-CAT Research Group, Electronics Engineering Department, Universitat Politècnica de Catalunya, 08034 Barcelona, Spain.

Digital Object Identifier 10.1109/JSEN.2020.2976517

As described by Lumpkin et al. [6], power autonomy is one of the main challenges in the evolution of drifters. Depending on the instruments carried and the sampling period of the units, their lifespan may vary from hours up to a few years when powered from primary batteries. To extend their autonomy, some manufacturers include photovoltaic (PV) panels around the drifters' case, achieving unlimited lifespan at some low transmitting interval and favorable solar conditions (Sofar: Spotter, Fastwave: Voyager Solar). Nevertheless, if the drifter is strictly dedicated to current monitoring, its body should be mostly submerged to avoid the wind effect [7] and, thus, the irradiation at the panels is attenuated. Also, in many oceanic regions solar irradiation is low during some periods of the year. For this reason, other energy sources may be explored, such as the oscillatory movement of waves.

Previous works have shown many harvesting possibilities from kinetic sources in marine environments [8], [9]. Inertia-based harvesters are one of the main solutions for low-power, non-anchored oceanic devices, which is the case of drifters, and they can be further classified as gyroscopic or pendulum systems [10]. Ding *et al.* have proposed pendulum-type harvesters for underwater gliders [11] and mooring platforms [12]. These medium size and weight systems (1500 cm^3 - 5 kg) were tested on a Stewart platform at the laboratory, reporting average power production of hundreds of milliwatts. However, power was directly measured across a load resistor without using a power management unit (PMU), which is normally used to power the electronic sensors. In addition, no sea tests were performed. Li *et al.* designed a small size and weight (630 cm^3 - 0.3 kg) pendulum harvester for non-anchored floating platforms such as ocean buoys [13], which is more aligned with the objective of our work. In the laboratory tests, the harvester included a PMU to charge a 50 mAh rechargeable lithium battery that could be used to power the sensors. However, the PMU and the battery were not present during the sea test, in which only the AC open circuit voltage at the output of the harvester was measured by an embedded system. They reported a maximum peak-to-peak voltage of 15.9 V and from it they inferred a maximum peak output power of 130 mW.

This paper continues and extends two previous works. A first design of a Kinetic Energy Harvester (KEH) system for spherical oceanic drifters was presented in [14], including a preliminary characterization of the electrical generator and the PMU followed by first results of the prototype when located in an anchored buoy placed on a water tank. Later, in [15], an improved version of the KEH device was presented, as well as a first approach of a specially designed oceanic drifter for testing purposes. An Inertial Measurement Unit (IMU) placed inside the drifter allowed to obtain its dynamic behavior and determine the natural frequency of its motion when placed at sea. However, no power data of the KEH system were produced. In this work, the acquisition setup has been updated to gather that data as well as the rotation speed of the generator during the drifter's deployment at sea. In addition, the electrical generator has been replaced by a more rugged and reliable one.

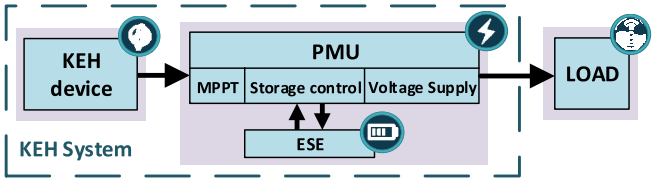

Fig. 1. Kinetic Energy Harvesting (KEH) system composed by the KEH device, the Power Management Unit (PMU) and the Energy Storage Element (ESE). The Load represents the remaining drifter electronics.

The main objective of this paper is to present a novel small-size KEH device and its ensuing PMU, as well as to validate their functionality and performance in a spherical test drifter in a real environment. To assess the performance, an embedded system was designed to measure the drifter motion, rotation speed of the generator and input and output power of the PMU. Data were sent wirelessly to a nearby point. Simulations were also performed for the drifter motion. These are important advances so far not fully achieved by previous studies. The paper is organized as follows. First, the KEH system is described in section II. Section III describes the test drifter. Section IV presents the materials and method used to obtain the simulation and experimental data, which are summarized and discussed in section V. Finally, section VI concludes the work.

II. Kinetic Energy Harvesting System

A KEH system can be structured as shown in Fig. 1 [16]. First, a KEH device, in which a mechanical converter transforms the waves' oscillation into DC current. Secondly, an Energy Storage Element (ESE), which handles the power variability from both the KEH device and the drifter, e.g. the load; so, it either gathers energy when the KEH device produces more power than required or provides energy to the load in the opposite case. Thirdly, a PMU, an electronic system that fits the generated power to the power supply requirement of the load and which oversees the power flow control. The three are fully described below.

A. KEH Device

Harvesting the energy from the waves at non-anchored autonomous devices is usually done by inertial systems. These systems rely on a proof mass which moves in relation to the main body thanks to the excitation of the waves. That relative motion drives an electrical generator which converts the energy from mechanical to electrical. The harvested energy depends on the physical characteristics of the harvester, achieving higher power levels with higher sizes and weights. Also, this energy is directly proportional to the wave frequency and amplitude [17].

Recently, a first prototype of an inertial KEH device was designed and manufactured [14], which is a mixture of gyroscopic and pendulum systems. It consists of three gyroscopic arms which capture the oscillation induced by waves and transforms it into rotation in a DC generator. In this work, a modified version of the KEH device, previously presented

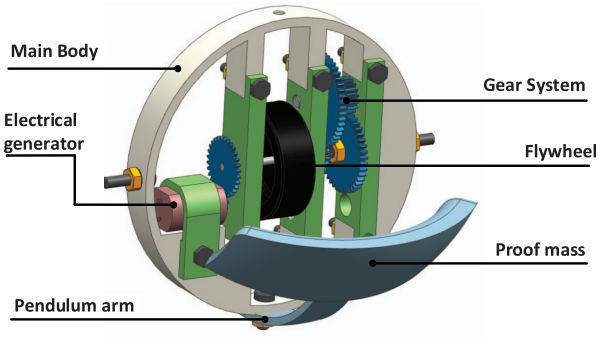

Fig. 2. Architecture of the proposed KEH device with the description of the different parts.

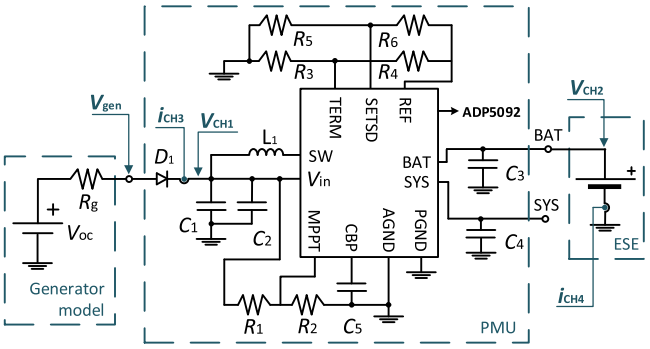

Fig. 3. Thévenin equivalent circuit of the electrical generator (left). Circuit schematic of the ADP5092 configured to work as the PMU (center) and ESE (right).

in [15], is used. Fig. 2 shows a 3D model of the design with the description of the different parts. Relative to the device introduced in [14], the three gyroscopic arms have been replaced by an articulated pendulum arm with a proof mass. This way, the design of the KEH device is simplified and its size is reduced, thus increasing its power density. The proof mass moves relatively to the drifter with pendulum motion. Then, through a gear system, energy is accumulated in a flying wheel which drives a DC electrical generator. The gear system also increases the rotation velocity with a positive ratio of 35 and, thanks to a one-way gear mechanism, the flying wheel only rotates in one angular direction, at which energy is accumulated.

The electrical generator, updated with respect to [14], [15], is a miniature DC motor, which can be modelled as an equivalent Thévenin circuit [18], as shown in the leftmost part of the circuit in Fig. 3, where R_g is the internal equivalent resistance and V_{oc} is the generated electromotive force (EFM) in volts. On the other hand, V_{gen} is the voltage at the output terminals. Using the maximum power transfer theorem, maximum power is extracted when $V_{gen} = 0.5V_{oc}$, which is known as the maximum power point (MPP) voltage (V_{MPP}) [19]. So, the maximum achievable power (P_{MPP}) is given by

$$P_{MPP} = V_{oc}^2/(4R_g) \quad (1)$$

with V_{oc} given by

$$V_{oc} = K_g \varphi \omega \quad (2)$$

where K_g is the constructive constant, φ the magnet field generated by the permanent magnet, and ω the generator rotor speed [18]. Since K_g and φ are constants, V_{oc} is proportional to ω. Within one single pendulum cycle, while the pendulum applies torque through the one-way gear, the flywheel accelerates, increasing ω and thus V_{oc}, whereas when the pendulum moves in the other direction the one-way gear rotates freely, so that the flywheel slows down, thus reducing ω and V_{oc}. Therefore, ω and V_{oc} will have both DC and AC components, even for a constant excitation source. The AC component will be periodic with the same frequency of the mechanical movement of the pendulum. Anyhow, the flywheel increases the system inertia thus reducing the variability (i.e. the amplitude of the AC component) on ω and thus on V_{oc}. In principle, a lower variability is desirable for the ensuing PMU, as will be argued later in Section V-B.

B. PMU and ESE

In self-powered autonomous systems, energy management is crucial in order to maximize the lifespan of the device and to guarantee the most efficient way to handle the generated energy [20]. To achieve this, a PMU with a MPP tracker (MPPT) of the harvester device is required. Toh *et al.* designed in [21] a system to follow the MPP of an electrical generator by controlling the duty cycle of a boost converter, who delivers power to a dc-link, and a flyback converter to adjust the voltage level at the load. From then, many conversion systems have been developed depending on the energy source; a summary is presented in [22]. On the other hand, the ESE can be a regular capacitor, a supercapacitor, a rechargeable battery, or even an hybrid system [23].

Recently, many commercial PMU have become available. In this work, the ADP5092 (Analog Devices) has been used as the core unit. This PMU is based on a boost regulator working on PFM mode [24] and with MPPT functionality. It is a low-power module with a very low internal consumption and works with input voltages (V_{in}) as low as 80 mV. On the other hand, it provides a main output terminal (SYS) and a battery charging terminal (BAT), which the ESE is connected to, with programmable overcharge (V_{high}) and discharge (V_{low}) voltages to protect the ESE, e.g. a rechargeable battery. Each programmable voltage counts on a hysteresis range (V_{hyst1} and V_{hyst2}) to prevent the PMU from switching continuously when achieving these voltage thresholds (see Fig. 3).

Fig. 3 shows the circuit schematic of the designed PMU together with the electrical generator of the KEH device (left) and the ESE (right). The energy produced by the generator is first collected in the input capacitors C_1 and C_2 (placed in parallel). A diode (D_1) prevents the generator acting as a load. Capacitors C_3 and C_4 are respectively connected to BAT and SYS terminals.

The PMU can work in three modes, depending on the voltages at the SYS (V_{SYS}) and BAT (V_{BAT}) terminals: Fast-Cold Start-Up, Asynchronous and Synchronous. Fig. 4 illustrates the temporal evolution of these voltages from the Fast-Cold Start-Up mode when a net power is produced. During the Synchronous mode, BAT and SYS terminals are internally connected. This mode is the most power efficient and thus

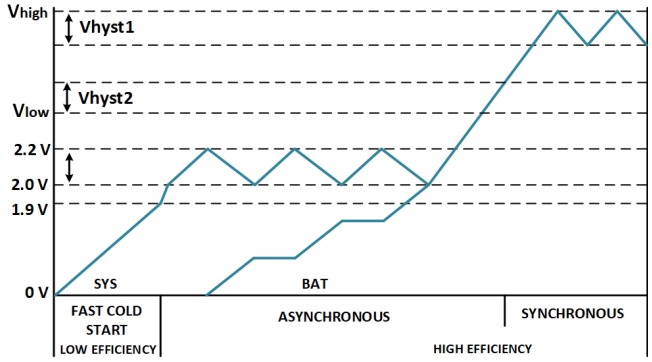

Fig. 4. Fast cold start-up sequence at the PMU. Source: Analog devices (appropriately modified).

desirable. The PMU stays in this mode whenever the voltage V_{SYS} lies between V_{high} and V_{low}, which are settable via resistors R_3 to R_6.

As for the MPPT functionality, different options are available. Here, the dynamic sensing mode is selected, which is based in the well-known fractional open circuit voltage (FOCV) technique. In this technique, the open circuit voltage of the harvester device (V_{oc}) is periodically sampled and a fraction of it is used to dynamically fix its output (V_{gen}) at its MPP (here $0.5V_{oc}$). Due to the presence of D_1, it is the PMU input voltage ($V_{in} = 0.5V_{oc}$) that is actually fixed via resistors R_1 and R_2, which act as a voltage resistor divider. The MPPT sampling time and period are predetermined by the chip to 256 ms and 16 seconds, respectively. The sampled MPP voltage is held at C_5.

III. WAVY and Test Drifters

The EC-funded MELOA project [25] aims to develop a new family of spherical drifters (WAVY) for marine monitoring that are low-cost, easily deployable, high versatile, and low maintenance systems. The WAVY family of products will include from coastal drifters for short deployments to oceanic drifters with energy scavenging solutions for long term deployments. One of these units is the WAVY Ocean-plus drifter, whose aim is to measure Lagrangian currents at the ocean surface. It is planned as an undrogued drifter with GNSS (Global Navigation Satellite System) for positioning and equipped with two thermistors used for the calibration of satellite sea surface temperature data. Furthermore, ocean wave parameters will be analyzed through an IMU and the satellite communication will be ARGOS-based [26].This WAVY drifter will be equipped with a hybrid energy harvesting system consisting of a solar panel and a KEH system. TABLE I shows some mechanical parameters of the WAVY drifter. Its buoyancy is optimized to prevent the drifter trajectory responding to the wind instead of the ocean current, while providing just enough exposure of the antenna to ensure acquisition of the GNSS signal and reliable near real-time satellite communications.

In this work, a specific test drifter with an embedded measuring system and with the same mechanical characteristics of the WAVY drifter (TABLE I) has been designed, so that the same motion behavior is obtained. The aim of this test drifter is to become a test platform of the KEH system that will be

TABLE I
PARAMETERS OF THE WAVY OCEAN-PLUS DRIFTER

Symbol	Parameter	Value	Units
m_b	Drifter mass	3.472	kg
R	Drifter radius	0.1	m
c_m	Center of mass[a]	0.06	m

[a]Center of mass taken from the bottom of the drifter body.

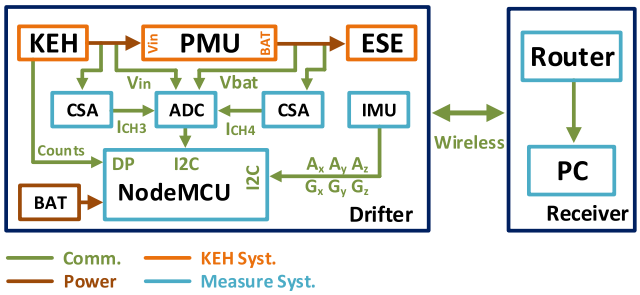

Fig. 5. Block diagram of the experimental setup that includes the test drifter (left) and the receiver (right).

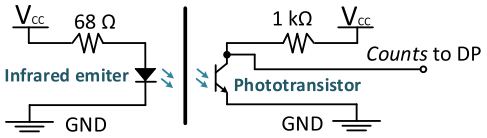

Fig. 6. Schematic of the circuit used to infer the rotation speed of the electrical generator, based on an infrared emitter and a phototransistor.

embedded in the WAVY drifters. This test drifter does not include the temperature sensors, the communication units nor the solar panels of the WAVY unit, but it still contains the KEH system and an IMU (MPU-9250, Invensense). In addition, an embedded measurement system is included as well as a Wi-Fi connection for wireless transfer of the measured data to a nearby Personal Computer (PC). Fig. 5 shows a block diagram of the experimental setup with the test drifter (left) and the user receiver (right). The receiver includes a Wi-Fi router to collect the data from the drifter and a PC to plot them in real time. The KEH system is represented in orange, the measurement system in light blue, the power connections links in brown, and the communication links in green. An open-source low-power NodeMCU development kit (https://www.nodemcu.com) has been selected as the control unit of the measurement system in the test drifter. It is based on the ESP8266-Module (Espressif Systems), which contains a Wi-Fi communication module.

The IMU provides the data corresponding to linear acceleration (A_x, A_y, A_z) and angular velocity (G_x, G_y, G_z) along the three axes through an I2C bus; the rotation speed of the KEH generator is inferred using the circuit shown in Fig. 6, which has been improved with respect to that used in [15]. An infrared emitting diode (VSMG2000X01, Vishay), attached to the main body of the KEH device, points to an also attached phototransistor (PT100MF0MP1, Sharp), whose collector terminal is connected to a digital port (DP) of the NodeMCU and through a pull-up resistor to the power

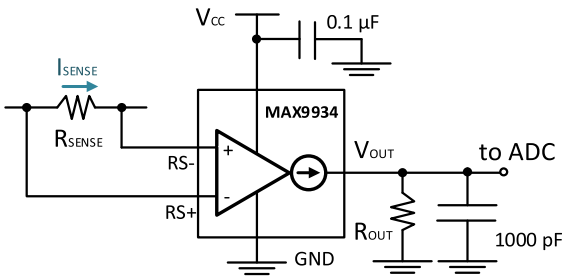

Fig. 7. Circuit schematic of the Current Sense Amplifier based on a MAX9934 (Maxim).

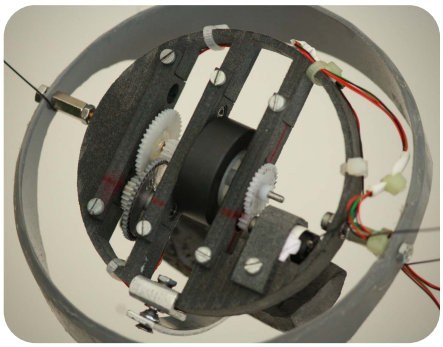

Fig. 8. Photograph of the designed KEH device.

supply (V_{cc}). One of the gear wheels with a hole on its surface spins in between; whenever the hole is aligned with the emitter-receiver couple, a logic "0" is generated at the digital input. Contrariwise, a logic "1" is generated.

The measurement system has been upgraded with respect to that used in [15] to measure input and output power to the PMU; the Adafruit module based on the Analog-to-Digital Converter (ADC) ADS1115 (Texas Instruments) has been selected for this task. Its main characteristics are: 4 multiplexed analog channels, maximum data rate of 860 samples/s, 16 bit, and I2C communication. Referring to Fig. 3, the first (V_{CH1}) and the second (V_{CH2}) channels measure V_{in} and V_{BAT}, respectively. The third (i_{CH3}) and fourth (i_{CH4}) channels are used for the measurement of the input and output (BAT terminal) currents of the PMU, respectively (see Fig. 3). Each current measurement is achieved using a Current Sense Amplifier (CSA) placed before the respective ADC channels. Fig. 7 shows the circuit schematic of the CSA, which includes an input shunt resistor (R_{SENSE}), which the current to be measured (I_{SENSE}) goes through, and an output resistor (R_{OUT}). The output terminal (V_{OUT}) is connected to the ADC channel. The CSA is based on a MAX9934 chip (Maxim) with a transconductance gain of 25 μA/mV.

IV. Materials and Method

A. KEH System and Test Drifter

Fig. 8 shows the manufactured prototype of the KEH device. It has a proof mass of 220 g and a total diameter of 10 cm. The main body has been 3D printed with polyamide and the proof mass made with lead. The total gear ratio is 35. The miniature DC motor referred to in [14], [15], used as electrical generator, has been replaced here by the 118391 model from Maxon Motors, presenting a nominal voltage of 12 V and a terminal resistance (R_g) of 114 Ω. Apart from being more rugged and reliable, it provides higher voltage outputs at the same mechanical excitation, letting the PMU to work at higher efficient rates.

A BAT47 schottky diode was chosen for the PMU; according to manufacturer information of the ADP5092, the following capacitor and inductor values were used: $C_1 = 10$ uF, $C_2 = 100$ nF, $C_3 = 220$ uF, $C_4 = 4.7$ uF, $C_5 = 10$ nF, and $L_1 = 22$ μH. The selected ESE was a Li-ion battery of 3.6 V and 2.2 Ah, which sets V_{BAT}. In order to protect it, V_{high} and V_{low} were set at 4.2 V and 2.4 V, respectively, using $R_3 = 3.57$ MΩ, $R_4 = 6.49$ MΩ, $R_5 = 4.12$ MΩ, and $R_6 = 5.9$ MΩ, as indicated by the chip manufacturer. Thus, the PMU mostly worked in the synchronous mode. The MPPT was set at dynamic sensing mode with a ratio of 0.5 with respect to V_{oc}, programmed with $R_1 = R_2 = 10$ MΩ.

As for the embedded measuring system, which is upgraded from that described in [15], as described in section III, the NodeMCU was configured to send collected data every 20 ms through its Wi-Fi connection. The data collected consist of the following: IMU (A_x, A_y, A_z, G_x, G_y, G_z), the rotation speed of the generator in the KEH device (in number of counts) and the input and output voltages and currents at the PMU (V_{CH1}, V_{CH2}, i_{CH3}, and i_{CH4}). The IMU was placed on the center of mass of the drifter. The mean rotation in the generator shaft was inferred during a time interval long enough to achieve a tolerable resolution. The ADC was set with single-shot operation and a data rate of 475 samples/s. The first CSA (i_{CH3}) used $R_{SENSE} = 0.5$ Ω and $R_{OUT} = 22$ kΩ, resulting in a gain of 275 V/A, whereas the second CSA (i_{CH4}) used $R_{SENSE} = 3.3$ Ω and $R_{OUT} = 12$ kΩ, resulting in a gain of 990 V/A. The NodeMCU was powered by a 9V Li-Ion battery; an internal linear regulator (AMS1117, Advanced Monolithic Systems) provided 3.3 V to the IMU, the pair emitting diode–phototransistor, and the CSAs. In addition, an external switching regulator (TSRN 1-2450A, TracoPower) provided 5 V to the ADC. Fig. 9 shows a 3D design of the test drifter with the distribution of the different components (top) and a photo of the drifter with the cover removed (bottom left).

B. Tests Performed

The first step was to characterize the Maxon DC motor, working in reverse mode as an electrical generator, in the laboratory. Its shaft was excited by attaching it to the shaft of another DC motor at different rotation speeds (ω) and the generator output (V_{gen}) was connected to a source measurement unit (SMU, Agilent B2901), in order to emulate different electrical loads (R_{LOAD}) as shown in Fig. 10. For each rotation speed (ω), a voltage sweep was performed with the SMU while measuring the output power.

A laboratory test was then performed to the test drifter (Fig. 5 left box), which consisted on placing it on a linear shaker (APS Dynamics: 129) with displacements in a single direction with controllable acceleration amplitude and frequency. The IMU X-axis was aligned with the shaker direction so accelerations were restricted to this axis. The pendulum arm of the KEH device was also aligned with that direction to

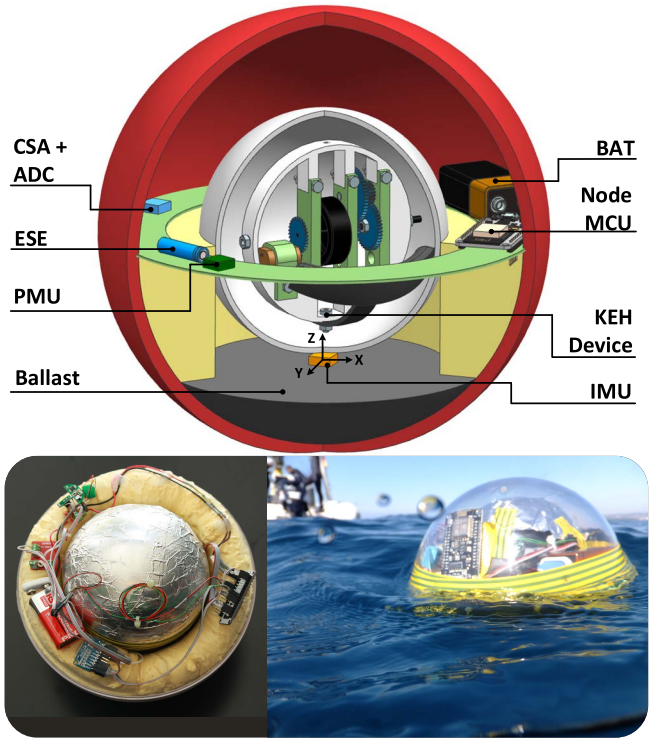

Fig. 9. (Top)The 3D model of the test drifter with the internal axis position and the distribution of the components. (Bottom) Photos of the drifter (left) with the cover removed and (right) during the deployment at sea.

TABLE II
WAVE PARAMETERS DURING THE DEPLOYMENT[b]

Parameter	Mean Value	Max./Min Value	Units
Wave height	1.43	2.12	m
Wave Frequency	0.29	0.15	Hz
Wave Direction	195.94	-	°(N)

[b]Data from the ADCP located in the OBSEA observatory

maximize the energy conversion. This test allowed to assess the performances of all subsystems.

Finally, a test was performed in real sea conditions near the OBSEA observatory [27] off the coast of Vilanova i la Geltrú, Spain. It is a controlled area in which sea conditions are monitored and measured by an Acoustic Doppler Current Profiler (ADCP). Fig. 9 (bottom right) shows images of the test drifter deployed at sea. A boat was used to carry the PC where the data were collected. In addition, the drifter motion was also simulated in OrcaFlex (Orcina), which is a dynamic analysis software for offshore marine systems. The drifter was modelled with the parameters shown in TABLE I, with the sphere modelled by 24 stacked flat cylinders of appropriate diameters [15]. The sea state was modelled using the average values shown on TABLE II and the Ochi-Hubble wave spectrum [28]; this spectrum was considered more appropriate than that used in [15]. These simulations were then compared with the experimental results.

V. EXPERIMENTAL RESULTS

A. Electrical Generator Characterization

Fig. 11 shows the output power and current versus the output voltage (V_{gen}) of the electrical generator at different

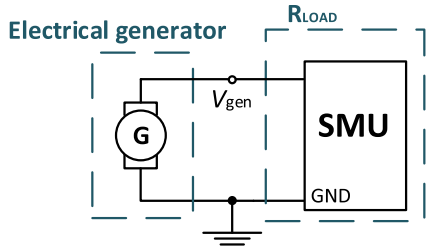

Fig. 10. Setup for the characterization of the electrical generator.

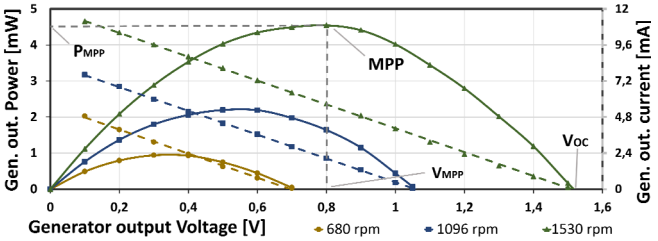

Fig. 11. Results of the generator characterization: output power (solid lines, left axis) and current (dashed lines, right axis) versus output voltage (V_{gen}) at different rotation speeds.

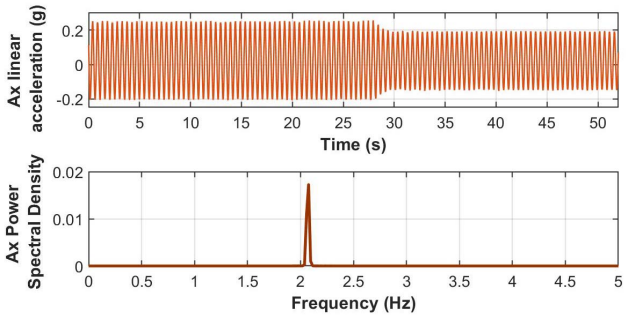

Fig. 12. Linear acceleration of the drifter along the X axis (A_x) when attached to the shaker (above) and its Power Spectral Density (PSD, below).

rotation speeds (ω defined in revolutions per minute, rpm), with no load connected to the generator output. It can be seen that the maximum power (P_{MPP}) happens at around half V_{oc}, which is coherent with the Thévenin model of the generator presented in Section II-A. In addition, P_{MPP} and V_{oc} are found to be nearly proportional to the square of V_{oc} and to ω, respectively, as predicted by (1) and (2). From the corresponding current-voltage characteristic (in dashed lines), an equivalent internal resistance of around 125 Ω is inferred, which nearly matches the terminal resistance (R_G) specified by the manufacturer (114 Ω).

Comparing these results with those of the generator used in [14], [15], a three-fold increase in voltage is achieved. This benefits the performance of the PMU, since low input voltages (below ~0.2 V) lead to a significant decrease of the power efficiency, according to data provided by the chip manufacturer. This behavior can also be observed in Fig. 9 of [14], in which the PMU was characterized. In addition, the values of P_{MMP} also increase.

B. Shaker Test

Fig. 12 (top) shows the drifter linear acceleration A_x registered by the IMU during a time interval of 52 s when the

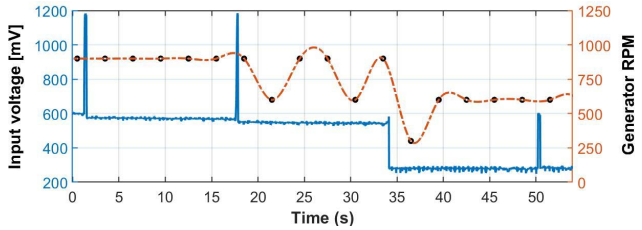

Fig. 13. Rotation speed (dotted-orange, right axis) and V_{in} (solid-blue, left axis) with the drifter attached to the shaker.

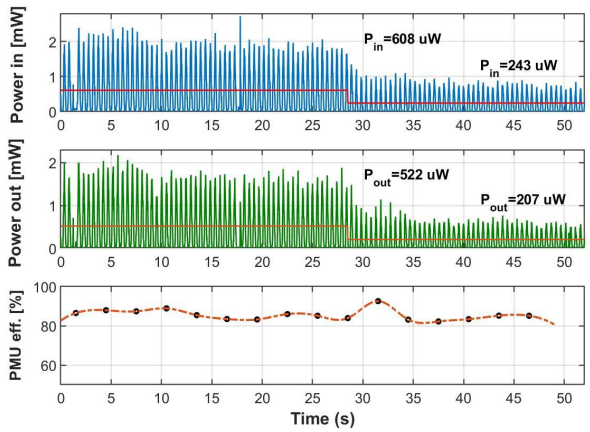

Fig. 14. PMU input (top plot, in blue) and output (middle plot, in green) powers. Both with their mean value (in red and orange, respectively) before and after the step change in A_x amplitude. The bottom plot shows the PMU efficiency averaged at intervals of 3 s. The drifter was attached to the shaker.

acceleration frequency of the shaker was configured to 2.1 Hz. It can be readily seen that the peak-to-peak amplitude was changed from an initial value of 0.45 g to 0.34 g (rms values of 0.16 g to 0.12 g, respectively) at time 28 s. Fig. 12 (bottom) shows the power spectral density (PSD) of A_x obtained by applying the Fast Fourier Transform (FFT) with MATLAB software. The frequency detected in the PSD matches with that programmed for the shaker. A constant vertical (Z-axis) acceleration of 1 g (not plotted in Fig. 12) was also found, corresponding to the gravitational acceleration.

Fig. 13 shows the corresponding generator rotation speed (in rpm and averaged in time intervals of 3 s) and V_{in} at the PMU. The ESE was previously charged to 3.9 V (V_{BAT}). While the A_x amplitude was high, rotation speed was around 900 rpm and the PMU V_{MPP} about 0.6 V ($V_{oc} \sim 1.2$ V). When the A_x amplitude decreased, rotation speed fell to around 600 rpm and V_{MPP} decreased to about 0.3 V ($V_{oc} \sim 0.6$ V). These changes in rotation speed and V_{MPP} happened at a later time (at time 34 s) than the change in A_x amplitude due to the interval update of V_{MPP} of 16 s. Correspondence between rotation speeds and voltages are coherent with the results shown in Fig. 11.

Fig. 14 shows the input (blue line, top plot) and output power (green line, middle plot) at the PMU with peak values of 2.73 mW and 2.17 mW, respectively, before the step change, and 0.97 mW and 0.72 mW after the step. In both plots, the mean power (P_{in} and P_{out} for input and output power, respectively) before and after the step change in A_x amplitude are also represented. Before the step, P_{in} was 608 μW and P_{out} was 522 μW. After the step, P_{in} and P_{out} fell to 243 μW and 207 μW, respectively.

Peak input powers are coherent with the results of Fig. 11. However, power generation is not constant, but pulsating. The frequency of this pulsating power production is 2.1 Hz, matching with the frequency of A_x, which is coherent with the performance of the KEH device described in section II-A. As mentioned, V_{oc} presents an AC component with the same frequency of the movement of the pendulum and thus of A_x. Since V_{in} is constant between the update intervals (16 s), the input power and thus the output power will be pulsating. The variation of V_{oc} between update intervals also prevents the system from continuously working at the generator's MPP and thus from achieving the maximum energy production. However, this problem is minimized by reducing the variability on V_{oc}, done by the flying wheel as described in Section II-A. On the other hand, the diode avoids draining power from the generator whenever V_{oc} (which changes within an update interval) is lower than V_{in} (which is constant within an update interval) but also introduces some losses. To quantify them, both the diode voltage drop and the current through the diode were monitored during the first 28 seconds, before the step change in A_x, resulting in average values of 0.18 V and 1.2 mA, respectively. The average power loss at the diode was 310 μW, which is significant compared to P_{in} (608 μW). Future designs should tackle this loss and reduce it.

The bottom plot of Fig. 14 shows the evolution of the PMU efficiency averaged in time intervals of 3 seconds. Most values are around 85 %. This is a significant improvement compared to the generator used in [14] and [15], in which the efficiency significantly decreased for rotations speeds below 900 rpm, as shown at Fig. 9 of [14], due to the lower generator voltage as previously stated.

C. Test at Sea

TABLE II shows the wave parameters data provided by the OBSEA ADCP during the test at sea. The mean values of the wave height and frequency were 1.43 m and 0.29 Hz, respectively.

1) Drifter Motion Behavior: Drifter hydrodynamic motions are composed of two movements, the vertical lineal oscillation and the horizontal angular oscillation. The first one (along the Z axis) is originated by the drifter buoyancy when an external excitation sinks it. The horizontal angular oscillation is due to the center of mass displacement relative to the geometrical center (TABLE I). A previous, exhaustive analysis of the drifter hydrodynamic motion behavior was presented in [15]; it consists of an analysis of the accelerometer (A_x, A_y, A_z) and gyroscope (G_x, G_y, G_z) data provided by the IMU sensor. The inferred drifter orientation (Roll, Pitch and Yaw) were also studied. Here, some of those parameters considered relevant for this work (A_x and A_Z) are shown and analyzed with new data acquired during the test at sea.

Fig. 15 shows A_x and A_z during a time interval of 142 s when the drifter was placed at sea, as well as their PSD. For the horizontal component, only data corresponding to the X

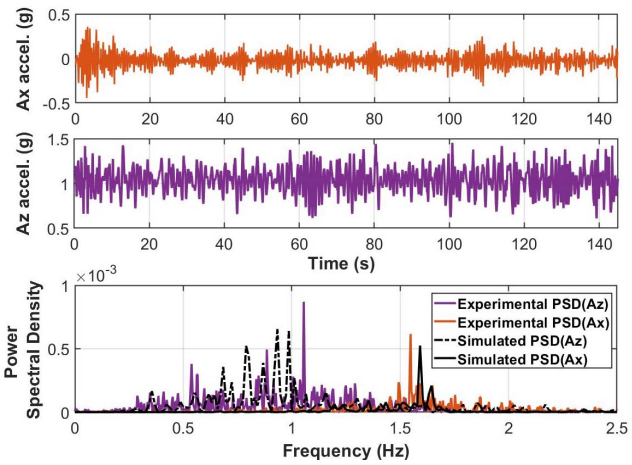

Fig. 15. Drifter linear accelerations at X (A_x) and Z (A_z) axis when placed at the sea and their respective PSD compared with the PSD from the simulated results.

axis is shown since the PSD of the Y axis component was found to be similar. It can be seen that A_x has a peak-to-peak amplitude of 0.8 g (with a rms value of 0.08 g) and a peak frequency (PSD graph) around 1.5 Hz. On the other hand, A_z is centered at 1 g due to the gravitational acceleration, with a peak-to-peak amplitude of also 0.8 g (with a rms value of its AC component of 0.14 g). The DC component of the gravitational acceleration is not shown in the PSD to facilitate the visualization of the other components, showing a peak frequency around 1 Hz and also lower frequency components related to the wave movement. Peak frequencies are similar to that obtained in [15].

Fig. 15 also includes the PSD of A_x and A_z from the simulation results. These spectra are similar to those of the experimental results, which validates the simulation model. The OrcaFlex model is thus a powerful tool with which to anticipate the behavior of the drifter in different sea states. Availing of this, different sea conditions have been simulated with the model. The results show that the PSD peak frequencies of the vertical and horizontal oscillations do not depend on the sea conditions but rather on the constructive parameters of the drifter. This is coherent with [29], where it is stated that the natural frequency of oscillation of a body placed in a fluid depends on the fluid properties (density) and the physical parameters of the body. On the other hand, the amplitude of the accelerations and therefore the potential generated power depends on the wave height and frequency [17]. So, by using the validated OrcaFlex model, future simulations may provide information about how to tune parameters from TABLE I to maximize the power generated in the drifter.

2) KEH System Analysis: Fig. 16 shows the generator rotation speed and V_{in} at the PMU for the same time frame as in Fig. 15. Here, the ESE was charged at 4.1 V before the test. As expected, both the rotation speed and voltage have a much higher variability than in the shaker test. Rotation data in Fig. 16 are plotted with values averaged over time intervals of 6 s to reduce their higher variability. The average rotation speed was 437 rpm. Again, MPP voltages were updated every 16 seconds. When the generator rotates at low motion or even

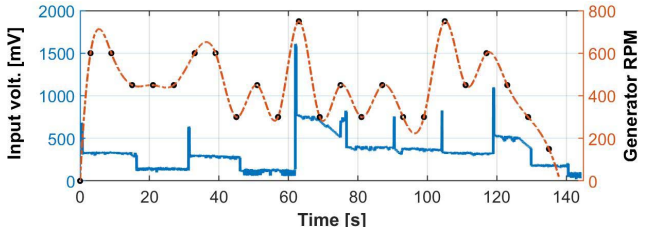

Fig. 16. Rotation speed (dotted-orange, right axis) and V_{in} (solid-blue, left axis) with the drifter deployed at sea.

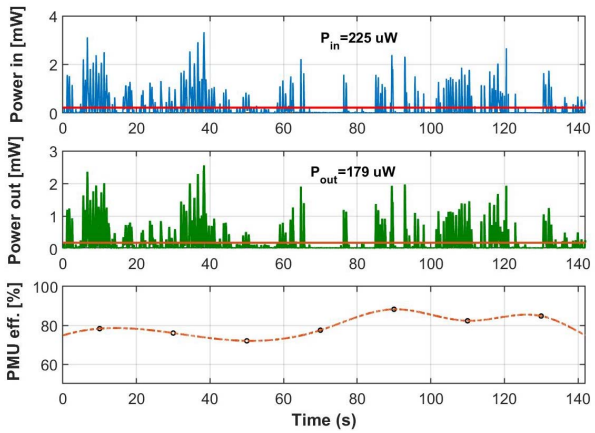

Fig. 17. PMU input (top plot, in blue) and output (middle plot, in green) powers. Both with their mean value (in red and orange, respectively). The bottom plot shows the PMU efficiency average at intervals of 20 s. The drifter was deployed at sea.

stops ($t = 140$ s), V_{in} falls to 0 V, harvesting no energy during the next 16 seconds until V_{in} is updated again.

Fig. 17 shows the corresponding PMU input and output power. As in the shaker test, power signals are pulsating, now with peak values of 3.5 mW and 2.6 mW, respectively. The average power values were $P_{in} = 225$ μW and $P_{out} = 179$ μW. These values are lower but not far from those achieved in the shaker test when using the low acceleration (rms of 0.12 g), which is coherent with the lower acceleration for A_x achieved in the sea test (rms of 0.08 g). Finally, the bottom plot presents the mean PMU efficiency for 20 s intervals, ranging from 70 % to 90 % with an average of 80%.

In a previous work [30], the power consumption of a TD1205P, including sensing, processing and transmitting, was evaluated as an option for tracking drifters in coastal areas. Since the energy used per transmitting cycle was 1.49 J, 10 transmissions per day would be feasible with the power generated during the sea test (average of 179 μW). This issue will be better assessed in the near future with longer term deployments.

From the related literature presented in section I, only the work of Li *et al.* [13] is similar to this paper with regard to the KEH device size and weight and to testing it in an actual sea environment. However, they did not use any PMU and only gathered the AC open circuit voltage at the output of the KEH device using a commercial measurement system. This paper goes beyond that work by including a PMU after the KEH device with MPPT functionality in a test at sea,

able to recharge a battery and power electronic loads and sensors. In addition, a custom-made embedded measuring system was developed, enabling the acquisition of several crucial parameters such as accelerations and velocities of the drifter, rotation speed of the generator and input and output powers of the PMU. Future work is foreseen in improving both the KEH device and the PMU to increase the overall power output.

VI. Conclusions

A novel KEH device has been designed and developed for powering undrogued drifters. It is comprised of a gearing system that transforms the pendulum oscillations induced by wave motion into rotation of a flywheel, which are then transmitted to an electrical generator. Its output is further processed by a PMU, which includes an MPPT to gather the maximum energy from the generator. To assess the performance of the KEH system at sea, a specific test drifter has been designed. The drifter contains the KEH system together with an embedded measurement system which counts on an IMU and other parts to estimate the rotation speed of the generator and the input and output power in the PMU. A Wi-Fi connection for transferring data at short distances is also present. First, the generator was characterized, verifying that it behaves as an equivalent Thévenin circuit. Then, the test drifter was validated on a linear shaker and later deployed at sea. Results of the test at sea, with waves of 1.43 m height and 0.29 Hz in average, show horizontal and vertical oscillations with peak-to-peak accelerations of 0.8 g and power spectra centered around 1.5 Hz and 1 Hz, respectively. This resulted in a mean power of 179 μW achieved at the PMU output with peaks of 2.2 mW. *A priori*, this would be enough for powering a TD1205P low-power module, proposed for tracking drifters, transmitting 10 times a day, but this result must be further verified with longer term deployments.

Acknowledgment

The authors express their thanks to Orcina for their kind support and offer of the academic license OrcaFlex N2703 (2018) to Universitat Politècnica de Catalunya.

References

[1] R. E. Thomson and W. J. Emery, *Data Analysis Methods in Physical Oceanography*, 3rd ed. Newnes: Oxford, U.K., 2014.

[2] H. Nam, "Data-gathering protocol-based AUV path-planning for long-duration cooperation in underwater acoustic sensor networks," *IEEE Sensors J.*, vol. 18, no. 21, pp. 8902–8912, Nov. 2018.

[3] R. Al-Zaidi, J. C. Woods, M. Al-Khalidi, and H. Hu, "Building novel VHF-based wireless sensor networks for the Internet of marine things," *IEEE Sensors J.*, vol. 18, no. 5, pp. 2131–2144, Mar. 2018.

[4] S. Subbaraya *et al.*, "Circling the seas: Design of Lagrangian drifters for ocean monitoring," *IEEE Robot. Autom. Mag.*, vol. 23, no. 4, pp. 42–53, Dec. 2016.

[5] M. Postacchini, L. R. Centurioni, L. Braasch, M. Brocchini, and D. Vicinanza, "Lagrangian observations of waves and currents from the river drifter," *IEEE J. Ocean. Eng.*, vol. 41, no. 1, pp. 94–104, Jan. 2016.

[6] R. Lumpkin, T. Özgökmen, and L. Centurioni, "Advances in the application of surface drifters," *Annu. Rev. Mar. Sci.*, vol. 9, no. 1, pp. 59–81, Jan. 2017.

[7] P.-M. Poulain, R. Gerin, E. Mauri, and R. Pennel, "Wind effects on drogued and undrogued drifters in the eastern mediterranean," *J. Atmos. Ocean. Technol.*, vol. 26, no. 6, pp. 1144–1156, Jun. 2009.

[8] F. U. Qureshi, A. Muhtaroglu, and K. Tuncay, "Near-optimal design of scalable energy harvester for underwater pipeline monitoring applications with consideration of impact to pipeline performance," *IEEE Sensors J.*, vol. 17, no. 7, pp. 1981–1991, Apr. 2017.

[9] G. Bracco, A. Cagninei, E. Giorcelli, G. Mattiazzo, D. Poggi, and M. Raffero, "Experimental validation of the ISWEC wave to PTO model," *Ocean Eng.*, vol. 120, pp. 40–51, Jul. 2016.

[10] L. D. A. Thorner, P. D. Mitcheson, A. S. Holmes, and E. M. Yeatman, "Scaling laws for energy harvesters in a marine environment," in *Proc. PowerMEMS*, Washington, DC, USA, 2009, pp. 249–252.

[11] W. Ding, B. Song, Z. Mao, and K. Wang, "Experimental investigation on an ocean kinetic energy harvester for underwater gliders," in *Proc. IEEE Energy Convers. Congr. Expo. (ECCE)*, Montreal, QC, Canada, Sep. 2015, pp. 1035–1038.

[12] W. Ding, K. Wang, Z. Mao, and H. Cao, "Layout optimization of an inertial energy harvester for miniature underwater mooring platforms," *Mar. Struct.*, vol. 69, Jan. 2020, Art. no. 102681.

[13] Y. Li *et al.*, "Study of an electromagnetic ocean wave energy harvester driven by an efficient swing body toward the self-powered ocean buoy application," *IEEE Access*, vol. 7, pp. 129758–129769, 2019.

[14] M. Carandell, D. M. Toma, M. Carbonell, M. Gasulla, and J. D. Rio, "Design and development of a kinetic energy harvester device for oceanic drifter applications," in *Proc. IEEE Int. Instrum. Meas. Technol. Conf. (I2MTC)*, Auckland, New Zealand, May 2019, pp. 1718–1723.

[15] M. Carandell, D. M. Toma, M. Gasulla, and J. D. Rio, "Experimental validation of a kinetic energy harvester device for oceanic drifter applications," in *Proc. OCEANS*, Marseille, France, Jun. 2019, p. 17.

[16] H. Liu, Z. Ji, T. Chen, L. Sun, S. C. Menon, and C. Lee, "An intermittent self-powered energy harvesting system from low-frequency hand shaking," *IEEE Sensors J.*, vol. 15, no. 9, pp. 4782–4790, Sep. 2015.

[17] N. Pozzi, G. Bracco, B. Passione, A. S. Sergej, G. Vissio, and G. Mattiazzo, "Wave tank testing of a pendulum wave energy converter 1:12 scale model," *Int. J. Appl. Mech.*, vol. 9, no. 2, p. 30, 2017.

[18] M. E. El-Hawary, *Principles of Electric Machines with Power Electronic Applications*, 2n ed. Piscataway, NJ, USA: IEEE Power Engineering Society, 2002, chs. 4.3, pp. 185–187.

[19] S. Heo, Y. S. Yang, J. Lee, S.-K. Lee, and J. Kim, "Micro energy management for energy harvesting at maximum power point," in *Proc. Int. Symp. Integr. Circuits*, Dec. 2011, pp. 136–139.

[20] Q. Ju, H. Li, and Y. Zhang, "Power management for kinetic energy harvesting IoT," *IEEE Sensors J.*, vol. 18, no. 10, pp. 4336–4345, May 2018.

[21] T. T. Toh, A. Bansal, G. Hong, P. D. Mitcheson, A. S. Holmes, and E. M. Yeatman, "Energy harvesting from rotating structures," in *Proc. PowerMEMS*, no. 50, 2007, pp. 327–330.

[22] J. Kokert, T. Beckedahl, and L. Reindl, "Medlay: A reconfigurable micro-power management to investigate self-powered systems," *Sensors*, vol. 18, no. 1, p. 259, Jan. 2018.

[23] M. T. Penella and M. Gasulla, "Runtime extension of low-power wireless sensor nodes using hybrid-storage units," *IEEE Trans. Instrum. Meas.*, vol. 59, no. 4, pp. 857–865, Apr. 2010.

[24] F. Reverter and M. Gasulla, "Optimal inductor current in boost DC/DC converters regulating the input voltage applied to low-power photovoltaic modules," *IEEE Trans. Power Electron.*, vol. 32, no. 8, pp. 6188–6196, Aug. 2017.

[25] *MELOA Project*. Accessed: Oct. 21, 2019. [Online]. Available: https://www.ec-meloa.eu/

[26] X. André, B. Moreau, and S. Le Reste, "*Argos-3* satellite communication system: Implementation on the Arvor oceanographic profiling floats," *J. Atmos. Ocean. Technol.*, vol. 32, no. 10, pp. 1902–1914, Oct. 2015.

[27] M. Nogueras *et al.*, "OBSEA an oceanographic seafloor observatory," *Sea Technol.*, vol. 51, no. 7, pp. 37–39, 2010.

[28] M. K. Ochi and E. N. Hubble, "Six-parameter wave spectra," in *Proc. Coastal Eng.*, Honolulu, HI, USA, 1976, pp. 301–328.

[29] Z. Ballard and B. P. Mann, "Two-dimensional nonlinear analysis of an untethered spherical buoy due to wave loading," *J. Comput. Nonlinear Dyn.*, vol. 8, no. 4, p. 12, Jul. 2013.

[30] M. Carandell, D. Mihai, J. del Río, K. Ganchev, and J. Peudennier, "Evaluation of Sigfox LPWAN technology for autonomous sensors in coastal applications," *Instrum. Viewp.*, vol. 20, pp. 36–37, Dec. 2018.

Matias Carandell was born in Barcelona, Spain, in 1991. He received the B.Sc. degree and the M.S. degree in industrial engineering from Universitat Politècnica de Catalunya (UPC), with the specialty of electrical engineering, in 2015, where he is currently pursuing the Ph.D. degree in electronic engineering with the Remote Acquisition Systems and Data Processing (SARTI) research group. After that, he spent one year at the Universidad Técnica Federica Santa Maria (UTFSM), Chile, working with solar power converters. His current research interests include energy harvesting in marine environment, energy conditioning systems for autonomous sensors, and autonomy concerning Lagrangian drifter electronics.

Daniel Mihai Toma received the M.Sc. degree in electrical engineering from Technical University Gheorghe Asachi, Iasi, Romania, in 2008, and the Ph.D. degree in electronic engineering from the Universitat Politècnica de Catalunya (UPC), Barcelona, Spain, in 2012. He is currently a member of the Remote Acquisition Systems and Data processing (SARTI) research group, Electronic Engineering Department, UPC. His current research interests include electronic instrumentation, wireless ad hoc networks, interoperability in sensor networks, and synchronization and scheduling.

Montserrat Carbonell was born in Catalonia, Spain, in 1963. She received the B.Sc. degree in geology from the University of Barcelona (UB) in 1986 and the master's degree in groundwater hydrology and the Ph.D. degree in industrial engineering from the Universitat Politècnica de Catalunya (UPC), Barcelona, Spain, in 1987 and 2000, respectively. Since 1990, she has been a Professor with the Fluid Mechanics Department, UPC. She was a member of the Modeling and Environmental Technology (MTA) research group, from 2004 to 2013. Since 2013, she has been a member of the Remote Acquisition Systems and Data Processing (SARTI) research group. Her current research interests include the study and design of devices for marine renewable energy harvesting with applications to wireless sensor networks of marine environment monitoring.

Joaquín del Río (Member, IEEE) was born in Catalonia, Spain, in 1976. He received the B.Sc., M.Sc., and Ph.D. degrees in telecommunication engineering and electronic engineering from the Universitat Politècnica de Catalunya (UPC), Barcelona, Spain, in 1999, 2002, and 2011, respectively.

Since 2001, he has been a Professor with the Electronic Engineering Department, UPC. He is a member of the Remote Acquisition Systems and Data Processing (SARTI) research group. His research focuses on electronic instrumentation, interoperability in marine sensor networks, and wireless sensor networks. Prof. del Río is a member of the National Institute of Standards and Technology (NIST) IEEE1451.2 Working Group and the Smart Ocean Sensors Consortium and PUCK Standard Working Group (SWG). He is involved in numerous projects within the industry and is a National Instruments Certified Instructor for teaching official LabVIEW courses.

Manel Gasulla (Senior Member, IEEE) was born in Vinaròs, Spain, in 1967. He received the M.Eng. and Ph.D. degrees in telecommunications from the Universitat Politècnica de Catalunya (UPC BarcelonaTech), Barcelona, in 1992 and 1999, respectively. Since 1993, he has been with UPC, where he is an Associate Professor, engaged in teaching on analog and power electronics and electronic instrumentation. From 2001 to 2002, he was a Visiting Postdoctoral Fellow with the Electronic Instrumentation Laboratory, Delft University of Technology, The Netherlands. He presently leads the research group e-CAT (Electronic Transducers and Interfaces), UPC, which focuses on new electronic circuits applied to transducers for signal and power processing with the aim of developing energy-autonomous smart sensors. He is co-author of more than 70 articles in journals and conferences, seven Spanish patents, several chapters in books, and the book *Powering Autonomous Sensors* (Springer, 2011). His research interests include capacitive sensors, direct sensor-to-microcontroller interfaces, and energy harvesting and wireless power transfer circuits for autonomous sensors.

A.3 Article 3

P.[42] - Optimum MPPT Strategy for Low-Power Pendulum-Type Wave Energy Converters

---

Conference: IEEE Sensors Conference - 2020 Rotterdam
Publisher: IEEE
Date of Publication: 9 December 2020
DOI: 10.1109/SENSORS47125.2020.9278610

Optimum MPPT Strategy for Low-Power Pendulum-Type Wave Energy Converters

Matias Carandell[1]*, Daniel Mihai Toma[1], Joaquín del Río[1] and Manel Gasulla[2]
[1] SARTI, Universitat Politècnica de Catalunya, Vilanova i la Geltrú, Spain
[2] e-CAT Group, Universitat Politècnica de Catalunya, Castelldefels, Spain. *matias.carandell@upc.edu

***Abstract*—Maximum Power Point Tracking (MPPT) techniques for low-power pendulum-type Wave Energy Converters were evaluated. A Kinetic Energy Harvester previously designed, together with a Power Management Unit, were tested on a linear shaker to compare three MPPT techniques, the Constant Voltage versus two variants of the Fractional Open Circuit Voltage (FOCV). Results show a 25% improvement on the scavenged energy with one of the proposed FOCV techniques with respect to the other ones.**

Keywords— Drifter, Kinetic Energy Harvesting (KEH), Power Management Unit (PMU), Maximum Power Point Tracking (MPPT), Fractional Open-Circuit Voltage (FOCV).

I. INTRODUCTION

Ocean monitoring has become crucial to preserve marine biodiversity. Lagrangian Drifters are autonomous floating devices that provide oceanographic surface data. They are low-cost, low-power and easy-deployable marine instrumentation. Power autonomy is desirable in order to avoid maintenance costs and waste generation [1]. To achieve this autonomy, some manufacturers use photovoltaic (PV) panels (Sofar: Spotter, Fastwave: Voyager Solar). Nevertheless, if the drifter is strictly dedicated to current monitoring, its body must be mostly submerged to avoid the wind effect [2] and, thus, the irradiation at the PV panels is attenuated.

As an alternative, other energy sources may be explored, such as the oscillatory movement of waves. Wave Energy Converters (WEC) have proved their viability in high-power electric generation plants to work as Kinetic Energy Harvesters (KEH) and now they are also showing up to supply low-power devices such as gliders and drifters [3], [4]. In this latter case, a Power Management Unit (PMU) is used, which can also include a Maximum Power Point Tracker (MPPT) to extract maximum energy from the KEH device.

In [5], a KEH system embedded into an ocean drifter was presented, which included a KEH energy transducer (KEH device, hereafter), a PMU with an MPPT, and an energy storage element (ESE). In [6], the KEH system was assessed on a wave flume using a couple of MPPT techniques. This paper extends those works by comparing three MPPT techniques using a laboratory setup to find the most optimum.

II. MPPT TECHNIQUES ON KEH SYSTEMS

MPPTs are used in energy harvesters to extract maximum energy. Suitable MPPT techniques can be applied once the electrical model of the KEH device is known. So, Section II.A presents the KEH device and its electrical model and Section II.B describes several MPPT techniques and selects some of them to be compared.

A. KEH device

A novel prototype of a KEH device was designed, manufactured and tested in [5]. It is a pendulum-type system which uses the motion of the waves to generate power (Fig. 1, left). The KEH device consists of an articulated pendulum arm with a prof mass. This mass relatively moves with respect to the main body, attached to the drifter, with pendulum motion. Then, through a gear system, rotation is accumulated in a flying wheel which drives a DC electrical generator. The gear system increases the rotation velocity with a ratio of 35 and, due to a one-way gear mechanism, the flying wheel only rotates in one direction, at which energy is accumulated.

The electrical generator is a miniature DC motor, which can be modelled as a Thévenin equivalent circuit [7], as presented in Fig. 1 (right). R_G is the internal equivalent resistance, V_{OC} is the generated electromotive force (EFM) and V_{GEN} is the voltage at the output terminals [8]. Using the maximum power transfer theorem, maximum power is extracted when $V_{GEN} = 0.5V_{OC}$, which is known as the maximum power point (MPP) voltage (V_{MPP}). So, the maximum achievable power (P_{MPP}) is given by

$$P_{MPP} = V_{OC}^2/(4R_G) \quad (1)$$

with

$$V_{OC} = K_G\varphi\omega \quad (2)$$

where K_G is the motor constructive constant, φ the magnet field generated by the permanent magnet, and ω the generator rotor speed. Since K_G and φ are constants, V_{OC} is proportional to ω. Within one single pendulum cycle, while the pendulum applies torque through the one-way gear, the flywheel accelerates, increasing ω and thus V_{OC}, whereas when the pendulum moves in the other direction the one-way gear rotates freely, so that the flywheel slows down, thus reducing ω and V_{OC}. Therefore, ω and thus V_{OC} will have both DC and

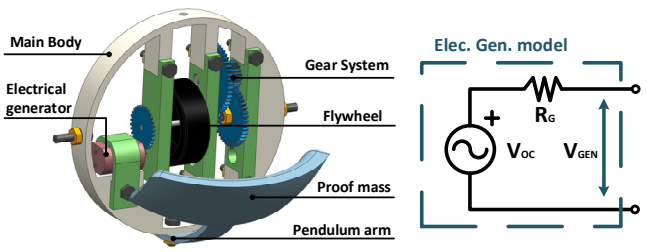

Fig. 1. KEH device with its main components (left, [5]) and its electrical model (right).

This work was supported by the project MELOA from the European Commission's Horizon 2020 research and Innovation program under Grant Agreement No. 776825 and by the Spanish Ministry of Economy and Competitiveness and the European Regional Development Fund under project TEC2016-76991-P. The first author has a grant from the Secretariat of Universities and Research of the Ministry of Business and Knowledge of the Government of Catalonia on the FI program (ref. BDNS 362582).

978-1-7281-6801-2/20/$31.00 ©2020 IEEE

AC components, even for a constant excitation source. The AC component will be periodic with the same frequency of the mechanical movement of the pendulum [5].

B. MPPT techniques

In EH-powered systems, a wise and efficient energy management is crucial. Kokert et. al. [9] presented a reconfigurable micro-power management platform and summarized different MPPT techniques. Two of the most popular ones are the Fractional Open Circuit Voltage (FOCV) and the Perturb and Observe (P&O). The P&O technique [10] requires the measurement of the output power of the harvester device (P_{GEN}). Usually, this is performed via the measurement of voltage and current but in [11] power was estimated via the charging time of a capacitor. Anyway, the P&O technique is based on the following principle: V_{GEN} is periodically perturbed and P_{GEN} measured. Whenever P_{GEN} increases, V_{GEN} moves towards V_{MPP} and thus must be further perturbed in that direction. Otherwise, if P_{GEN} decreases, V_{GEN} moves away V_{MPP} and thus must be perturbed in the opposite direction. In low-power harvesters, as the KEH device presented here, the harvested energy may not pay-off the energy consumed by the required computation resources. Contrariwise, the FOCV technique [12] is simpler. Here, the output of the harvester device is periodically open to sample V_{OC} and then is dynamically fixed at its MPP by forcing V_{GEN} to a fraction of V_{OC}. This fraction is not precisely defined for some harvesters devices such as photovoltaic cells, which can prevent working at the true MPP [13]. But for the KEH device, this fraction is well defined to 0.5, as described in section II.A. So, this technique will be used here. Still, since the harvester device opens periodically to sample V_{OC}, some inherent losses are present. Finally, an even simpler technique, the constant voltage (CV) will also be used. It is based on providing a fixed voltage as the V_{MPP} to the PMU eliminating the inherent losses of the FOCV. The aim is that this voltage be near the actual V_{MPP}. Nevertheless, V_{OC} and thus V_{MPP} of the KEH device will depend on the specific sea conditions. Moreover, V_{OC} includes an AC component, as mentioned in Section II.A. So, the suitable fixed voltage must be experimentally tuned.

A preliminary evaluation of the CV and FOCV techniques using the ADP5092 (Analog Devices) PMU was done on the LIM-UPC wave flume and results were reported in [6]. It was concluded that different voltages should be tested on the CV and the sampling period should be lowered on the FOCV. This article is focused on achieving these goals to determine the most suitable MPPT technique.

III. Materials and Method

A linear shaker with controllable acceleration amplitude and frequency was used to emulate in the laboratory the drifter's movement under a sea environment. The drifter prototype presented at [5], with its embedded KEH and measurement systems, was used. The drifter movement was restricted here to a fixed acceleration frequency and amplitude. Three MPPT techniques were compared, the CV and two based on the FOCV.

A. Testing system

The setup of the testing system is shown in Fig. 2. A function generator FG1 (HP 33120A) generates a sinusoidal voltage which is connected to a power amplifier (APS 124). The amplifier transforms this signal into a sinusoidal current which controls the acceleration amplitude and frequency of the linear shaker (APS 129).

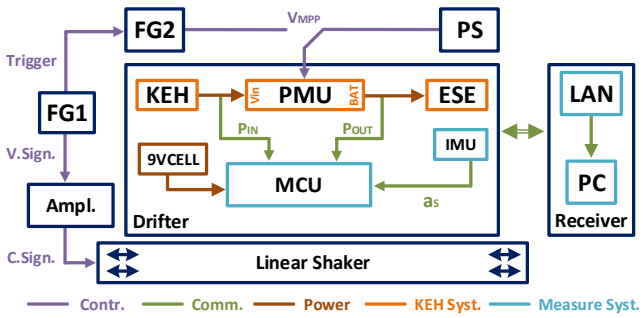

Fig. 2. Block diagram of the testing system that includes the instrumentation for the excitation of the drifter and the measurement of the data.

The drifter was attached to the shaker with the KEH device's pendulum aligned to the movement axis. The drifter included the KEH system and a measurement unit that provides the input and output PMU powers (P_{IN} and P_{OUT}, respectively) and the drifter (and thus the linear shaker) acceleration (a_s) via an inertial measuring unit (IMU). Data were taken every 20 ms with an Arduino based microcontroller (MCU) and wirelessly sent to a PC that processed and logged them. Measuring system is independently powered by a 9 V cell (9VCELL). Further information about this drifter prototype is given at [5].

FG1 voltage signal was swept from 0.4 to 2 V peak-to-peak amplitude at a frequency of 2 Hz and a_s was measured to obtain the transfer characteristic of the excitation subsystem. Then, FG1 voltage amplitude was set to 1 V for the rest of the tests.

As can also be seen in Fig. 2, a power supply PS (HP E3631A) provided a constant voltage (V_{MPP}) to the PMU needed for the CV technique. On the other hand, FG1 trigger output was used to synchronize another function generator FG2 (HP 33120A), whose output signal was used to generate V_{MPP} for one of the FOCV techniques. This will be further described in section III.B.

B. PMU setup

In this work, the ADP5092 (Analog Devices) has been used as the PMU. It is based on a boost regulator with MPPT functionality and with a very low internal consumption that operates with input voltages (V_{in}) as low as 80 mV. On the other hand, it provides a battery charging terminal (BAT) to which the ESE is connected. Fig. 3 shows the circuit schematic with the generator model on the left, where the manufacturer specified valued for R_G is 114 Ω, the PMU on

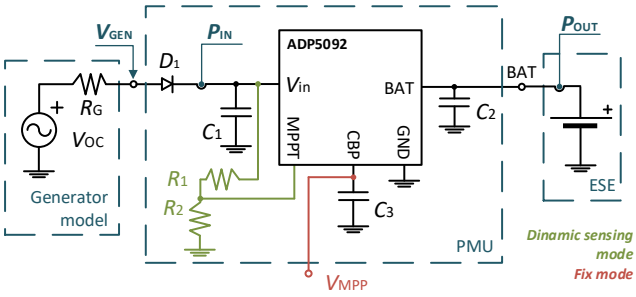

Fig. 3. Thévenin equivalent circuit of the generator (left). Circuit schematic of the ADP5092 configured to work as the PMU (center) and ESE (right).

the center, and the ESE on the right. Further information about the PMU and the selected components values are given in [5]. For this work, the Schottky diode was substituted by the PMEG3050EP (Nexperia) to reduce forward losses. Also, a smaller Po-Li ESE of 300 mA and 3.7 V (LP-402933-IS-3, BAK) was chosen.

As for the ADP5092 MPPT functionality, two configurations were used. One corresponds to the FOCV technique described in section II.B (named FOCV1), where V_{OC} is periodically sampled every 16 s during 256 ms (fixed by the ADP5092). Then, its 50 % value is obtained at the MPPT pin through a resistor divider ($R_1 = R_2 = 10$ MΩ) and held at C_3 (CBP pin) as the V_{MPP}. In the second configuration, V_{MPP} is set externally by providing the voltage directly to the CBP pin (and removing R_1 and R_2). This configuration was used for the CV and the other FOCV-based technique (FOCV2). V_{MPP} was provided for the CV by the PS and for the FOCV2 by the FG2 (synchronized with FG1 and thus with a_s).

First, V_{OC} was acquired with a scope in order to find the ideal V_{MPP} signal, i.e. $0.5V_{OC}$, which should be used for the PMU. Then, tests with the three techniques (CV, FOCV1 and FOCV2) were performed. For the CV, several DC voltages were generated. For the FOCV2, FG2 was programmed with different offsets and amplitudes at a frequency of 2 Hz in order to continuously resemble $0.5V_{OC}$. In both cases (CV and FOCV2), the aim was to find out the V_{MPP} signals that provided the maximum power.

IV. Results

A. Acceleration characterization

From the experimental results, the following regression line was obtained

$$a_s\,[\text{g}] = 0.26 \cdot V_{FG1} + 0.01\,[\text{V}] \quad (3)$$

According to (3), with FG1 set to 1 V, a_s resulted in 0.27 g (peak-to-peak at a frequency of 2 Hz), which can be observed in Fig. 4 (top graph, blue line). Some offset can be observed, due to the gravity effect and the fact that movement axis may not be perfectly horizontal. Both acceleration amplitude and frequency were similar to those used in [5] for the shaker test.

B. MPPT test

Fig. 5 shows $0.5V_{OC}$ (black), which approximately presents 1 V offset and 0.6 V amplitude at a frequency of 2 Hz. This agrees with the behavior described for V_{OC} at the end of section II.A.

Experimental results for the three MPPT techniques are shown at TABLE I, where column one specifies the MPPT technique, columns two and three present the V_{MPP} control signal, columns four and five show the measured mean power at the PMU input and output ($P_{IN,AV}$ and $P_{OUT,AV}$, respectively), and last column shows the mean PMU efficiency (η). As can be seen for the V_{MPP} signal, CV technique only uses DC voltages (offset), FOCV1 automatically generates it, and FOCV2 uses both DC and AC components. The following conclusions can be drawn:

1) CV technique shows higher harvested power for V_{MPP} = 0.8 V, where $P_{IN,AV}$ = 4.44 mW. Nevertheless, P_{OUT} is slightly higher at V_{MPP} = 1 V because ADP5092 provides better efficiencies at higher voltages. This value agrees with the offset voltage of $0.5V_{OC}$ in Fig. 5.

2) FOCV1 technique updated V_{MPP} every 16 s, so much slower than required to track $0.5V_{OC}$ (with a frequency of 2 Hz and thus a period of 0.5 s, as can be seen in Fig. 5). Even so, results are similar to the best results of the CV technique, since V_{MPP} values were around 1 V, with the advantage that no tuning process is necessary since V_{MPP} is set automatically.

3) FOCV2 technique provides the best results (power improvement around 25%) for FG2 providing a V_{MPP} signal of 1 V offset and 0.7 V amplitude. Fig. 5 shows this signal (in orange) jointly with $0.5V_{OC}$. As they are similar, the KEH device operates near the MPP continuously, which justifies the power improvement. Fig. 4 shows more results of the FOCV2 test. Top graph shows the syncronization between a_s (blue) and V_{MPP} (orange) and bottom graph shows P_{IN}, with an average value of 5.54 mW. Instanteneous values of P_{IN} agree with (1). Future work will address the application of the FOCV2 technique in a simpler and automatic way, for example using the FOCV1 technique at a higher sample rate.

TABLE I. MPPT TEST RESULTS

MPPT technique	V_{MPP} (V)		*PMU power results*		
	Offset	*Ampl.*	$P_{IN,AV}$ (V)	$P_{OUT,AV}$ (V)	η (%)
CV	0.8	-	4.44	3.97	89.4
	1	-	4.42	4.02	90.9
	1.2	-	4.23	3.92	92.5
FOCV1	-	-	4.41	3.97	90.1
FOCV2	0.8	0.6	5.42	4.85	89.6
	1	0.7	5.54	5.07	91.5
	1.2	0.8	5.09	4.71	92.5

V. Conclusions

Three MPPT techniques have been tested on a linear shaker for maximizing the harvested energy of a KEH system embedded into an ocean drifter. Results show that harvested energy improves up to 25% by providing an V_{MPP} signal that nearly matches half the open circuit voltage of the KEH device. The generation of this signal was implemented using specific instrumentation and tuning the V_{MPP} signal. Future work will address the generation of this signal in a simpler and more automatic way.

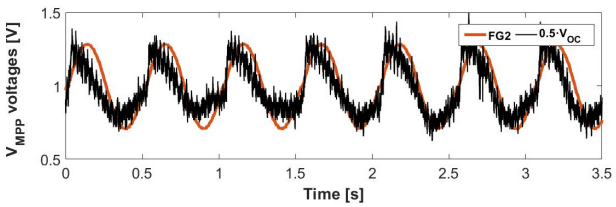

Fig. 5. Signals $0.5V_{OC}$ (black) and V_{MPP} provided by FG2 of 1 V offset and 0.7 V amplitude (orange).

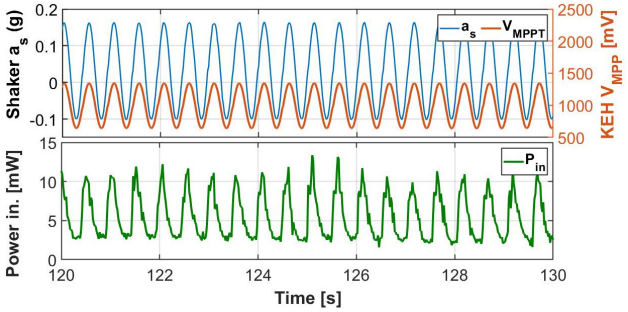

Fig. 4. FOCV2 test results with FG1 set to 1 V and 2 Hz and FG2 set to 1 V offset and 0.7 V amplitude. Above, a_s (left – blue) and V_{MPP} signal (right – orange); below, PMU input power P_{IN} (green).

REFERENCES

[1] R. Lumpkin, T. Özgökmen, and L. Centurioni, "Advances in the Application of Surface Drifters," *Ann. Rev. Mar. Sci.*, vol. 9, no. 1, pp. 59–81, 2017.

[2] P. M. Poulain, R. Gerin, E. Mauri, and R. Pennel, "Wind effects on drogued and undrogued drifters in the eastern Mediterranean," *J. Atmos. Ocean. Technol.*, vol. 26, no. 6, pp. 1144–1156, 2009.

[3] W. Ding, B. Song, Z. Mao, and K. Wang, "Experimental investigation on an ocean kinetic energy harvester for underwater gliders," in *IEEE Energ. Conv. Congr. and Expos. - Montreal*, 2015, pp. 1035–1038.

[4] Y. Li *et al.*, "Study of an Electromagnetic Ocean Wave Energy Harvester Driven by an Efficient Swing Body Toward the Self-Powered Ocean Buoy Application," *IEEE Access*, vol. 7, pp. 129758–129769, 2019.

[5] M. Carandell, D. M. Toma, M. Carbonell, J. del Río, and M. Gasulla, "Design and Testing of a Kinetic Energy Harvester Embedded into an Oceanic Drifter," *IEEE Sens. J.*, 2020.

[6] M. Carandell, D. M. Toma, M. Gasulla, and J. del Río, "Evaluation of two MPPT techniques in Low-Power Pendulum-Type Wave Energy Converters," in *9th Int. Works.on Marine Tech. - Vigo*, 2021, p. "in press."

[7] M. E. El-Hawary, "Principles of Electric Machines with Power Electronic Applications," in *IEEE Power Engineering Society*, 2n ed., 2002, pp. 185-187. Chap. 4.3.

[8] M. Carandell, D. M. Toma, M. Carbonell, M. Gasulla, and J. del Río, "Design and development of a kinetic energy harvester device for oceanic drifter applications," in *Instr. and Measur.Techn. Conf. - Auckland*, 2019, pp. 1718–1723.

[9] J. Kokert, T. Beckedahl, and L. M. Reindl, "Medlay: A reconfigurable micro-power management to investigate self-powered systems," *Sensors*, vol. 18, no. 1, p. 259, 2018.

[10] N. Femia, G. Petrone, G. Spagnuolo, and M. Vitelli, "Optimization of perturb and observe maximum power point tracking method," *IEEE Trans. Power Electron.*, vol. 20, no. 4, pp. 963–973, 2005.

[11] O. López-Lapeña, M. T. Penella, and M. Gasulla, "A new MPPT method for low-power solar energy harvesting," *IEEE Trans. Ind. Electron.*, vol. 57, no. 9, pp. 3129–3138, 2010.

[12] D. Dondi, A. Bertacchini, D. Brunelli, L. Larcher, and L. Benini, "Modeling and optimization of a solar energy harvester system for self-powered wireless sensor networks," *IEEE Trans. Ind. Electron.*, vol. 55, no. 7, pp. 2759–2766, 2008.

[13] M. T. Penella and M. Gasulla, "A simple and efficient MPPT method for low-power PV cells," *Int. J. Photoenergy*, vol. 2014, Article ID 153428, 7 pages, 2014.

A.4 Article 4

P.[130] - Real-time Wave Monitoring on Coastal Areas Using LPWAN-Based Embedded Systems

---

Conference: IEEE International Instrumentation and Measurement Technology Conference – 2021 Glasgow

Publisher: IEEE

Date of Publication: 28 June 2021

DOI: 10.1109/I2MTC50364.2021.9459805

Real-time Wave Monitoring on Coastal Areas Using LPWAN-Based Embedded Systems

Matias Carandell[1*]
SARTI Group,
Electronic Engineering Department
Universitat Politècnica de Catalunya
Vilanova i la Geltrú, Spain
matias.carandell@upc.edu

Daniel Mihai Toma[1]
SARTI Group,
Electronic Engineering Department
Universitat Politècnica de Catalunya
Vilanova i la Geltrú, Spain
daniel.mihai.toma@upc.edu

Carola Artero
SARTI Group,
Electronic Engineering Department
Universitat Politècnica de Catalunya
Vilanova i la Geltrú, Spain
carola.artero@upc.edu

Manel Gasulla
e-CAT Group,
Electronic Engineering Department
Universitat Politècnica de Catalunya
Castelldefels, Spain
manel.gasulla@upc.edu

Joaquín del Río
SARTI Group,
Electronic Engineering Department
Universitat Politècnica de Catalunya
Vilanova i la Geltrú, Spain
joaquin.del.rio@upc.edu

2021 IEEE International Instrumentation and Measurement Technology Conference (I2MTC) | 978-1-7281-9539-1/21/$31.00 ©2021 IEEE | DOI: 10.1109/I2MTC50364.2021.9459805

Abstract— A new embedded system is presented for real-time wave monitoring on coastal areas using SigFox communication. SigFox is a Low-Power Wide-Area Network technology that has been rarely used in coastal marine monitoring. The system is based on the low-power TD1205P module that includes a microcontroller, an accelerometer, a GNSS receiver and a SigFox transceiver. Each hour, the module estimates the wave's maximum height (H_{max}) and mean period (T_z), determines the GPS position, and wirelessly transmits the data through the SigFox network. The procedure for wave parameter estimation is based on the zero-upcrossing method using the vertical acceleration data. It was experimentally validated by attaching the embedded system to a moored buoy and comparing H_{max} and T_z with that provided by a seafloor acoustic wave and current profiler, used as a reference. Results over a period of two months show a good match for H_{max} but less for T_z, which cross-correlation values at zero lag of about 0.85 and 0.5, respectively. Power tests of the embedded system were also performed resulting in a lifetime estimation of 420 days with a battery pack of 3 Ah.

Keywords— *Marine monitoring, Wave Height, Wave Period, Low-Power Wide-Area Network (LPWAN), SigFox, Offshore data transmission, Acoustic Wave And Current profiler (AWAC)*

I. INTRODUCTION

Oceans are a key indicator of earth's health. Small changes in the seawater can have a strong effect on the weather but also on many species' behavior. Thus, oceanographic monitoring becomes essential in terms of understanding biological and meteorological changes. In addition, in-situ measurements provide valuable data which can also be used, among others, to calibrate satellite ocean observation systems [1] or wave forecast models.

Acoustic Wave And Current profilers (AWAC) are in-situ marine instruments commonly used in shallow waters and placed at the sea bottom to measure waves and sea currents profiles, collecting data from waves such as their height, period and direction. Underwater deployments, though, are usually associated with high-costs. Furthermore, to monitor real-time data from an AWAC, a moored buoy with wireless communication or an underwater link [2] are also required, which further increases the costs. Coastal waves can also be measured with HF radar systems [3]. Nevertheless, this infrastructure also implies high costs and cannot be deployed in all coastal areas.

Small moored and free-drifting buoys equipped with embedded Inertial Measurements Units (IMU) also estimate wave parameters. These small-size solutions require lower energy than previous ones, so they can achieve long term power autonomy with primary batteries or even use solar panels to achieve "perpetual" power. In [4], a surface buoy for wave and current studies was presented, where Iridium satellite communication was used. A similar system was presented in [5], where several small-size buoys powered with PV cells were moored in coastal areas. Even so, in these solutions, the satellite communication module is the most energy consuming part and significantly increases the budget both for the module initial cost and for that related with the data transmission (paid service).

Nowadays, Low-Power Wide Area Networks (LPWAN) are starting to be used in coastal marine monitoring because they provide small data transmission packages with relatively low power and costs. Among them, LoRa and SigFox excel [6]. In [7], LoRa communication was used to transmit temperature and humidity from an Indonesian island and in [8] the authors showed data transmission over the sea at distances up to 28 km by placing expensive antennas between 50 and 100 meters above the sea level. In [9], LoRa was proposed in coastal drifting buoys equipped with an embedded system to acquire the wave parameters. However, this system has not been fully implemented yet. On the other hand, SigFox provides longer communication ranges than LoRa [6], becoming more suitable for marine offshore applications. And although the payload of SigFox messages is smaller than in LoRa, so that just small amounts of data can be transmitted, this is enough for remote marine wave monitoring. But just few works can be found using SigFox, as the one presented in [10], which aimed to track endangered salmons on Sweden river zones.

In this paper, we designed and tested a low-cost and low-power embedded system to estimate in real time some wave

This work was supported by the Spanish Ministry of Economy and Competitiveness and the European Regional Development Fund under project TEC2016-76991-P and by the project MELOA from the European Commission's Horizon 2020 research and Innovation program under Grant Agreement No. 776280. The first author has a grant from the Secretariat of Universities and Research of the Ministry of Business and Knowledge of the Government of Catalonia on the FI program (ref. BDNS 362582).

[1] These authors contributed equally to this work.
* Corresponding author.

978-1-7281-9539-1/21/$31.00 ©2021 IEEE

parameters at coastal areas using SigFox LPWAN technology. It is a smaller and more compact solution than the ones proposed in [9] and [10] and is less energy consuming than [4] and [5]. The paper is organized as follows. First, the estimation of the selected wave parameters is described in Section II. Section III describes the materials and method used to evaluate the proposed system, and the results are summarized and discussed in section IV. Finally, Section V concludes the work.

II. Estimation of the Wave Parameters

Wave parameters can be estimated by evaluating the time series of the sea surface elevation (D_z) from a single point. The zero-upcrossing technique [11] uses the Still Water Level (SWL) reference from the time series data to obtain the height (H) and period (T) of each wave, as represented in Fig. 1. The SWL is the sea surface level in the absence of wind and waves. Then, multiple common parameters can be obtained such as the significant wave height (H_3), which is the mean height of the third highest waves in the record, and the significant wave period (T_3), which is the corresponding mean period. The maximum wave height (H_{max}) is the largest measured wave in the record and the mean zero-upcrossing wave period (T_z) is obtained by

$$T_z = \frac{T_r}{N_z} \tag{1}$$

where T_r is the time length of the record and N_z is the number of zero-upcrossings in that record, considering the SWL as the zero level ($D_z = 0$).

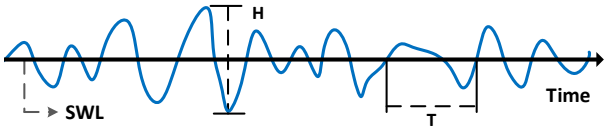

Fig. 1. Time series of the sea surface elevation (Dz), where the Still Water Level (SWL) is used in the zero-upcrossing method to obtain the wave height (H) and period (T).

In [12], we presented a drifting buoy prototype with a measuring system that included an IMU. The buoy was deployed on a Wave-Flume and the IMU raw data was recorded and later processed off-line with a MATLAB algorithm to obtain the wave parameters with the zero-upcrossing technique. There, D_z was obtained from the vertical acceleration (a_z), which is the normal procedure with floating buoys [13]. However, unlike in [12], an IMU is not available in the embedded system used in this paper (to be described in Section III) but just a 3-axis accelerometer, so the gyroscope data cannot be used to correct the potential tilt of a_z. This simplification was also used in [13] and proved to be accurate enough. Furthermore, due to memory and processing constraints, only H_{max} and T_z are provided here. Fig. 2 shows the steps followed to estimate them for each record.

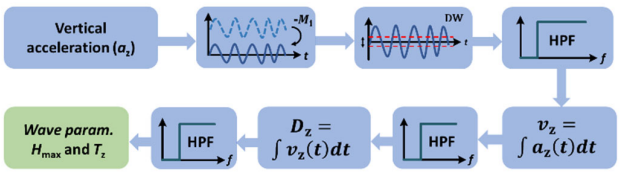

Fig. 2. Steps for the estimation of the wave parameters H_{max} and T_z.

First, the gravity effect is removed from a_z by subtracting its mean value, incrementally calculated as

$$M[i] = \frac{(i-1)M[i-1] + a_z[i]}{i} \tag{2}$$

Second, a discrimination window (DW), consisting on assigning a zero value to values of $a_z \leq 5$mg, smooths out accelerometer's errors due to vibration and mechanical noise during flat sea states. Third, a digital first-order high-pass filter (HPF) removes the slow motion of the infra-gravity waves (e.g. larger than 30 s), resulting in the wave orbital acceleration. The implementation of the HPF in discrete-time is given by

$$y[i] = \alpha \cdot (y[i-1] + x[i] - x[i-1]) \tag{3}$$

where $x[i]$ and $y[i]$ are the data set of samples before and after the HPF, respectively, i is the number of the current sample and α is given by

$$\alpha = \frac{1}{1 + 2\pi f_c T_s} \tag{4}$$

where T_s is the sampling period of the accelerometer data and f_c is the cut-off frequency of the HPF. Fourth, the vertical velocity v_z is obtained performing a numerical time integration given by [14]

$$v_z[i] = v_z[i-1] + \frac{a[i-1] + a[i]}{2} T_s \tag{5}$$

with the first value forced to zero. Again, (3) is used to filter v_z and D_z is obtained by integrating the velocity using

$$D_z[i] = D_z[i-1] + \frac{v_z[i-1] + v_z[i]}{2} T_s \tag{6}$$

with the first value forced to zero. Then, (3) is subsequently applied. Overall, applying three concatenated HPF better removes the slow motion of infra-gravity waves.

Finally, T_z is obtained using (1) and H_{max} is determined from the difference of the maximum and the minimum values of D_z for each time interval T_r.

III. Materials and Method

A TD1205P tracker module (TDnext) was used to obtain H_{max} and T_z and wirelessly transmit the data. It was selected because of its low power consumption and reduced size (30×38×10.5 mm). Fig. 3 shows a block diagram of the module, which includes an EFM32G (32-bit ARM Cortex-M3-based) microcontroller unit (MCU), an ultra-low power 3D Accelerometer, a Hall-Effect sensor (not used here), a GNSS receiver, and a SigFox communication transceiver. A range of ± 8 g for the accelerometer and an output transmission power of +16 dBm for the SigFox transceiver were selected. The SigFox transceiver allows to send up to 140 messages of 12 bytes per day.

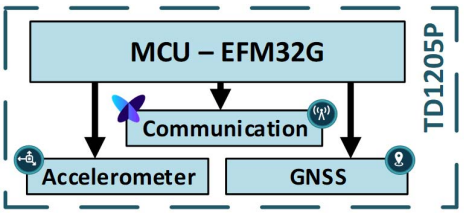

Fig. 3.TD1205P block diagram including the MCU, the accelerometer, and the communication and GNSS modules.

The TD1205P module was programed to wake up every hour. After wake-up, the execution routine is divided in five

stages: 1) acquires 5 min (T_r = 300 s) of a_z at 5 Sa/s (T_s = 200 ms), resulting in 1500 data samples; 2) calculates H_{max} and T_z using the algorithm described in Section II with f_c = 1/15 Hz in order to remove the infra-gravity waves; 3) determines the GPS position with an acquisition time that depends on the current ephemeris and is limited to 60 s to avoid excessive power consumption; 4) sends the data through the SigFox network in a 12 bytes message that includes H_{max}, T_z, an internal temperature, the battery voltage, and the GPS latitude and longitude; and 5) returns to sleep mode. Fig. 4 shows the structure of the hexadecimal coded message. Latitude and Longitude bytes are 0 whenever the GPS position cannot be fixed.

Fig. 4. 12 bytes SigFox message. From left to right, GPS Latitude (4 bytes) and Longitude (4 bytes), battery voltage (1 byte), internal temperature (1 byte), H_{max} (1 byte), and T_z (1 byte).

The TD1205P module was encapsulated within an IP64 case (83×35×57 mm) that also included two 3V batteries (CR123A, GP Batteries) connected in parallel through two Schottky diodes (PMEG1020EA), as shown in Fig. 5. The batteries powered the TD1205P module providing an overall capacity of around 3 Ah at a nominal voltage of 3 V.

Fig. 5. TD1205P module encapsulated with two CR123A 3V batteries within an IP64 case (83×35×57 mm).

A power consumption test that included the five steps following a wake-up was performed to estimate the lifespan of the TD1205P module. The EFM32TG (Energy Micro) Starter Kit was used for this purpose. This kit contains an energy monitoring interface that allows the measurement of current and voltage. Current range is from 0.1 µA to 50 mA with accuracies of 1 µA and 100 µA for values lower and higher than 200 µA, respectively. Resolution in the sub 200 µA range is 100 nA. Results are shown in Section IV.A.

The algorithm for the estimation of the wave parameters was preliminary debugged using the OrcaFlex simulator (Orcina). In [12] we describe how we modeled a drifting buoy and the sea environmental parameters using this tool. Then, the algorithm was validated on a real sea test by comparing the TD1205P results (H_{max} and T_z) with that provided by a seafloor AWAC (1 MHz – Nortek) used as a reference, which presents an accuracy of 1 % on the wave height estimation. To do so, the encapsulated system of Fig. 5 was attached to the upper part of a moored buoy placed at 4 km off the coast of the city of Vilanova i la Geltrú [15]. This buoy is above a 20 meters depth underwater cabled observatory (OBSEA) to which the AWAC is connected. The configuration and work principle of this sensor is described in [2]. Mainly, it acquires 10 minutes of wave data each hour, calculates the wave parameters and transmits the data through the OBSEA network. Both, the encapsulated TD1205P module and the AWAC, were deployed during the summer of 2020. Data H_{max} and T_z were acquired during several weeks between the months of July and October and later compared. Results are shown in Section IV.B.

IV. Experimental Results

A. Power consumption

Fig. 6 shows the supply voltage and current profile of the TD1205P module acquired every 10 ms. Voltage is 3.3 V and a logarithmic scale is used for current to account for the large dynamic range. Stages 1 to 5 occur sequentially, with stage 5 also taking place between stages 2 and 3. TABLE I summarizes the average value of the measured current for each stage as well as the associated time durations and electrical charges. As can be seen, the main two contributors are stages 3 (GPS) and 4 (SigFox data transfer) whereas the charge wasted in the rest of stages is negligible. For stage 3 an average time of 30 s, after several tests in near-real conditions, has been considered. With these conditions, the batteries will last about 420 days, assuming their full capacity of 3 Ah.

A significant battery lifetime increase could be achieved by decreasing the duration of stage 3, e.g. by shifting the estimation of the GPS position from the device to a database. This is a paid service offered by some companies [16] but it cannot be implemented in the SigFox modules of TDnext, such as the TD1205P. Another option would be to save the current ephemeris during the sleep mode. As reported in [17], stage 3 can be reduced down to about 4 seconds at the cost of increasing the current consumption of stage 5 up to 16 µA. However, ephemeris is valid for only 4 hours, hence it must be updated regularly (average time duration of 30 s, TABLE I). Overall, the battery lifetime would be just nearly doubled. Nevertheless, more experimental tests about this issue should be carried out.

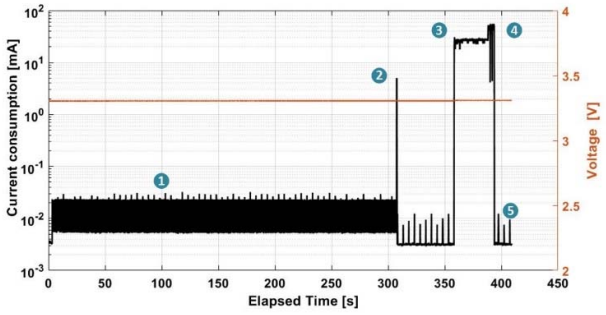

Fig. 6. Supply voltage and current profile of the TD1205P module.

TABLE I. Supply average currents and associated times and charges of the TD1205P module.

Ref	Current (A)	Time (s)	Charge (C)
1	14 u	300	4.2 m
2	3.7 m	0.5	1.85 m
3	26.4 m	30	792 m
4	46.5 m	5.5	256 m
5	3 u	3264	10 m
1-5	0.29 m (average)	3600	1.07

B. *Wave monitoring*

Fig. 7 and Fig. 8 show the time series values of H_{max} and T_z during the sea test. As can be seen, H_{max} and T_z exceed 4 m and 10 s, respectively, in some specific episodes. On the other hand, there are missing data from the AWAC at the beginning of the time series due to a later deployment than the TD1205P module and afterwards (mainly during September) due to communication failures. In the overlapped intervals, the data of both sensors mainly match, in particular that of H_{max}. More quantitatively, the mean of H_{max} and T_z are 0.87 m and 3.34 s, respectively, for the TD1205P, and 0.82 m and 3.20 s for the AWAC, thus showing a good agreement.

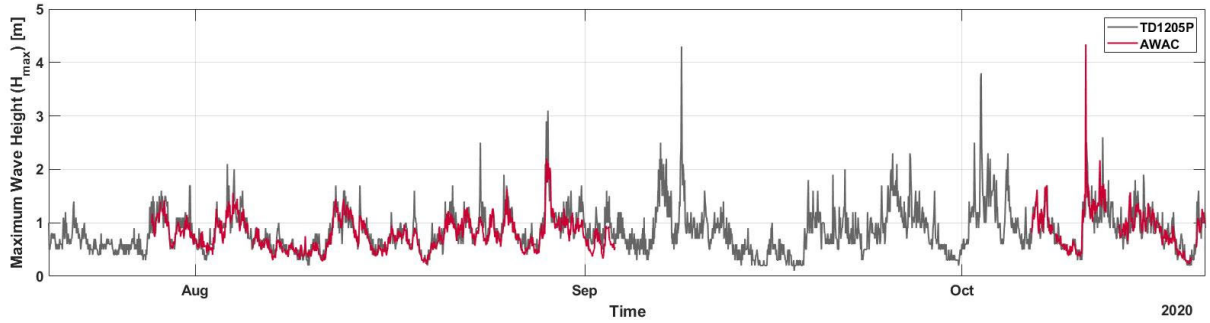

Fig. 7. Experimental values of H_{max} acquired each hour with the TD1205P module (grey) and with the AWAC (red) for 3 months, starting at July 20, 2020. Note some missing data from AWAC measurements due to a communication failure.

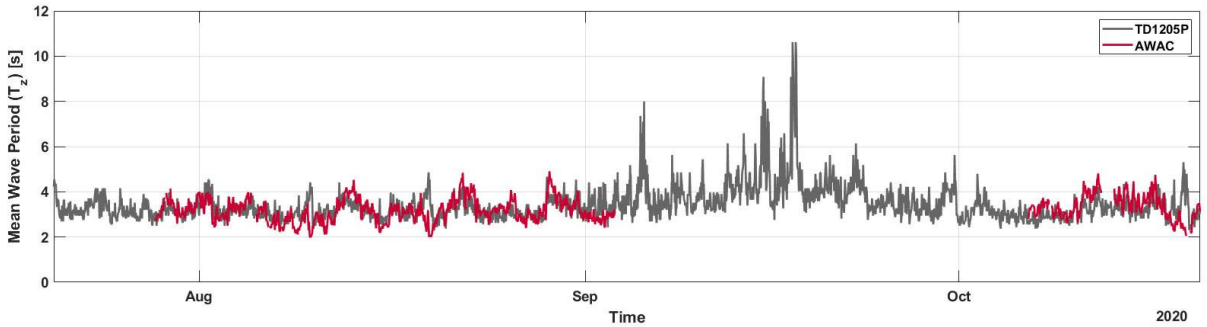

Fig. 8. Experimental values of T_z acquired each hour with the TD1205P module (grey) and with the AWAC (red) for 3 months, starting at July 20, 2020. Note some missing data from AWAC measurements due to communication failures.

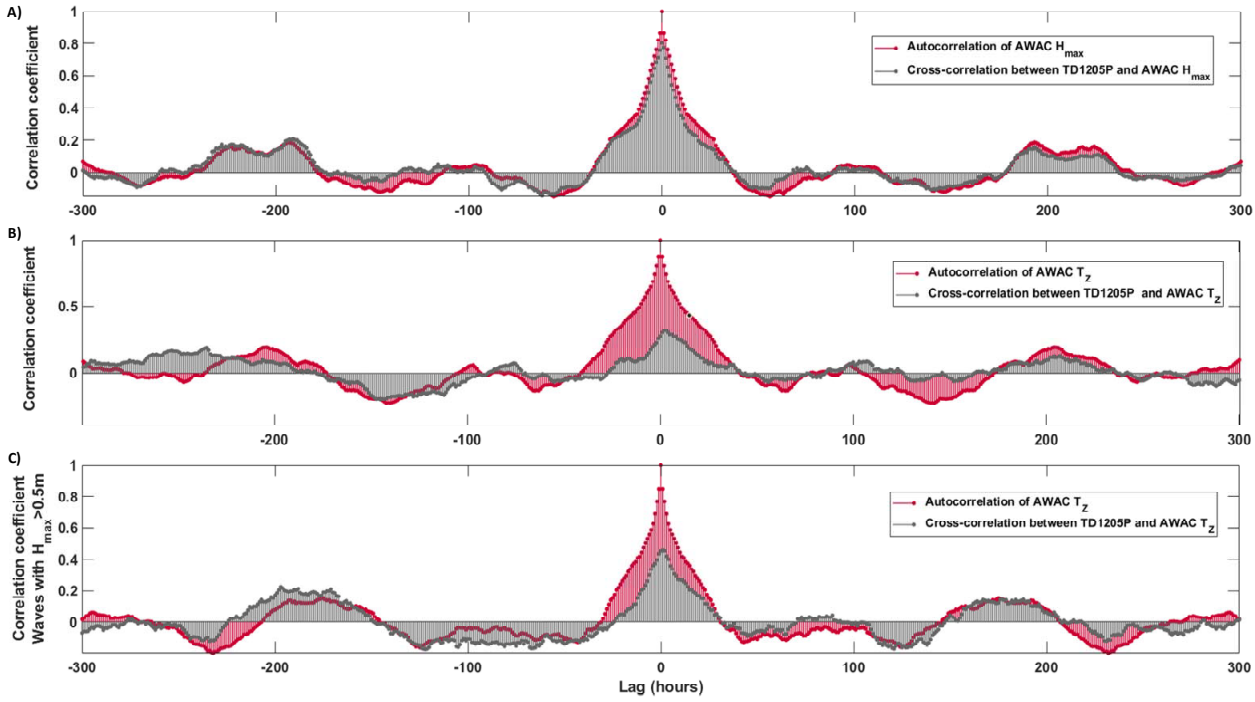

Fig. 9. Correlation analysis for A) H_{max}, B) T_z, and C) T_z when $H_{max} > 0.5$m. In all plots, Auto-correlation is performed using the AWAC temporal series as a reference (in red) and Cross-correlation using the AWAC and TD1205P temporal series (in grey).

Further statistical methods are next presented to better assess the matching between the parameters of the TD1205P and the AWAC. In particular, this analysis was performed using the MATLAB cross-correlation function from the Econometrics Toolbox [18]. Only the data of the overlapped intervals in Fig. 7 and Fig. 8 were used.

Fig. 9-A shows the correlation analysis of H_{max} with lags up to ±300 h, where the sample auto-correlation of the AWAC time series is shown in red and the sample cross-correlation between the AWAC and TD1205P time series in grey. Comparing the auto-correlation of a reference signal (AWAC) with the cross-correlation of this reference with another target signal (TD1205P) for different lags is useful for gaining insight in their similarity and where the best match occurs [19]. As can be seen, both sample correlations present a high overall resemblance, with a maximum cross-correlation value at zero lag (∼0.85), which also indicates the synchronization of both time series [20]. Thus, the estimation procedure of H_{max} with the TD1205P is feasible.

Fig. 9-B shows the correlation analysis of T_z. Similarity between the sample correlations is lower here. Still, both time series are synchronized because the maximum cross-correlation value is at zero lag, though below 0.4. At Fig. 9-C, only T_z values corresponding to $H_{max} > 0.5$ m measured with the AWAC were considered. As can be seen, the cross-correlation value at zero lag increases to ∼0.5, stating that the TD1205P estimates better T_z when sea is rough. Further research is required to state the reason for this behavior.

V. Conclusions

A new embedded system has been designed and tested to estimate the wave's maximum height (H_{max}) and mean period (T_z) and transmit them wirelessly using the LPWAN SigFox network. The system, based on a TD1205P module, obtains the sea surface displacement from the embedded accelerometer and calculates H_{max} and T_z through the zero-upcrossing method.

The wave estimation method has been validated by attaching the embedded system to a moored buoy placed above an acoustic wave and current profiler, used as a reference. Both systems have provided H_{max} and T_z each hour during a period of three months. The mean values of H_{max} and T_z have been 0.87 m and 3.34 s, respectively, for the TD1205P, and 0.82 m and 3.20 s for the AWAC, thus showing a good agreement. A cross-correlation analysis has also been performed, resulting in a high cross-correlation value at zero lag of 0.85 for H_{max}. However, a lower value (< 0.4) is obtained for T_z. Considering only T_z values corresponding to $H_{max} > 0.5$ m, the cross-correlation value has increased to ∼0.5. Further research is required on this issue.

The power consumption of the TD1205P has also been measured, being the GPS location stage the most energy demanding. Using a 3 Ah battery, a lifetime autonomy of 420 days is predicted. A couple of techniques to reduce the consumption of the GPS location stage have been presented to be further explored.

Acknowledgment

The authors extend their thanks to Orcina for their kind support and offer of the academic license OrcaFlex N2703 (2021) to Universitat Politècnica de Catalunya.

References

[1] R. Scharroo *et al.*, "Jason continuity of services: continuing the Jason altimeter data records as Copernicus Sentinel-6," *Ocean Sci.*, vol. 12, no. 2, pp. 471–479, 2016.

[2] M. Carandell and M. Nogueras, "Data comparison between three acoustic doppler current profilers deployed in OBSEA platform in north-western Mediterranean," *Instrum. Viewp.*, no. 19, pp. 87–89, 2016.

[3] J. B. D. Jaffrés and M. L. Heron, "Wave climate in the Southern Great Barrier Reef, Australia - Evaluation of an ocean HF radar system and WaveWatch3," in *OCEANS - Kona Hawaii*, 2011, pp. 144–149.

[4] P. V. Guimarães *et al.*, "A surface kinematics buoy (SKIB) for wave-current interaction studies," *Ocean Sci.*, vol. 14, no. 6, pp. 1449–1460, 2018.

[5] K. Raghukumar, G. Chang, F. Spada, C. Jones, T. Janssen, and A. Gans, "Performance Characteristics of 'Spotter', a Newly Developed Real-Time Wave Measurement Buoy," *J. Atmos. Ocean. Technol.*, vol. 36, no. 6, pp. 1127–1141, 2019.

[6] K. Mekki, E. Bajic, F. Chaxel, and F. Meyer, "Overview of Cellular LPWAN Technologies for IoT Deployment: Sigfox, LoRaWAN, and NB-IoT," *PerIoT'18 - Second IEEE Int. Work. Mob. Pervasive Internet Things*, pp. 413–418, 2018.

[7] N. A. Azmi Ali and N. A. Abdul Latiff, "Environmental Monitoring System Based on LoRa Technology in Island," in *IEEE International Conference on Signals and Systems - Bandung*, 2019, pp. 160–166.

[8] N. Jovalekic, V. Drndarevic, E. Pietrosemoli, I. Darby, and M. Zennaro, "Experimental study of LoRa transmission over seawater," *Sensors*, vol. 18, no. 9, 2018.

[9] I. B. Shirokov, A. S. Mironov, and A. N. Grekov, "Ocean Surface State Monitoring with Drifters Array," in *Zooming Innovation in Consumer Technologies Conference - Novi Sad*, 2020, pp. 113–117.

[10] M. Blinge, "Construction of an IoT-device transmitting data of the endan- gered Atlantic salmon via Sigfox-LPWAN," *Master's Thesis. Chalmers University of Technology*. 2019.

[11] Z. Demerbilek, "Water Wave Mechanics," in *Coastal Engineering Manual*, vol. Part II, 2008.

[12] M. Carandell, D. M. Toma, J. P. Pinto, M. Gasulla, and J. del Río, "Impact on the Wave Parameters Estimation of a Kinetic Energy Harvester Embedded into a Drifter," in *OCEANS - Singapur and U.S. Gulf Coast*, 2020.

[13] E. D. Skinner, M. M. Rooney, and M. K. Hinders, "Low-cost wave characterization modules for oil spill response," *J. Ocean Eng. Sci.*, vol. 3, pp. 96–108, 2018.

[14] K. Seifert and O. Camacho, "Implementing positioning algorithms using accelerometers," *App. Note, Free. Semicond. -NXP*, pp. 1–13, 2007.

[15] E. Molino *et al.*, "Oceanographic Buoy Expands OBSEA Capabilities," *Instrum. Viewp.* -, vol. 11, pp. 14–15, 2011.

[16] Ubiscale, "UbiGNSS: low-power geolocation." [Online]. Available: https://ubiscale.com/.

[17] M. Carandell, D. Mihai, J. del Río, K. Ganchev, and J. Peudennier, "Evaluation of Sigfox LPWAN technology for autonomous sensors in coastal applications," *Instrum. Viewp.*, vol. 20, pp. 36–37, 2018.

[18] MATLAB, "Cross-correlation function." [Online]. Available: https://es.mathworks.com/help/econ/crosscorr.html.

[19] B. Croke, P. Cornish, and A. Islam, "Modeling the Impact of Watershed Development on Water Resources in India," in *Integrated Assessment of Scale Impacts of Watershed Intervention: Assessing Hydrogeological and Bio-Physical Influences on Livelihoods*, Elsevier Inc., 2015, pp. 99–148.

[20] J. Cryer and K. Chan, *Time series analysis: with applications in R*, vol. 2. 2008.

A.5 Article 5

P.[58] - Experimental Validation of a Kinetic Energy Harvester Device for Oceanic Drifter Applications

---

Conference: IEEE OES/MTS Oceans – 2019 Marseille
Publisher: IEEE
Date of Publication: 14 October 2019
DOI: 10.1109/OCEANSE.2019.8867143

Experimental Validation of a Kinetic Energy Harvester Device for Oceanic Drifter Applications

Matias Carandell
Sarti Research Group.
Electronics Engineering Dep.
Universitat Politècnica de Catalunya
Vilanova i la Geltrú, Spain
matias.carandell@upc.edu

Daniel Mihai Toma
Sarti Research Group.
Electronics Engineering Dep.
Universitat Politècnica de Catalunya
Vilanova i la Geltrú, Spain
daniel.mihai.toma@upc.edu

Manel Gasulla
e-CAT Group.
Electronics Engineering Dep.
Universitat Politècnica de Catalunya
Castelldefels, Spain
manel.gasulla@upc.edu

Joaquín del Río
Sarti Research Group.
Electronics Engineering Dep.
Universitat Politècnica de Catalunya
Vilanova i la Geltrú, Spain
jaquin.del.rio@upc.edu

***Abstract*— A Kinetic Energy Harvester (KEH) device under design for drifter applications has been tested at real sea conditions in a controlled area. The KEH consists on a pendulum system capable to transform the oscillations of the waves into rotation which will be converted into electrical energy thanks to a dc micro generator. The KEH has been placed inside a drifter. First, the motion of the drifter was obtained through an embedded Inertial Measurement Unit, showing natural pendulum frequency of 1.5 Hz. Simulations with OrcaFlex validate the experimental results. Then, the rotation speed of the micro generator was measured. Results show a prevalence of speed of 1400 rpm, which should lead to a potential power output of 2 mW.**

Keywords*— *Lagrangian Drifter, Kinetic Energy Harvester (KEH), Micro generator, Natural Frequency, Power Management Unit (PMU), Maximum Power Point Tracking (MPPT).

I. INTRODUCTION

Oceans are a key indicator on earth's health. Small changes on the seawater can strongly affect the weather, but also on many species' behaviors. Oceanographic monitoring becomes crucial in terms of understanding biological and meteorological changes. Many different sensor platforms fulfill this monitoring function. Seafloor cabled observatories, for example, can provide a huge volume of data from a specific underwater position with no power restrictions, while underwater gliders, as another example, cover large portions of the ocean providing smaller data products with some power constrains.

Lagrangian drifters are a low-cost easy-to-deploy solutions for sea monitoring. These are versatile and easy to maintain units that monitor the ocean while passively following the surface currents. Nevertheless, drifters do not offer a high volume of data compared to other platforms and power restrictions are higher. Applications where these platforms are used are diverse; climate research, oil spill tracking, weather forecasting and search and rescue operation. Lately, drifters have found a useful field of work, helping to calibrate HF radar and satellite measuring systems of sea surface parameters.

Autonomy is one of the main challenges at drifter design [1]. Depending on the carried instruments and the duty cycle of the units, its lifespan may vary from hours up to two years when powered from primary batteries. To expand its autonomy, some manufacturers include PV panels around drifters' body, achieving unlimited lifespan at some low transmitting interval and propitious solar conditions [2]–[5]. Nevertheless, if the drifter is strictly dedicated to the current monitoring, the body should be mostly submerged to avoid the wind effect [6] and, thus, the irradiation at the panels is attenuated. Also, many oceanic regions may provide really low solar irradiation at some year periods. For this reason, other Energy Harvester (EH) sources may be explored as the kinetic oscillatory movement of the waves.

Previous works have shown different harvesting possibilities from a kinetic ocean source [7]–[9]. Inertial based harvesters are one of the main solutions for non-anchored oceanic devices [10]–[13]. These systems relay on a proof mass whose relative movement is caused by the waves and drive a generator. The cleverness of these systems relay on achieving the resonant frequency of the Kinetic Energy Harvesting (KEH) near to the motion frequency of the drifter [14], to maximize the power extraction.

Figure 1. MELOA coastal WAVY drifter design for sea monitoring.

Scientific community has started to pay attention to the drifter development that includes alternative EH generation. The MELOA project [15] is an example of that. This is a European project that aims to develop a new family of WAVY drifters for marine monitoring which are low-cost, easily deployable, high

This work was supported by the project MELOA from the European Commission's Horizon 2020 research and Innovation program under Grant Agreement No. 776280. The first author has a grant from the Secretariat of Universities and Research of the Ministry of Business and Knowledge of the Government of Catalonia on the FI program (ref. BDNS 362582).

978-1-7281-1450-7/19/$31.00 ©2019 IEEE

versatility, and low maintenance systems. The WAVY family of products will include from coastal drifters for short deployments (Figure 1), to oceanic drifters with EH solutions for long term deployments.

This paper follows the work done at [16], where a first design of a kinetic energy harvesting to be placed on the oceanic MELOA drifter was presented. Also, a preliminary characterization of the micro generator and the Power Management Unit (PMU) was shown followed by the first results of the prototype when placed on a water tank.

Work presented in this paper is focused on characterizing the operation of an improved KEH when placed on a drifter under real sea conditions in a controlled area. The drifter has been designed with the same dimensions of the WAVY Ocean drifter of MELOA's project. In addition, the dynamic behavior of the drifter has been assessed with an Inertial Measurement Unit (IMU). Results have been validated with OrcaFlex simulation Software. Finally, the KEH power possibilities have been further analyzed.

The paper is organized as follows. First, the proposed KEH is presented at section II. Then, the materials and method are described in section III. At section IV, the results of the drifter motion and KEH behavior under real sea conditions are shown. Finally, conclusions are summarized at section V.

II. Proposed Kinetic Energy Harvester Device

Harvesting the energy from the waves at non-anchored autonomous devices is usually done by inertial systems, which can be classified in gyroscopic and pendulum [17]. These systems relay on a proof mass which moves in relation to the main body thanks to the excitation of the waves. That relative motion drives a micro generator which converts the energy from mechanical to electrical. The difference between the gyroscopic and the pendulum systems bases basically on the way they capture the external motion. The first ones count on an inertial flywheel which continuously rotates by the external effect. At the second ones, a proof mass can be found outside the device at the end of an arm which pendulates.

The harvested energy depends on the physical characteristics of the devices, achieving higher power levels with higher sizes and weights. Also, this energy is directly proportional to the wave frequency and amplitude [18]. The resonant frequency of the KEH should be tuned to the frequency of motion of its carrier platform to maximize the power extraction.

Recently, we have designed and manufactured a first prototype of an inertial KEH for drifter applications [16]. This is a mixture of the gyroscopic and pendulum systems. It consists of three gyroscopic arms which capture the movement of all directions and excite a proof mass. This mass relatively moves respect the drifter with pendulum motion. Then, through a gear system, rotation is accumulated in a flying wheel which drives the dc micro generator. The gear system also increases the rotation velocity with a positive ratio. Thanks to a one-way gear system, the flying wheel only rotates at one angular direction at which energy is accumulated.

In this work, the device presented in [16] has been slightly modified. The three gyroscopic arms have been replaced by an articulated pendulum arm with a prof mass. Now, the relative motion is caused by the articulated arm that can freely rotate excited by the drifter motion. This drives the flywheel through the one-way gear system. Also, the Power Take Off (PTO) element is the same micro generator. This modification simplifies the device which can now be reduced and its power density increased. A 3D model of the modified design is shown at Figure 2 with the description of the different parts.

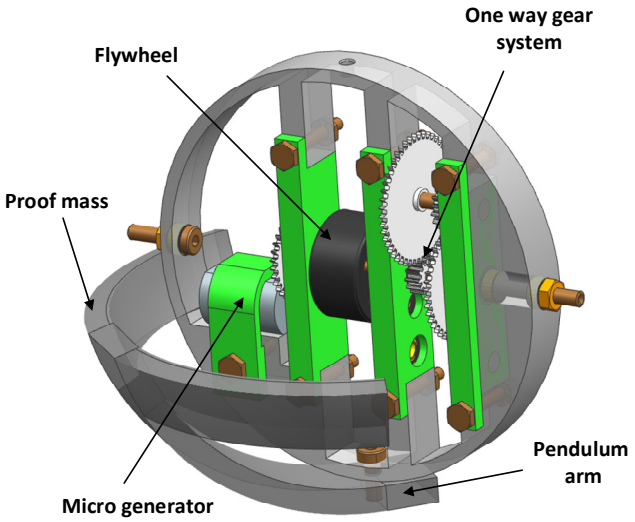

Figure 2. 3D model of the Kinetic Energy Harvesting (KEH) to be placed on a spherical drifter with the description of the different parts.

Figure 3 shows the manufactured prototype. It has a proof mass of 220 g and a total diameter of 10 cm. The main body has been 3D printed with polyamide and the proof mass made with lead. The total gear ratio is 35.

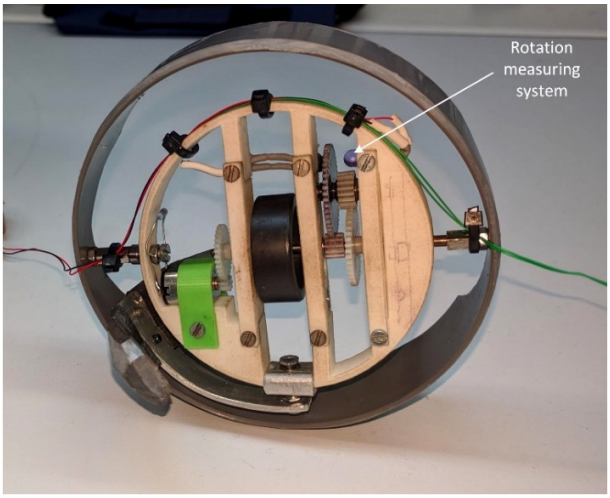

Figure 3. Image of the manufactured KEH prototype.

The dc micro generator has previously been characterized at different rotation speeds [16]. Figure 4 shows the results, where the rotation speed in rpm is defined with no load connected to the generator output (output voltage is V_{oc}). As can be seen, for the three curves, the Maximum Power Point (MPP) is found

around half V_{oc}, which matches with the Thévenin model of the generator [19]. Furthermore, V_{oc} is directly proportional to the rotation speed and the maximum power is proportional to its square. The optimal load corresponding to the MPP is found around 18.5 Ω (R_{LOAD}), which should match with the internal generator load (R_G).

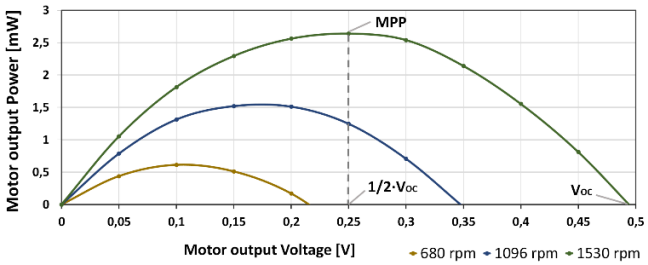

Figure 4. Generator output power against output voltage for different rotation velocities (determined at generator open circuit) [16].

III. Materials and Method

This work is divided in two objectives. On the one hand, study the motion of the drifter body in real sea conditions as well as determine its natural frequency. From this information, the resonant frequency of the KEH could be tuned in future designs to maximize the power extraction. On the other hand, corroborate the correct operation of the KEH under the excitation of wave motion by measuring the continuous rotation of the micro generator. It is important to verify that the KEH optimally converts the waves oscillation into usable rotation. In previous works we tested the device in a water tank [16] that emulates sea conditions, and the present work aims to experimentally validate it in the sea.

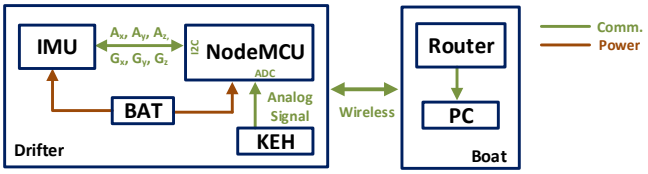

Figure 5. Experimental set up, with the different components placed on the drifter and on the boat, with its communication links.

Figure 5 shows the experimental set up, where the left box represents the drifter and the right box the boat. For this figure, brown has been used as power connections and green as communication links.

A WAVY ocean drifter from MELOA project with the parameters of TABLE I has been used with an Inertial Measurement Unit (IMU) placed on its mass center. This unit has provided the linear acceleration in the three axes (A_x, A_y, A_z) as well as the angular velocities data (G_x, G_y, G_z). Figure 13 presented later on this article shows the axes distribution.

TABLE I. Spherical WAVY ocean drifter parameters

Parameter	*Symbol*	*Value*	*Units*
Drifter mass	m_b	3.472	kg
Drifter radius	R	0.1	m
Center of mass[a]	c_m	0.06	m

[a] Center of mass taken from the bottom of the spherical drifter body.

The KEH has been placed on the geometric center of the drifter, above the IMU sensor. The micro generator has been connected to a constant load of 18.5 Ω, which is the optimum load found on its characterization. That condition would provide a resistive torque to the KEH.

As shown in Figure 3, an infrared emitter has been placed on the main body of the KEH pointing to a diode photoreceptor. Between them, one of the transmitting gears can be found with a hole placed on its circular surface. This gear is solidary to the micro generator so knowing the gear rotation the micro generator speed could be determined. Figure 6 shows the electrical scheme of the pair photo emitter-receiver. An Analog to Digital Converter (ADC) has measured he photodiode open voltage signal.

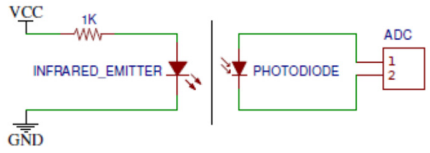

Figure 6. Electrical scheme of the pair photo emitter-receiver.

NodeMCU development board has been selected for its low-power consumption as the main control. It counts on a Wi-Fi communication module and is based on the ESP8266 Microcontroller Unit (MCU) from *Espressif Systems*. Every 10 ms, the MCU takes one package of data from the IMU (MPU-9250) consisting on six parameters (A_x, A_y, A_z, G_x, G_y, G_z). Also, through the 10-bit ADC, takes one sample of the analog input coming from the photoreceptor. Then, the microcontroller calculates the pitch, roll and yaw orientation of the drifter [20], packages all the data and sends it through Wi-Fi connection. Data is received on the boat router where a PC is continuously logging it and plotting in real time.

Finally, to validate the experimental results, a drifter has been simulated in OrcaFlex with the same parameters of TABLE I. Since the experiment has taken place in a controlled area, sea state could have been monitored during the experiment in order to replicate the same wave parameters. An Acoustic Doppler Current Profiler (ADCP) connected to an underwater observatory has provided the real wave height and period [21].

Figure 7 shows the drifter before the deployment at the sea.

Figure 7. Oceanic drifter with the KEH, the measuring electronics and the communication system on it.

IV. RESULTS

The experimental test was done on April 12th 2019 at the surroundings of OBSEA observatory {Lat.: 41.181954º, Long.: 1.752644º} in front of the coast of Vilanova i la Geltrú. As it is a monitored area, wave data could be obtained from the ADCP and it is shown at TABLE II.

TABLE II. Wave parameter during the experiment given by the ADCP.

Parameter	*Mean value*	*Max. Value*	*Units*
Wave height	0.49	0.73	m
Wave period	2.67	*6.47*	s
Wave direction	60	-	º(N)

Results are shown in two sections. Section A presents and analyzes the IMU data as well as the simulation results. At section B the performance of the KEH is discussed.

A. Drifter motion

Accelerometer IMU data has been analyzed. A_x, A_y and A_z linear acceleration obtained at the mass center are plotted at Figure 8, where 1 g is the gravity acceleration.

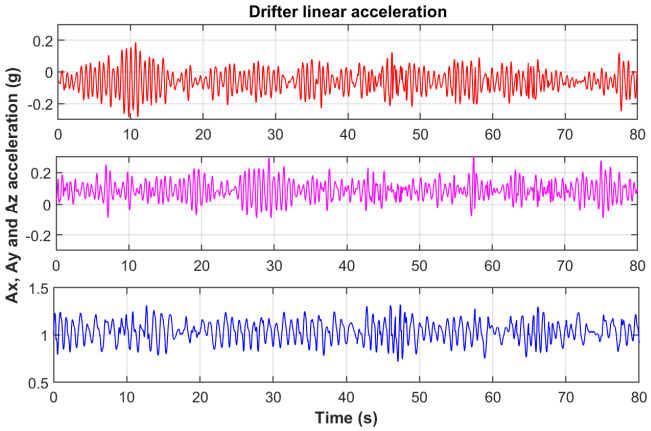

Figure 8. A_x, A_y and A_z linear accelerations from IMU sensor. In this section, red will be used for X axis, pink for Y axis and blue for Z axis.

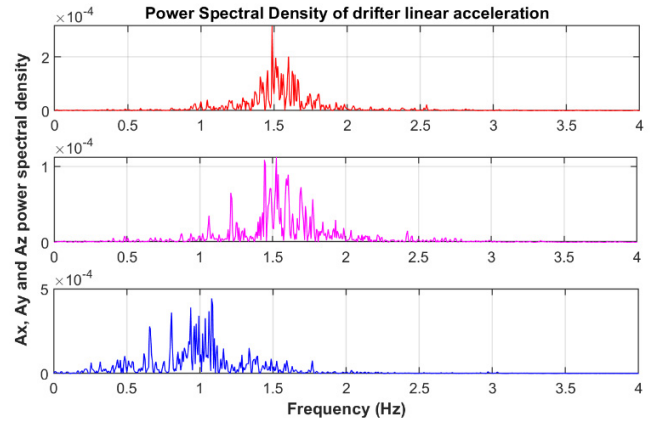

Figure 9. Power Spectrum of A_x, A_y and A_z linear accelerations from IMU sensor.

At the horizontal plane composed by X-Y axes, which are symmetrical, accelerations reach up to 0.2 g. The frequency domain of the signals has also been studied. The Fast Fourier Transform (FFT) has been applied to the whole signal (around 200 seconds) and it is shown at Figure 9. For horizontal axes, the natural frequency is found at 1.5 Hz. This movement represents the pendulum oscillation of the drifter due to the mass center displacement from the geometrical center (TABLE I). This frequency is not the waves frequency, which following ADCP information can be found at 0.4 Hz, but the natural frequency of the drifter when placed into a fluid.

Dynamics are different at the vertical axe, where acceleration moves between ± 0.2 g with an offset of 1 g due to gravity alignment. Its main frequency can be found at around 1 Hz, which is the rhythm of vibration at vertical axe. Vertical acceleration has also lower components as the one placed at 0.4 Hz originated by the wave oscillation.

Gyroscope IMU data has also been analyzed and G_x, G_y and G_z angular velocities plotted at Figure 10 in rad/s. The natural frequency of this movement has been calculated from the FFT and it is shown at Figure 11. Notice that this 1.5 Hz matches with the natural frequency of the linear acceleration at the horizontal plane that corresponds to the pendulum drifter motion.

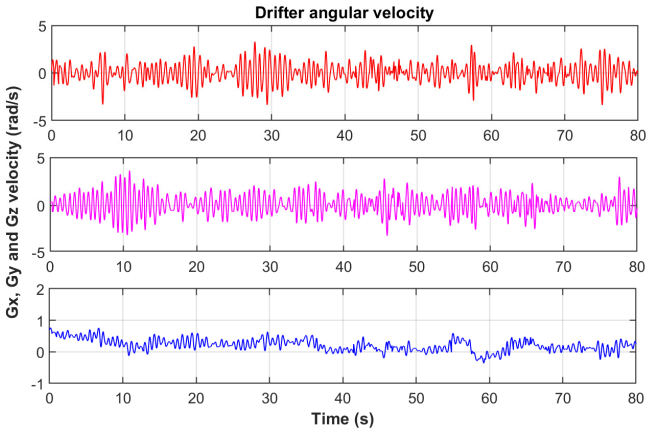

Figure 10. G_x, G_y and G_z angular velocities from the IMU sensor.

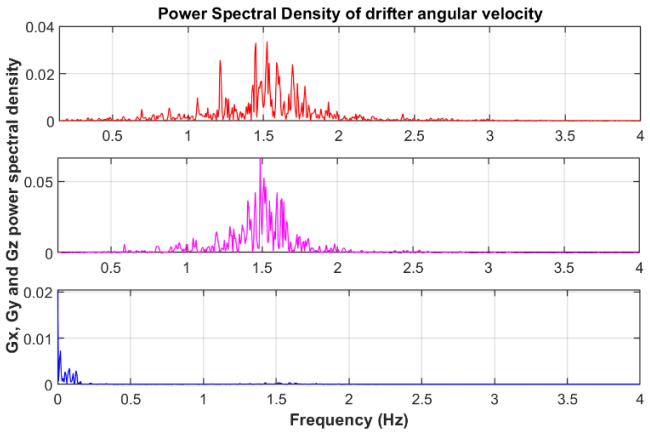

Figure 11. Power Spectrum of G_x, G_y and G_z angular velocities from IMU sensor.

Yaw motion has some low frequency component than generates its slow continuous rotation. This can be seen at G_z power spectrum plotted at Figure 11 where, apart from the 1.5

Hz pendulum motion, it contains some low frequency components. This can also be seen at Figure 10 where G_z contain positive offset that keeps yaw orientation rotating. This movement is supposedly caused by a small constructive error that causes a displacement of the center of mass of the vertical axis and, therefore, generates a torque among Z axe.

Pitch, Roll and Yaw orientation have been calculated from IMU data at NodeMCU and are plotted at Figure 12. Pitch and Roll oscillate with an amplitude of ±20º and Yaw from 180º to -180º repetitively at low motion.

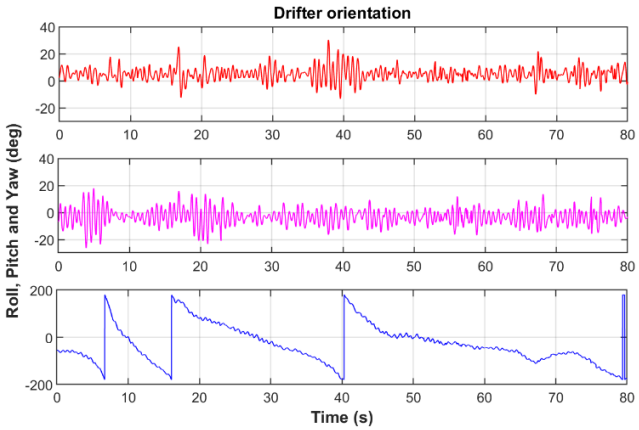

Figure 12. Roll, Pitch and Yaw orientation positions of the drifter during the experimental test calculated from IMU data.

To validate the obtained results, OrcaFlex simulation software has been used. A drifter as the one described in TABLE I has been modeled with a sphere composed by 24 stacked flat cylinders of different diameter (Figure 13). Mass center has been placed at 0.06 m of the sphere bottom. Sea state measured by ADCP and shown at TABLE II has been parametrized with JONSWAP model [22].

Figure 14 shows the power spectrum of linear acceleration obtained from simulation. Natural frequency of the pendulum motion at X-Y axis is found around 1.5 Hz. At vertical axe, the 1 Hz vibration can also be seen as well as the 0.4 Hz of sea elevation.

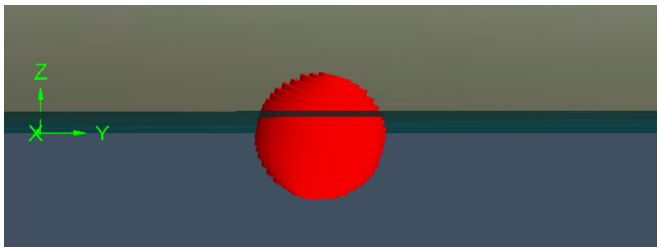

Figure 13. Oceanic WAVY drifter modeled by 24 stacked flat cylinders during the OrcaFlex simulation.

Figure 15 shows the power spectrum of the angular velocities obtained from the simulation. As expected, natural frequency of the drifter pendulum motion (1.5 Hz) can be found at X-Y axis. G_z power spectrum has no frequency component because, unlike the experimental case, the center of mass is placed on the vertical axis with no asymmetries.

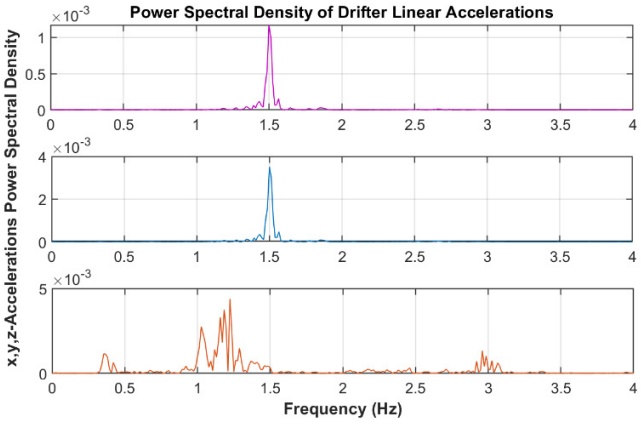

Figure 14. Power Spectrum of A_x, A_y and A_z linear acceleration from OrcaFlex Simulation tool. In this section, purple will be used for X axis, blue for Y axis and orange for Z axis

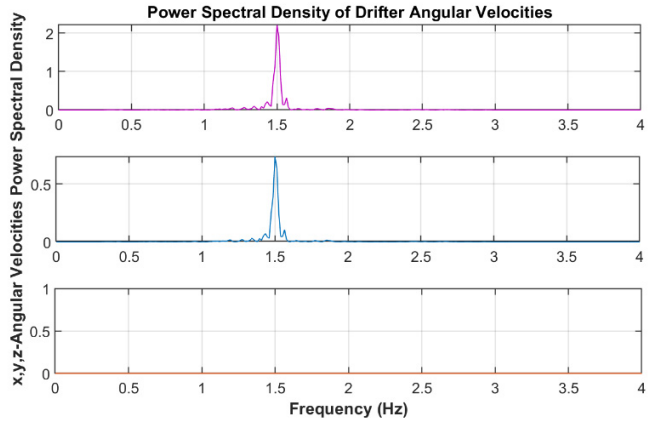

Figure 15. Power Spectrum of G_x, G_y and G_z angular velocities from OrcaFlex Simulation tool.

Later, different sea conditions have been simulated with the same drifter presented at TABLE I. Results show that the pendulum natural frequency of the drifter does not depend on the sea conditions but on its constructive parameters. As exposed at [23], the natural frequency of a body placed on a fluid depends on the fluid itself properties (density) and the spherical body design. Nevertheless, the magnitude of the accelerations and the potentially extractable power extraction do depend on the sea parameters such as wave frequency and height.

B. KEH rotation

Data obtained at the ADC coming from the photodiode has provided information about the KEH rotation. Figure 16 shows the digital signal of the ESP8266 ADC read after erasing the signal offset. Each pulse represents a complete rotation of the measured gear, which is supportive to the flywheel, being the high signal level the instant in which the emitter-receiver pair is aligned with the hole. The signal value grows with the infrared light intensity. At Figure 17, the ADC signal frequency domain has been plotted after applying the FFT and the main rotation frequency of the studied gear can be found between 1 and 2 Hz.

From the information provided by previous plots, the nearly continuous rotation of the device can be verified. The flywheel

does not have a pulsating motion so it rotates continuously between 1 and 2 Hz.

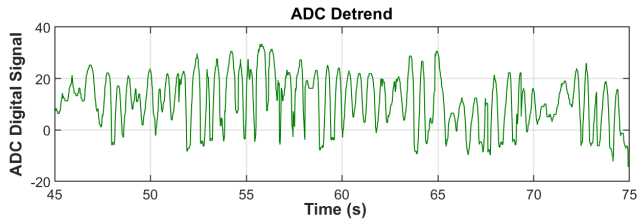

Figure 16. Analog read from the ESP8266 ADC showing the rotation behavior of the KEH.

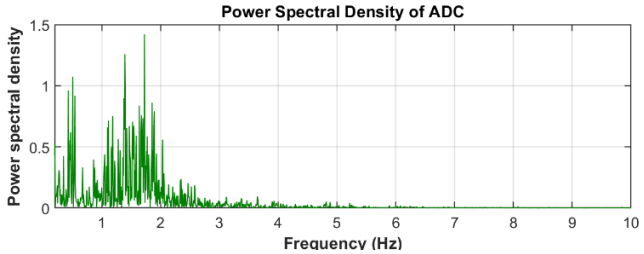

Figure 17. Power Spectrum of the Analog read from the ESP8266 ADC.

Given a transmission ratio of 15 between the studied gear and the micro generator, the micro generator rotation would be approximately 1400 rpm. Furthermore, according to the characterization done at previous works [16] (Figure 4), and assuming the PMU would achieve the MPPT, it can be concluded that about 2 mW could be generated. Finally, if the ADP5092 PMU also characterized in [16] is used, an efficiency of 80% would be obtained with this power input. That would mean 1.6 mW of useful power can be generated.

V. Conclusions

A designed KEH to be placed on a drifter has been tested at real sea conditions in a controlled area. The KEH consists on a pendulum system capable to transform the oscillations of the waves into rotation which would be converted into electrical energy thanks to a micro generator. A real drifter with the KEH has been deployed while an IMU sensor has provided information about its motion. The natural frequency of the pendulum motion of the drifter once deployed at the sea has been found at 1.5 Hz.

The same drifter has been modeled in OrcaFlex with the same experimental sea conditions read with an ADCP. Results show the natural frequency, similar to the one obtained at the experimental phase. Differences may be originated by the modeling of the spherical drifter. From the simulation of different sea states, it has been concluded that natural drifter pendulum motion does not depend on the wave parameters but on the drifter design.

The correct rotation of the KEH has also been monitored during the experiment thanks to a couple of infrared emitter-receiver. The rotation at the micro generator has been about 1400 rpm at nearly continuous operation. Also, its useful power output has been estimated at around 1.6 mW with the usage of the ADP5092 PMU.

For future woks, the frequency of resonance of the future KEH should be tuned at 1.5 Hz to maximize the power extraction. This is the natural frequency of the MELOA oceanic WAVY drifter. Also, to better understand the power generation, an in-situ power measurement system should be placed at the micro generator to know in real time the generated energy.

Acknowledgment

The authors extend their thanks to Orcina for their kind support and offer of the academic license OrcaFlex N2703 (2018) to Universitat Politècnica de Catalunya.

References

[1] R. Lumpkin, T. Özgökmen, and L. Centurioni, "Advances in the Application of Surface Drifters," *Ann. Rev. Mar. Sci.*, vol. 9, no. 1, pp. 59–81, 2017.

[2] "Albatros." [Online]. Available: http://albatrosmt.com/inicio/.

[3] Marine Instruments, "M3i Sounder buoy." [Online]. Available: https://www.marineinstruments.es/.

[4] Spoondrift, "Spoondrift Spotter." [Online]. Available: https://spoondrift.co/.

[5] Fastwave, "VOYAGER SOLAR DRIFTER BUOY." [Online]. Available: http://systems.fastwave.com.au/media/2102/fastwave-voyager-solar.pdf.

[6] P. M. Poulain, R. Gerin, E. Mauri, and R. Pennel, "Wind effects on drogued and undrogued drifters in the eastern Mediterranean," *J. Atmos. Ocean. Technol.*, vol. 26, no. 6, pp. 1144–1156, 2009.

[7] N. V Viet, N. Wu, and Q. Wang, "A review on energy harvesting from ocean waves by piezoelectric technology," *J. Model. Mech. Mater.*, vol. 1, no. 2, 2017.

[8] B. Drew, A. R. Plummer, and M. N. Sahinkaya, "A review of wave energy converter technology," *Proc. Inst. Mech. Eng. Part A J. Power Energy*, vol. 223, no. 8, pp. 887–902, 2009.

[9] S. P. Bastien, R. B. Sepe, A. R. Grilli, S. T. Grilli, and M. L. Spaulding, "Ocean wave energy harvesting buoy for sensors," *2009 IEEE Energy Convers. Congr. Expo. ECCE 2009*, pp. 3718–3725, 2009.

[10] Z. Zhang, B. Chen, S. R. K. Nielsen, and J. Olsen, "Gyroscopic power take-off wave energy point absorber in irregular sea states," *Ocean Eng.*, vol. 143, no. February, pp. 113–124, 2017.

[11] G. Bracco, E. Giorcelli, and G. Mattiazzo, "ISWEC: A gyroscopic mechanism for wave power exploitation," *Mech. Mach. Theory*, vol. 46, no. 10, pp. 1411–1424, 2011.

[12] W. Ding, B. Song, Z. Mao, and K. Wang, "Experimental investigation on an ocean kinetic energy harvester for underwater gliders," *2015 IEEE Energy Convers. Congr. Expo. ECCE 2015*, no. 20116102110009, pp. 1035–1038, 2015.

[13] Q. Guo *et al.*, "Design and experiment of an electromagnetic ocean wave energy harvesting device," *IEEE/ASME Int. Conf. Adv. Intel. Mechatronics*, pp. 381–384, 2018.

[14] B. D. Paul Mitcheson *et al.*, "Energy Harvesting From Human and Machine Motion for Wireless Electronic Devices," *Proc. IEEE*, vol. 96, no. 9, pp. 1457–1486, 2008.

[15] "MELOA project." [Online]. Available: https://www.ec-meloa.eu/.

[16] M. Carandell Widmer, D. Mihai Toma, M. Carbonell Ventura, M. Gasulla Forner, and J. del Río Fernández, "Design and development of a kinetic energy harvester device for oceanic drifter applications," *Instrum. Meas. Technol. Conf. - I2MTC.*, no. Accepted, 2019.

[17] L. D. A. Thorner, P. D. Mitcheson, A. S. Holmes, and E. M. Yeatman, "Scaling laws for energy harvesters in a marine environment," *PowerMEMS*, pp. 249–252, 2009.

[18] Z. Ballard and B. P. Mann, "Two-Dimensional Nonlinear Analysis of an Untethered Spherical Buoy Due to Wave Loading," *J. Comput. Nonlinear Dyn.*, vol. 8, no. 4, p. 041019, 2013.

[19] S. Heo, Y. S. Yang, J. Lee, S. Lee, and J. Kim, "Micro Energy Management for Energy Harvesting at Maximum Power Point," *Integr. Circuits*, vol. 13th, no. International Symposium, pp. 136–139, 2011.

[20] G. Grenon, P. E. An, S. M. Smith, and A. J. Healey, "Enhancement of the inertial navigation system for the Morpheus autonomous underwater vehicles," *IEEE J. Ocean. Eng.*, vol. 26, no. 4, pp. 548–560, 2001.

[21] A. Mànuel Làzaro, M. Nogueras, and J. del Río, "OBSEA an Oceanographic Seafloor Observatory," *Sea Technol.*, vol. 51, no. 7, pp. 37–39, 2010.

[22] M. S. Liew, E. S. Lim, and T. N. T. Shahdan, "Spectral Analyses of Sea-State Wave Data for the Development of Offshore Metocean Applications : A Malaysian Case Study," *Univ. Teknlogi Petronas, Malaysia.*, pp. 246–253, 2015.

[23] Z. Ballard, "Dynamics of Ocean Buoys and Athlete Motion for Energy Harvesting," no. Doctoral Thesis. Duke University. 2013.

A.6 Article 6

P.[57] - Design and Development of a Kinetic Energy Harvester Device for Oceanic Drifter Applications

---

Conference: IEEE International Instrumentation and Measurement Technology Conference – 2019 Auckland

Publisher: IEEE

Date of Publication: 9 September 2019

DOI: 10.1109/I2MTC.2019.8826996

Design and development of a kinetic energy harvester device for oceanic drifter applications

Matias Carandell
Sarti Research Group. Electronics Engineering Deparment.
Universitat Politècnica de Catalunya
Vilanova i la Geltrú, Spain
matias.carandell@upc.edu

Daniel Mihai Toma
Sarti Research Group. Electronics Engineering Deparment.
Universitat Politècnica de Catalunya
Vilanova i la Geltrú, Spain
daniel.mihai.toma@upc.edu

Montserrat Carbonell
Sarti Research Group. Electronics Engineering Deparment.
Universitat Politècnica de Catalunya
Vilanova i la Geltrú, Spain
montse.carbonell@upc.edu

Manel Gasulla
e-CAT Group. Electronics Engineering Department.
Universitat Politècnica de Catalunya
Castelldefels, Spain
manel.gasulla@upc.edu

Joaquín del Río
Sarti Research Group. Electronics Engineering Deparment.
Universitat Politècnica de Catalunya
Vilanova i la Geltrú, Spain
joaquin.del.rio@upc.edu

***Abstract*—A novel electronic energy harvester (EH) has been developed for oceanic undrogued drifter applications. First, spherical body motion simulation has been performed at sea environment in Orcaflex. Results help to understand the acceleration and forces applied on the drifter where the device will be placed. Second, the design of the EH is presented, consisting on a gyroscope pendulum system capable to transform the oscillations into rotation on a flying wheel. This rotation is converted into a DC current by a micro generator and further processed by a power management unit (PMU). Both, the generator and the PMU are characterized. Preliminary results in a water tank show that an average power of 0.22 mW can be produced. Finally, the feasibility of the proposed harvester is assessed as a backup power of a drifter using SigFox for coastal communications at low tracking rates.**

Keywords— Lagrangian Drifter, Energy Harvester (EH), Autonomous Sensor, Power Management Unit (PMU), Maximum Power Point Tracking (MPPT), low-power wide-area network (LPWAN), SigFox

I. INTRODUCTION

Science community needs related to oceanographic data are growing fast. Seas should be monitored in order to preserve their biodiversity and predict their evolution. This means that huge amounts of data from a very wide range of sensors should be generated and delivered as fast as possible. Research vessels collecting data from the ocean during long periods are becoming unusual due to their high-cost [1]. As a consequence, cabled observatories, gliders, pop-up drifters and long-term moorings are taking their place and are delivering enormous amounts of real or near-real time data to this community. One of these sea data providers are Lagrangian Drifters. These are autonomous floating passive devices that provide oceanographic surface data such as oceanic current flow, temperature, or salinity. They are used in climate research, oil spill tracking, or search and rescue operations. The National Oceanic and Atmospheric Administration counts on a drifter array of more than 1300 units deployed around the world and their data can be online accessed for scientific community in [2].

Many commercial drifters can be found in the market, from drogued to undrogued, depending on the ocean depths to be monitored. Basic drifters offer ocean current tracking and near surface temperature but they are evolving and now some of them can be found with Acoustic Doppler Current Profilers, salinity sensors, or weather stations. On the other hand, wireless communication is performed via GSM near-shore or via satellite (mostly Iridium-based) off-shore. Most of them also offer the possibility of bidirectional communication to modify parameters of the buoy [3]–[9].

Lumpkin et al. [10] describe the challenges related to the evolution and applications of drifters: measurement of currents, near-surface temperature and salinity or ocean dispersion, among others. Autonomy is one of the key points at drifters. Depending on the carried instruments and the duty cycle of the units, its lifespan may vary from hours up to two years when powered from primary batteries. If unlimited lifespan is pretended, some companies present drifters with PV solar panels that at some sampling interval may work at "perpetual" lifespan. The installed PV power is around units of watts [11]–[14].

Drifters strictly dedicated to monitor superficial ocean current should not be exposed to wind. Consequently, they must be mostly submerged with the exception of the communication antenna, which has to be out of the water. Even so, as demonstrated in [15], the downwind "slippage" at undrogued drifters is around 1% of the wind speed. This problem can be magnified when using PV panels that are out of water to ensure direct irradiation, as in [13]. On the other hand, when PV panels are inside the drifter sunlight is greatly attenuated by the water, as in [11].

In this work, as an alternative, a kinetic energy harvester (EH) system is presented, which uses the motion of the waves and the current flow to generate power. The EH is inside the drifter and thus does not increases the wind slippage of the unit. However, the generated power is relatively low and cannot provide the main power supply yet. The aim at this stage is to serve as an unlimited backup powering system, when the primary batteries are exhausted, allowing the drifter to send messages about its location in order to recover it.

This work was supported by the project MELOA from the European Commission's Horizon 2020 research and Innovation program under Grant Agreement No. 776280 and by the Spanish Ministry of Economy and Competitiveness and the European Regional Development Fund under project TEC2016-76991-P. The first author has a grant from the Secretariat of Universities and Research of the Ministry of Business and Knowledge of the Government of Catalonia on the FI program (ref. BDNS 362582).

978-1-5386-3460-8/19/$31.00 ©2019 IEEE

The paper is organized as follows. First, the simulation of a drifter motion in a fluid is presented at section II. Then, the proposed kinetic EH device is shown in section III. At section IV, the micro generator and the power management unit (PMU) are characterized while preliminary results show up at section V. Finally, the feasibility of the present system for drifter applications is discussed at section VI and section VII concludes the work.

II. Motion Simulation

A. Model

A spherical object of radius R (the drifter) mostly submerged into the water will be exposed to water-structure interaction. Fig. 1 shows a representation, where z is the vertical axis (positive upwards) and w is the position of the water line of the waves with respect to the still case. Therefore, understanding the dynamic motion response of a drifter due to external wave loading is essential in order to properly design kinetic EH devices.

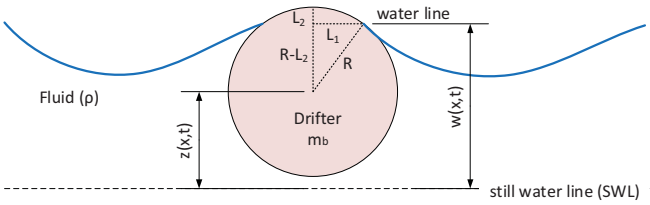

Fig. 1. Model of a mostly submerged drifter subjected to wave loading.

A study is performed in [16] and is concluded that a particle placed in a fluid with sufficiently deep water will follow the water line in a circular motion, as can be seen at Fig. 2. That motion will depend on the body characteristics, such as buoyancy and center of mass, and sea wave parameters such as the height and period.

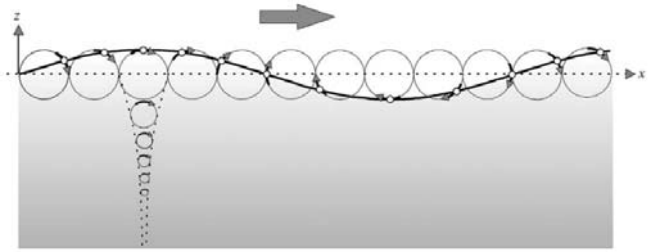

Fig. 2. Particle surface movement under wave interaction [16].

B. Numerical simulations

OrcaFlex 9.3c, a marine dynamics software implemented by Orcina based on Morison's equations [17], was used to study the dynamics of the spherical body into the water Simulations were performed with a spherical body such as that of Fig. 1 with the parameter values of TABLE I, coming from a planned undrogued drifter. Sea wave parameters were set between 1 to 6 meters for height and 4 to 12 seconds for period, which according to [18] are the most probable ocean conditions for North Atlantic Ocean. The ocean waves have been simulated in OrcaFlex using the JONSWAP spectrum, which is suitable for simulating deep-water waves.

TABLE I. Spherical drifter parameters on OrcaFlex simulation

Parameter	*Symbol*	*Value*	*Units*
Drifter mass	m_b	3.472	kg
Drifter radius	R	0.1	m
Fluid density	ρ	1027	kg/m^3
Center of mass[a]	c_m	0.08	m

[a] Center of mass taken from the bottom of the spherical drifter body.

C. Results

Results of the simulation are summarized in Fig. 3, where drifter vertical (z direction) and pitch accelerations are plotted. Values represent the average of the absolute instantaneous acceleration during a 100 seconds simulation. The unusual wave conditions have not been simulated. So, waves of high heights and low periods and of low heights and high periods have not been considered. Vertical body acceleration is between 0.1 to 2 m/s^2 and pitch acceleration is between 0.1 to 15 rad/s^2. Maximum accelerations, which should lead to a higher mechanical power of the EH presented in section III, occur at higher heights and lower periods (higher frequencies). In [16], the mechanical power at the axis of a gyroscope is modelled and found to also increase with the wave height and frequency.

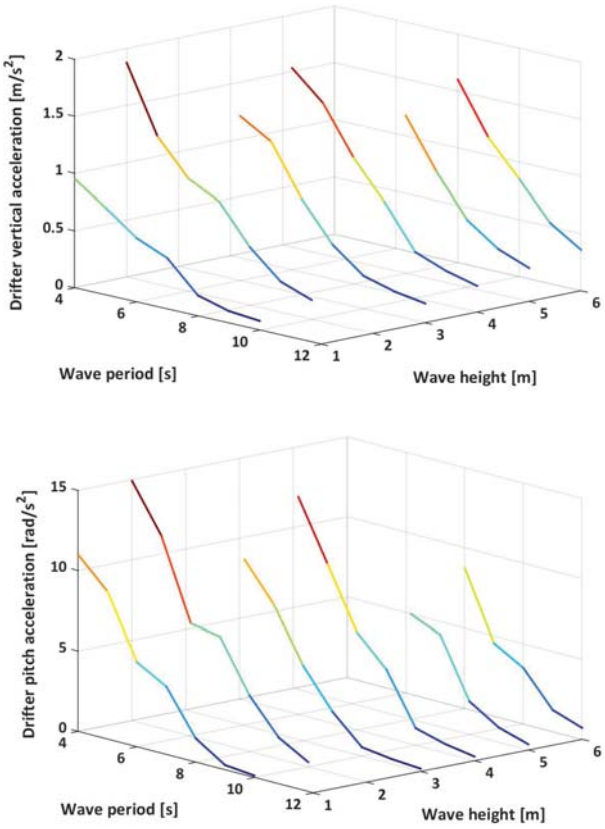

Fig. 3. Drifter vertical (above) and pitch (below) accelerations at different wave heights and periods.

III. Proposed Kinetic Energy Harvester Device

Many works propose EH devices that use kinetic energy from an anarchic source at relative low frequencies and high amplitudes (like sea motion). For example, for biomedical applications, walking body motion is used to generate power using an electromagnetic transducer. In [19], a sprung eccentric rotor is used in order to induce an electrical current. Higher energy levels are achieved using a pendulum and a dc micro generator at [20] and converting the bidirectional rotating movement into unidirectional through a gear system.

At sea environment, recent works show that the most usual approach to generate electrical energy is turning oscillations into rotations and using a generator as a transducer. Work done at [21] shows an ac generator based harvester placed on an underwater glider. It reaches 150 mW of mean output power with a volume around 0.1 m^3 and waves of 100 cm height and 1.3 s period. At [22], they use a dc generator that reaches 64 mW of maximum output power with a 500 cm^3 volume device and waves of 20 cm height and 1 s period. In [23], a design similar to our design (presented below) is reported, as it uses a gyroscope with a flying wheel, reaching a mean output power level of watts with a 0.5 m^3 volume (much larger than ours). However, it is an anchored buoy.

A general schematic of the designed kinetic EH device is shown in Fig. 4. The design is comprised of a gymbal system, a gearing transmission to transform the oscillations to rotation, a proof mass, a flywheel, and a micro electromagnetic generator. As a result of the interaction with the waves, the drifter, which contains the EH (Fig. 5), rotates with a pitching, roll and yaw motion. Then, the proof mass, which tries to maintain the vertical position by the gravity effect, rotates in relation with the drifter thanks to the gymbal arms. That generates a torque along the axis that through the gear system gets to the flywheel. There, the rotational movement is accumulated and then transmitted to the micro generator responsible for converting the torque into electrical power. Thanks to the one-way gear system, the generator only turns in one direction.

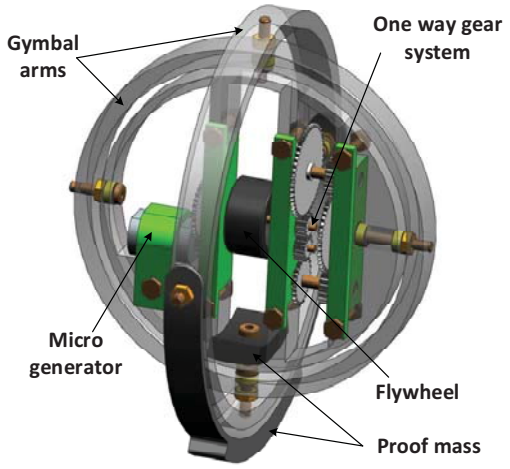

Fig. 4. Architecture of the proposed EH.

A first prototype of the EH has been manufactured with a mass of 360 g and a diameter of 12 cm. A picture of this prototype is shown at Fig. 6. Gimbal arms are made of methacrylate and the green supports are manufactured in a 3D printer with ABS plastic. The gear ratio is of 35 and the micro generator is a miniature DC motor with a nominal voltage of 3 V used in a reverse mode, i.e. using the electrical input as the output. An sketch is shown at Fig. 5 of the EH placed inside an undrogued drifter with the corresponding battery pack, the electronics and the antenna.

IV. Power Generation and Transfer

A. Generator and PMU description

In self-powered autonomous systems, energy management is crucial in order to maximize the lifespan of the device and to guarantee the most efficient way to handle the generated energy. Here, energy provided by the micro generator of the EH has to be managed. To achieve this, a PMU with a maximum power point tracker (MPPT) is required. Toh et al. designed in [24] a system to follow the maximum power point (MPP) of a micro generator by controlling the duty cycle of a boost converter who gives the power to a dc-link and a flyback converter to adequate the voltage level at the load. From then, many conversion systems have been developed depending on the energy source and [25] presents a summary. These ultralow PMU follow the MPP of the energy transducer and transfer the energy to a storage device, which tend to be a Li-ion battery, a super capacitor, or a hybrid storage system [26].

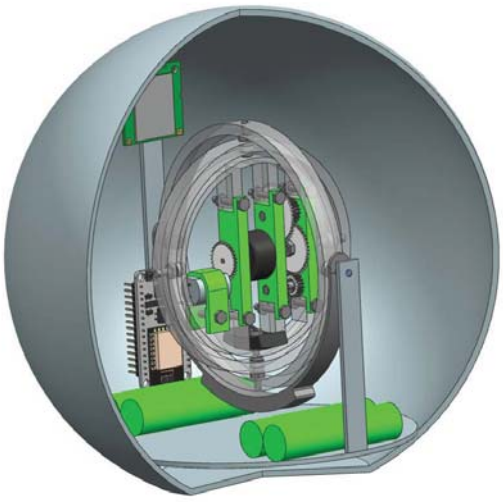

Fig. 5. Sketch of the kinetic EH placed inside an undrogued drifter, with battery pack, antenna and electronics.

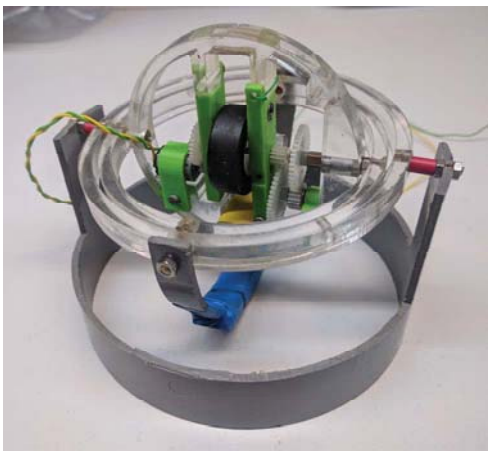

Fig. 6. Picture of the prototype of the designed kinetic EH.

Recently, many commercial PMU are showing up. In this work, the evaluation board of the ADP5092 (Analog Devices) has been used. This PMU is based on a boost regulator working on PFM mode [27], which fixes the input voltage (V_{IN}) as a fraction of the open circuit voltage (V_{oc}) of the EH in order to work at the MPP . It is able to control the charge with a very low internal consumption and work with V_{IN} as low as 80 mV. On the other hand, it provides a main output (SYS terminal), a battery charging terminal (BAT) with a programmable overcharge voltage from 2.2 to 5.2 V, and a regulated output settable from 1.5 to 3.6 V. The micro generator can be modelled as a Thévenin equivalent,

consisting of a voltage source (V_{oc}) in series with a resistor R_G. Maximum power will be harvested when loaded with a load (R_{LOAD}) equal to R_G. At this condition, V_{IN} will be half V_{oc}. Fig. 7 shows the connection of the micro generator, modelled as an equivalent Thévenin, to the ADP5092 PMU evaluation board.

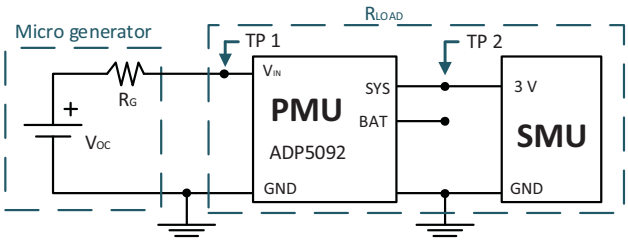

Fig. 7. Schematic of the generator and PMU.

B. *Preliminary characterization of the generator and PMU*

First, the micro generator was characterized. The shaft of the generator was rotated with the shaft of another DC motor at different rotation speeds, which aims to emulate those obtained from the designed device of Fig. 4, and the generator output was connected to a source measurement unit (SMU, Agilent B2901), in order to emulate different electrical loads. For each rotation speed, a voltage sweep was performed with the SMU while measuring the output power. Fig. 8 shows the experimental results, where the rotation speed in rpm is defined with no load connected to the generator output (output voltage is V_{oc}). As can be seen, for the three curves, the MPP happens around half V_{oc}, which is coherent with the Thévenin model of the generator [28]. In addition, V_{oc} is directly proportional to the rotation speed whereas the maximum power is proportional to its square. From the corresponding voltage-current characteristic (not shown), a load of around 18.5 Ω (R_{LOAD}) is inferred, which should match with the internal generator load (R_G). For the micro generator characterization, the uncertainty was determined at the MPP of the green curve (1530 rpm at OC). At this point, the standard deviation was 400 µW given by the uncertainty of the generator output calculated from 12 measurements.

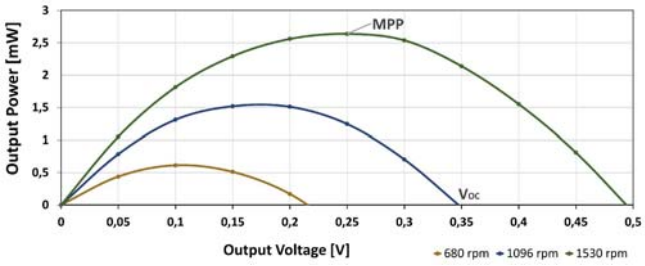

Fig. 8. Generator output power against output voltage for different shaft velocities (determined at generator open circuit).

Then, another test was performed to characterize the PMU efficiency, using the setup of Fig. 7 with the generator rotated as before. The ADP5092 was configured with V_{IN} at half V_{oc}, the regulated output disabled, and the BAT terminal floating (a capacitor of 100 µF is present in the evaluation board). Its SYS output was set at 3 V with the SMU. Two test point were defined for measuring the input and output power (TP1 and TP2, respectively). Input power was inferred using a multimeter for measuring the average current and an oscilloscope for measuring the average voltage (fixed by the PMU at half V_{oc}). Output power was directly measured by the SMU. Fig. 9 shows the measured powers and the PMU efficiency in function of the rotation speed of the micro generator. As can be seen, all increase as the shaft speed grows. At low rotation speed, the efficiency of the ADP5092 is low because the corresponding input MPP voltage approaches the lower limit of 80 mV but steeply increases with the rotation speed reaching almost 90%.

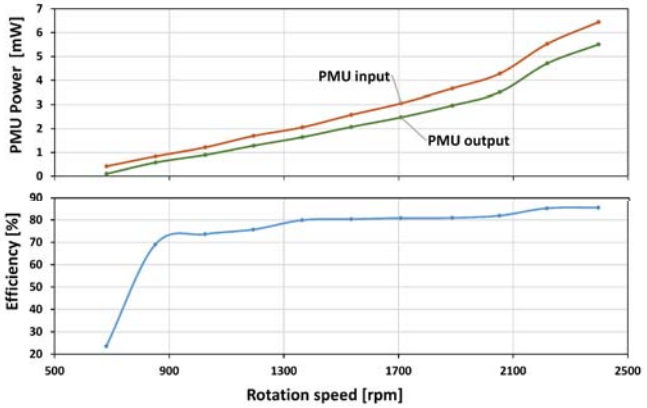

Fig. 9. PMU output power (above) and efficiency (below) in function of the rotation shaft speed.

V. Preliminary Results

The EH prototype described at section III was tested in an anchored buoy placed in a water tank simulating waves of 10 cm height with periods in the 3 s to 6 s range. Fig. 10 shows the output power of the EH loading the output of the generator with a 50 Ω resistor (that of the oscilloscope used to measure its output voltage). The PMU was not used here. As can be seen, the output power presents a high variability, since the rotation speed is not constant, with an average value of 0.22 mW. Maximum power is within the MPP range found at Fig. 8.

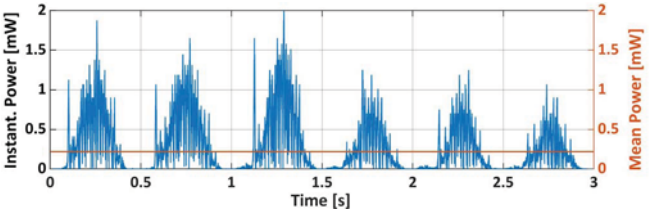

Fig. 10. Instantaneous output power of the EH device tested on the water tank with 50 Ohms load.

Then, the EH placed at the water tank was connected to the ADP5092 module to test its functionality in almost real conditions. The connection was similar to that of Fig. 7 but without the SMU. Instead, an oscilloscope was connected to TP1 (CH1) and TP2 (CH2), and a 470 mF super capacitor was placed at BAT terminal, at 3.6 V. Fig. 11 shows V_{IN} (pink – TP1) and the SYS output of the PMU (yellow). Three different regions can be appreciated, from left to right:

- First region: SYS voltage is dropping from 3.6 because the V_{IN} is below the minimum working value (80 mV, marked with a dashed white line).
- Second region: SYS signal is 0 V. EH is now generating power and the PMU enters in the cold startup operation.
- Third region: The EH continues generating power so SYS output terminal raise again to 3.6 V.

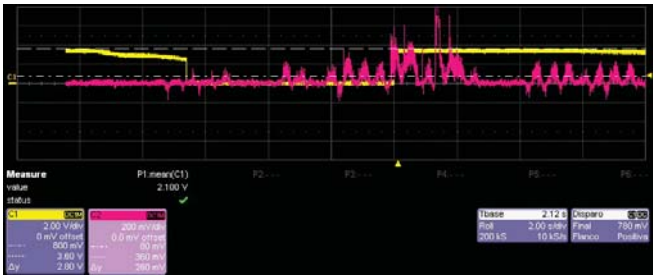

Fig. 11. Oscilloscope screenshot of system operation at water tank test.

VI. Feasibility for Drifter Coastal Application

As said in section I, coastal (near-shore) drifters tend to be GSM communication-based. However, low-power wide-area network (LPWAN) offer an attractive solution as a tracking coastal communication since they allow to send small packages at long distances with low power consumption, which is suitable for self-powered drifters as the proposed here. In particular, SigFox is a payable LPWAN technology that includes the Base Stations and the Backend Services and works at 868 MHz (ISM band). It offers to send up to 140 messages/day per device with a payload of 12 bytes each one. Although it is a short package it is enough to send the position and some data as the temperature. The TD1205P model is a low power SigFox module that also includes the Global Navigation Satellite System (GNSS), and temperature and accelerometer sensors for tracking applications in a 30×38×10.5 mm size.

In previous works [29], the TD1205P power consumption was evaluated at transmitting and sleeping mode in a coastal area. Considering a transmitting cycle every 2 hours, the required energy per day is 18 J. With the power generated at the water tank test (average of 0.22 mW), 19 J can be generated per day, so the TD1205P could be fed from this EH. Moreover, with a 470 mF super capacitor at 3.6 V as the one used previously, the peaks of energy at the transmitting phase (1.3 J) would lead to a minimum voltage of 2.73 V, which is assumable. However, for these calculations the PMU is not considered, so further work is needed.

VII. Conclusions

A novel EH device has been designed and developed. It counts on a gearing system that transform the pendulum oscillations into rotation in a flywheel transmitted to a micro electromagnetic generator. Furthermore, the micro generator and the ensuing ADP5092 PMU have been characterized, showing an increasing electrical power and efficiency with the rotation speed. In addition, the EH system has been tested on a water tank generating an average power of 0.22 mW. Finally, a LPWAN technology based on SigFox is assessed as a tracking system for drifter coastal applications which can achieve 12 transmissions per day. The generated output power of 0.22 mW is estimated to be enough to power the SigFox module; however, the efficiency of the PMU has not already been taken into account.

Acknowledgment

The authors extend their thanks to Orcina for their kind support and offer of the academic license OrcaFlex N2703 (2018) to Universitat Politècnica de Catalunya. Also, the authors want to acknowledge Albert Garcia-Benadí for the uncertainty calculations of the measurements.

References

[1] R. E. Thomson and W. J. Emery, *Data Analysis Methods in Physical Oceanography: Third Edition*. 2014.

[2] National Oceanic and atmospheric Administration. Atlantic Oceanographic and Meteorological Laboratory, "Global Drifter Array. NOAA." [Online]. Available: http://www.aoml.noaa.gov/phod/gdp/index.php.

[3] L. Emery, R. Smith, R. McQuary, B. Hughes, and D. Taylor, "Autonomous River Drifting Buoys," *Oceans*, pp. 1–5, 2011.

[4] "Lagrangian Drifter Laboratory." [Online]. Available: http://gdp.ucsd.edu/ldl_drifter/index.html.

[5] "Pacific Gyre." [Online]. Available: https://www.pacificgyre.com/.

[6] K. Raghukumar, G. Chang, F. Spada, C. Jones, W. Gans, and T. Janssen, "Wave-Measuring Performance Characteristics of Spoondrift Spotter," *5th Annu. Mar. Energy Technol. Symp.*, p. 2017, 2017.

[7] "Albatros." [Online]. Available: http://albatrosmt.com/inicio/.

[8] "Fastwave." [Online]. Available: http://www.fastwave.com.au/.

[9] "Marine Instruments." [Online]. Available: http://www.marineinstruments.es/.

[10] R. Lumpkin, T. Özgökmen, and L. Centurioni, "Advances in the Application of Surface Drifters," *Ann. Rev. Mar. Sci.*, vol. 9, no. 1, pp. 59–81, 2017.

[11] Albatrosmt, "Ocean Drifter iridium buoy."

[12] Marine Instruments, "M3i Sounder buoy."

[13] Spoondrift, "Spoondrift Spotter.," pp. 1–2, 2017.

[14] Fastwave, "VOYAGER SOLAR DRIFTER BUOY." [Online]. Available: http://systems.fastwave.com.au/media/2102/fastwave-voyager-solar.pdf.

[15] P. M. Poulain, R. Gerin, E. Mauri, and R. Pennel, "Wind effects on drogued and undrogued drifters in the eastern Mediterranean," *J. Atmos. Ocean. Technol.*, vol. 26, no. 6, pp. 1144–1156, 2009.

[16] M. Carlsen *et al.*, "Efficiency of a gyroscopic device for conversion of mechanical wave energy to electrical energy," *Technical report from ESGI-83 workshop in industrial mathematics*. 2011.

[17] J. R. Morison, J. W. Johnson, and S. A. Schaaf, "The Force Exerted by Surface Waves on Piles," *J. Pet. Technol.*, 1950.

[18] R. Atan, J. Goggins, and S. Nash, "A Detailed Assessment of the Wave Energy Resource at the Atlantic Marine Energy Test Site," *Proc. 11th Eur. Wave Tidal Energy Conf.*, pp. 1–8, 2016.

[19] M. A. Halim, R. Rantz, Q. Zhang, L. Gu, K. Yang, and S. Roundy, "An electromagnetic rotational energy harvester using sprung eccentric rotor, driven by pseudo-walking motion," *Appl. Energy*, vol. 217, pp. 66–74, 2018.

[20] L. Xie, C. G. Menet, H. Ching, and R. Du, "The Automatic Winding Device of a Mechanical Watch Movement and Its Application in Energy Harvesting," *J. Mech. Des.*, vol. 131, no. 7, 2009.

[21] W. Ding, B. Song, Z. Mao, and K. Wang, "Experimental investigation on an ocean kinetic energy harvester for underwater gliders," *2015 IEEE Energy Convers. Congr. Expo. ECCE 2015*, no. 20116102110009, pp. 1035–1038, 2015.

[22] Q. Guo *et al.*, "Design and experiment of an electromagnetic ocean

wave energy harvesting device," *IEEE/ASME Int. Conf. Adv. Intel. Mechatronics*, pp. 381–384, 2018.

[23] Z. Zhang, B. Chen, S. R. K. Nielsen, and J. Olsen, "Gyroscopic power take-off wave energy point absorber in irregular sea states," *Ocean Eng.*, vol. 143, no. February, pp. 113–124, 2017.

[24] E. M. Y. Tzern T. Toh, A. Bansal, G. Hong, Paul D. Mitcheson, Andrew S. Holmes, "Energy harvesting from rotating structures," no. 50, pp. 4461–4462, 2007.

[25] J. Kokert, T. Beckedahl, and L. M. Reindl, "Medlay: A reconfigurable micro-power management to investigate self-powered systems," *Sensors (Switzerland)*, vol. 18, no. 1, 2018.

[26] M. T. Penella and M. Gasulla, "Runtime extension of low-power wireless sensor nodes using hybrid-storage units," *IEEE Trans. Instrum. Meas.*, vol. 59, no. 4, pp. 857–865, 2010.

[27] F. Reverter and M. Gasulla, "Optimal Inductor Current in Boost DC/DC Converters Regulating the Input Voltage Applied to Low-Power Photovoltaic Modules," *IEEE Trans. Power Electron.*, vol. 32, no. 8, pp. 6188–6196, 2017.

[28] S. Heo, Y. S. Yang, J. Lee, S. Lee, and J. Kim, "Micro Energy Management for Energy Harvesting at Maximum Power Point," *Integr. Circuits*, vol. 13th, no. International Symposium, pp. 136–139, 2011.

[29] M. Carandell, D. Mihai, J. Río, K. Ganchev, and J. Peudennier, "Evaluation of Sigfox LPWAN technology for autonomous sensors in coastal applications," *Instrum. Viewp.* -, vol. 20, 2018.

UNIVERSITAT POLITÈCNICA
DE CATALUNYA
BARCELONATECH